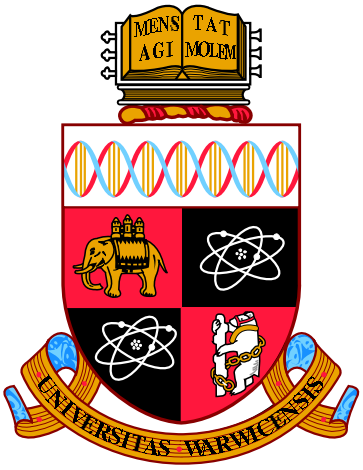

Quantitative Electrical Characterisation of Organic Semiconductors by Atomic Force Microscopy

by

Dawn Wood

Thesis

Submitted to the University of Warwick

for the degree of

Doctor of Philosophy

Chemistry

July 2017

THE UNIVERSITY OF WARWICK

Contents

List of Tables

List of Figures

Acknowledgments

Firstly, I would like to thank the EPSRC and Oxford Instruments Asylum Research for their funding to carry out this project, in particular Chris Mulcahy and Jonathan Moffat for your continued support. My gratitude also goes to my supervisors Neil Wilson and Tim Jones for their guidance and patience over the past 4 years.

Productive and fulfilling work cannot be done without the friendship and intellectual discussion that comes from being part of two great research teams. So for their input into this work my thanks go to the Warwick Microscopy group: Zac, Alex M, Alex H, Sam, Jon, Natalie, Reza, Ali, Keith, Adam, Volker, Jeremy, Ana, Richard, Steve Y and Steve H; and the Tim Jones group: Luke, Ian, Paul, Chloe, Natalie, Gavin, Nicola, Ed and Tom.

Honourable mentions go to my mum and brother, who may not have helped with the actual work, but they taught me the patience to continue trying, even when the problems feel bigger than you can handle. Thank you dad for pushing me to want to exceed my own expectations and boundaries. Jess, your positivity and late night discussions gave me inspiration in the long nights of writing, I am eternally grateful. Wrath, MJF and Alto, thank you all for proof reading my grammar, your friendship is invaluable. Finally, thank you Mark, for your help with coding, and life in general; I couldn't have done this without you.

Declarations

I declare that this thesis contains an account of my research carried out at the Department of Chemistry, University of Warwick between October 2012 and September 2016 under the supervision of Prof. T. S Jones and Dr N. R. Wilson. The work reported here has not been previously submitted, wholly or in part, at this or any other academic institution for admission to a higher degree.

Parts of this thesis have been published by the author between October 2012 and September 2016:

- The work on temperature dependent C-AFM of P3HT in Section 3.1 was published under the title "Quantitative Nanoscale Mapping with Temperature Dependence of the Mechanical and Electrical Properties of Poly(3-Hexylthiophene) by Conductive Atomic Force Microscopy" [1].

- The work on FVBS of VOPc in Section 3.2 was published under the title "Growth of Large Crystalline Grains of Vanadyl-Phthalocyanine without Epitaxy on Graphene" [2].

All the work presented here was completed by myself, except for the following:

- VOPc depositions on graphene in Section 3.2 were done by Alex Marsden and Luke Rochford.

- PTB7:$PC_{70}BM$ samples in Chapter 4 were made by Martin Tyler.

- TEM images of AFM tips in Figure 2.10 were taken by Steve York.

Dawn Wood, September 2016

Abstract

Organic photovoltaics (OPVs) may be the future of energy production, one day possibly solving the energy crisis we currently face. However, OPVs still have lower efficiencies than conventional silicon technologies and suffer from low carrier mobilities and stability problems. To improve OPV performance and stability we need to characterise them, both on a device level and on a nanoscale level. The nanoscale is especially relevant to polymer:fullerene solar cells as their performance is heavily dependent on their morphologies.

This thesis presents three techniques that use atomic force microscopy (AFM) to measure the nanoscale, electrical and mechanical properties of these systems, whilst maintaining access to the morphology of the sample. Force volume bias spectroscopy (FVBS) combines traditional force-volume measurements and current-voltage (IV) measurements using the Johnson-Kendal-Roberts model of contact mechanics to accurately determine the sample's Young's modulus and the tip-sample contact area. The calculated contact area is then used to calculate the current density from the associated IV curve. A modified Mott-Gurney model allows the extraction of mobility and charge carrier density dependence. The temperature dependence of P3HT between 70 and 130°C is investigated with FVBS, showing an increase in mobility with temperature. The properties of as-cast and annealed P3HT are also compared; with annealed P3HT showing a correlation between mechanical and electrical properties that is not present in the as-cast film.

Time resolved EFM (Tr-EFM) is a non-contact technique that uses the change of phase of an oscillating cantilever in response to an applied pulse of light, to characterise the surface photovoltage (SPV) and timescale of charge accumulation and decay in photovoltaic materials. Two bulk heterojunction systems were studied; P3HT:PCBM and PTB7:PC_{70}BM. The SPV and the dynamic response were studied as a function of illumination intensity and temperature. The dynamic response showed no clear trend with temperature or light intensity for either system. For P3HT:PCBM the SPV has complex temperature dependent behaviour, showing increased SPV with temperature and an SPV peak at 90°C. SPV decreased with temperature for PTB7:PC_{70}BM. Both systems showed logarithmic behaviour of the SPV with light intensity, suggesting that the SPV is a measure of the open circuit voltage of the bulk heterojunction.

Intensity modulated Kelvin probe force microscopy (IM-KPFM) uses a modulated light to dynamically modulate the SPV in the thin film devices. Changing the frequency of modulation allows the timescale of charge depletion to be measured. The temperature dependence of this is investigated for P3HT:PCBM and PTB7:PC_{70}BM. Both P3HT:PCBM and PTB7:PC_{70}BM showed decreasing timescales with temperature. The behaviour of P3HT:PCBM was more complicated than PTB7:PC_{70}BM, showing peaks in the timescale measured. The results and benefits of IM-KPFM and Tr-EFM are then compared.

Abbreviations

AFM	atomic force microscopy
BHJ	bulk heterojunction
CAFM	conductive atomic force microscopy
CVD	chemical vapour deposition
DAC	digital to analogue converter
DMT	Derjaguin-Muller-Toporov model of contact mechanics
DSC	differential scanning calorimetry
EFM	electrostatic force microscopy
EQE	external quantum efficiency
FET	field effect transistor
FVBS	force volume bias spectroscopy
HOMO	highest occupied molecular orbital
IM-KPFM	intensity modulated Kelvin probe force microscopy
ITO	indium tin oxide
IV	current vs. voltage measurements
JKR	Johnson-Kendall-Roberts model of contact mechanics

J_{SC}	short circuit current density
JV	current density vs. voltage
LED	light emitting diode
KPFM	Kelvin probe force microscopy
LUMO	lowest unoccupied molecular orbital
MoO_x	molybdenum oxide
OMBD	organic molecular beam deposition
OPV	organic photovoltaic
OSC	organic semiconductor
P3HT	poly-3-hexylthiophene
pc-AFM	photoconductive atomic force microscopy
PCBM	phenyl-C61-butyric acid methyl ester
$PC_{70}BM$	phenyl-C71-butyric acid methyl ester
PEDOT:PSS	poly(3,4-ethylenedioxythiophene):poly(4-styrene sulphonate)
PMMA	polymethylmethacrylate
PPV	poly(p-phenylene vinylene)
PTB7	poly[[4,8-bis[(2-ethylhexyl)oxy]benzo[1,2-b:4,5-b']dithiophene-2,6-diyl][3-fluoro-2-[(2-ethylhexyl)carbonyl]thieno[3,4-b]thiophenediyl]]
QCM	quartz crystal microbalance
RAM	random access memory
SAM	self assembled monolayer
SCLC	space charge limited current

SEM	scanning electron microscopy
SKPM	scanning Kelvin probe microscopy
SPV	surface photovoltage
STM	scanning tunnelling microscope
TEM	transmission electron microscopy
TPV	transient photovoltage
Tr-EFM	time resolved electrostatic force microscopy
UHV	ultra high vacuum
V_{OC}	open circuit voltage
VOPc	vanadyl oxide phthalocyanine
XRD	X-ray diffraction

Chapter 1

Introduction

1.1 History and Motivation

In recent years, due to the need for clean, renewable energy solutions, photovoltaic technologies have been extensively researched [3, 4, 5]. Even though the photovoltaic effect was discovered in 1839 by Edmond Bequerel [6], we are still discovering the potential of materials to exhibit photovoltaic properties, with the recent emergence of perovskite solar devices [7]. Over the course of this time the progress of photovoltaics has been widespread, with the first commercial solar devices being used exclusively on space craft [8]. Since then, by far the most common photovoltaic devices have been made from silicon, with crystalline silicon solar cells being the most efficient at 25% [9, 10]. However, the need to lower the production costs (5 \$/W for c-si [11] compared to 2.1 \$/W for coal power plants [12]) of solar devices has led to increased research into thin film solar technologies, such as amorphous silicon [13].

More recent developments in this area include cadmium telluride (CdTe) and copper indium gallium diselenide (CIGS) devices, both of which show promising efficiencies of 22.1% and 22.3% respectively in thin film devices [14, 15]. These, along with amorphous silicon devices, are known as second generation solar devices. Their benefits over the first generation of crystalline silicon devices include lower manufacturing costs (resulting in purchasing costs of 0.240 \$/W for a-Si compared to 0.296 \$/W for c-Si [16]) and a degree of flexibility in substrate choice allowing for devices to evolve from a flat panel design [17]. However, these devices are often made from materials that are toxic and in limited natural supply [18, 19], consequently the search for viable alternatives to these is ongoing [20]. Second generation solar technologies also have a lower efficiency than the first generation, for this reason

and the environmental considerations a third generation of photovoltaic devices is being studied [21].

The third generation of solar cell technologies aims primarily to exceed the Shockley-Quisser limit of efficiency (30% with a 1.1 eV band gap) which exists for a single band-gap material [22]. There are multiple ways of achieving this aim including using tandem cells, hot carrier cells, multiband cells and thermovoltaic cells [21, 23]. The second goal of third generation solar power is to deliver scalable, cheap and environmentally friendly solar cells, in this regard organic photovoltaics (OPVs) are promising as they are predominantly made from highly abundant carbon, and have the capability to be roll-to-roll printed [24]. Figure 1.1 shows the record efficiencies for research solar cells of each generation. The gradient of the efficiency curve is notably high for both perovskite technologies, which have shown a high potential [7], and for OPVs.

1.2 Organic Photovoltaics (OPVs)

The optical and electronic properties of organic semiconductors such as acenes have led to 30 years of development of organic photovoltaic (OPV) devices [25]. Since then a range of devices have been demonstrated and optimized sufficiently to be used for commercial applications, such as organic light emitting diodes (OLEDs) [26, 27], small molecule and polymer OPVs [28, 29]. In 1986, Tang demonstrated an organic heterojunction photovoltaic device from copper phthalocyanine (CuPc) and a perylene tetracarboxylic derivative, deposited by vacuum evaporation achieving an efficiency of around 1% [30]. This device shared the planar heterojunction format favoured by inorganic semiconducting junctions. However, it was determined that these devices could be made more efficient by intermixing the donor and acceptor materials. The intermixing of the donor and acceptor domains throughout the device is known as a bulk heterojunction (BHJ). Subsequent to Tang's device, it was realised that the lifetime of excitons in OPV devices is short, around 100 ps - 1 ns, so the interfaces where the excitons can separate need to be within a short distance of their creation as the diffusion length directly depends on the exciton lifetime, and is typically 10-20 nm [31]. Equally, the device cannot be made this thin as it would not absorb the photons efficiently. Figure 1.2 shows a schematic of a single heterojunction device compared to a bulk heterojunction. An exciton created in most places of the BHJ can diffuse to an interface whereas excitons created near either surface of the discrete heterojunction may not arrive at the donor acceptor interface.

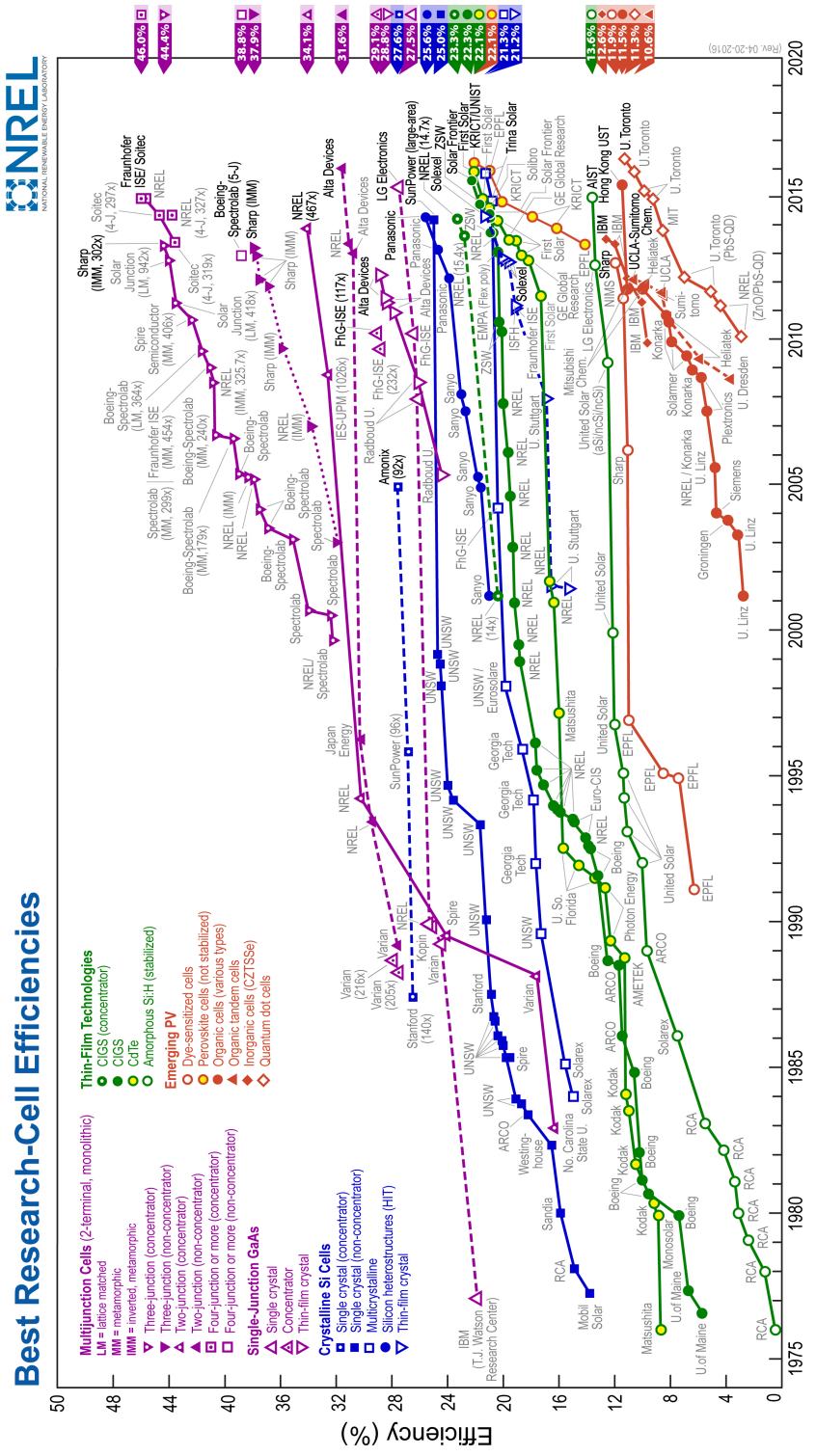
Best Research-Cell Efficiencies
NREL
Efficiency (%)
Rev. 04-20-2016)
Multijunction Cells (2-terminal, monolithic)
LM = lattice matched
MM = metamorphic
IMM = inverted, metamorphic
Three-junction (concentrator)
Three-junction (non-concentrator)
Two-junction (concentrator)
Two-junction (non-concentrator)
Four-junction or more (concentrator)
Four-junction or more (non-concentrator)
Single-Junction GaAs
Single crystal
Concentrator
Thin-film crystal
Crystalline Si Cells
Single crystal (concentrator)
Single crystal (non-concentrator)
Multicrystalline
Silicon heterostructures (HIT)
Thin-film crystal
Thin-Film Technologies
CIGS (concentrator)
CIGS
CdTe
Amorphous Si:H (stabilized)
Emerging PV
Dye-sensitized cells
Perovskite cells (not stabilized)
Organic cells (various types)
Organic tandem cells
Inorganic cells (CZTSSe)
Quantum dot cells
45.6%
44.4%
38.8%
37.9%
34.1%
31.6%
28.1%
28.8%
27.6%
27.5%
25.6%
25.0%
23.3%
23.3%
22.1%
22.1%
21.3%
21.2%
13.6%
13.6%
11.9%
11.5%
11.3%
10.6%
Sharp (IMM, 302x)
Soitec (4-J, 297x)
Solar Junction (LM, 942x)
Fraunhofer ISE/ Soitec
NREL
Spire Semiconductor (MM, 406x)
NREL (4-J, 327x)
Soitec (4-J, 319x)
Boeing-Spectrolab (5-J)
Sharp (IMM)
Solar Junction (LM, 418x)
Boeing-Spectrolab (LM, 364x)
Fraunhofer ISE (MM, 454x)
Boeing-Spectrolab (MM, 240x)
NREL (IMM, 325.7x)
Sharp (IMM)
Boeing-Spectrolab (MM,299x)
Boeing-Spectrolab (MM,179x)
NREL (IMM)
NREL
Boeing-Spectrolab
Sharp (IMM)
NREL (467x)
Alta Devices
NREL
Alta Devices
FhG-ISE (117x)
Alta Devices
IES-UPM (1026x)
Radboud U.
FhG-ISE (232x)
Amonix (92x)
LG Electronics
Panasonic
SunPower (large-area)
NREL (14.7x)
Solexel
ZSW
Solar Frontier
KRICT/UNIST
First Solar
EPFL
Trina Solar
NREL (154x)
ZSW
EMPA (Flex poly)
Solexel
ISFH
Fraunhofer ISE
KRICT
Solibro
Solar Frontier
GE Global Research
KRICT
Alta Devices
Panasonic
FhG-ISE
Sanyo
NREL
ZSW
First Solar
Global Research
EPFL
AIST
Hong Kong UST
U. Toronto
IBM
Sharp
NIMS
LG Electronics
United Solar (aSi/mcSi/ncSi)
Mitsubishi
IBM
Konarka
Helietek
UCLA
Sumi-tomo
UCLA-Sumitomo Chem.
MIT
U. Toronto
U. Toronto (PbS-QD)
NREL (ZnO/PbS-QD)
U. Dresden
Solarmer
Konarka
Plextronics
Helietek
NREL / Konarka
U. Linz
Siemens
U. Linz
Groningen
U. Linz
Sharp
IBM
United Solar
EPFL
Photon Energy
Boeing
AMETEK
ARCO
Solarex
Kodak
Boeing
Kodak
Kodak
Boeing
Kodak
Monosolar
Boeing
U.of Maine
U.of Maine
Matsushita
Mobil Solar
Sandia
RCA
No. Carolina State U.
Solarex
Westing-house
ARCO
UNSW
Spire
Stanford
Varian
Varian (205x)
Varian (216x)
Varian
Kopin
Spire
IBM (T.J. Watson Research Center)
NREL
Stanford (140x)
SunPower (96x)
Japan Energy
NREL
NREL/ Spectrolab
Spectrolab
Spectrolab
Spectrolab
Spectrolab
Boeing-Spectrolab
Boeing-Spectrolab
Boeing-Spectrolab
Boeing-Spectrolab
Boeing-Spectrolab
Radboud U.
Amonix (92x)
FhG-ISE
Sanyo
Sanyo
Sanyo
Sanyo
FhG-ISE
UNSW / Eurosolare
NREL (14x)
Georgia Tech
Georgia Tech
Georgia Tech
Georgia Tech
U. So. Florida
Matsushita
NREL
Euro-CIS
United Solar
United Solar
EPFL
EPFL
EPFL
EPFL
United Solar
NREL
NREL
NREL

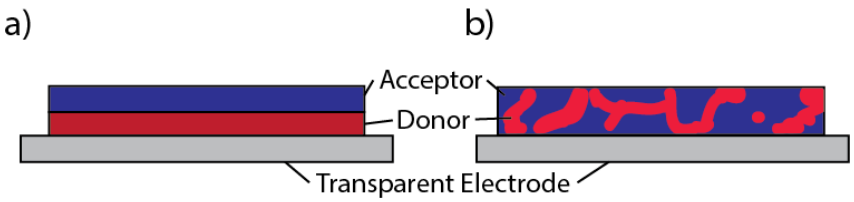

Figure 1.2: A comparison of a) a single heterojunction and b) a bulk heterojunction.

The first BHJ was demonstrated by Halls et al., and was made from a phase segregated mixture of two poly(p-phenylene vinylene) PPV derivatives CN-PPV and MEH-PPV [32]. In addition to having a higher efficiency than the device made by Tang, Hall's device was solution processed, demonstrating that these devices could be made in large areas without the high temperature and often expensive processing needed for earlier generation photovoltaics.

Current research aims to make these organic devices efficient, large area, long lived, flexible and easy to manufacture. Each of these aims has its own challenges. Stability is an ongoing challenge for OPVs, as many of the materials used are susceptible to chemical degradation caused by activation of oxygen by UV light or the diffusion of water into the active material [33, 34]. Some effects of degradation can be limited by encapsulation of these devices, but this is an imperfect solution [35, 36]. Significant progress has been made in large area manufacture and flexibility, the ability to solution process OPVs makes screen and roll-to-roll printing a viable way to scale up manufacture of these devices [37]. Roll-to-roll printing techniques require the use of flexible electrodes and substrates.

One common choice of electrode for inflexible devices is indium tin oxide (ITO), which is both highly transparent in the visible spectrum and has a low electrical resistivity of 2 - 4 $\times$ 10^{-4} Ωcm [38]. However, ITO is inherently brittle and cannot be used for flexible devices. Developing alternatives to ITO is also advantageous as indium is expensive and rare with supplies dwindling [39, 40, 41]. Viable alternatives to ITO that can be roll-to-roll processed include silver electrodes of various forms [41, 42], poly(3,4-ethylenedioxythiophene):poly(4-styrene sulphonate) (PEDOT:PSS) [43, 44, 45, 46], and even graphene [47]. Increasing the efficiency is one of the key steps towards achieving commercial success with OPVs [48, 49].

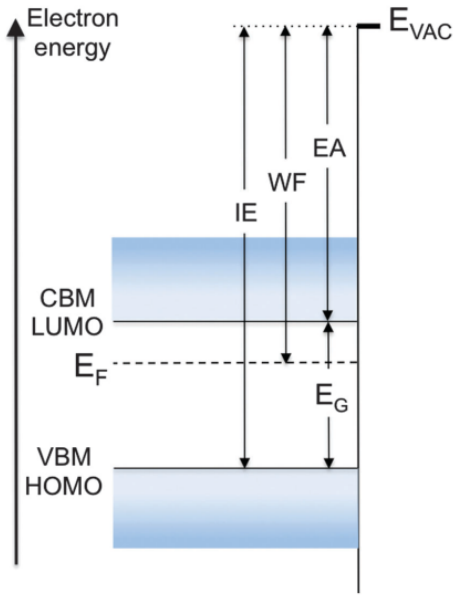

Figure 1.3: Energy diagram of a semiconductor with flat bands, showing the conduction band minimum(CBM) or LUMO, and the valence band maximum (VBM) or HOMO levels. The local vacuum level (E_{VAC}), electron affinity (EA), work function (WF), ionisation energy (IE), Fermi level (E_F) and band gap (E_G) are also shown. Figure taken from [50].

1.2.1 Definition of Terms

Before discussing how an OPV device operates, it is useful to define a few terms and quantities needed in the discussion of electronic materials. Figure 1.3 shows an energy level diagram of a semiconductor with these key parameters. Transport of electrons and holes occurs at the conduction band minimum (CBM) and the valence band maximum (VBM) respectively for inorganic semiconductors. It should be noted that the flat bands drawn here are rarely present in inorganic semiconductors due to dangling surface bonds creating trapped charges. However, flat bands can be seen in OSCs which do not have dangling bonds. The transport of electrons and holes in the case of an OSC takes place in the lowest unoccupied molecular orbital (LUMO) and the highest occupied molecular orbital (HOMO) respectively. The difference between these two energy bands is called the band gap (E_G).

The local vacuum level (E_{VAC}) refers to the energy level at which an electron can exist at rest outside of a solid material. To get to this point the electron must overcome a large energy barrier culminating at E_{VAC}. Unless doped or thermally

excited the electrons closest to E_{VAC} exist at the HOMO level and the energy taken to remove them from the material is defined as the ionisation energy (IE). The energy gained when an electron moves from the E_{VAC} to the LUMO level is defined as the electron affinity (EA) of the material. Electron affinity can define whether a material is a good electron acceptor with large electron affinities or an electron donor with a low electron affinity.

The Fermi level (E_F) is a hypothetical energy level such that at thermal equilibrium there is a 50% chance of finding an electron at this energy. The difference between E_{VAC} and E_F is called the work function. In a metal the electron affinity and ionization energy are equal to the work function, as metals have a continuum of energy states. Whereas, in an intrinsic semiconductor E_F exists in the band gap of the material. The quantitative position of E_F is dependent on the carrier density, temperature, doping concentration and density of states in the material. The work function and in consequence the ionisation energy and electron affinity can only be defined at the surface of a material, this is due to the work function having two components- a solid and a bulk component.

The bulk component of the work function is the chemical potential defined by the electronic density and density of states in the solid. The surface component of the work function refers to the redistribution of charge at the surface of a material, creating a surface dipole. In metals this component is large as the electrons can tunnel to exist slightly outside the metal. This effect depends on the orientation and completion of the crystalline lattice at the metal surface. This effect is much smaller in OSCs as they have a much smaller free electron density. A more complete discussion of these topics can be found [50].

1.2.2 Device Operation

Figure 1.4 shows a schematic diagram illustrating how an OPV device operates. Firstly, a photon is absorbed by the active material and a neutral quasi-particle called an exciton is created. Excitons consist of a hole and an electron bound together by the Coulomb force between them and are created in organic materials due to their low dielectric constants [51]. For a photon to be absorbed it must match the absorption spectra of the material and the material needs to be thick enough that the chance to absorb a photon is high. Conjugated polymers have good absorption strengths, $\sim 1 \times 10^6$ /cm at 500 nm for P3HT:PCBM [52], but their spectra do not match that of the sun particularly well [53].

Once an exciton is formed it must then diffuse to a donor/acceptor interface. Exciton diffusion is affected by the nanomorphology of the acceptor and donor blend,

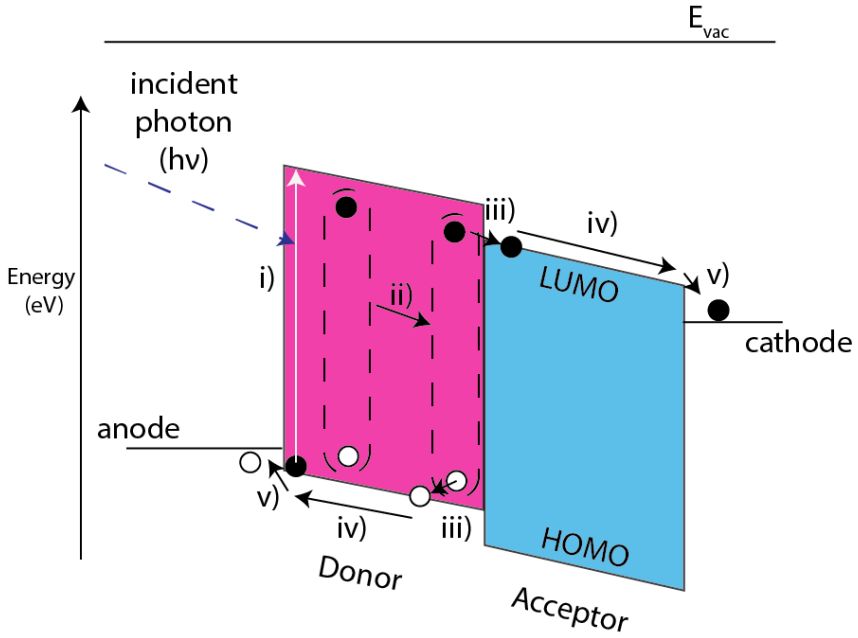

Figure 1.4: A schematic showing how an OPV device works, showing i) a photon being absorbed and an exciton being created, ii) exciton diffusion, iii) charge separation, iv) charge transport and v) charge collection. Electrons are shown in black, holes in white.

i.e. an interface needs to be within the diffusion length of the exciton, as determined by the exciton lifetime typically (100 ps - 1 ns) [53]. The specific diffusion lengths for materials can be measured by photoluminescent quenching, and for organic materials are $\sim$ 10 nm [54]. Once at a donor/acceptor interface an exciton can dissociate into separate charges if its energy is higher than that of the charge separated states. In the simplest picture the exciton splits into separate charges when the difference between the lowest unoccupied molecular orbital (LUMO) of the acceptor and donor is greater than that of the binding energy of the exciton (usually between 0.1 - 0.5 eV) [53], so an electron is transferred from the donor to the acceptor. The reality of exciton dissociation is much more complex, often occurring by means of energy transfer whilst the hole and electron are still bound across the interface [31].

Once free charges are obtained, to power an external circuit the free charges must travel to the collecting electrodes. The efficiency with which they do this depends on their respective mobilities. The mobility of a charge carrier defines how fast it moves in an electric field: $v_d = \mu E$ where v_d is the drift velocity, μ is the charge carrier mobility and E is the applied electric field. This process is known as charge transport and will be discussed in detail later. Charge collection at the electrodes

is also a complex process and depends on the specific interactions between the electrode and the organic material. The charge collection efficiency can be improved by adding interfacial layers between the active material and the electrodes. Interfacial layers are layers between the active material and the collecting electrodes acting to adjust the barrier height between active materials and electrodes, allowing selective collection of carriers, and can act as optical spacers increasing the absorption of photons [55]. Charge collection can also be improved by modifying electrodes to improve workfunction compatibility [56].

1.2.3 Device Characterisation

One common method of testing the functionality of OPV devices is to measure current density vs. voltage (JV) relations in illuminated conditions on fully assembled devices, i.e. with the active material sandwiched between a transparent top electrode and opaque metal electrodes. There are normally multiple metal electrodes per device to improve the statistics when testing the devices, and their dimensions are carefully controlled by deposition through a shadow mask. The dimensions and layout of these electrodes can affect the accuracy of measurement [57].

OPV devices are particularly sensitive to spectral mismatches as they have relatively narrow absorption profiles compared to inorganic devices, hence the lamp used to create the testing irradiance needs to be a close match to the solar spectrum [58]. It is preferential to use a xenon arc lamp fitted with spectral filters as this has the most similar spectrum to the solar spectrum [59]. The irradiance on the sample also needs to be well characterised. Devices are tested most commonly under 100 mW/cm^2 to match the average solar flux hitting the Earth's surface with the sun at an angle of 48.2° from the equator, also called the AM1.5G standard. The irradiance can be calibrated using a photodiode and corrected using neutral density filters.

Figure 1.5 shows a representative JV curve taken on a boron subphthalocyanine chloride (SubPc):C_{60} device. From this curve the device's open circuit voltage (V_{OC}) and short circuit current density (J_{SC}) are immediately evident, in this case being 1.065 V and -3.72 mA/cm^2 respectively. V_{OC} defines the bias at which the photogenerated current fully cancels the dark current present in the cell, resulting in no current flow, hence V_{OC} is found at zero current. J_{SC} represents the device's photocurrent generation with no external resistance, hence J_{SC} is found when the applied bias is zero. Fill factor (FF) describes how close the device comes to its ideal output and can be found by comparing the power at the maximum power point, to

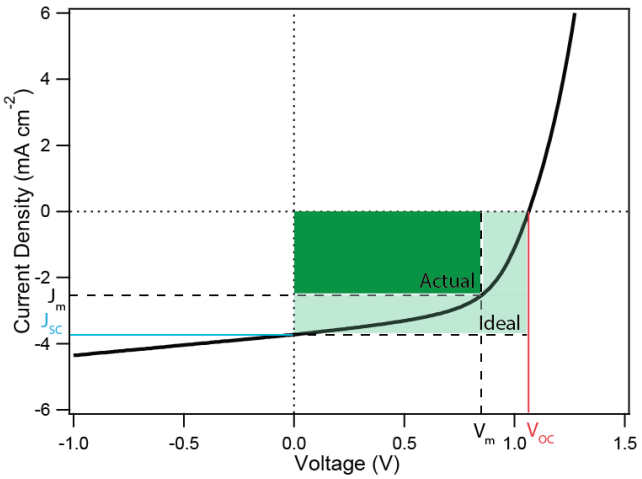

Figure 1.5: An example JV curve of a subPc:C_{60} device showing the locations of the short circuit current density (J_{SC}) and open circuit voltage (V_{OC}). A representation of the fill factor is also displayed as a measure of the highest power output of the device (the sum of J_m and V_m) compared to the maximum possible J_{SC} times V_{OC}.

the power from the ideal conditions of V_{OC} and J_{SC}, i.e.

$$FF = \frac{V_m J_m}{V_{OC} J_{SC}} \tag{1.1}$$

where V_m is the voltage and J_m is the current at the maximum power point. In the case of Figure 1.5 the fill factor is 0.8. The fill factor is decreased by parasitic resistances in the cell. Contact resistances and resistance through the active layers of the cell increase the series resistance. The shunt resistance of the cell should preferentially be infinite, and is reduced by leaky contacts and charge recombination [60]. The efficiency of the device can be described as

$$\eta = \frac{V_{OC} J_{SC} FF}{P_{in}} \tag{1.2}$$

where P_{in} is the power incident on the device which is the 100 mW/cm^2 from the calibrated xenon arc lamp; for this device the efficiency is 3.17%.

1.2.4 Charge Transport

The mechanisms of charge transport in partially ordered, e.g. semicrystalline semiconductors is still an active field of study in which a consensus has not been

reached [61]. In inorganic semiconductors the perfectly ordered periodic lattice allows delocalisation of charge carriers. This delocalisation gives rise to conduction bands, which contain a continuum of states in these semiconductors. Breaks in this continuum occur at defects in the crystal structure this limits conduction. The mobility in inorganic semiconductors decreases with increasing temperature as this introduces deviations in the crystal structure causing scattering.

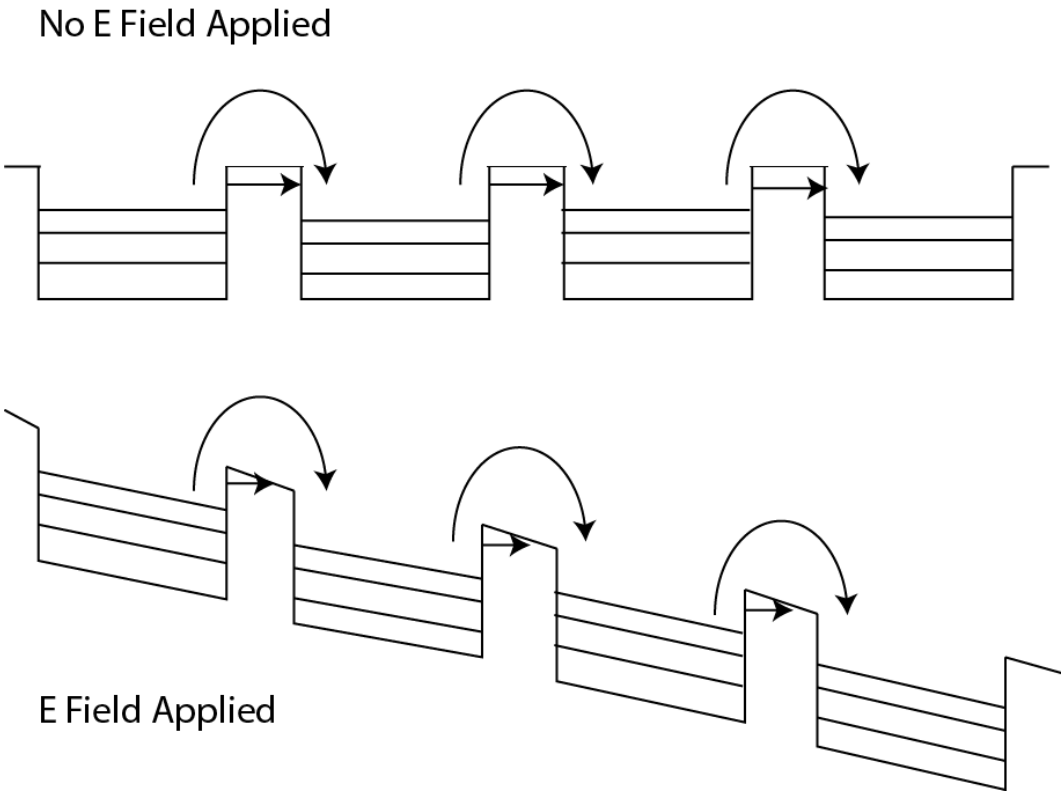

Figure 1.6: An organic semiconductor modelled as a series of potential wells with and without an external electric field.

In organic semiconductors charges do not occupy a continuum of states, they tend to be contained in localised potential wells in single molecules, or as parts of a polymer chain. Figure 1.6 shows an organic semiconductor modelled as a series of potential wells. Wells are separated by barriers that represent breaks in the crystal structure of the semiconductor, in the case of polymers these can be twists or kinks in the polymer chain which change the alignment of the pi bonds. When there is no electric field applied charges must "hop" from one potential well to the next [62]. Increasing the temperature of the system produces higher hopping probabilities, yielding strong Arrhenius relationships with temperature as the charges have an

effective "activation energy" [63].

The alternate method of transporting charge in this system is to tunnel through the barriers separating the potential wells. The probability of tunnelling through these barriers increases when an electric field is applied as the field makes the effective barrier width thinner. This increases the rate of charge transport and hence the mobility of charges with the electric field strength. This field dependent mobility is a feature not shared by inorganic semiconductors.

Semi-ordered semiconducting polymers contain both localised and delocalised charges, though delocalisation tends to occur in one dimension along the polymer backbone and is often impeded by impurities and torsional effects, creating the barriers described [64]. There are arguments for and against using band-like models and hopping models of charge transport, though molecular modelling has proven to be a useful tool in improving the mobility in future designs of these systems [65]. There have also been a number of attempts to understand and model the charge transport of these systems by combining molecular modelling and quantum chemistry methods which can link the measured charge mobility with theory [66]. In reality a model that contains elements of both band like transport with regard to intrachain defects and hopping transport would possibly be closer to the physical reality [67]. To find a theory that matches experiential results of charge carrier mobility, the mobility must first be measured experimentally.

1.2.4.1 Space Charge Limited Current(SCLC)

One of the methods for measuring mobility is space charge limited current (SCLC), that being the current due to the flow of charge injected by a high field into a dielectric or semiconductor from a metal electrode. For SCLC to occur the number of injected carriers must be greater than that of the intrinsic carrier and dopant concentrations. Since this current is dominated by the drift of injected charges, the current density is given by

$$J = \rho\mu E \tag{1.3}$$

where $\rho(x)$ is the charge density and is itself a function of the distance into the semiconductor, and the carrier velocity $\nu = \mu E$ is the product of the mobility μ and electric field E [68]. Since the space charge is determined by injected carriers, this yields the Poisson equation of the form

$$\frac{dE(x)}{dx} = \frac{\rho(x)}{\epsilon_0 \epsilon_r}. \tag{1.4}$$

Substituting for $\rho(x) = J/\mu E$, this can be rewritten as

$$\frac{dE}{dx} = \frac{J}{\mu E(x)\epsilon_0\epsilon_r}. \tag{1.5}$$

This can the be rearranged and integrated

$$\int E(x)dE = \int \frac{J}{\mu\epsilon_0\epsilon_r}dx \tag{1.6}$$

yielding

$$E = \sqrt{\frac{2Jx}{\mu\epsilon_0\epsilon_r}} + \text{const.} \tag{1.7}$$

Upon application of boundary conditions, primarily that E(0) = 0, the constant equates to 0. A more thorough discussion of this can be found in [69]. From Equation 1.7 it is clear that in the SCLC regime the electric field depends on V^2 (further proven subsequently), and is distinct from an ohmic (linear) or tunnelling (exponential) regime, due to the excess of charge carriers injected into the material.

Since the electric field is by definition $E = -\frac{dV}{dx}$ a further integration assuming ohmic contacts

$$-\int dV = \int \sqrt{\frac{2J}{\mu\epsilon_0\epsilon_r}} x^{1/2} dx \tag{1.8}$$

yields the familiar Mott-Gurney equation for a material of thickness d

$$J = \frac{9}{8}\mu\epsilon_0\epsilon_r \frac{V^2}{d^3}. \tag{1.9}$$

This can be expanded to include carrier trapping [70], and further empirical modifications to this equation to include electric field dependence of charge transport can be made [71], this yields

$$j = \frac{9}{8}\mu_0\epsilon\epsilon_0 e^{0.89\gamma(V/d)^{\frac{1}{2}}} \frac{V^2}{d^3} \tag{1.10}$$

where μ_0 is the zero field mobility and γ is the strength of the field dependence. This equation is commonly used to characterise the behaviour of solar cells, though there are other methods that have their own advantages [72]. In a normal device this can be measured by taking a JV curve in dark conditions. Figure 1.7 shows a representative dark curve on P3HT, with the fitting of Equation 1.10 yielding a measured mobility of 1.76 ± 0.1 × 10^{-8} cm^2/Vs and a field dependence of 1.4 ± 0.1 × 10^{-4} $m^{1/2}/V^{1/2}$. The modulus of the current has been taken. Besides the

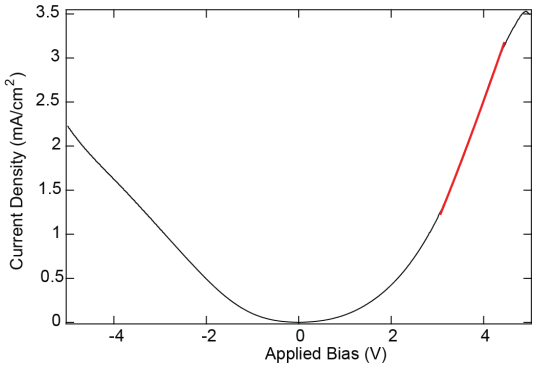

Figure 1.7: An example JV curve of Al/MoO_x/P3HT/MoO_x/ITO/glass in dark conditions showing a fit of Equation 1.10, with a mobility of 1.76 $\pm$ 0.1 $\times$ 10^{-8} cm^2/Vs.

mobility, there are several factors which affect the charge transport of carriers in OPV systems, most importantly, trapping and recombination.

1.2.4.2 Trapping and recombination

Charge trapping and recombination are somewhat intertwined, because depending on where the charges are energetically and physically trapped, charges are likely to recombine without producing useful electrical energy output. Trapping of charges at the donor/acceptor interface is most likely to produce germinate pair recombination - recombination of a bound electron and hole pair - as the charges may be in close spacial proximity with limited screening [73]. In this context, a trap is a local energy minimum surrounded by higher available energy states. Therefore for a charge to move spatially and energetically out of a trap state additional energy must be provided to it. Physically traps can be formed by impurities or disorder in the materials of the system. The effects of trapping on mobility with respect to carrier concentration [72], applied bias and temperature [74], have been extensively studied.

Recombination is the main limitation of efficiency in OPV devices and also depends on temperature and electric field [75]. Significant research has also been performed in this area, however, it is again not completely understood. There are also many different mechanisms for recombination that dominate in different systems. The main recombination mechanisms here are trap assisted recombination, which occurs in systems where there are many defects that absorb carriers making it likely for travelling carriers to meet and recombine with trapped carriers; and bi-

molecular recombination, recombination of an electron from absorption of a photon, with a hole from another absorption event in close proximity. Both of these processes occur in OPV devices, though each dominates in different regimes [76, 77, 78, 79].

1.2.4.3 Surface Photovoltage (SPV) Measurements

Surface photovoltage (SPV) is defined as the illumination induced change in the surface potential. Contactless measurements of the SPV are used regularly in the characterisation of semiconductors. When light is incident on a photovoltaic device charges are generated and subsequently redistributed in the surface and the bulk regions inside the semiconductor. This redistribution of charges changes the effective Fermi levels in the space charge region of the semiconductor, the region where charge carriers are depleted from, leading to an effective change in work function [80]. This effect can be seen schematically in Figure 1.8, and can be measured using Kelvin probe methods comparing the work function of a metal probe with that of the semiconductor.

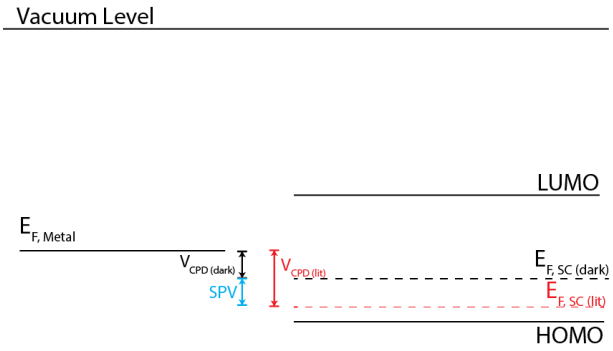

Figure 1.8: A schematic of the energy levels involved when a p-type organic semiconductor surface is illuminated. Flat band conditions are shown for simplicity. The illumination moves the effective Fermi level of the semiconductor and the difference between the contact potential difference (V_{CPD}) when dark and when illuminated is the surface photovoltage (SPV).

It has also been shown that SPV measurements are not only able to measure charges generated at the surface, but also those in bulk materials or buried interfaces [81, 82]. The SPV can be used to determine a range of bulk properties including the carrier diffusion length and timescale, by measuring the relaxation of the SPV after switch off of the incident illumination [83], although this method only proved effective for relatively low recombination rates. Frequency based techniques, using a modulated light to measure the timescales involved, have also been

developed which can directly determine the charge carrier lifetime [84, 85].

The SPV has also been shown to be equivalent to V_{OC} for inorganic semiconductors [81]. In OPV devices the relationship between SPV and V_{OC} has been studied, and shows the two to be strongly correlated. Figure 1.9 shows the relation-

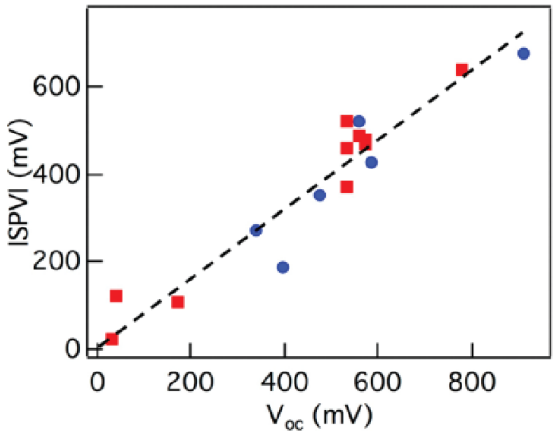

Figure 1.9: The relationship between the measured SPV and V_{OC} for normal and inverted architecture P3HT:PCBM reproduced from [86].

ship found by Lee et al. between V_{OC} and SPV for inverted and normal architecture P3HT:PCBM devices [86]. The data for SPV and V_{OC} were taken at slightly different light levels which may account for the V_{OC} and SPV not being identical, however, the linear relation is clearly shown.

1.2.5 Poly-3-hexylthiophene (P3HT) and phenyl-C_{61}-butyric acid methyl ester (PCBM)

Poly-3-hexylthiophene (P3HT) and phenyl-C_{61}-butyric acid methyl ester (PCBM) are, to date, the most studied active materials for BHJ solar devices. In 2010 nearly 2000 publications featured this particular material system. Whilst it is possible to get power conversion efficiencies over 5% for devices using this active material, the average certified efficiency recorded is between 3.5 and 4%. Even with, and possibly due to, such extensive study there is a large spread of results and conclusions relating to the device behaviour with respect to the processing and properties of each device [87]. However, such extensive interest in this system allows for certain aspects of these devices to be well characterised.

Figure 1.10 shows the chemical structures of P3HT, the electron donor, and

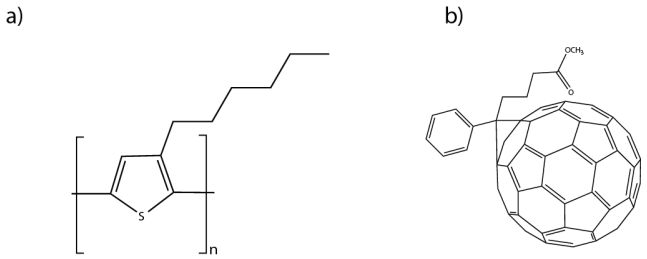

Figure 1.10: The chemical structures of a) poly-3-hexylthiophene (P3HT) and b) phenyl-C_{61}-butyric acid methyl ester (PCBM).

PCBM, the electron acceptor. When blended together into a BHJ device, P3HT and PCBM make a phase segregated thin film device the properties of which improve upon annealing [88]. The temperature of annealing required for the best performances in devices [89, 90], or indeed whether annealing should be done prior to or post electrode deposition, are still contested [88]. This is further complicated by the roles of the casting solvent used [91], the molecular weight [92, 93, 94, 95], structure [96, 97, 98], and regioregularity of the P3HT used [99], and even the ratio of P3HT to PCBM [100, 101, 102].

Although there may still be active discussion on the specific conditions required to maximise the power conversion efficiency of P3HT:PCBM devices, it is well established that morphology has a large influence on the device's performance and understanding why this is the case may lead to improvements in device performance [103, 104, 105, 76]. The wealth of research on this system makes it an obvious choice to test the viability of new techniques to measure the morphology and electrical properties of these devices.

1.2.6 PTB7:$PC_{70}BM$

Poly[[4,8-bis[(2-ethylhexyl)oxy]benzo[1,2-b:4,5-b']dithiophene-2,6-diyl][3-fluoro-2-[(2-ethylhexyl)carbonyl]thieno[3,4-b]thiophenediyl]:Phenyl-C_{71}-butyric acid methyl ester (PTB7:$PC_{70}BM$) is another polymer system which has seen a large amount of research in recent years, in this case due to the high efficiencies (of over 9%) recorded for BHJ devices [106].

PTB7 has many of the desirable properties of a successful electron donor material for OPV devices from strong absorption, low band gap and high crystallinity with low torsional angles of the relaxed polymer [106]. PTB7 also has a much higher mobility than P3HT (1×10^{-3} cm^2/Vs and 2×10^{-4} cm^2/Vs respectively) adding to its superior device performance [107, 64]. Like the case of P3HT:PCBM, the

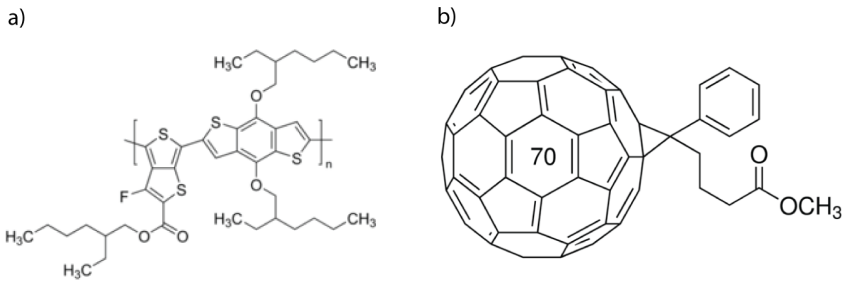

Figure 1.11: The chemical structures of a) PTB7 and b) phenyl-C_{71}-butyric acid methyl ester ($PC_{70}BM$).

performance of PTB7:$PC_{70}BM$ devices is also highly dependent on the morphology of the film [108], and can be improved by solvent additives [109, 110]. Though this system is similar to P3HT:PCBM, it may be interesting to compare new techniques across the two systems.

1.2.7 Vanadyl phthalocyanine (VOPc)

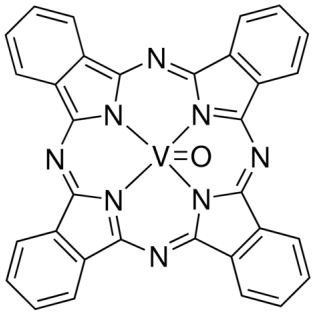

Figure 1.12: The chemical structure of VOPc [111].

Vanadyl phthalocyanine (VOPc) is a non-planar phthalocyanine that has shown been used in organic field effect transistor (OFET) devices [112, 113, 114]. Planar phthalocyanines have been extensively studied and used in OPV devices as they have high absorption coefficients in wide spectra, coupled with simple purification and deposition methodologies [115]. Non-planar phthalocyanines have also shown promising optical properties and high performances in OPVs [116], hence including VoPc in this work demonstrates the application of these techniques to emerging and distinct materials.

1.3 AFM

Atomic force microscopy (AFM) has the ability to probe both the physical and the electrical properties of a material on the nanoscale and thus has been used extensively to study OPVs [117]. The AFM was invented in 1986 by Binnig et al [118]. The first version consisted of a cantilever used as the scanning probe and a second tip above the first in a scanning tunnelling microscope (STM) setup to sense the deflection of the cantilever. This first AFM demonstrated a lateral resolution of 30 Å and a vertical resolution of 1 Å [118]. The modern AFM uses the same concepts, however instead of measuring the cantilever deflection by STM, most use a "light lever" approach instead, as shown schematically in Figure 1.13. A laser

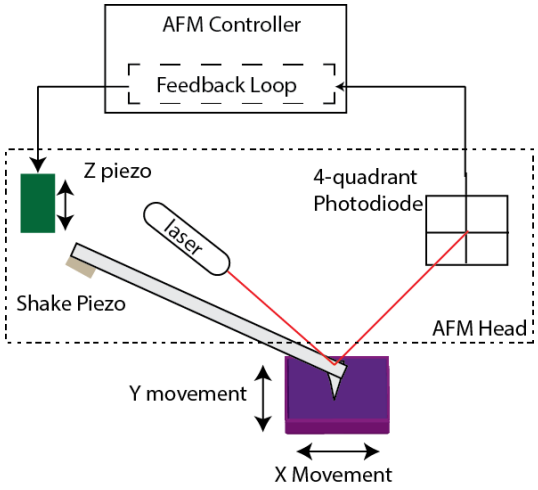

Figure 1.13: A schematic of a "light lever" based AFM, showing decoupled x,y and z movement axes.

is focussed onto the back of the cantilever such that its reflection strikes a four-quadrant photodiode. As the cantilever bends or twists, the position of the laser spot moves on the photodiode. By recording the voltages from the photodiode the vertical and lateral deflection of the cantilever can thus be measured.

Intermolecular forces between the tip and sample cause the cantilever to deflect. The nature of this interaction can be approximated by the Lennard-Jones potential, explaining how as the tip gets closer to the sample that interaction is initially attractive and becomes repulsive at much closer tip-surface distances [119]. This is seen in the AFM as an initial deflection towards the surface (or decrease), followed by an increase in the deflection measured by the photodiode. Pushing further against the surface yields a steadily increasing deflection.

A feedback loop can be used to maintain a constant deflection (and hence

force) by moving the cantilever base using the z-piezo. It is possible to gain an image of a sample's topography by raster scanning across the sample using the x and y piezos. Moving the z-piezo in turn to maintain a constant deflection and recording this z-movement yields the topography. This is known as contact mode scanning. Scanning in this manner compares the signal between the bottom and top quadrants of the photodiode. However, it is also possible to compare the signal between the lateral quadrants and, if scanning perpendicular to the cantilever, this signal corresponds to the torsional motion of the cantilever which under the right conditions can correspond to the friction applied by the sample. This can be useful for samples with low contrast in the height domain, for example single layer graphene [120].

Softer samples can be adversely affected by the lateral force between tip and sample, whilst large vertical forces will deform the surface. This can be used advantageously in lithography [121], or to clean a particular sample area of particulates [122, 123].

1.3.1 Force Curves and Contact mechanics

The force applied on a sample's surface by the AFM tip can be calculated by measuring the deflection of the cantilever when the tip is engaged onto the sample, providing the cantilever and photodiode behaviour have been calibrated (Section 2.2.3). With a calibrated cantilever, the behaviour of the force as a function of the distance of the tip from the sample can give valuable insight into the nature of the sample's surface. This requires the application of contact mechanical models, requiring a force curve to be performed. A force curve is generated when the tip is approached to the surface at a set velocity. The z-piezo maintains this velocity towards the surface until a set deflection is reached. The z-piezo then stops and is retracted at the same velocity.

As the tip approaches the surface, before any surface forces are felt only the distance changes. When the tip gets very close to the surface the attractive (e.g. van der Waals) forces overcome the stiffness of the cantilever and the tip jumps into contact. Repulsive interactions between the tip and surface then dominate, and as the piezo drives the tip harder onto the surface the cantilever flexes, increasing the measured deflection. When the desired deflection is reached, the tip is withdrawn from the surface initially following the loading curve, however, as the tip is leaving the surface additional adhesive interactions cause the deflection to dip lower than the contacting deflection. The magnitude of this interaction depends on the material properties of tip and sample, as well as the contact area between tip and sample and the medium they are in [124]. When the tip pulls away from the surface with

sufficient force the cantilever snaps back to the free deflection.

The simplest of the contact mechanical models is the Hertz model. The tip and surface are modelled respectively as an infinitely hard sphere and a deformable plane [125]. Since the Hertz model assumes only elastic interactions, the unloading/retract sections of the curve match the engage/loading [126]. The radius of contact is described as

$$r_{Hertz} = \left(\frac{r_{tip}F}{E_{tot}}\right)^{\frac{1}{3}} \tag{1.11}$$

where r_{tip} is the radius of the tip, F is the applied force, and E_{Tot} is the combined modulus of tip and sample defined as

$$\frac{1}{E_{tot}} = \frac{3}{4}\left(\frac{1-\nu_t^2}{E_t} + \frac{1-\nu_s^2}{E_s}\right) \tag{1.12}$$

where E_t and E_s are the Young's moduli of tip and sample respectively, likewise ν_t and ν_s are the Poisson ratios of tip and sample.

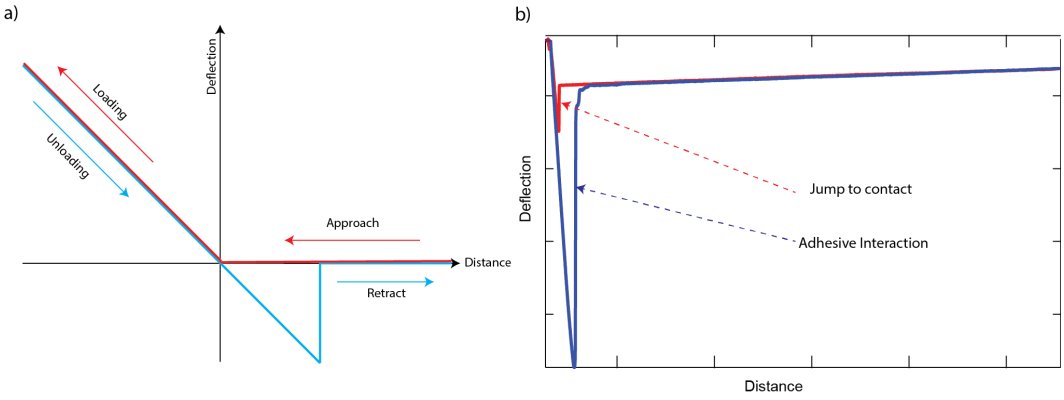

Figure 1.14: Showing a) a schematic of a force curve in the Hertz model and b) an experimental force curve of a platinum/iridium coated silicon cantilever on a P3HT surface.

Figure 1.14 compares the Hertz model force curve with an experimental force curve. The addition of van der Waals interactions in the experimental case adds a small jump to contact. Due to its simplicity, the Hertz model is a popular choice for estimating contact areas between tip and sample and the elasticities of surfaces studied. The Hertz model has been used for a variety of applications, including making improvements to SCLC modelling in OPVs [127, 128, 129]. In biological applications the Hertz model has been used to investigate the elasticity of cancer cells, helping to explain their propagation through tissue [130], and modelling different contact models on single cells has shown the Hertz model to be suited for use

at low cell deformations [131].

Introducing surface interactions between the interacting bodies allows the modelling of adhesive surfaces. The Derjaguin-Muller-Toporov (DMT) model has the addition of adhesion outside the contact area without a change in the contact profile between tip and sample. The contact radius in this model is described as

$$r_{DMT} = \left(\frac{r_{tip} \left[F + F_{ad} \right]}{E_{tot}} \right)^{\frac{1}{3}} \tag{1.13}$$

where F_{ad} is the adhesive force between tip and surface. This model is best applied with small tip radii with respect to the contact area, on comparatively stiff materials [132].

In comparison the Johnson-Kendall-Roberts (JKR) model includes adhesion only within the contact area and includes necking of the sample's surface as the tip is withdrawn. The JKR model applies for larger tips and softer samples than the DMT model. In the JKR model the radius of contact between the tip and sample is

$$r_{JKR} = \left(\frac{r_{tip}}{E_{tot}} \left[\sqrt{F_{ad}} + \sqrt{F + F_{ad}} \right]^2 \right)^{\frac{1}{3}}. \tag{1.14}$$

Maugis later showed that the DMT and JKR models are limits of the same model and a continuous transition can be seen from the JKR to the DMT model with the increase of a parameter which is the ratio of the adhesion to elasticity of the sample's surface and is now known as the Tabor parameter [133, 134]. Figure 1.15 shows schematically the different contacts described by these three models whilst Table 1.1 shows a comparison of the deformations and contact radii predicted. The DMT and JKR models have been applied to many different systems to characterise the mechanical properties [135, 136, 137, 138, 139], or indeed the contact area for electrical characterisation [140, 141, 142].

	Hertz	DMT	JKR
r_c	$\sqrt[3]{\frac{r_{tip}F}{E_{tot}}}$	$\sqrt[3]{\frac{r_{tip}}{E_{tot}}\left(F + F_{ad}\right)}$	$\left(\frac{r_{tip}}{E_{tot}} \left[\sqrt{F_{ad}} + \sqrt{F + F_{ad}} \right]^2 \right)^{\frac{1}{3}}$
D	$\left(\frac{F^2}{r_{tip}E_{tot}^2} \right)^{\frac{1}{3}}$	$\frac{(F+F_{ad})^{\frac{2}{3}}}{\sqrt[3]{r_{tip}E_{tot}^2}}$	$\frac{r_c^2}{r_{tip}} - \frac{4}{3}\sqrt{\frac{F_{ad}r_c}{r_{tip}E_{tot}}}$

Table 1.1: The contact radii and deformations predicted from the Hertz (no attractive forces), DMT (attractive forces including short range non-contact forces) and JKR (adhesive forces allowing for deformation of the tip or sample when pulled apart) models respectively.

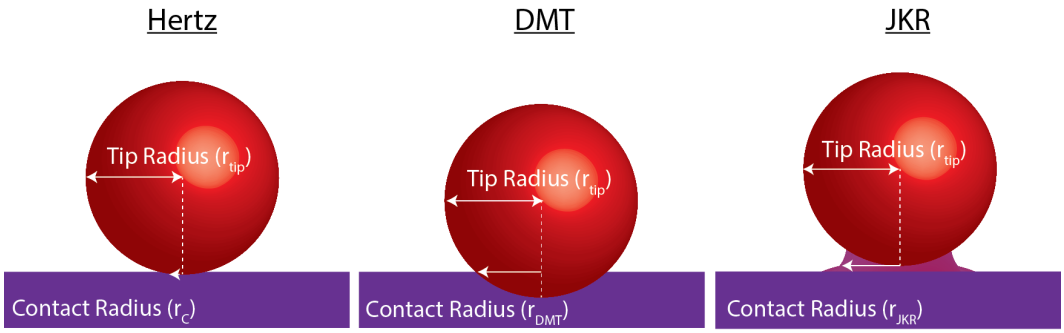

Figure 1.15: Schematics of the different contact regimes described by the Hertz, DMT and JKR contact models.

Naturally, these models are approximations of the AFM tip interactions with the surface, and there are other models that are also used [143], the most common example being the Oliver-Pharr model [144, 145, 146]. There are also improvements and modifications of each of these models to apply to specific purposes [147, 148], or to aid fitting algorithms [139].

1.3.2 Conductive AFM (CAFM)

If a conductive tip and cantilever are used, the current flow between tip and sample can be measured. This relies on the tip surface contact and hence is usually done during contact mode scanning with a potential difference applied between tip and sample. This is known as scanning conductive AFM (CAFM). The current can be measured vertically through a sample of interest by arranging the sample in a diode configuration, with the layer of interest between a back electrode and the AFM tip. This is particularly useful for measuring OPV devices [149, 150], investigating the properties of electrode materials [151, 152], or testing the conductivity of single structures like DNA [153]. CAFM can also be used in a lateral or transistor like geometry to investigate how current travels laterally through a device [154], self assembled monolayer (SAM) [155], or conjugated polymer [127].

Naturally, the point of contact between the AFM tip and the semiconductor surface is of great importance here. Figure 1.16 shows the energy levels of the tip and surface before and after contact is made by the AFM tip. To conduct charges between the species the Fermi levels of the metal and semiconductor must align, in order to do this the semiconductor bands bend. This creates a depletion region between the metal and semiconductor. This acts as a barrier to transport and hence the closer the energy level alignment between the valence band of the semiconductor

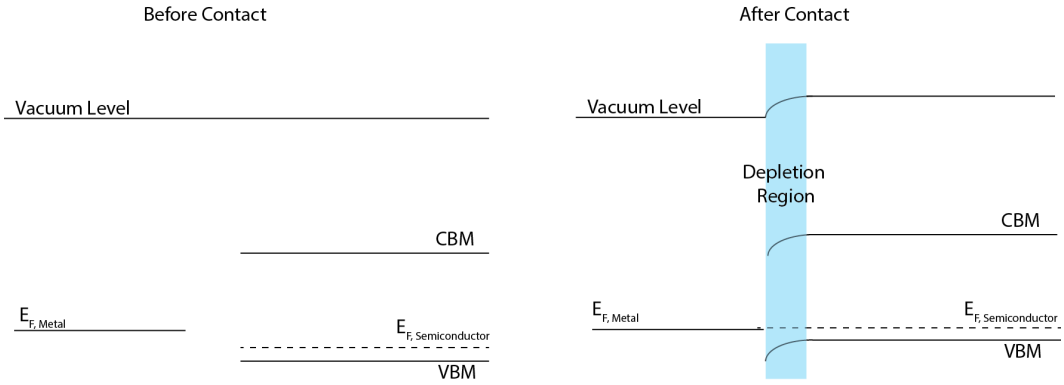

Figure 1.16: An energy level diagram of a p type semiconductor and a metal before and after contact is made.

and the Fermi energy of the metal the easier charge collection will be at the metal electrode.

IV curves are commonly taken to more quantitatively analyse the charge transport at specific locations on a sample's surface, and the power law dependence of such curves can characterise the efficiency of charge injection or collection though the electrode [156]. Unlike devices with defined planar electrodes the mobility in CAFM cannot be accurately derived by applying the standard Mott-Gurney model to dark JV curves. Complications arise, firstly due to the unknown nature of the tip-surface contact, converting from a current to a current density is not as simple as dividing by the electrode area as it is in a standard device. Secondly, the geometry of the standard Mott-Gurney model is that of two infinite planes. In the case of an AFM contact, the geometry is more of an infinite plane and a point contact. For this reason the standard Mott-Gurney model does not determine an accurate charge carrier mobility when applied to JV curves taken in an AFM [150].

With the corrections made by Reid et al. [150], the SCLC density can be described as

$$J = 8.2\epsilon\epsilon_0\mu_0 e^{0.89\gamma(V/L)^{1/2}} \frac{V^2}{L^3}\delta_J \left(\frac{L}{r_c}\right)^{1.6\pm0.1} \tag{1.15}$$

where ϵ_0 and ϵ are the vacuum permittivity and the relative permittivity of the thin film respectively, μ_0 is the zero field mobility, γ is the strength of the field-dependence of the mobility, and L is the thickness of the semiconductor thin film. The prefactor 8.2 replaces that of 9/8 in planar devices in the original Mott-Gurney equation. δ_J is an empirically derived factor determined by Reid et al., to correct for the differences between planar and tip based mobility measurements [150].

Even with the appropriate care and attention, electrical measurements in

contact with the surface tend to be unreliable due to the unknown nature of the tip and its tendency to change due to forces present during the experiment. This is where non-contact techniques become useful.

1.3.2.1 Photoconductive AFM

Photoconductive AFM (pc-AFM) is a popular application of CAFM applying illumination to a sample and scanning in the same way as CAFM. If the current measured in pc-AFM is compared to that in the dark in standard CAFM, photovoltaic properties of the surface can be measured. Switching the direction of the bias between the tip and sample allows selectivity of the charge carrier being measured so areas in which holes or electrons congregate can be seen independently.

Photoconductive AFM has been used to correlate morphological and electronic properties of OPV materials [149, 157, 158, 159], and also to measure more quantitatively, the nanoscale efficiency [160]. The polarization of the incident illumination can yield information on the orientational order of the sample [161]. pc-AFM does, however, suffer from the same downfalls as CAFM: tip and sample wear as well as unreliable contacts, and unknown contact areas.

1.3.3 Tapping Mode

A common approach to avoiding the lateral forces which can damage tip and sample is to oscillate the cantilever so that the tip makes intermittent contact with, or taps, the sample's surface. Usually, the cantilever is driven to oscillate near its resonant frequency by a piezoelectric actuator. The drive amplitude and frequency are kept constant while tip surface interactions change the oscillation amplitude. To image the surface, a feedback loop is used to maintain a constant oscillation amplitude (rather than the deflection used in contact mode) by changing the z-piezo voltage. Hence this imaging mode is properly called amplitude modulation scanning, but is more commonly referred to as tapping mode, intermittent contact mode, or AC mode.

The amplitude of the cantilever's oscillation depends on how close the drive frequency is to the resonant frequency of the cantilever. Short range interactions with the sample's surface change the effective resonant frequency of the cantilever causing the amplitude of oscillation to change when the drive frequency and amplitude remain fixed. Since the cantilever is moving there is a force gradient between the tip and sample, if this is attractive the effective resonant frequency decreases, likewise if the force gradient is repulsive the resonant frequency increases. Fig-

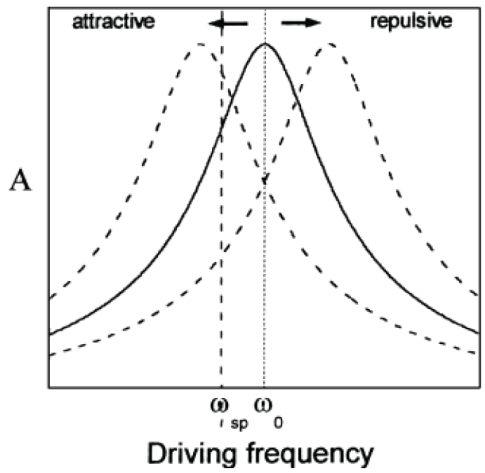

Figure 1.17: Perturbations of the cantilever resonance curve from its natural resonance frequency (ω_0) to a new effective resonance frequency (ω_{sp}) in response to an attractive or repulsive interaction force, where A is the cantilever's amplitude [162].

ure 1.17 shows how these attractive and repulsive interactions move the resonance curve of a cantilever's oscillation without changing the shape or form [162].

The phase of the cantilever's motion with respect to the driving oscillation, is also recorded while imaging and contains information about the energy loss of the cantilever as it interacts with the surface. The energy dissipated by the tip surface interactions of the cantilever depends on the elasticity of the sample, the more compliant the sample, the more energy is dissipated [163]. This causes changes in the phase of oscillation of the cantilever and can be used as an imaging technique. However, care must be taken when interpreting the phase image as other effects also affect the phase of the cantilever. Since the cantilever oscillation is large, a single oscillation of the cantilever may pass through force gradients that are both attractive and repulsive. For certain oscillation amplitudes there can exist more than 1 tip-surface distance at which a single amplitude of oscillation is possible. However, since the force gradient of these is very different, the phase of the oscillation is very different also. During imaging this kind of bi-stability can be seen as a sharp phase change crossing the 90°phase regime.

Figure 1.18 shows the topography and phase images of two different P3HT: PCBM samples. The topography and phase of (a) and (b) were measured at 60°C. The topography is in general homogeneous, showing no particularly prominent features. It's phase, however, shows two distinct regions: one of a high phase and the second of a lower phase. It is likely that the two phases correspond to the segre-

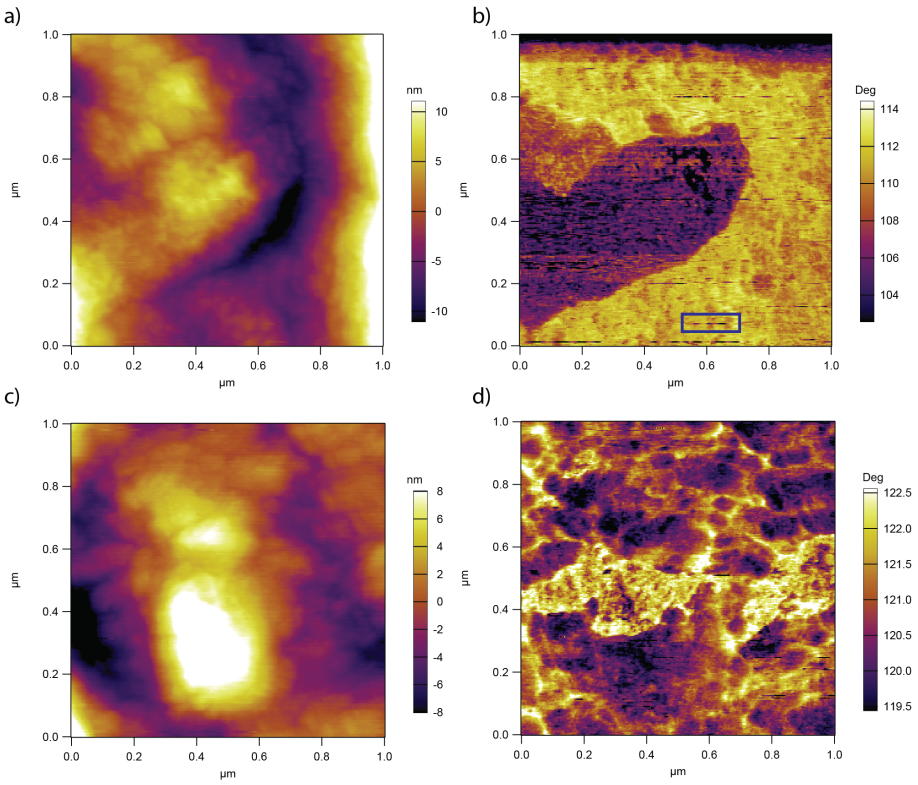

Figure 1.18: a) and b) show the topography and phase of a P3HT:PCBM sample at 60°C. The blue box highlights an imaging instability as opposed to phase contrast. c) and d) Show the topography and phase of a second P3HT:PCBM sample at 70°C.

gation of PCBM rich and P3HT rich domains. The phase shift does not cross the 90° boundary, indicating a material property change rather than an imaging instability. A phase shift due to a bi-stability is shown in the blue box. The sample shown in Figure 1.18 (c) and (d) was measured at 70°C and again shows a relatively homogeneous topography, and a much more varied phase contrast showing networks in a higher phase.

1.3.4 Electrostatic Force Microscopy (EFM)

Electrostatic forces between tip and sample are sufficient to perturb the cantilever oscillation in the same manner that the interactions between the tip and surface do. However, electrostatic forces persist over a longer range than the tip-surface forces, so that if a tip is oscillated around 50 nm off the surface, out of range of the tip-surface forces, and electrostatic forces are present it is these that cause changes in the cantilever's behaviour.

If the capacitance, C, between the tip and surface is considered, then for a given potential difference between the tip and sample, V, the capacitive energy is $U = \frac{1}{2}CV^2$. The capacitance depends on the tip surface separation and so the electrostatic force between the tip and surface can be approximated by

$$F = \frac{1}{2}\frac{\partial C}{\partial z}V^2 \tag{1.16}$$

where z the separation between tip and sample. Thus, when the cantilever and tip are oscillated near the sample's surface the amplitude of oscillation is dependent on the capacitive gradient between tip and sample. Changes in tip-surface separation or capacitance cause changes in the cantilever's oscillation amplitude.

EFM measurements are generally implemented in dual pass mode. Dual pass mode first tracks the topographic surface using standard tapping mode, then the cantilever is lifted to a desired height above the surface. A bias is then applied between the tip and sample, as the AFM then scans back over the topography from the previous scan, maintaining a fixed distance between tip and sample. The amplitude and phase of the cantilever are measured for both passes. In the first pass the topography is measured by maintaining the amplitude of oscillation as normal, in the second pass the amplitude modulation is turned off and the frequency shift of the cantilever resonance is measured. This can either be done directly using a phase locked loop (a feedback loop that changes the drive frequency to maintain a constant phase), or by measuring the phase and using the linear relationship between frequency and phase close to resonance to determine frequency shift.

This has been used to investigate the surface potential of semiconductors as early as 1988 [164]. This has been effective on integrated circuits [165], and cathode arrays [166]. In insulators the charging and speed of discharging have been measured, showing that PMMA holds charge for much longer timescales than quartz and sapphire [167, 168]. The behaviour on cathode arrays emphasises that the response of the cantilever is highly dependent on both the bias applied to the system and the tip surface distance, most notably that the dependence on tip surface separation is heavily influenced by the geometry of the surface [166].

EFM can be used for more applications than simply imaging electrostatic forces with spatial resolution; Stern et al. used EFM to determine the length of time several insulating materials hold charge [167].

1.3.5 Time Resolved EFM (Tr-EFM)

Time resolved EFM (Tr-EFM) measures the frequency shift of the cantilever in response to an applied perturbation of the electric field of the sample, this can be performed with high time resolutions as the phase is recorded by the AFM with a time resolution of 2×10^{-5} s, as standard. At relatively low time resolutions, but high spatial resolution, this was used by Jaquith et al. to measure the trapping rate of holes in pentacene [169]. In this case voltage pulses across a transistor device were employed, and the AFM tip was scanned across the channel revealing areas where charges were trapped. They also measured the time it took for the trapped charges to reach a steady state value, in this case around 30 seconds [169].

In 2006 Coffey and Ginger published their initial results using Tr-EFM on organic semiconductors [170]. Unlike Jaquith's work, Coffey and Ginger used an LED to excite charges in the F8BT/PFB system and measured the response of the cantilever in a single location in response to the light. They showed that the charging rate depended logarithmically on light intensity, and was also heavily dependent on the processing conditions used. Coffey and Ginger also showed that for their system the external quantum efficiency (EQE) correlated with the charging time they measured with Tr-EFM. This suggests that Tr-EFM can be used as a measure of device efficiency. Later work by Cox et al. showed that this held true for excitations in MDMO-PPV:PCBM devices [171].

Whilst, for Ginger's application, Tr-EFM has a high time resolution of around 100 μs, the Ginger group added sophisticated triggering circuitry which improved the time resolution to the 100 ns range, allowing the study of faster more efficient photovoltaic systems. They called this technique feedback free Tr-EFM (FF-trEFM) [172].

1.3.6 Kelvin Probe Force Microscopy(KPFM)

Kelvin probe force microscopy (KPFM) is similar to EFM in that it uses the cantilever's response to the electrostatic field of the sample. However, KPFM does not apply a large external bias to the sample; instead it seeks to nullify the differences in potential between the tip and sample. This can be used to study the workfunctions of samples, by measuring the workfunction difference between tip and sample. For a metal sample and tip, the difference between their workfunctions is the contact potential difference, V_{CPD}. For a semiconductor and metal probe this is more complicated: V_{CPD} still describes the difference between the vacuum level and the Fermi level of the semiconductor and metal, however, the electron affinity of the semiconductor must be taken into account.

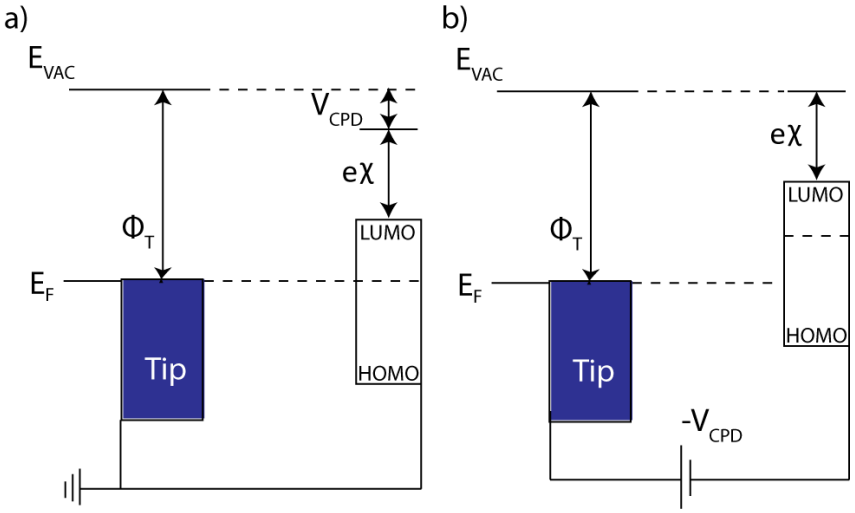

Figure 1.19: Principle of KPFM measurements, showing the initial alignment of the energy levels in sample and tip. a) With their Fermi levels (E_F) aligned there is an electric field between sample and tip corresponding to the difference in their workfunctions (Φ). b) The electric field is neutralised by applying -V_{CPD} to the tip, where $V_{CPD}/q = \Phi_T - \Phi_S$, and q is the electron charge.

In KPFM the cantilever is driven at its resonant frequency by an a.c. bias of the form $V_{AC}\sin(\omega t)$, and since the force acting on a cantilever from the electric field can be described as

$$F = \frac{1}{2}\frac{dC}{dz}V^2 \tag{1.17}$$

in the case of KPFM $V = V_{DC} - V_{CPD} + V_{AC}\sin(\omega t)$, where V_{DC} is an applied DC component of the bias applied to the tip or sample, and V_{CPD} is the contact potential difference between the tip and sample. When expanded out, the force as a function of the applied bias has only one component at the applied frequency,

$$F_\omega = \frac{dC}{dz}\left[V_{DC} - V_{CPD}\right]V_{AC}\sin(\omega t) \tag{1.18}$$

and minimization of this force can be achieved by adjusting the DC component of the bias to be equal to the contact potential difference. When a feedback loop is used to minimise the cantilever's response at ω, the contact potential difference can be measured. Figure 1.19 shows a schematic of the energy level alignment and the operating principle of KPFM.

KPFM can be used either in a point by point approach or as a scanning technique. As a scanning technique, KPFM can be operated in single or dual pass

methodologies. Like for the case of EFM, in dual pass mode, the topography is first measured in tapping mode, then the tip is withdrawn to a set distance above the sample and oscillated with V_{AC}. A potential feedback loop is then applied and the AFM controller adjusts V_{DC} to minimise the amplitude of oscillation. The potential map can then be measured almost simultaneously to the topography. Single pass KPFM (also called dual frequency KPFM) can truly measure topography and potential simultaneously. In this mode the cantilever is oscillated at two separate frequencies; near resonance for the tapping mode topography, and at a much lower frequency for the potential feedback signal. Whilst this is more efficient it is less sensitive to potential changes due to the potential signal being off resonance [173, 174].

KPFM has been used to study the interactions between materials, in the hope of improving charge transport between graphene oxide and P3HT [175]. It is also possible to study the contact potential of single P3HT nanofibers [176], and even the distinction of single atomic species, distinguishing adatoms on a silicon surface [177]. There are many examples of similar nanoscale characterisations using KPFM [178, 179, 180], but one of the more common uses for KPFM is looking at the doping in semiconductors, where the doping profiles can be mapped [181, 182, 183, 184, 185]. KPFM has also proven to be useful in measuring the properties of organic photovoltaics, and has the ability to image the local photovoltaic properties of heterojunctions [186, 176, 187, 188].

Figure 1.20 shows how this technique can be used to measure the photovoltaic properties of materials as well as their work functions. Initially, standard KPFM is used to cancel the contact potential difference between the tip and sample, then a light is applied to the sample. Any further change in the feedback bias is thus due to a surface photovoltage (SPV). This has been used to find the V_{OC} of both organic [86], and inorganic PV devices [189]. Similarly to the standard KPFM, this can also be used to image the photogenerated charges in a donor/acceptor blend [190]. KPFM is very useful to measure the magnitudes of potential differences on the sample's surface, however, it offers only steady state behaviour of the system; in order to improve on this intensity modulated KPFM was devised.

1.3.7 Intensity Modulated KPFM (IM-KPFM)

Intensity modulated KPFM (IM-KPFM) combines the techniques of measuring the workfunction and the SPV to achieve a time resolved method of investigating the SPV behaviour. In 2008 Takihara et al., showed that it is possible to measure the carrier lifetime behaviour in a polycrystalline silicon solar cell by measuring the time averaged KPFM response of a sample to a modulated light source. Using

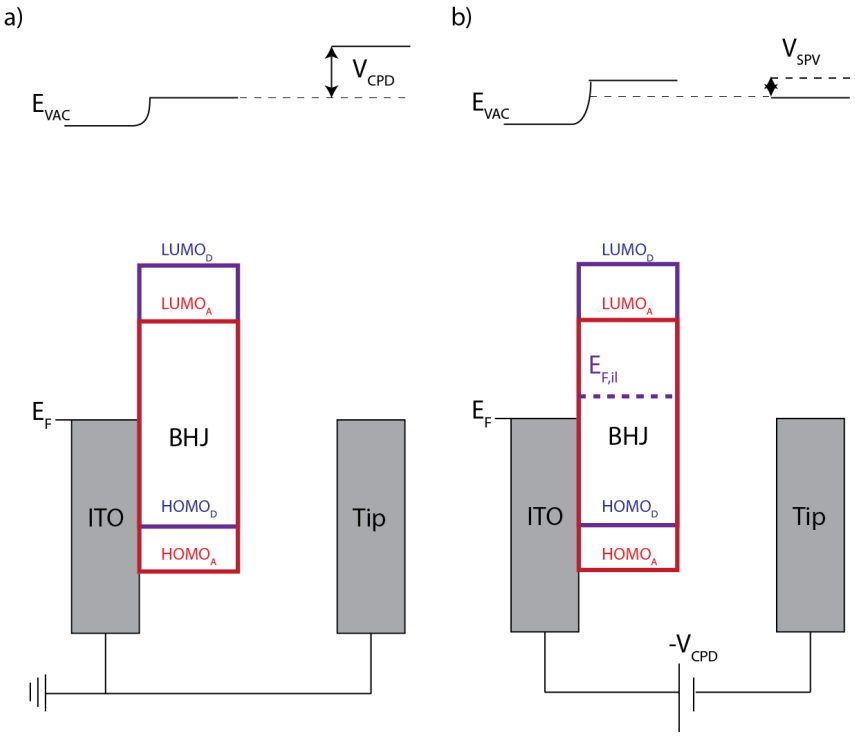

Figure 1.20: A schematic of how KPFM can be used to measure the photovoltage generated by a BHJ device. a) shows the KPFM operation in the dark, where the potential difference is solely caused by the contact potential difference. b) After negating the contact potential difference the sample is illuminated and the potential difference is caused by charge generation in the BHJ increasing the effective Fermi level of the electron acceptor. This is measured as an effective increase in workfunction, from the generated photovoltage (V_{SPV}).

this they showed that the carrier lifetime decreases closer to grain boundaries in polycrystalline silicon solar cells [191].

In 2014, Shao et al., used this technique with the addition of a background light bias to measure the carrier lifetimes of an organic solar system [192]. In this technique the KPFM experiment is setup as normal, and the feedback is turned on in the dark so that V_{CPD} is compensated for. In the case of Shao et al,. the SPV of the background white light bias is also compensated for. Then a modulated light is applied to the sample, causing near instantaneous charging of the sample, as the light turns off the charge dissipates at a rate depending on the physical processes occurring. At low modulation rates it can be assumed that all the charge is dissipated, causing the time averaged KPFM signal to be equal to 0.5 SPV. At

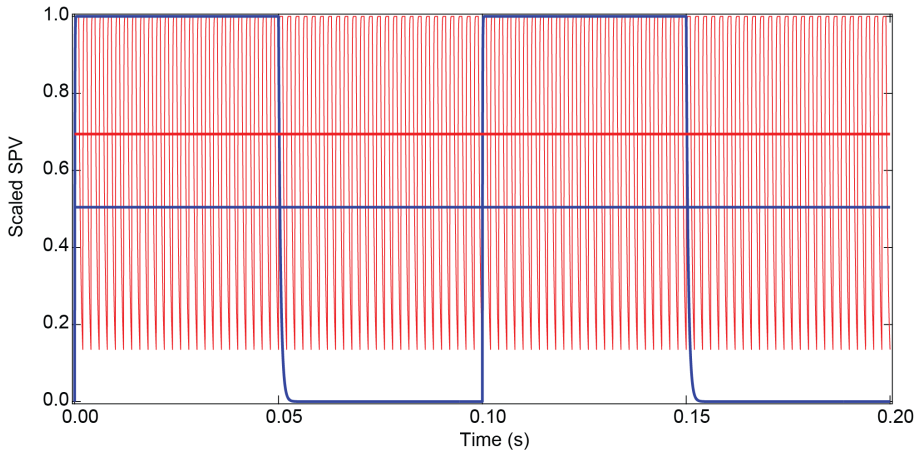

Figure 1.21: Simulated surface potential with a modulation (blue) and a faster modulation (red). Their time average over the period are shown by solid horizontal lines.

higher modulation frequencies the time averaged KPFM signal rises as the amount of charge dissipated between light pulses decreases.

Figure 1.21 shows a simulation of this effect, with the low frequency modulation shown in red and the higher frequency in blue. Fitting the average KPFM response as a function of modulation frequency with a stretched exponential function yields the timescale of carrier dissipation in the sample. Shao et al., showed that an increased light intensity led to increased recombination rates in their PCDTBT: $PC_{70}BM$ samples. They also showed that this technique can be used to look at the chemistry of buried interfaces [192].

1.4 Scope of this Thesis

In this thesis, the local electrical properties of OPVs are investigated using AFM, with the aim of relating measured values to the device properties. The temperature dependence of these measurements is investigated to try to further understand the annealing and operating behaviours of OPVs. It is common for the properties of OPVs to change when they are thermally annealed.

Chapter 3 explores the use of conductive AFM to measure the temperature dependence of the mobility of P3HT. Contact mechanical methods allow this to be related to the physical properties of the polymer, such as the adhesion and the Young's modulus. The mobility of P3HT increases with temperature indicating that the charge transport is via a hopping mechanism. In annealed P3HT there is a

correlation between the Young's modulus and mobility of P3HT that is not present in the as-cast sample, implying that physical changes affect the electrical properties.

In Chapter 4 non contact methods of Tr-EFM and IM-KPFM are used to look at the dynamic behaviour of charge carrier generation and depletion by measuring the response of the SPV to either a single light pulse (Tr-EFM), or a modulated applied light (IM-KPFM). A logarithmic dependence of SPV on light intensity is seen in the case of Tr-EFM, but is not seen in IM-KPFM, indicating that the two techniques are measuring different properties. The dynamic behaviour measured between them is also different with Tr-EFM showing longer timescales than IM-KPFM.

Chapter 2

Methodology

2.1 Sample Preparation

2.1.1 Substrates

Devices were fabricated on indium tin oxide (ITO) coated glass substrates, from Thin Film Devices with an ITO thickness of 145 nm offering a sheet resistance of 15 Ω/sq. Prior to use the ITO was cleaned by sonicating for ten minutes, first in a solution of Decon 90 or Helmanex (1:10) with deionised water, then deionised water and finally in propan-2-ol. They were then dried under a nitrogen jet. Depending on the subsequent layer they were then either used bare or were first UV/ozone treated for 30 minutes. UV/ozone treatment has the advantage that it removes carbon contaminants from the substrate, however it also increases the work function of the ITO [193]. This can be beneficial if an interlayer is used between substrate and active layer. These interfacial layers are selected to promote the transport of either electrons or holes accordingly. A 5 nm hole extracting layer of molybdenum oxide MoO_x was used to achieve favourable electronic contact between the P3HT and ITO electrodes. Despite its high 6.4 eV workfunction, favourable band bending and plentiful gap states make MoO_x a good hole transport layer between P3HT and ITO [194].

2.1.2 Evaporation

MoO_x interfacial layers were grown by evaporation in a Kurt J Lesker Spectros high vacuum chamber held at $<10^{-7}$ mbar, providing clean conditions for layer deposition. The process of evaporation is shown schematically in Figure 2.1.

Firstly, substrates were loaded into the rotating substrate holder near the top of the evaporation system. A scroll pump was used to achieve a rough vacuum

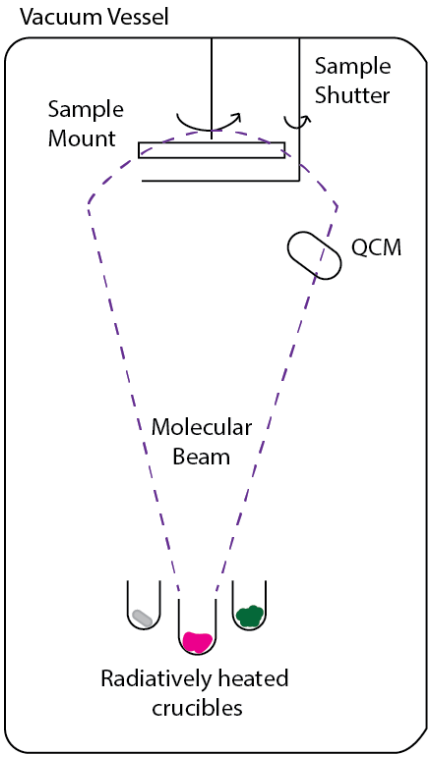

Figure 2.1: A schematic of an evaporation system.

of $\sim 10^{-2}$ mbar, then a cryogenic pump was engaged to reach a base pressure of $\sim 10^{-8}$ mbar. The metal source containing the raw material was then radiatively heated.

When the deposition material reaches the correct temperature it sublimes into a cloud which spreads from the crucible. The rate of deposition was measured by a quartz crystal microbalance (QCM), located beneath the sample shutter. Applying an AC current to the quartz induces oscillations at its resonant frequency. When evaporated material is deposited on the QCM its resonant frequency decreases, and the amount of material deposited can be determined due to the Sauerbrey equation [195]. When the rate of deposition was high enough (< 0.2Å), the sample shutter was withdrawn and the desired amount of material was deposited onto the substrates, using the QCM to gauge the material deposited. The shutter was then re-engaged, and the metal source was cooled. Samples were then transferred into the attached glove box subsequent to the spin coating of active layers.

2.1.3 Active Layers

2.1.3.1 P3HT

Solutions of P3HT were made by dissolving 0.2 mg of Rieke Materials (Sepiloid P200 16k Ma) P3HT in 1 ml di-chloro-benzene in a nitrogen atmosphere. Solutions were then stirred for 24 hrs in dark conditions at 40 °C. Prior to deposition of P3HT, UV/ozone treated substrates were coated with a 5 nm layer of MoO_x, by evaporation. The P3HT was then deposited onto the MoO_x by spin coating.

2.1.3.2 P3HT:PCBM

Solutions of P3HT:PCBM were made by dissolving 0.2 mg of Rieke Materials (Sepiloid P200 16k Ma) P3HT and 0.2 mg PCBM in 1 ml di-chloro-benzene in a nitrogen atmosphere. Solutions were then stirred for a minimum of 24 hours in dark conditions at room temperature approx. 27 °C. Solutions were filtered by a 0.2 μm syringe driven filter before spin coating onto freshly cleaned substrates.

2.1.3.3 PTB7:$PC_{70}BM$

PTB7:$PC_{70}BM$ samples were made by Martin Tyler of the Ross Hatton group. PTB7:$PC_{70}BM$ films were spin cast from a solution of 97:3 dichlorobenzene:diiodoctane at a concentration of 10 and 15 mg/mL of PTB7 and $PC_{70}BM$, respectively. The solutions were stirred overnight at 50°C. Spin casting was then carried out at 1000 rpm for 60 s followed by 6000 rpm for 4 s. Spin coating was performed in an N_2 glovebox, also where the samples were stored before measurement [196].

2.1.3.4 VOPc on graphene

Graphene was grown by Alex Marsden on low cost copper foils via low pressure chemical vapour deposition (CVD) using methane as a feedstock [197], as described in [198]. First, the copper foils were electropolished in a solution containing orthophosphoric acid and urea (5 V, 1.5 A). After rinsing off the electrolyte with deionized water then isopropanol, the polished foils were sonicated in acetone, and then rinsed again with isopropanol and dried with nitrogen. They were loaded into a quartz tube in a tube furnace, which was pumped to vacuum below 1×10^{-3} mbar. Hydrogen was flowed at 10 standard cubic centimetres per minute (sccm), raising the pressure to 1×10^{-2} mbar. The furnace was heated to 1000°C, and left at this temperature for 20 min. To start the growth, methane was introduced at 20 sccm for 20 minutes while still held at 1000°C. The methane and hydrogen

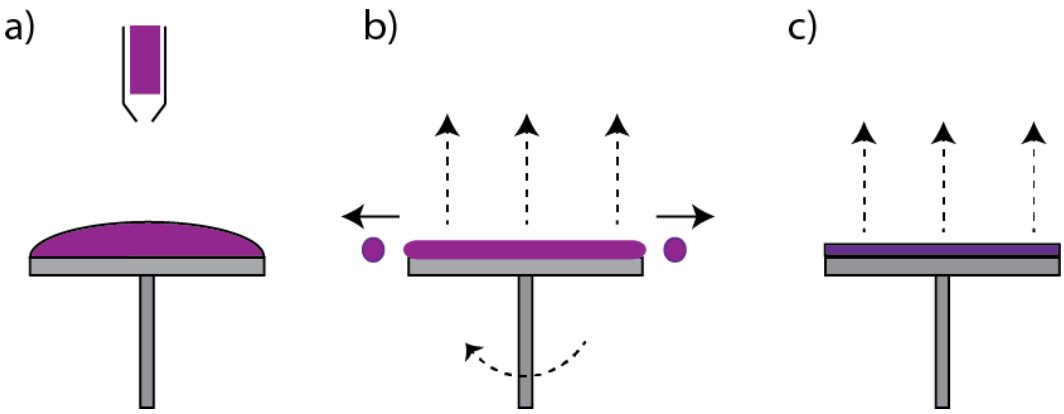

Figure 2.2: The stages of spin coating. a) Addition of solution. b) Spinning, with drive off of excess and evaporation of solvent. c) Final evaporation of solvent.

remained on during cooling to 600°C, after which the methane was turned off. This yields copper foils that are > 99% covered with predominantly single layer graphene of high-quality.

Vanadyl phthalocyanine (VOPc) was deposited by Luke Rochford, directly onto these graphene coated foils, or onto ITO, in a custom-built single chamber ultra high vacuum (UHV) system with a base pressure better than 1×10^{-8} mbar. VOPc (Acros Organics UK) was purified by three cycles of thermal gradient sublimation before use. All films were grown at a deposition rate of 0.03 nm/s which corresponded to a crucible temperature of ≈365°C. The graphene covered foils were heated to the target temperature and allowed to reach equilibrium over the course of 1 hour, during which time the VOPc deposition rate was stabilized. Once deposition was complete, the foils were left to cool before removal from UHV [2].

2.1.3.5 Spin Coating

Thin films of P3HT, P3HT:PCBM and PTB7:$PC_{70}BM$ were deposited on surfaces by spin coating; the former solutions were deposited in an N_2 glovebox on Laurell Technologies spin coater with acceleration/deceleration rates of 1000 rpm. Spin coating is a simple but effective technique, yielding flat homogeneous layers over a small surface area. This is useful for lab based batch techniques, however, it is not scalable to industrial sized devices. Figure 2.2 shows a schematic of how spin coating is achieved.

First, the prepared substrate is affixed by vacuum to a central platform. A solution is then added dropwise, to the extent where surface tension keeps it from

spilling off the edges of the substrate. This much solution is not generally required, but it ensures the whole of the substrate is wetted. The stage is then accelerated to the desired spin speed. This process rapidly removes material from the surface, sometimes creating defects in the form of vortices as the solution on the substrate spins faster than the solution on the surface [199]. Once the desired spin speed, between 600 and 2000 rpm, has been reached the solution spreads evenly due to centrifugal force. However edge effects do take place leaving droplets or rings at the very edge of the substrate. This is not particularly relevant to AFM work, as the area needed for AFM is small enough to be unaffected by this. However, it can be detrimental to larger device tests where an electrode needs to cover a homogeneously thick layer.

The solvent, in this case 1-2-dichlorobenzene, evaporates during this process. However, viscous flow dominates the outflow of material at the beginning of the spin cycle. Eventually evaporation dominates material loss from the sample, and the coating begins to crystallise. Once spinning has stopped, after 60 s, the layers are left to complete the evaporation process. The thickness of the layers produced can be found by step edging in an AFM.

2.1.3.6 Calibration of Film Thickness

To determine the film thickness a scratch was made through the thin film to the hard surface beneath, typically using a razor blade or needle. The glass ITO substrate provides a good surface for step edging as the ITO is very hard and flat [200, 201]. These two properties ensure that when a line is scratched the exposed substrate area is clean and flat, making the distinction between sample and substrate clear. The importance of this is demonstrated in Figure 2.3, a flat region ensures that the flattening of the entire image is accurate.

Histograms of the flat areas are taken, while the area around the step is masked, to deduce the thickness of the layer. Layers spun at 1200 rpm for 1 minute had an average thickness of 70 $\pm$ 20 nm and those spun at 800 rpm gave a thickness of 100 $\pm$ 30 nm.

2.2 AFM

2.2.1 MFP3D

The entirety of this work took place on an Asylum Research MFP3D AFM with an extended range head. This is a flexure based, stage scanning AFM with separate X,

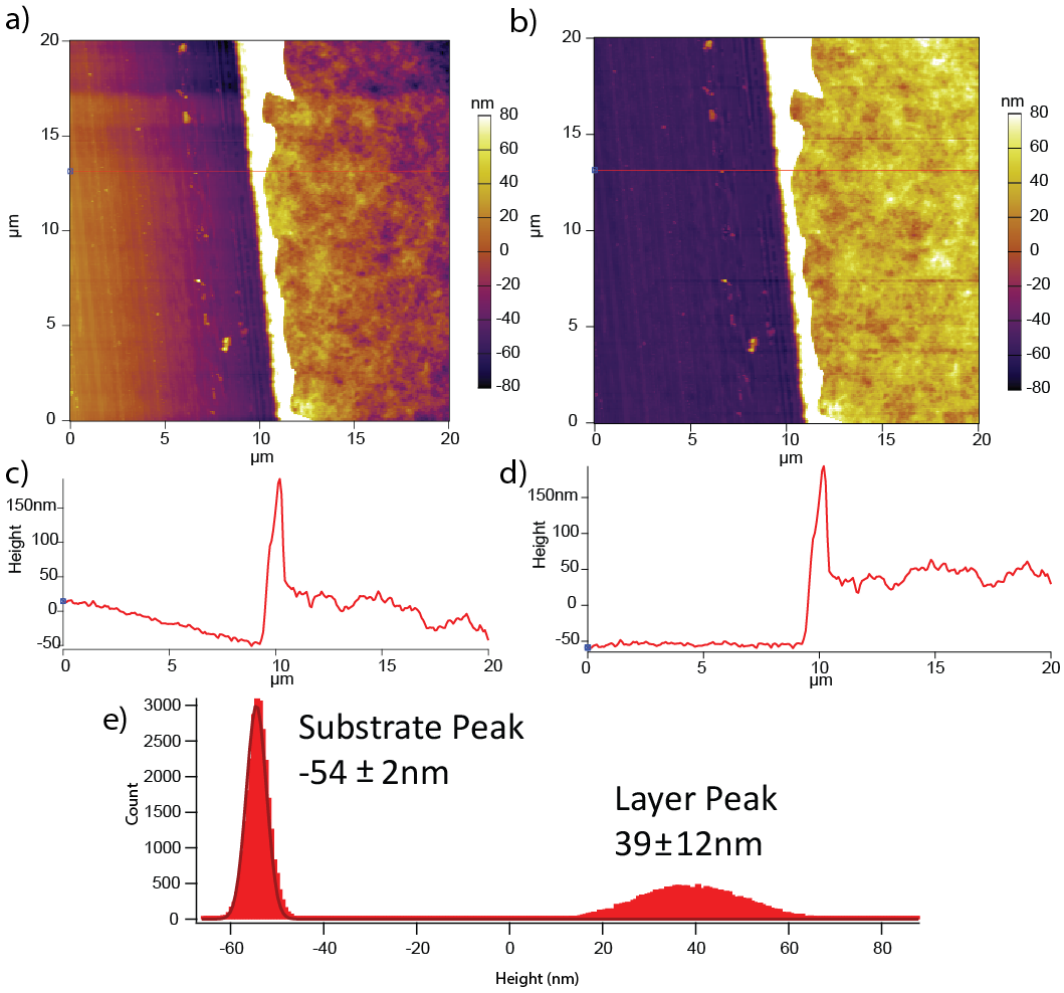

Figure 2.3: The topography of a step edge of spin coated P3HT on glass ITO before flattening a) and after flattening b). Line traces along the line shown in red can be seen in c) and d). Histograms of substrate and layer are fitted and shown in e).

Figure 2.4: Schematics of the Asylum Research MFP3D Standalone, taken from Asylumresearch.com

Y and Z piezos. The Z piezo is housed in the head, as shown in Figure 2.4. The X and Y piezos in the MFP3D operate in closed loop mode, correcting for hysteresis and creep. The Z piezo runs in open loop, however, it has a position sensor for accurate Z heights. The scanning stage of the AFM has a range of 90 μm in both X and Y directions, and the Z piezo has a range of 40 μm. The MFP3D uses a 4 quadrant photodiode with an IR laser to detect the cantilevers deflection. This model also features 2 separate optical paths to the sample. The first though the rear of the head and the second through a path directly beneath the sample.

The AFM is controlled by Wavemetrics, Igor Pro software. Igor Pro features a complete programming language allowing procedures for data capture and processing to be added directly to the AFMs operation.

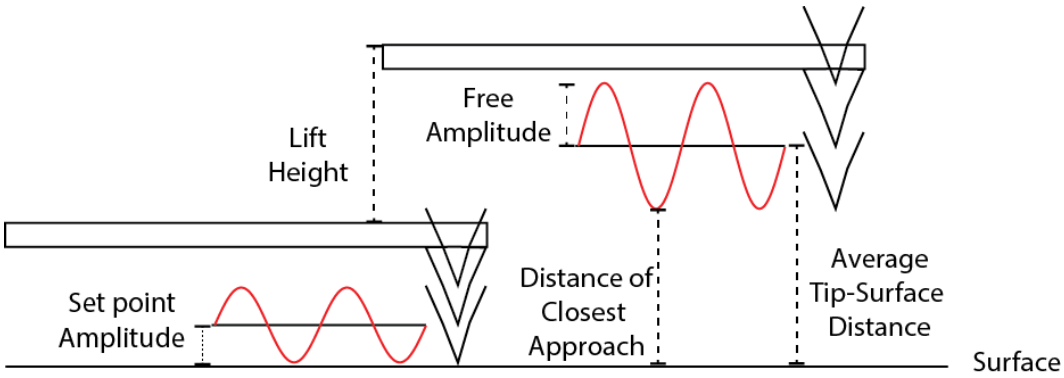

Figure 2.5: Definition of different heights of the tip above the surface.

2.2.2 Tapping Mode

Tapping mode images were performed with Olympus AC240-TM cantilevers, with a nominal spring constant and resonance frequency of 2 N/m and 75 kHz respectively. Cantilevers were tuned to 1 V (∼50 nm) oscillation amplitudes at a driving frequency 5% below the natural resonance frequency of the cantilever. Imaging was performed on areas between 1 and 20 μm squared in area at setpoint amplitudes of 650 - 750 mV.

2.2.2.1 Tip surface Distance

Both Tr-EFM and IM-KPFM require that the distance between tip and sample is carefully defined. Figure 2.5 shows the different tip heights above the surface, dependent on the oscillation of the tip. Upon engaging the tip to a set point less than the free amplitude of the cantilever, the tip can be defined as touching the surface at the bottom of its oscillation, and the average height above the surface is then defined by the set point amplitude. When the cantilever is withdrawn by the z piezo, the distance withdrawn is called the lift height. The average distance from the surface is then equal to the setpoint amplitude plus the lift height. The distance of closest approach to the surface is thus the average distance from the surface minus the free amplitude.

2.2.2.2 Converting Phase to Frequency

Figure 2.6 shows a standard tuning curve taken during a Tr-EFM experiment at 50°C. The target amplitude is 1 V at 5% below the resonant frequency, at this point the phase is set to be 90°. Assuming that measured phase shifts, $\Delta\phi$, are due

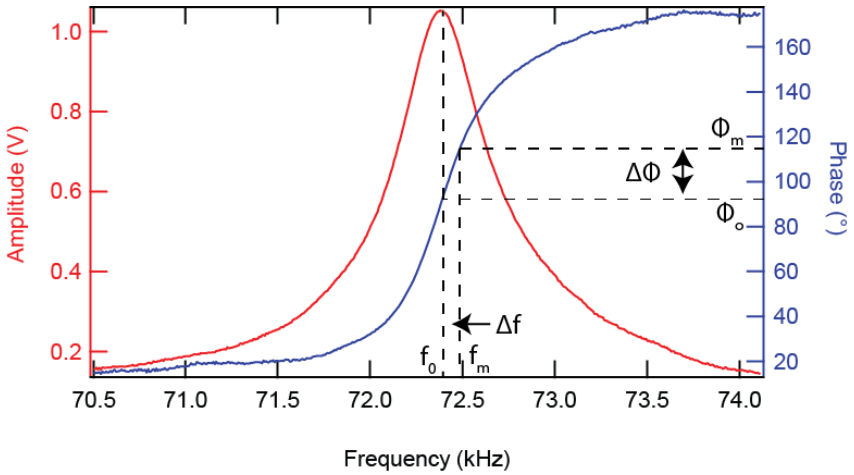

Figure 2.6: A standard tuning curve showing the amplitude and phase response of a cantilever taken during a Tr-EFM experiment at 50°C. The conversion between phase and frequency is also displayed; ϕ_m is the measured phase corresponding to the new effective resonant frequency f_m, respectively ϕ_0 and f_0 correspond to the initial phase and frequency.

to changes in the effective resonant frequency of the cantilever without changes of quality factor, the phase shift can be converted to a frequency shift by interpolation of the tuning curve. The difference between the frequencies, f_m and f_0, is determined to be the frequency shift, Δf.

2.2.3 Cantilever Calibration

Though the process for making cantilevers is now a reproducible practice, the qualities of cantilevers can vary greatly. There are a number of different methods to calibrate the properties of cantilevers [202], here the Sader method was used [203].

The Sader method determines the spring constant of a cantilever from its resonant frequency and physical characteristics. The length, width, Q factor and resonant frequency need to be known. The length and the width of the cantilever are easily measured with optical microscopy, but the manufacturer's specifications are usually accurate. The quality factor, or Q factor (Q_f), indicates how much energy is lost per oscillation of the cantilever and is measured as the full width half maximum of the power spectral density peak at resonance of the cantilever. The power spectral density is found by performing a thermal tune. A thermal tune records the deflection of the cantilever with a very high time resolution without an applied drive. A Fourier transform is then taken of this, showing the amplitude of

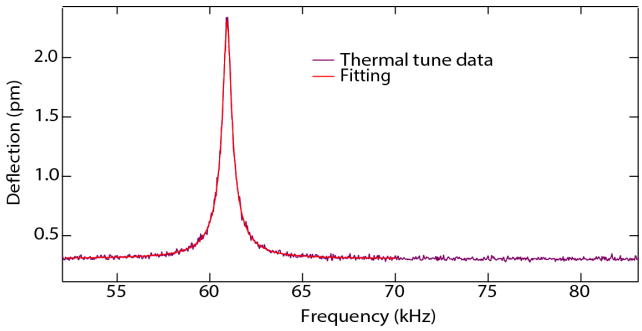

Figure 2.7: A thermal tune fitted with Equation 2.1 showing the amplitude spectral density of the AC240TM cantilever with a resonant frequency of 61 kHz and a Q factor of 138.

the frequency response of the cantilever. This is fitted with

$$A(f) = \sqrt{\frac{\left(A\frac{f_0}{f}\right)^2}{\left(\frac{f_0}{f} - \frac{f}{f_0}\right)^2 + \left(\frac{1}{Q_f}\right)^2} + B^2} \tag{2.1}$$

where A is the resonant peak amplitude, B is the background noise level, f is the frequency and f_0 is the resonant frequency. Figure 2.7 shows typical thermal tune data with the fitting of Equation 2.1.

The spring constant (k) is then related to the physical parameters by

$$k = 0.19\rho_f b^2 L Q_f \Gamma_i(Re)\,(2\pi f_0)^2 \tag{2.2}$$

where the width and length of the cantilever (b and L), the resonant frequency and Q factor (f_0 and Q_f), are specific to each cantilever and the remaining factors are constants: the fluid density ρ_f and the imaginary part of the hydrodynamic function $\Gamma_i(Re)$.

The spring constant is needed for quantitative analysis of the forces used in AFM as the force applied by the cantilever is described by Hooke's Law

$$F = -kz \tag{2.3}$$

where z is the displacement of the spring. In an AFM the displacement z also needs to be calibrated. This requires determination of the optical lever sensitivity which relates the measured voltage from the photodiode to the actual displacement of the cantilever in nm, by performing a force curve in contact mode on a hard

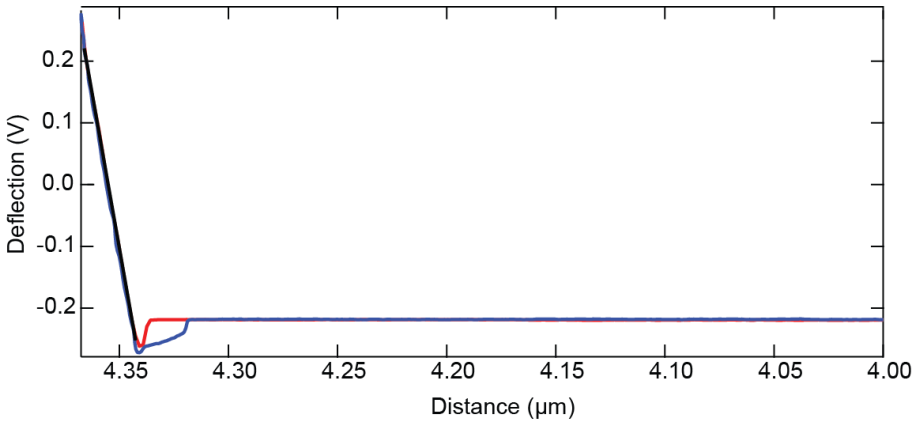

Figure 2.8: Calibration of the deflection InvOLS showing a force curve on silicon, with a linear fit to the loading curve finding the deflection InvOLS = 49.8 nm/V.

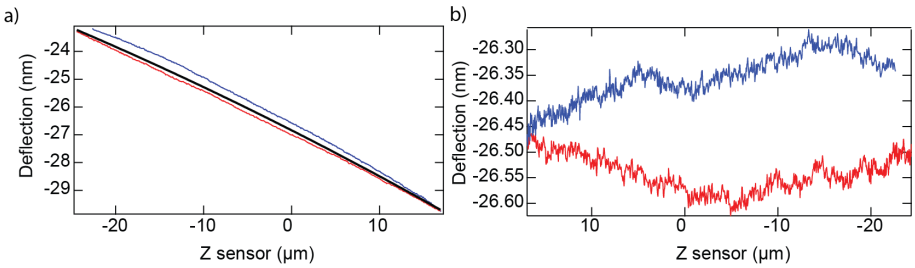

Figure 2.9: Calibration of the virtual deflection, showing the change in deflection across the full z-piezo range the approach in red and the retract in blue a) before calibration, with polynomial fitting and b) after calibration.

sample. Figure 2.8 shows an example of a force distance curve on a hard (silicon oxide) surface, with a linear fit to the loading curve. Against such a hard sample, it is assumed that once the AFM tip is in contact with the surface then every nanometer moved by the z piezo deflects the cantilever by a nanometre (i.e. there is no indentation). Thus the gradient of this line yields the rate of deflection of the cantilever with photodiode voltage in nm/V. This is called the deflection inverse optical lever sensitivity (InVOLS) and in this case the deflection InvOLS = 49.8 $\pm$ 0.3 nm/V.

In order to ensure the signal in the photodiode is only due to the bending of the cantilever and not to other reflection or interference effects of the laser, the virtual deflection should be calibrated also. The virtual deflection is calibrated by measuring a force curve across the entire movement of the z-piezo, making sure the

tip does not come into contact with the sample. Figure 2.9 (a) shows an example force curve measured in this manner. The fitting shown is a second order polynomial and when this is subtracted from the response curve the result is shown in (b). Calibrating in this way reduces the background noise of the photodetector signal increasing the force resolution.

Determining nanomechanical properties, as described in Section 1.3.1, requires that the deflection and distance data be converted to force and indentation data. This requires the calibration described above and accurate determination of the zero point of the force, and of the indentation. The zero point of the force can be found by fitting the non contact region of the force curve with a linear fit, as when the tip is far from the sample the force is zero. If the virtual deflection has been properly calibrated, the gradient of this line should be zero. However, an imperfect calibration or a change in conditions can result in this line having a non zero gradient, so the more rigorous option is to extend the line across the whole data range and subtract it from the data. Determining the force accurately thus requires: 1) calibration of the cantilever spring constant to relate the deflection in nm to force in nN; 2) calibration of the optical lever sensitivity to convert deflection in Volts to deflection in nm; 3) correction of the virtual deflection to remove interference artefacts; 4) determination of offsets, defining the zero value of deflection through analysis of the deflection whilst far from the surface. Finding the zero point of indentation is more complicated and model dependent, and will be discussed further in Section 2.2.5.3.

2.2.4 Cantilevers

Choice of cantilever and tip is equally important. Here, Olympus Cantilevers' AC240TM-R3 tips were predominantly used. They are a silicon based cantilever with a titanium interlayer and a conductive platinum coating. The have nominal resonant frequencies of 70 kHz, spring constants of 2 N/m and tip radii of 15 nm.

For conductive AFM, the tip and cantilever need to be electronically conducting, leaving the choice of tips between solid metal, metal coated, or speciality tips such as boron doped diamond tips. Boron doped diamond tips, apart from being expensive (£100 per tip), are best used for hard surface applications. Constant friction against a hard surface does not wear the tip, and hence decreased resolution is not observed when used in this manner. A metal coated silicon tip, can not only lose conduction when the coating wears off, but can also wear, resulting in the common imaging convolutions and reduced resolution. When imaging soft, sticky polymer samples, decreases in conductivity and resolution during imaging are most

likely due to adhesion of the polymer to the tip (Figure 2.10), and hence using a hard tip does not in this case improve the resolution of the technique.

Both metal coated silicon and solid metal tips suffer from adhesion of polymer to the tip's surface during imaging, however each has its own advantages and disadvantages. Coated silicon tips are made in reproducible batches, with many well characterised shapes and stiffness. They can be relatively accurately calibrated using standard techniques and tend to be easy to mount and use. However, the coatings are fairly easy to wear off, being usually 20 nm thick. In addition to this, because the process of making silicon tips is so well refined, they can be made very sharp: whilst this is good for high resolution imaging, the tips themselves can be extremely brittle. If the AFM or the sample drifts vertically, or if the initial engage is too forceful, the end of the tip can break off.

Solid metal tips, however, have the advantage that even if the tip breaks off, the probe still remains conductive, albeit with a larger contact between tip and sample. However, since these tips are made by breaking a piece of wire, then subsequently bending and flattening one end, they are not as uniform as silicon cantilevers, and are much more difficult to calibrate.

Figure 2.10 shows a comparison between a pristine tip in (a) and tips in various stages of contamination after use imaged with transmission electron microscopy (TEM). The visible bending of the tips was due to the electron beam. It is likely that the tip shown in (b) and (c) would show little drop in current, though the contact area would be increased. In the case of d) this kind of coverage and tip damage is indicative of the tip engaging too deeply on the sample, this can happen with thermal expansion of the sample if it expands beyond the range of the z-piezo.

2.2.5 Force Curves and Force Volume Mapping

2.2.5.1 Force Curves

Force curves can be performed in either contact mode or tapping mode, though contact mode is more common. The tip is approached towards the sample at a set rate, 2 μm/s was used here. The tip connects with the sample and begins to load force onto the sample at the same rate. The tip stops moving when the trigger point is reached. The trigger point is set by a predefined deflection value, thus corresponding to a desired force. At this point the tip can be made to dwell on the surface, for a set length of time called the dwell time, and can be used to study elastic properties or other phenomena [204, 205, 206]. The dwell period is also used to study electrical properties as the force on the sample is constant: the timing of

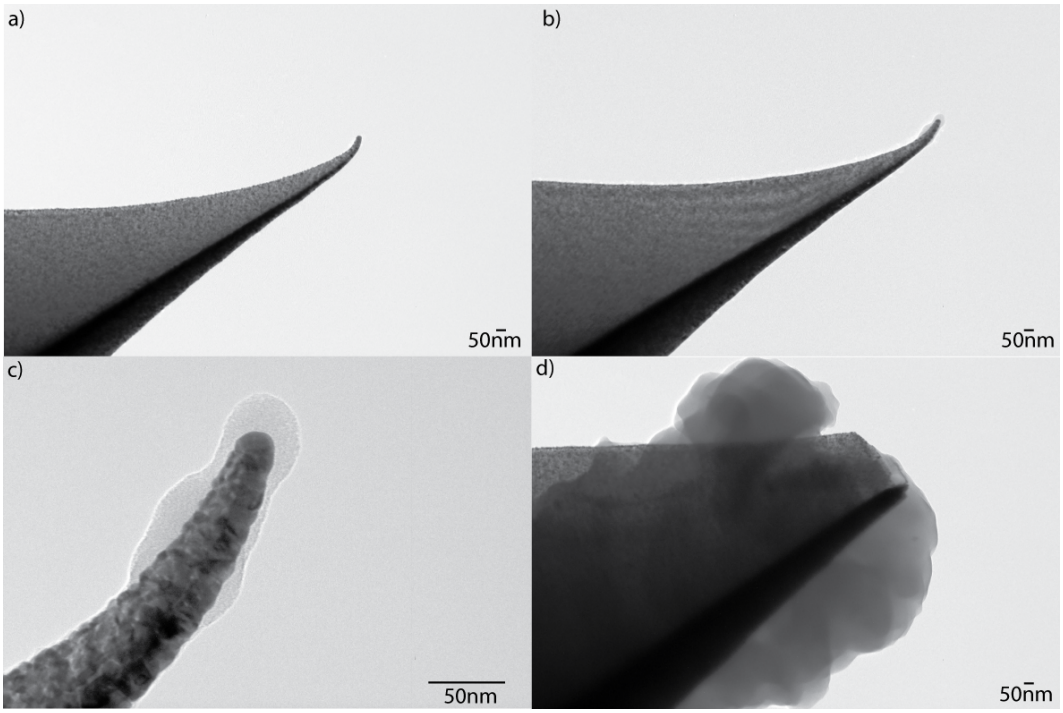

Figure 2.10: TEM images of AFM tips comparing a) a pristine tip with those in various stages of contamination after use. b) shows a small amount of P3HT contamination, c) a closer view of b) showing the P3HT contamination more clearly. d) Shows significant damage to the end of the tip with heavy P3HT contamination.

the electrical measurements for FVBS incurred a dwell time of 10 s. After the dwell, the tip unloads the force at the same rate as the loading, until it separates from the sample. Then it retracts at the same rate to a distance away from the sample called the force distance. Here, a distance of 1 μm was used, to ensure that the tip cleared any topographic features as it moves to a new position. A force volume map occurs when force distance measurements are repeated in a regular array over an area of the surface.

2.2.5.2 Trigger Point Force

When using force curves as a quantitative data gathering tool the set point force, or trigger force, needs to be carefully considered. An inadequate force on the sample can trigger a false engage, where the deflection reaches the set point value before the tip touches the surface. Also a low trigger force can yield a very small contact area between the tip and the sample's surface. A small contact area has the con-

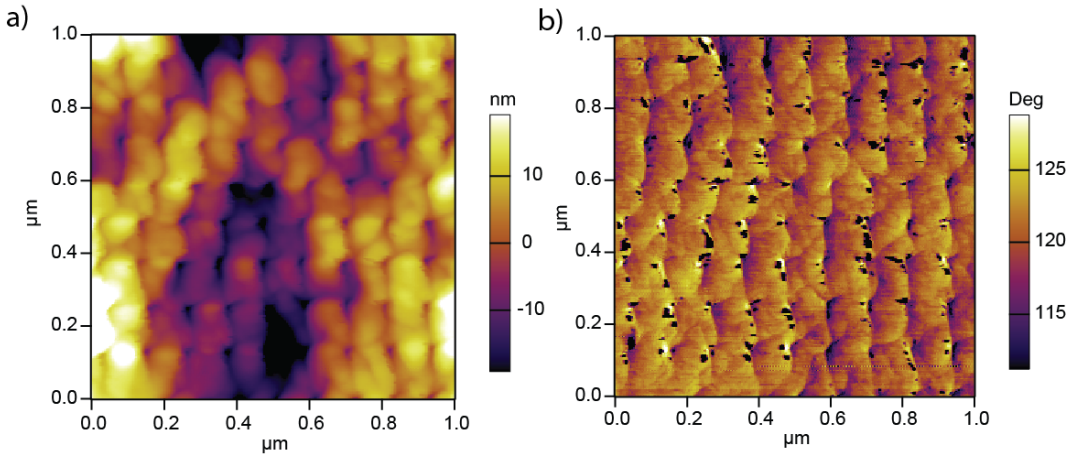

Figure 2.11: a) Topography and b) phase maps showing indentations evident on the sample after an FVBS map at 70 nN.

sequence of a small current, potentially compromising the signal to noise ratio of the experiment. Running a force curve with a bias applied to the sample can determine a suitable trigger point to use for electrical measurements. A solid electrical connection can be seen by monitoring the current: a suitable trigger point can be chosen by the force at which a good current response is observed.

On a similar note, too much force on the sample can result in inelastic indentation. This is shown in Figure 2.11, topography and phase images on a sample of P3HT after a FVBS map was taken using a 70 nN trigger point. The indentations where each of the FVBS points were taken are clearly visible. The high force here has two disadvantages: it is likely that this level of indentation causes polymer contamination of the tip, as shown previously; also the models for fitting force curves tend to only apply in the elastic limit of a material, making fitting of these curves invalid. Therefore, it is best to optimise the force applied before each experiment.

2.2.5.3 JKR Fitting

The Johnson Kendal Roberts model, Section 1.3.1, predicts that the indentation (δ) depends on force according to:

$$\delta = \frac{1}{r_{tip}}\left(\frac{r_{tip}}{E_{tot}}\left[\sqrt{F_{ad}}+\sqrt{F+F_{ad}}\right]^2\right)^{\frac{2}{3}} - \frac{4}{3}\sqrt{\frac{F_{ad}\left(\frac{r_{tip}}{E_{tot}}\left[\sqrt{F_{ad}}+\sqrt{F+F_{ad}}\right]^2\right)^{\frac{1}{3}}}{E_{tot}r_{tip}}}. \tag{2.4}$$

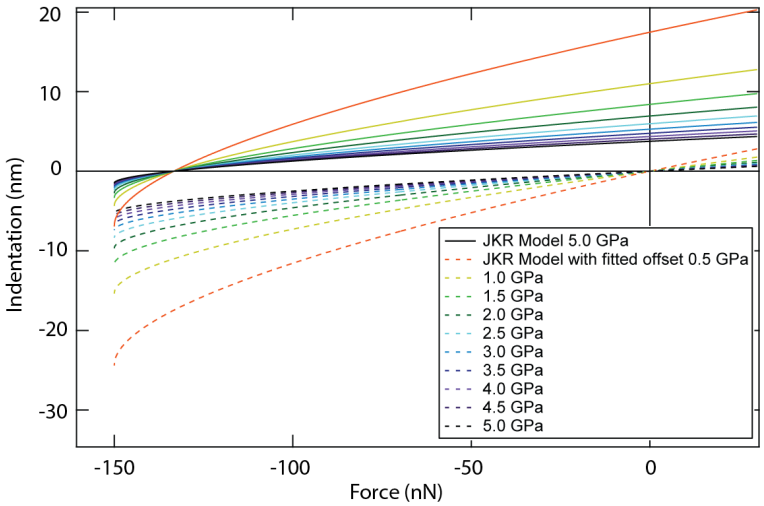

Figure 2.12: Simulated JKR curves in their original positions (full lines) and then shifted by the fitted offset at $\delta(F = 0)$ (dotted lines) for a sample with a surface adhesion of 150 nN and tip radius of 10 nm.

where r_{tip} is the tip radius, E_{tot} is the combined Young's modulus of tip and sample, F is the force applied by the tip and F_{ad} is the adhesion force between tip and sample. The adhesion force is taken to be the minimum in the force reached before the tip disengages in the retract section of the curve. The zero point of the indentation, i.e. the point of contact, is less easy to define due to the necking of the sample's surface as it adheres to the tip on the retract curve, and the jump to contact on the approach [139]. However, it can be found by noting that the indentation at zero force is also a function of these variables, more precisely

$$\delta(F = 0) = 8 \left(\frac{F_{ad}}{r_{tip} E_{tot}} \right)^{\frac{2}{3}} - \frac{32}{3} \left(\frac{F_{ad}^2}{r_{tip} E_{tot}^2} \right)^{\frac{1}{3}}. \tag{2.5}$$

The parameter $\delta(F = 0)$ was included as a variable in the fitting simultaneously to r_{tip} and E_{tot} , such that the JKR model was fitted with an indentation offset equal to $\delta(F = 0)$, and hence the undefined point of contact was indirectly determined. The effects of this can be seen in Figure 2.12 which shows simulated force curves with changing sample Young's modulus. These curves are then shifted by the fitted offset, retaining their shape but crossing the force and indentation axes simultaneously.

The fitting itself proceeds using the code shown in Appendix 5.3.1.

2.2.6 Current Voltage Measurements in the AFM

Current voltage measurements were taken using an Asylum Research ORCA, which is a virtual earth current pre-amplifier, with a gain of 5×10^6 V/A, corresponding to a current range of -2 μA to +2 μA.

2.2.6.1 IV calibration

Firstly the offset of the applied bias is calibrated by attaching a 5 MΩ resistor in place of the sample. The applied bias is then swept across the full range of values from -10 V to +10 V in a triangular wave at the frequency that will be used for measurement. Plotting the current versus bias yields two lines, corresponding to an increasing and decreasing bias. Since the circuit consists of a resistor, a current of 0 A should correspond to a 0 V applied bias, hence using a linear fit and extracting the value of the bias corresponding to a zero current, returns the value of the voltage offsets.

Secondly the current offsets are calculated. This can be achieved before measurement or under the assumption that in dark conditions the current at 0 V applied bias is 0 A. Using this method, the average of the current measured at 0 V applied bias yields the current offset at each point. Before measurement, with the tip well above the sample, the bias is swept between -10 and +10 V. This should yield a flat current response the average of which can be taken as the offset.

2.2.6.2 Mobility Fitting

Chapter 3 describes measurement of the mobility of P3HT using CAFM. This requires fitting a modified Mott-Gurney model, Equation 1.10, to a specific section of an averaged IV curve, whilst using the contact area calculated from the dwell of the force distance data. This involves a large amount of data processing.

Firstly, the data is loaded into a structure, a convenient method of relating different pieces of information together, allowing IgorPro to access the relevant information simultaneously. At this point the user is asked to define the parameters needed for the data analysis, including the Young's modulus of the tip, the Poisson ratios of the tip and sample and the spring constant of the tip. Once completed, the current-voltage data is segregated into sections where the voltage is increasing and decreasing, before the bias offsets are removed. The current data for each voltage is averaged and their standard deviation is calculated. At this point, the current offset is calculated and subtracted from the data.

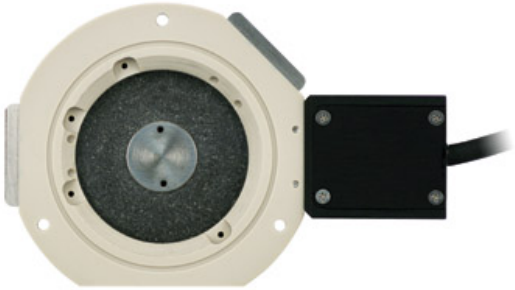

Figure 2.13: An Asylum Research PolyHeater, reproduced from [207].

The program then uses the code specified in Appendix 5.3.2 to fit the modified Mott-Gurney model, Equation 3.4, to the experimental data between the ranges specified by the user at the beginning of the process.

Like the JKR fitting described earlier, the modified Mott-Gurney fitting uses the Levenberg-Marquardt algorithm. In this case, however, the standard deviation of the current from the mean is used as a weighting to reduce the fitting error in response to noise in the data. This curve fitting is also sensitive to initial conditions and works best if the initial guess for the zero field mobility is within three orders of magnitude of the actual value.

2.2.7 Temperature Dependence

Temperature dependence of measurements of topography, mechanical and electrical properties were achieved with the use of an Asylum Research PolyHeater, shown in Figure 2.13. Using the standard cantilever holder or ORCA, temperatures up to 250°C can be maintained with a 0.2°C precision [207]. The PolyHeater can be completely controlled by the IgorPro AFM software.

The sample is mounted onto the central metal heating plate, ensuring no electrical contact between the earthed plate and the active regions of the sample. A metal arm is attached from one of the available mounting points. This serves two purposes; firstly holding the sample in place and secondly providing access to the sample for electrical connection. A contact wire is then attached magnetically to the arm, thus providing the rear electrical contact needed to apply a bias between tip and sample.

For air sensitive samples, nitrogen is flowed at a rate of 0.4 l/minute through one of the four ports around the PolyHeater. Only one other port is left open as an exit for the flowing gas. In this way a nitrogen positive pressure is created,

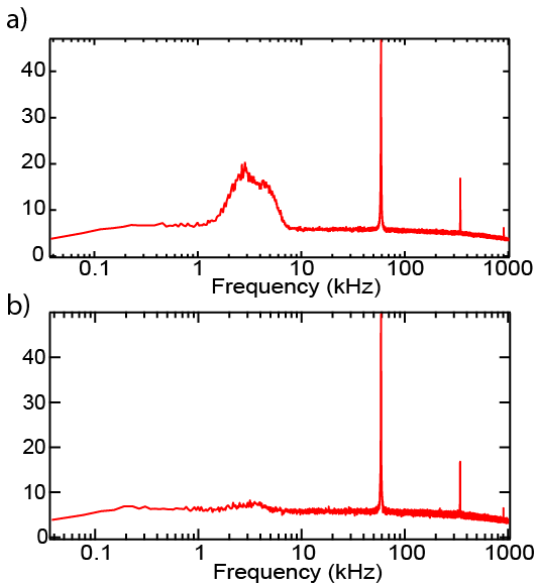

Figure 2.14: Thermal tune data taken for a) a high (detrimental) nitrogen flow and b) an optimised nitrogen flow.

slowing the oxygen degradation of the sample. The rate of nitrogen flow must be kept relatively low to minimise fluctuations of the cantilever. Figure 2.14 shows a comparison of the cantilever response as a function of frequency for a high nitrogen flow rate, and a lower optimised nitrogen flow rate. A high flow rate causes a peak in the cantilever response at frequencies around 1 to 5 kHz, which would influence the AFM measurements. At an optimised flow rate this peak is significantly reduced and the flow has minimal effect on the measurements.

2.2.8 Light Source and Calibration

For photodependent measurements a ThorLabs TLDC4100 was used, with LEDs of 455, 530, 590 and 625 nm wavelengths, chosen to match the absorption maxima of P3HT:PCBM [208]. This was connected directly to the MFP3D base, replacing the existing light source. This allowed illumination from above or below the sample, using the standard optics in the MFP3D dual view base.

The ThorLabs light had a few features that made it a good choice for this project. Firstly, the only adjustments needed to connect it to the existing light path were two relatively cheap adaptors. Once in place it readily attached to the existing light guide. Secondly, the controller for the lighting can be driven by IgorPro which also controls the AFM, so the operation of the light and the AFM can be simultaneous. Thirdly, each of the four LEDs can be modulated individually up to

1 MHz.

To calibrate the light output, a Vishay BPW21R silicon PN photodiode was first calibrated using an external quantum efficiency (EQE) setup, as discussed in [209] and shown schematically in Figure 2.15. A Newport Oriel solar simulator pro-

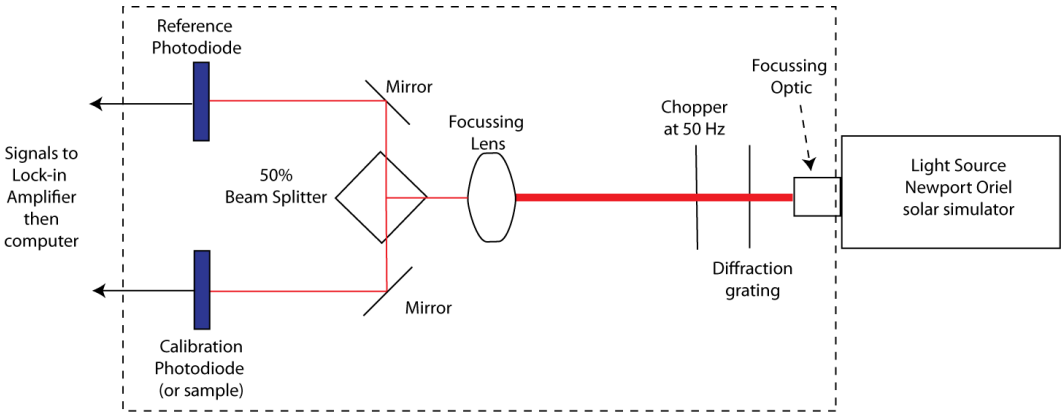

Figure 2.15: A schematic overview of the EQE system used for photodiode calibration

vides the incident light, which is then monochromated using an array of diffraction gratings, the first allows the continual changing of wavelength and the later gratings are used selectively to block lower order wavelengths when longer wavelengths are measured. The beam is chopped at 50 Hz allowing a Stanford research SR 830 lock in amplifier to be used, increasing the accuracy of measurement. The light is then focussed onto an approx. 50% beam splitter, whereupon two mirrors feed the light to a reference diode (D_R) and a calibration diode (D_C). A ratio is taken between the responses of D_C and D_R. For every mA measured on the calibration diode, the response on the reference diode is known. Then when a sample, in this case the photodiode, is tested the current measured is multiplied by the ratio between the two diodes to achieve the corrected response.

The EQE itself relates the number of photons converted into electrons at a specified wavelength incident on the active area of the device. From this a spectral responsivity can be calculated, that is the amount of electrical output to optical input. The responsivity is calculated as

$$R(\lambda) = EQE\frac{q\lambda}{hc} \tag{2.6}$$

where λ is the wavelength of the incident photon, h is Planck's constant and c the speed of light. The measured spectral responsivity of the photodiode used is shown

in Figure 2.16.

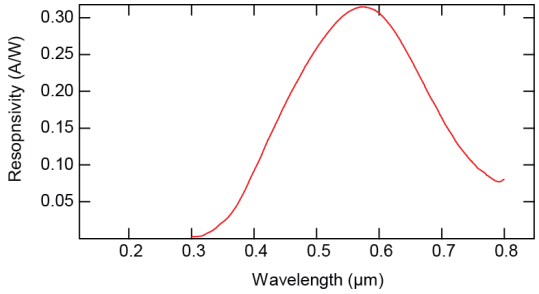

Figure 2.16: Spectral responsivity of a silicon PN photodiode.

Next, the spectral power of the light getting to the photodiode is needed. The transmittance of optics in the light path and the relative spectral radiance of the light are needed for this. This data can be seen in Figure 2.17.

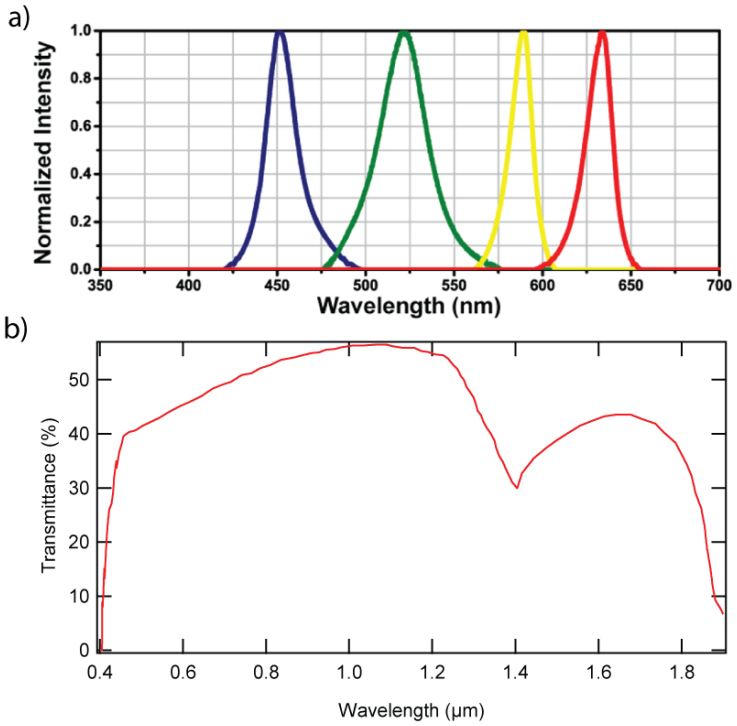

Figure 2.17: a) Relative power output spectra of light from the ThorLabs website [210]. b) Transmittance of the light guide attached to the AFM, from the Dolan-Jenner website [211].

Whilst the spectra of Figure 2.17 a) are most likely to be accurate, the intensity is relative and hence needs measuring, for this purpose, the calibrated

photodiode was employed (calibration as described earlier). By aligning the photodiode in the AFM light path, the current produced by each light over the 7.5 mm^2 of the photodiode can be measured. The results of this are shown in Table 2.1. This was performed with the light completely covering the photodiode, and so does not show the power of illumination going through the AFM optics, but instead shows the spectral intensity. Table 2.2 shows a comparison of the measured power at each

LED	Wavelength(nm)	Current on Photodiode (mA)	Power (W/m^2)
Red	625	0.182	83.74
Blue	455	0.093	52.24
Yellow	590	0.025	10.54
Green	530	0.054	23.23

Table 2.1: Current response of calibrated photodiode with incident light from ThorLabs 4LED light source and their calibrated power.

stage of the optical path from the light to the sample stage in the AFM. These numbers indicate that less than 1% of the light output actually reaches the sample. Approximately 50% of the light is lost in the light guide, the rest is lost in the AFM base itself. Focussing the light onto the photodiode with a small aperture, thereby

Position	Area (m^2)	Current on Photodiode (mA)	Power (W/m^2)
after fibre before AFM	7.5×10^{-6}	30	14000±1000
after AFM	7.5×10^{-6}	0.354	170±20
after AFM	4.1×10^{-8}	0.006	530±50

Table 2.2: Current response of calibrated photodiode with incident light from ThorLabs 4LED light source, and their calibrated power.

ensuring that all the light is hitting the photodiode across an area of 4.1×10^{-8} m^2 yields the total flux hitting the photodiode to be 525 W/m^2. Hence it can be assumed that 525 W/m^2 of light is incident on each sample with the illumination at full power. These calculations used the bottom optical path of the AFM, the top path is more difficult to measure as the photodiode cannot be in place while the AFM head is, however, this will be discussed later in Chapter 4.3.4.

When applying illumination through the bottom optical path of the AFM it is worth considering the possible enhancement of the electric field around the tip by surface plasmon resonance. It is unlikely that this will affect the top optical path as the tip itself will be shadowed by the cantilever. It is also unlikely that surface plasmon resonance will have a significant effect in this system as the expected

wavelength for plasmon resonance of platinum with a diameter <100 nm is around 295 nm [212], well into the UV spectrum.

2.2.8.1 Light Control and Tr-EFM Process

The light controller itself is connected to the computer by USB and the controller can be sent information by VISA commands. These commands can fully control the light sources, however, they incur a significant signal delay and cannot be used to send complex signals to the light source. Since for Tr-EFM the light pulses need to be sent at specific times, the Macrobuilder in IgorPro is used to control the lights. Appendix 5.3.3 shows how this is achieved.

2.2.8.2 Analysis - TrEFM

The analysis of the Tr-EFM data is somewhat similar to the analysis of the force volume maps, but in practice much simpler. Firstly the relevant waves are loaded into memory. Then the light oscillation wave is used to find the total length of an oscillation (of the light turning on and off). The program then converts the 1D wave into a matrix format where each row of the matrix corresponds to a single oscillation. From there an average across the rows is calculated.

This average wave is fitted from the point where the phase rises or falls by 10% after the light has been applied until 10 points before the light is turned off, if measuring τ_c. For τ_d, the fitting starts 10 points after the light turns off and is fitted until the end of the data, which is when the bias is turned off. This method ensures that the fitting does not get skewed by random noise in the data. The relevant parameters, namely the measured τ, can be extracted.

2.2.8.3 Signal Modulation and Speed

Tr-EFM is comparatively easy to implement, requiring no external equipment other than the AFM and light source. However, the speed of the electronics in the AFM introduces a limit to the time resolution.

Figure 2.18 shows the time resolution of the DAC from the AFM controller. Here, a programmed square wave is sent through the controller to an oscilloscope. The scope shows that there is a significant rise time of the signal being sent by the DAC. In order to eliminate this delay, the controlling signals can be sent via an external signal generator, as required for IM-KPFM.

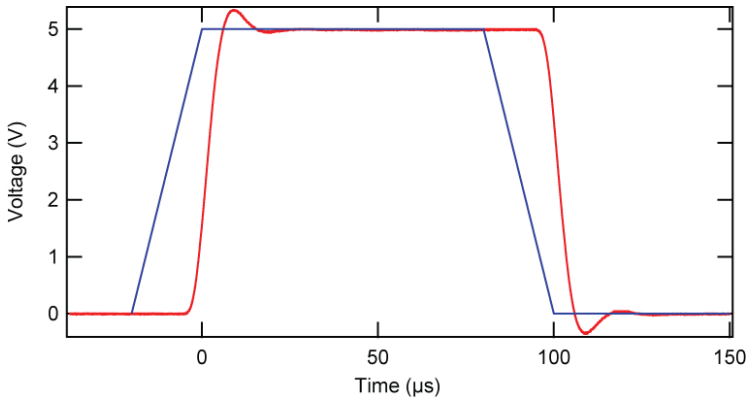

Figure 2.18: Square wave signal sent by the AFM in blue, and the actual signal as recorded by an oscilloscope.

2.2.9 IM-KPFM

IM-KPFM was performed using AC240-TM tips (nominal resonance frequency of 70 kHz, spring constant 2 N/m). Once the tips have been calibrated and tuned using the standard techniques, discussed previously, a force curve is acquired and the tip is retracted to a set distance (typically 50 nm) from the surface where a tuning curve is taken for an AC and DC bias of 3 V. Once completed, the DC bias feedback is turned on, allowing the feedback gains to be tested before beginning the experiment.

A Tektronix AFG3022B signal generator was used to provide the modulated signal to the ThorLabs light. The timing for the modulation is controlled by IgorPro, and the trigger wave is sent to the signal generator via a BNC cable. The background illumination is controlled directly by the AFM controller. Appendix 5.3.4 describes the experimental process for this. In addition, Appendix 5.3.5 details the process of analysing this data.

Chapter 3

Force Volume Bias Spectroscopy of OSCs

Force volume bias spectroscopy (FVBS) is a new technique combining Force-Volume Mapping (as discussed in 2.2.5.1), and the space charge limited current (SCLC) current-bias analysis introduced by Reid et al. [150]. FVBS provides simultaneous, quantitative insight into the electrical and mechanical properties of the material studied. This is achieved by fitting force-distance curves with a contact mechanics model, and extracting the Young's modulus similar to Nikiforov et al. [140]. However, unlike Nikiforov's work, we also extract the tip-sample contact area. This is used in the current-bias analysis to extract a quantitative measure of the mobility.

Much like the work of MacDonald et al. [156], this can be achieved at a single point, but also as a map across an area of a sample, showing heterogeneity in mobility as a function of position. With the addition of an Asylum Research Polyheater, all of this can be achieved between 30°C and 200°C.

This chapter discusses the development and application of this technique on two different semiconducting materials, P3HT and VOPc. Both of these semiconductors show promise in the field of photovoltaic devices; P3HT for its ability to be solution processed, and VOPc for its high mobility, but P3HT is a soft polymer, whilst VOPc is a hard small molecule. Each presents challenges when aiming to gather quantitative electrical and mechanical data.

3.1 Temperature Dependent CAFM of P3HT

As discussed further in 1.2.5, P3HT is a highly studied electron donor whose mobility is dependent on its morphology and the processing conditions used [94, 88]. For

this reason FVBS is the perfect technique to characterise samples of P3HT at the nanoscale. Although contact mode scanning CAFM has been widely used to look at the nanoscale conductivity of P3HT [213], it suffers from a few drawbacks. Firstly, P3HT is soft, so scanning in contact mode incurs damage to both the tip and sample, limiting resolution, unless a more sophisticated technique is used, such as ultrasonic force microscopy (UFM) [214]. In either case the tip-sample contact area is ill-defined, resulting in a qualitative measurement of conductivity. With only one value of current at a set voltage, at each position, accurately converting conductivity to mobility cannot be done with confidence. Similarly, without force curves it is difficult to measure the sample stiffness in contact mode.

Improvements can be made to this by applying fitting to a more sophisticated scanning technique, such as PeakForce Tapping. In this case, the current and the Young's modulus can be mapped simultaneously across a sample area [140]. However, since this is still a scan at a single bias the mobility still cannot be quantitatively determined. MacDonald et al. solved this problem by mapping in a point-by-point approach across the sample, whilst collecting current-bias data at each point [156]. This allows fitting to be performed in the current-bias dimension while maintaining resolution in the spatial dimensions, giving a map of the "ohmicity" of the heterojunction tested. MacDonald et al. used this to show that oxygen plasma treated ITO gave more ohmic contacts to their heterojunctions, and therefore yielded more efficient devices. In contrast, Nikiforov showed that changes in the composition of the active layer on both the nanoscale and microscale can affect the device performance.

These works combined, point in the direction of quantitative measurements of electrical and mechanical properties with nanoscale resolution. Here, this is achieved by combining force-distance and current voltage measurements, acquired simultaneously in a point by point approach. Appropriate contact mechanical models are used to determine the contact area from the force-distance data, thereby removing the largest uncertainty in the electrical measurements.

Data acquisition and analysis methodology has been programmed into the AFM software allowing the practical capture and analysis of large datasets. This level of automation makes the gathering of temperature dependent measurements practical, giving greater insight into the dominant charge transport mechanisms at work in P3HT.

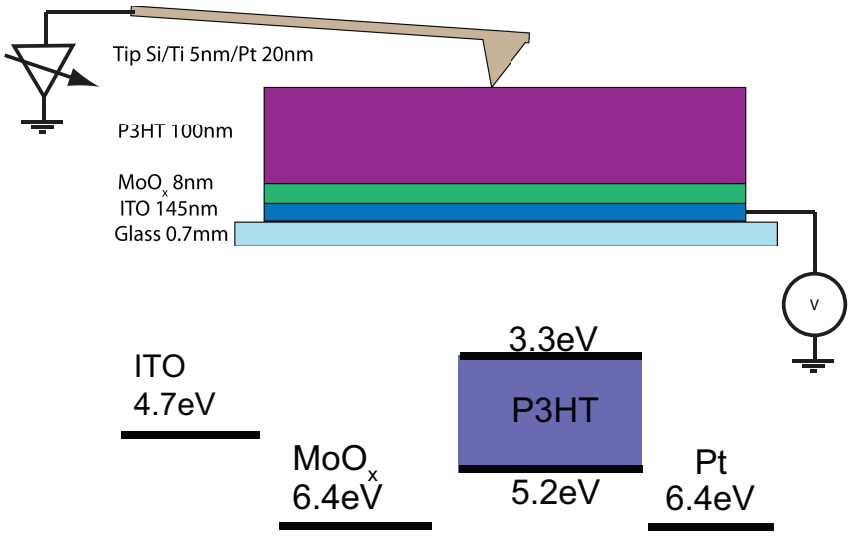

Figure 3.1: (top) Schematic of the experimental geometry; (bottom) schematic energy level diagram of the materials involved. The workfunctions of ITO, MoO_x and Pt are shown, in relation to the highest occupied molecular orbital (HOMO) and lowest unoccupied molecular orbital (LUMO) of P3HT.

3.1.1 Force-distance and Current-Voltage Acquisition from P3HT

Thin film samples of P3HT on ITO were prepared by the methods described in Section 2.1.3.1. Figure 3.1 shows the layout of the sample in the AFM with the layout of the associated orbitals and workfunctions, with no applied electric field. The workfunctions and HOMO/LUMO levels stated can be readily measured by ultraviolet photoemission spectroscopy (UPS) or x-ray photoemission spectroscopy (XPS) [215, 216]. When a negative bias is applied to the ITO, its Fermi level shifts down aligning with the gap states in MoO_x. This causes a favourable dipole between ITO and MoO_x, however a slightly unfavourable dipole is created between the MoO_x and HOMO of P3HT. It is however hard to predict quantitatively what this barrier might be because of the many gap states present in MoO_x [194, 215]. Due to Fermi level pinning there will be a beneficial interface dipole between the P3HT HOMO and the platinum tip, facilitating transport in this direction. The primary charge carrier here are holes because there is too great an energy barrier from the LUMO of the P3HT to the molybdenum oxide.

In this configuration, hole transport occurs through the ITO back electrode through the P3HT thin film and is collected by a Pt coated AFM tip acting as the top electrode. The current flow is measured by a virtual earth current amplifier

close to the tip, with the bias voltage applied to the back ITO electrode: a positive bias voltage here means that the back electrode is positively biased relative to the tip.

As further described in Section 2.2.5.1, FVBS is the amalgamation of traditional force-volume mapping and SCS measurements. A single measurement consists of an approach/retract force-distance curve, force vs. time dwell curve and a current-bias curve. An acquisition showing typical behaviour is shown in Figure 3.2, taken at 70°C on a 100 nm thick P3HT film under a 0.4 l/min nitrogen flow.

Figure 3.2(a) shows the expected behaviour in the loading curve with the tip jumping onto the surface when the gradient of the attractive tip-surface force exceeds the spring constant of the cantilever. Once in contact, the relatively low slope of loading is indicative of indentation on a soft sample [132]. The dwell stage can be seen in Figure 3.2(b). Here, the tip is held against the surface with a constant force. Analysis of the indentation creep under similar conditions has been shown to give information on the visco-elastic parameters of polymers [217, 148]. However, there is no evidence in the force-distance curves acquired here that visco-elastic deformation occurs during the dwell stage, indicating that the P3HT was deforming elastically. The small observed changes in z piezo displacement can be attributed to thermal drift due to differential thermal expansion [218]. During this dwell stage, the current is measured as a function of applied voltage (IV), with ten IV curves typically acquired during each dwell. The IV curves acquired are asymmetric, Figure 3.2c), as is commonly found in CAFM even for nominally electronically symmetric structures [219]. Here the higher current flow at negative bias indicates that hole injection was more efficient through the platinum tip than the MoO_x/ITO substrate.

During unloading, the retract curve shows hysteresis, due to adhesive forces keeping the tip in contact with the surface until the pull-off force is reached. The magnitude of the adhesion force F_{ad}, is determined here by the maximum attractive force prior to jump-off-contact.

As discussed in Section 2.2.5.2, the setpoint for the deflection is an important parameter in these measurements. Too much force can incur damage to the tip and/or sample. Too little force can result in false engage and/or insufficient data for fitting. Set point forces between 10-20 nN were found to maintain an electrical connection without incurring sample damage. Typical spring constants and optical lever sensitivities were 2.5 N/m and 50 nm/V respectively.

As explained in section 2.2.3, the deflection versus z displacement data is converted to force versus indentation ($F - \delta$), and the current versus voltage to current density versus voltage (JV). Each $F - \delta$ and JV curve can then be fitted

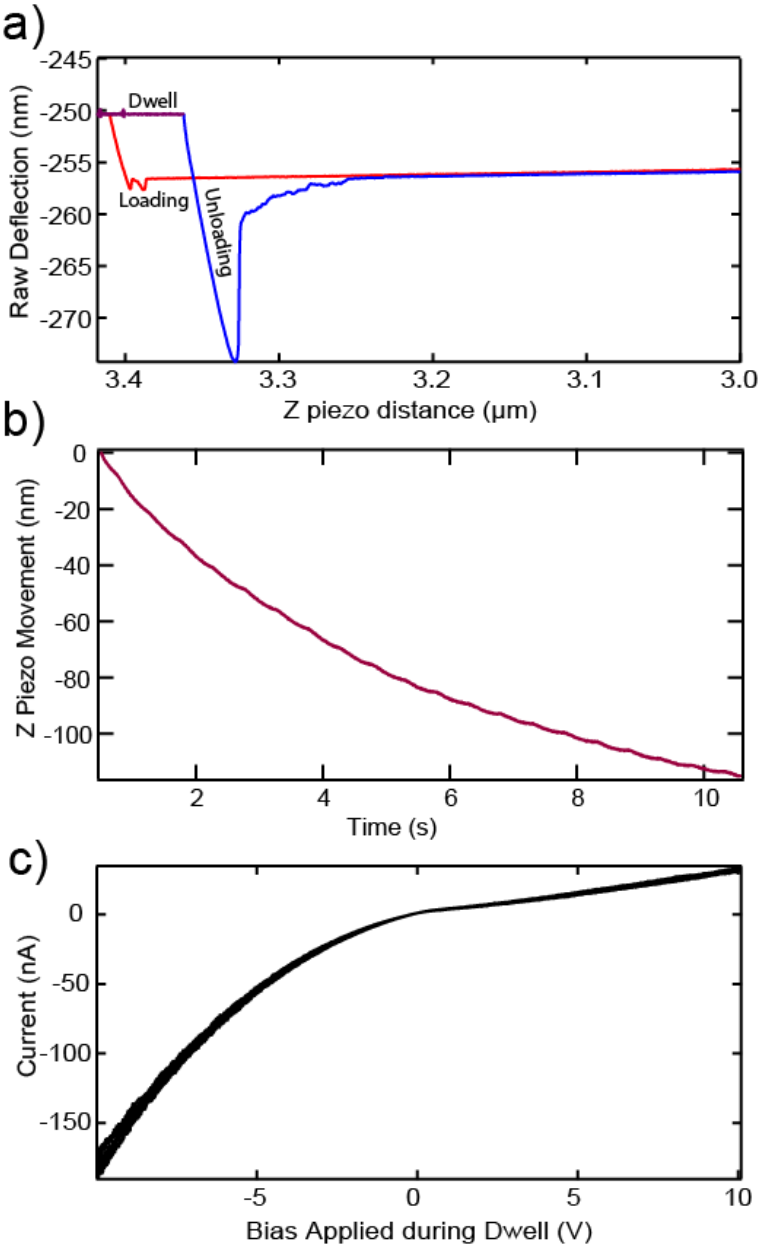

Figure 3.2: The variation of data gathered on P3HT at 70°C on a 100 nm thick P3HT film under a 0.4 l/min nitrogen flow. a) Force curve displaying three sections of data as labelled. b) Expanded dwell section, transposed into z piezo movement while force is constant against the time held. c) Ten IV curves acquired during the dwell period.

by an appropriate model to quantitatively extract the mechanical and electrical properties.

3.1.2 Analysis of Force-Distance Data

By accurate determination of the cantilever spring constant, optical lever sensitivity and the zero points for force and indentation, the z piezo displacement data can be converted to force versus indentation data, as explained in Section 2.2.3. Quantitative analysis requires that an appropriate contact mechanical model is fitted to force versus indentation data. Given the elastic deformation with significant adhesive force on a soft sample, the Johnson-Kendall-Roberts (JKR) model was chosen here for P3HT. Although the JKR and the Derjaguin-Müller-Toporov (DMT) are limits of the same model, the large adhesive forces and comparatively large tip size indicate that the JKR model is likely to be a better fit to the data [132]. The JKR model predicts that the indentation, δ, depends on the applied force, F:

$$\delta = \frac{1}{r_{tip}}\left(\frac{r_{tip}}{E_{tot}}\left[\sqrt{F_{ad}}+\sqrt{F+F_{ad}}\right]^2\right)^{\frac{2}{3}} - \frac{4}{3}\sqrt{\frac{F_{ad}\left(\frac{r_{tip}}{E_{tot}}\left[\sqrt{F_{ad}}+\sqrt{F+F_{ad}}\right]^2\right)^{\frac{1}{3}}}{E_{tot}r_{tip}}} \tag{3.1}$$

where E_{tot} is the reduced Young's modulus of tip and sample given by

$$\frac{1}{E_{tot}} = \frac{3}{4}\left(\frac{1-\nu_t^2}{E_t}+\frac{1-\nu_s^2}{E_s}\right) \tag{3.2}$$

and r_{tip} the radius of the tip. Known values from the literature were used for the mechanical properties of the tip (Young's modulus E_t = 169 GPa, and Poisson's ratio ν_t = 0.22 [220]). Previous work has found the Poisson's ratio for P3HT $\nu_s = 0.35$ [220] (note that E_{tot} is relatively insensitive to small changes in ν_s).

Figure 3.3 shows the fit of Equation 3.1 to experimental $F-\delta$ data, further details of the fitting process are given in section 2.2.5.3. The fit yields values for E_{tot} and r_{tip}. Given these values, it is then possible to determine the sample stiffness E_s using Equation 3.2 and the contact area during the dwell, i.e. during the acquisition of the current versus voltage data. Again using the JKR model, which accounts for the elastic deformation of the sample around the tip as shown in the inset in Figure 3.3, the contact radius (r_c) is given by:

$$r_c = \left(\frac{r_{tip}}{E_{tot}}\left[\sqrt{F_{ad}}+\sqrt{F_{dwell}+F_{ad}}\right]^2\right)^{\frac{1}{3}} \tag{3.3}$$

where the average of the force measured during the dwell, see Figure 3.2b,

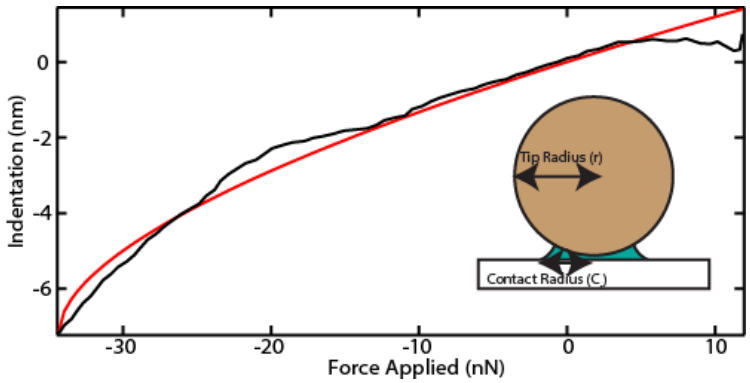

Figure 3.3: JKR fitting (red) as applied to the unloading section of the retract curve (black line). Inset: Schematic of the contact when unloading, as described by the JKR model.

gives F_{dwell}. It should be noted that the JKR model assumes that the radius of contact is smaller than the radius of the tip, as shown in Figure 3.3 (inset). This assumption is not always true in the data that is to follow, however, the JKR model is used as a simple framework and is likely to be accurate to within the precision of the experimental measurements, taking into account piezo drift and calibration of both the electrical and cantilever measurements. It is also important to note that not every force-curve acquired was well fitted by the JKR model. For the analysis of the current-voltage data described in the next section, poorly fitted force curves were ignored and their contact area taken as the average contact area of all of the fitted curves at the same temperature.

Within the constraints of the model used, analysis of the force-distance data gives values for the sample's Young's modulus, adhesion force, sample height, tip radius and contact radius (or contact area) at each point.

3.1.3 Analysis of Current Voltage Data

Quantitative analysis of current-voltage data requires conversion from current to current density and hence requires knowledge of the contact area between tip and sample. Figure 3.4 highlights the importance of calculating an accurate contact area. Figure 3.4a) shows the values of the contact area extracted from fitting force-distance data, plotted against the current measured at 5 V. Each of the 400 points corresponds to a distinct point (pixel) on the same sample, at each of these a force-distance curve and a set of current-voltage curves were taken. Each of the current points in Figure 3.4a) corresponds to the average current, at 5 V, of the 10 IV curves measured at that position. The points were arranged in a force-volume grid array.

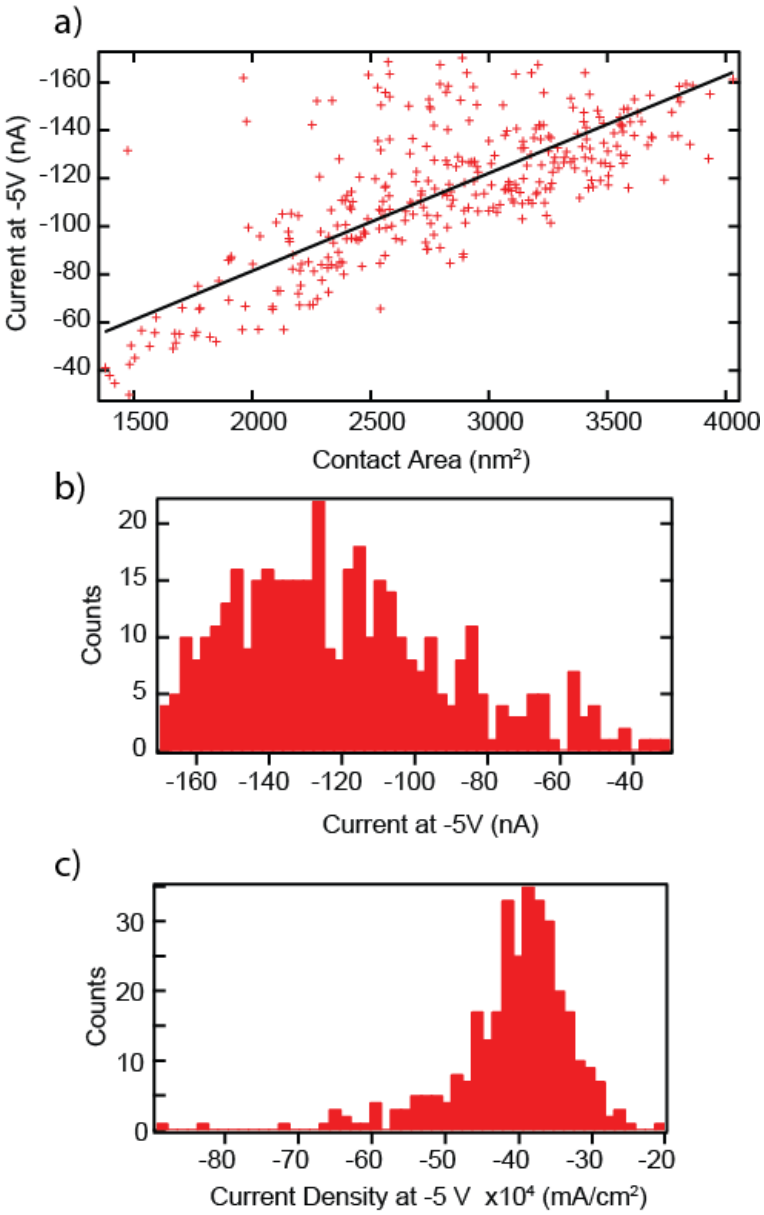

Figure 3.4: From simultaneously acquired force distance and current voltage data, a) shows the contact area calculated from the model JKR fittings is compared to the current measured at 5 V. b) Histogram of the measured current at 5 V. c) Histogram of current density values calculated using the contact area at each point.

Figure 3.4a) and b) show a large spread in the current data, with the current varying by a factor of 5 within this dataset. However, there is a clear linear relation between the extracted current and the measured contact area. Consequently, the current density, Figure 3.4c), which takes into account the measured contact area, has a much smaller spread of around a factor of 2. For comparison, the contact area calculated for the known tip diameter of 30 nm, assuming a circular contact area, would be 2800 nm^2, yielding current density values typically a factor of 2 to 3 times larger. Thus, using the force-distance data to quantify the contact area in this way significantly increases the precision and accuracy of the current density data obtained.

At each point, the 10 IV curves are averaged to reduce noise, offsets are corrected and the current converted to current density. The JKR and IV fitting procedures were implemented in the IgorPro software used to acquire the data and automated such that FVBS arrays can be quickly and automatically analysed. A detailed description of the process is given in section 2.2.6.1.

A typical resultant JV curve is shown in Figure 3.5 (inset). As explained previously, the response is asymmetric with higher current at negative bias, consistent with favourable hole injection from the Pt tip. For analysis, we consider only the negative bias regime.

For planar electrodes, the JV behaviour of P3HT is well established. At low bias (low field), the current is injection limited resulting in Ohmic behaviour ($J \propto V$). At intermediate field, the current is said to be trap limited, with $J \propto V^p$ where $p > 2$. At high field, the current should make a transition into a SCLC regime where $J \propto V^2$ in accordance with the Mott Gurney model [74].

The situation is more complicated in CAFM, where the electrodes are no longer planar and hence the electric field is not uniform through the film, and instead spreads in a conical-like manner from the tip. Reid et al. used finite element modelling to account for and visualise the effects of the non-local field [150], proposing a semi-empirical modified Mott-Gurney equation for space charge limited current in CAFM which incorporates the field-dependence of the mobility:

$$J = \alpha\epsilon\epsilon_0\mu_0 e^{0.89\gamma(V/L)^{1/2}} \frac{V^2}{L^3}\delta_J \left(\frac{L}{r_c}\right)^{1.6\pm0.1} \tag{3.4}$$

where ϵ_0 and ϵ are the vacuum permittivity and the relative permittivity of the thin film respectively, μ_0 is the zero field mobility, γ is the strength of the field-dependence of the mobility, and L is the thickness of the semiconductor thin film. α is the prefactor determined by Reid et al. from the finite element modelling

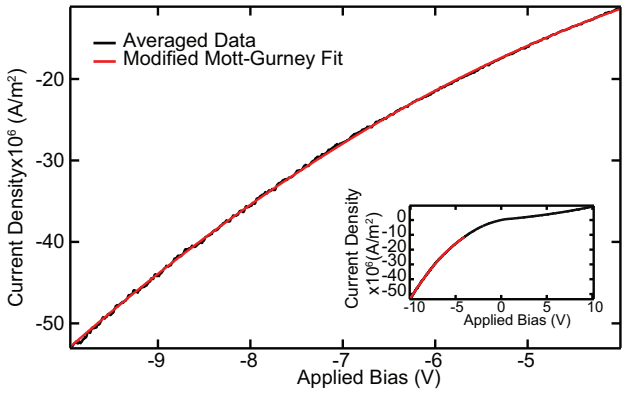

Figure 3.5: Average of 10 IV curves fitted with a modified Mott Gurney model (red), the inset here shows the full IV curve and the region fitted.

to account for the non-uniform electrical field ($\alpha = 8.2$ in place of 9/8 for the Mott-Gurney Law for planar electrodes). The factor $\mu_0 e^{0.89\gamma(V/L)^{1/2}}$ accounts for the electric field dependence of the mobility [221]. The constant $\delta_J = 7.8 \pm 1$ was included to empirically account for the difference between mobilities derived by Reid et al. from CAFM measurements and those from planar electrodes.

Note that for the contact radius, r_c, Reid et al. estimated the area of contact based on a circular patch the radius of which matched the tip radii measured by scanning electron microscopy (SEM). Due to deformation of the sample, and adhesion forces between tip and sample, the actual contact area is likely to be significantly larger than the estimate based solely on nominal tip radius. For the force and tip used by Reid et al, using Equation 3.3 the estimated actual contact area would be ~ 6 times larger than their value. Comparison with the results presented here suggests that correct quantification of the contact area removes the need for the extra empirical scaling factor, so in the results presented below $\delta_J = 1$ was assumed.

Figure 3.5 shows the average current density versus voltage curve acquired at a single point, with the red line showing the fit to the modified Mott Gurney model. The data is fitted in the high voltage regime where space charge limited current is expected, and at negative bias where the tip-surface contact gives Ohmic injection of holes as required for SCLC [222]. The two fitting parameters are the zero field mobility, μ_0, and the strength of the field dependence of the mobility, γ. A more detailed description of the fitting procedure can be found in section 2.2.6.2. The zero field mobility from the fit in Figure 3.5 is $\mu_0 = 2.50 \times 10^{-3}$ cm^2/Vs with $\gamma = -6.62 \times 10^{-5}$ m$^{1/2}$/V$^{1/2}$. This is consistent with the results of Kline et al., whose room temperature thin film measurements on 30 kDa P3HT (similar to the 25 kDa P3HT

used here) found mobilities of $\mu_0 = 8 \times 10^{-3}$ cm^2/Vs [94]. It is worthwhile to note that P3HT can be readily doped [223, 224], however since the V^2 dependence is obtained this should have minimal effect on the measured mobility. For P3HT the measured mobility depends greatly on the method of preparation, molecular weight and regio-regularity of the material. However, here, without the use of empirical scaling factors, values close to those reported for macroscopic devices with planar electrodes are obtained.

Analysis of the current-voltage data thus gives quantitative values for the zero field mobility and the strength of the field dependence of the mobility at each point. Importantly, this data is coincident with, and simultaneous to, the mechanical property information derived from analysis of the force-distance data.

The complete process of the analysis can be seen in Figure 3.6, which systematically describes the individual steps in the analysis of both force and electrical data and how they link together.

3.1.4 From One Measurement to Many

Since the AFM controls position in x, y and z directions, as well as the force and electrical data for each of these points the data can be neatly mapped and correlated.

Whilst this approach gives you more data, 27 MB for each map of 25 points, it also takes longer, around 30 minutes per map. This means that degradation becomes an issue, as does the amount of RAM available to the program. Images cannot be stored in memory, and must be saved to disk. Although this increases the requirements of the computer, there are a range of benefits for doing this. Firstly, more data generates statistically significant results. Secondly, in a spatially resolved grid the difference between random noise and spatially resolved heterogeneity are very clear.

3.1.5 Correlating Electrical to Mechanical Properties

Figure 3.7 illustrates the importance of high spatial resolution when measuring electrical and mechanical properties of polymer thin films. The untreated P3HT measured at 30 °C shows heterogeneity in both mobility and Young's modulus across a 1 μm^2 area. As the histograms show (Figure 3.7c-d)), broad distributions are found for both, with mobility varying by around an order of magnitude and Young's modulus by around a factor of 3. There are clear spatial correlations, i.e. patches of high or low mobility or stiffness, which indicate that the variation is real and due to local changes in material properties.

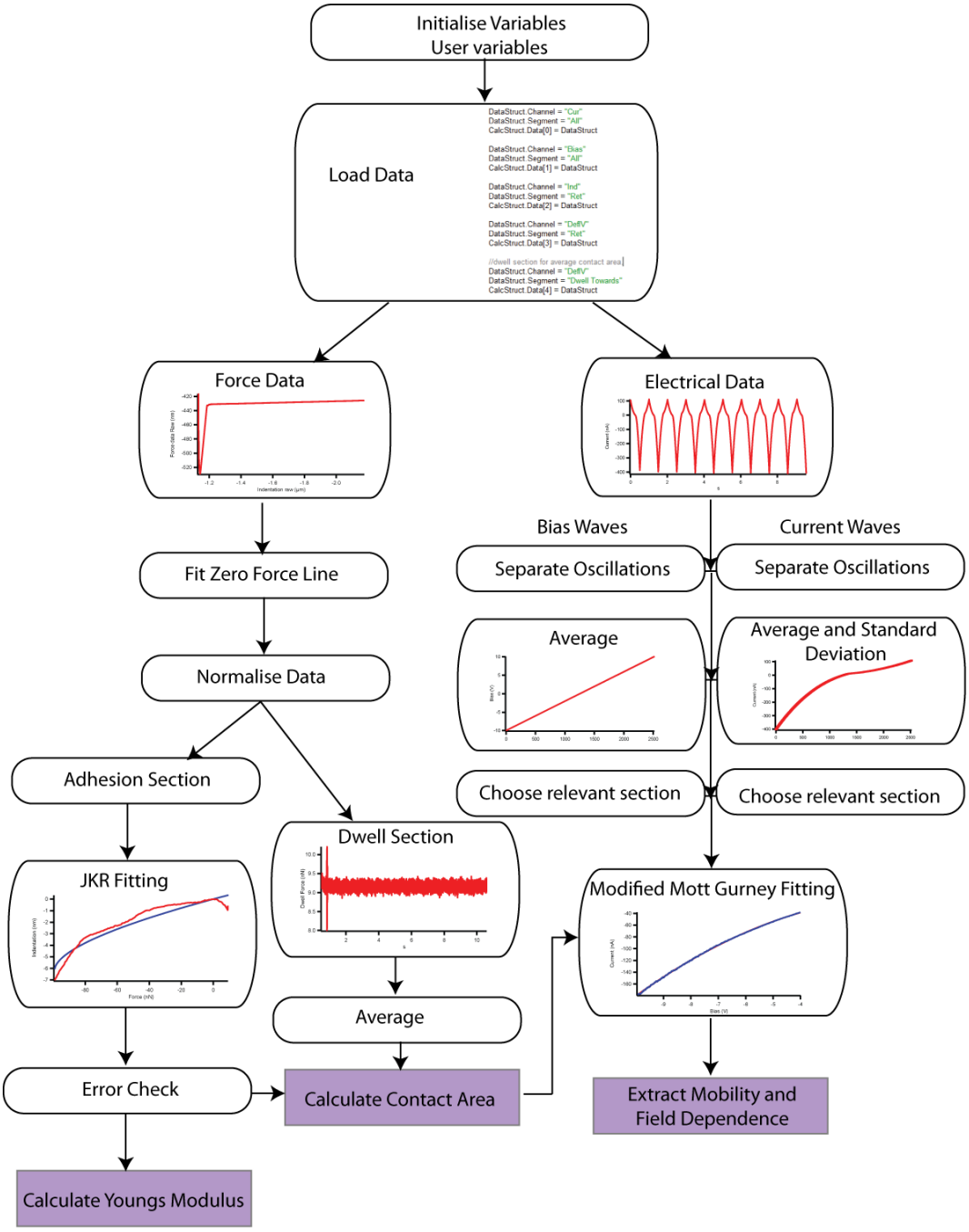

Figure 3.6: Flow diagram of the analysis procedure for FVBS data, showing the separate and linked stages for analysis of the electrical and mechanical data.

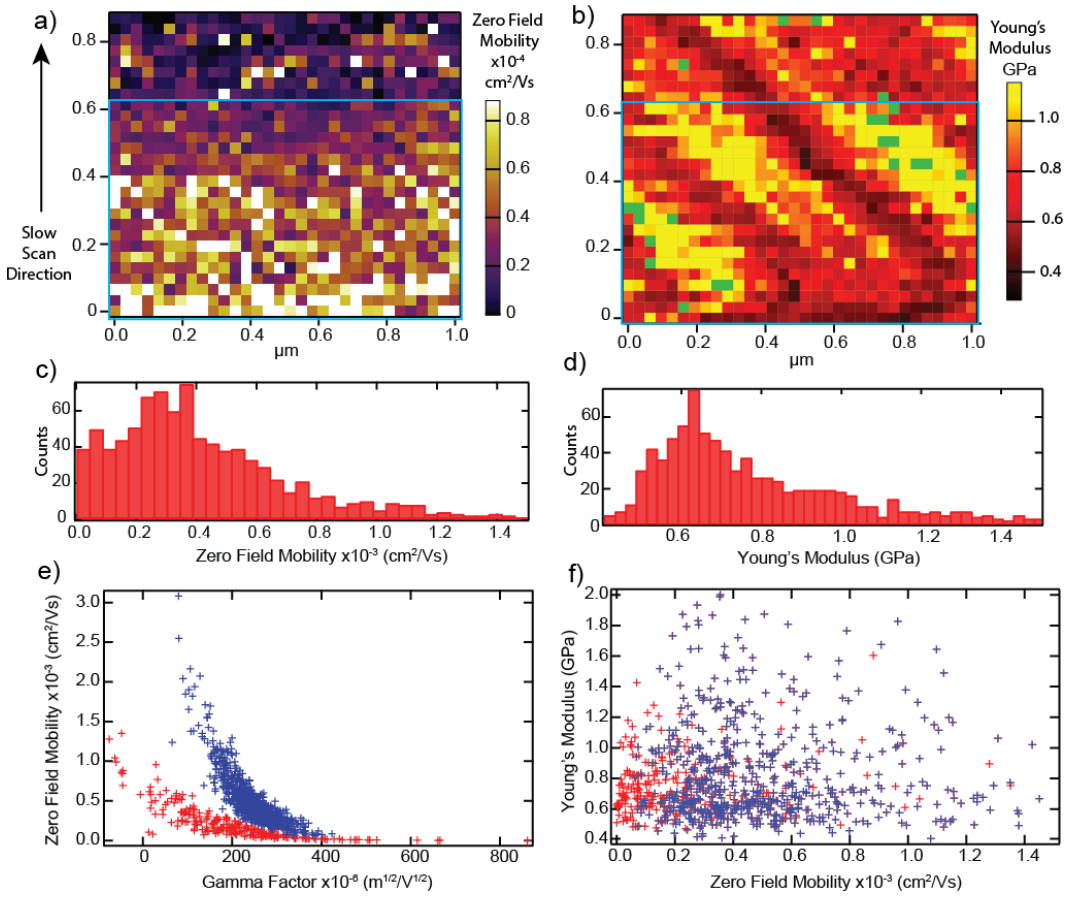

Figure 3.7: High resolution FVBS electrical and mechanical map of untreated P3HT at 30 °C, showing spatially resolved a) mobility and b) sample Young's modulus values. c) and d) show the distribution of mobility and modulus values respectively. The values for zero field mobility, μ_0, are plotted against the simultaneously derived field dependence of mobility, γ, in e) and sample Young's modulus, E_s, in f): the blue points are from pixels within the blue boxes shown in a) and b), and the red points from the remaining upper portions of those images.

The mechanical and electrical measurements are taken simultaneously at each point, allowing investigation of correlations between them. Figures 3.7e) and f) show the zero field mobility plotted against γ and against sample Young's modulus respectively, with each point on the graphs corresponding to a distinct spatial location on the sample (pixels in the images Figure 3.7a-b). The comparison between mobility and γ shows that the data lay on two distinct trend lines, emphasized by some of the points being shown in red and some in blue: for both sets, γ increases as mobility decreases, consistent with increased trapping resulting in lower mobility. The blue data points come from the region marked by the blue boxes in Figures 3.7a and b, with the red points from the upper portion of the images. Note that the scan direction is from the bottom to the top of the image. Comparison between the mobility and sample Young's modulus maps, and consideration of the correlation between γ and mobility, suggest that the tip condition changed at around the top of the blue box. This shows how acquiring large datasets and checking the correlations between them can give more information and hence enable more reliable determination of material properties.

Considering only the measurements within the blue box, for the untreated P3HT measured at 30 °C we find an average value of mobility of $5.1 \pm 0.1 \times 10^{-4}$ cm^2 / V s and of sample Young's modulus 0.86 ± 0.02 GPa. (Note that incorporating the systematic uncertainty due to calibration of the spring constant of the AFM cantilever, 5%, leads to an additional uncertainty of $\sim$ 5 % on these values when comparing against other measurements, but does not effect comparisons within the dataset).

From the graph of sample Young's modulus plotted against mobility, (Figure 3.7f) no clear correlation between stiffness and mobility is apparent. The electrical measurements rely on conduction through the thin film, whilst the mechanical measurements probe the surface and near sub-surface. Hence the lack of correlation suggests that the structural variations are occurring over length scales shorter than the thickness of the film. This is supported by the observation that the derived mobility values appear to change over length scales less than 100 nm, i.e. less than the film thickness.

For comparison, Figure 3.8 displays the corresponding results for an annealed P3HT sample measured at 130°C. Again there is a broad distribution of mobility and sample Young's modulus values, with clear spatial correlations demonstrating that they reflect real variations in material properties. However, the spatial variations are more smoothly varying (i.e. longer range), suggesting that the length scales of the structural variations are longer at this higher temperature after annealing.

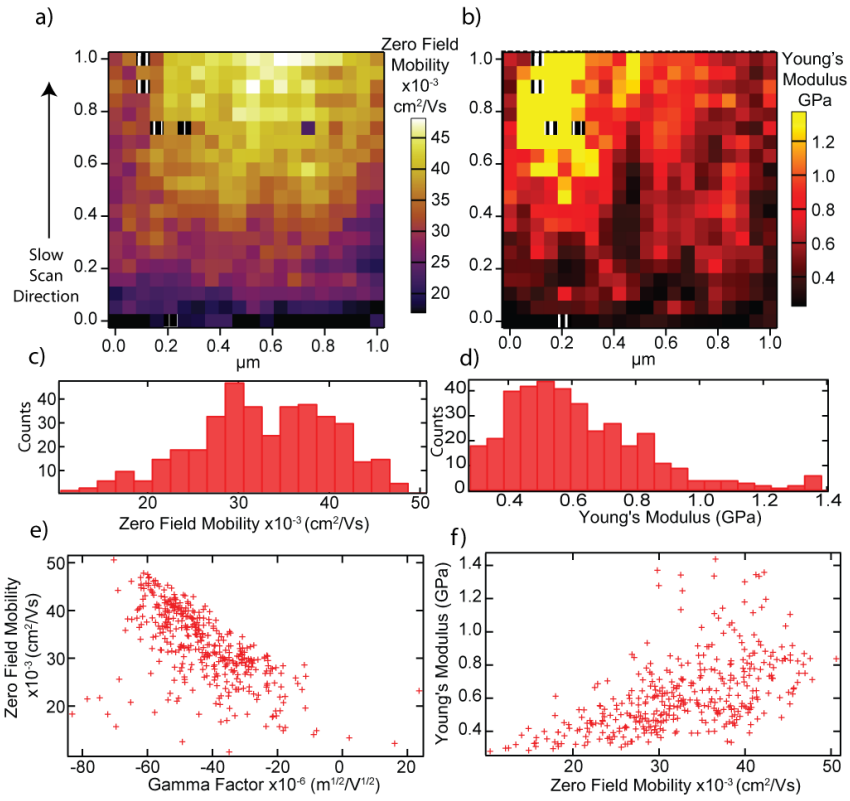

Figure 3.8: High resolution map of annealed P3HT at 130 °C, showing spatially resolved a) mobility and b) sample Young's modulus values. c) and d) show the distribution of mobility and modulus values respectively. The values for zero field mobility, μ_0, are plotted against the simultaneously derived field dependence of mobility, γ, in e) and sample Young's modulus, E_s, in f).

An obvious additional feature is that the mobility and sample Young's modulus both increase over time for this dataset (note that the slow scan direction, and hence time, goes from bottom to top). It is not clear whether this is a feature of this region of the sample, or of changes in the film due to prolonged annealing at this temperature, but it does show a clear correlation between mobility and stiffness which is also apparent in the scatter plot in (Figure 3.8f). While it is not possible to directly determine the morphology of the sample directly with the AFM, a more crystalline structure would feasibly have a higher stiffness. As such a correlation between the mobility and the stiffness could be expected as a more crystalline material should have a higher mobility.

Interestingly, at this higher temperature on an annealed sample the correlation between zero field mobility and γ is less pronounced, (Figure 3.8e), suggesting

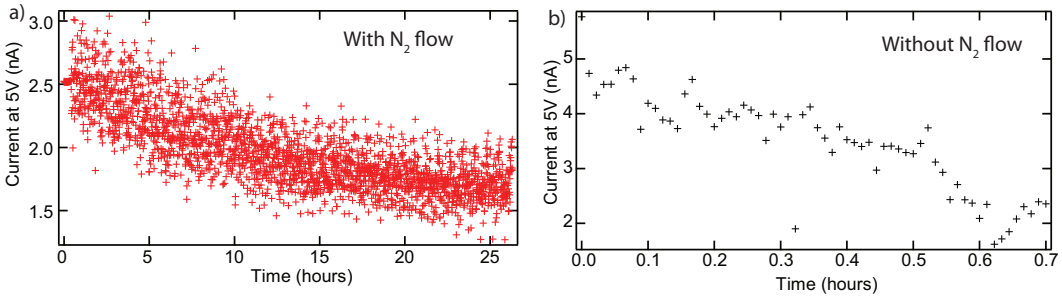

Figure 3.9: Measured current at 5 V bias as a function of time with nitrogen flow a) and a sample without b).

that under these conditions transport is less trap dominated. The increase in mobility is surprising and significant because with air sensitive materials such as P3HT degradation over time tends to decrease the mobility. The rate of degradation is reduced here by measuring in a nitrogen environment.

Figure 3.9 shows the decrease in current measured at 5 V over time due to sample degradation. The reduced effect of degradation when a constant flow of nitrogen is maintained, (a) relative to measurements in air, (b), is clear. The characteristic degradation time, the time over which the current decreases by a factor of e, in air is around 0.5 hours, compared to nearly 12 hours in N_2 flow. Nitrogen flow therefore allows longer measurements to be viable.

From the results shown in Figures 3.7 and 3.8, direct comparison can be made between the room temperature and high temperature behaviour of P3HT. At 130°C the average mobility has increased by almost an order of magnitude to $32.5 \pm 0.4 \times 10^{-4}$ cm^2 / V s whilst the sample Young's modulus has decreased by more than 20 % to 0.69 ± 0.02 GPa. The field dependence of the mobility has also dropped between the low temperature and the high temperature. This is in agreement with work by Blom et al., further suggesting that the charges in P3HT are transported by thermally assisted intermolecular hopping [225]. Note that these measurements were taken with different tips and on different samples, but due to the large datasets these changes are statistically significant.

Figures 3.10 and 3.11 show all the data that can be gathered simultaneously from an FVBS measurement. Data from the force curves are: the dwell force a), the adhesion force b), the contact area c), the Young's modulus f) and the height, which has been flattened for clarity in g). The data from the JV curves are: the mobility d), gamma e) and the current at a 3 V bias in h). The current can be mapped at any value of the bias from the JV curves. White pixels with black bars signify points at which the JKR model did not fit satisfactorily. The current-voltage

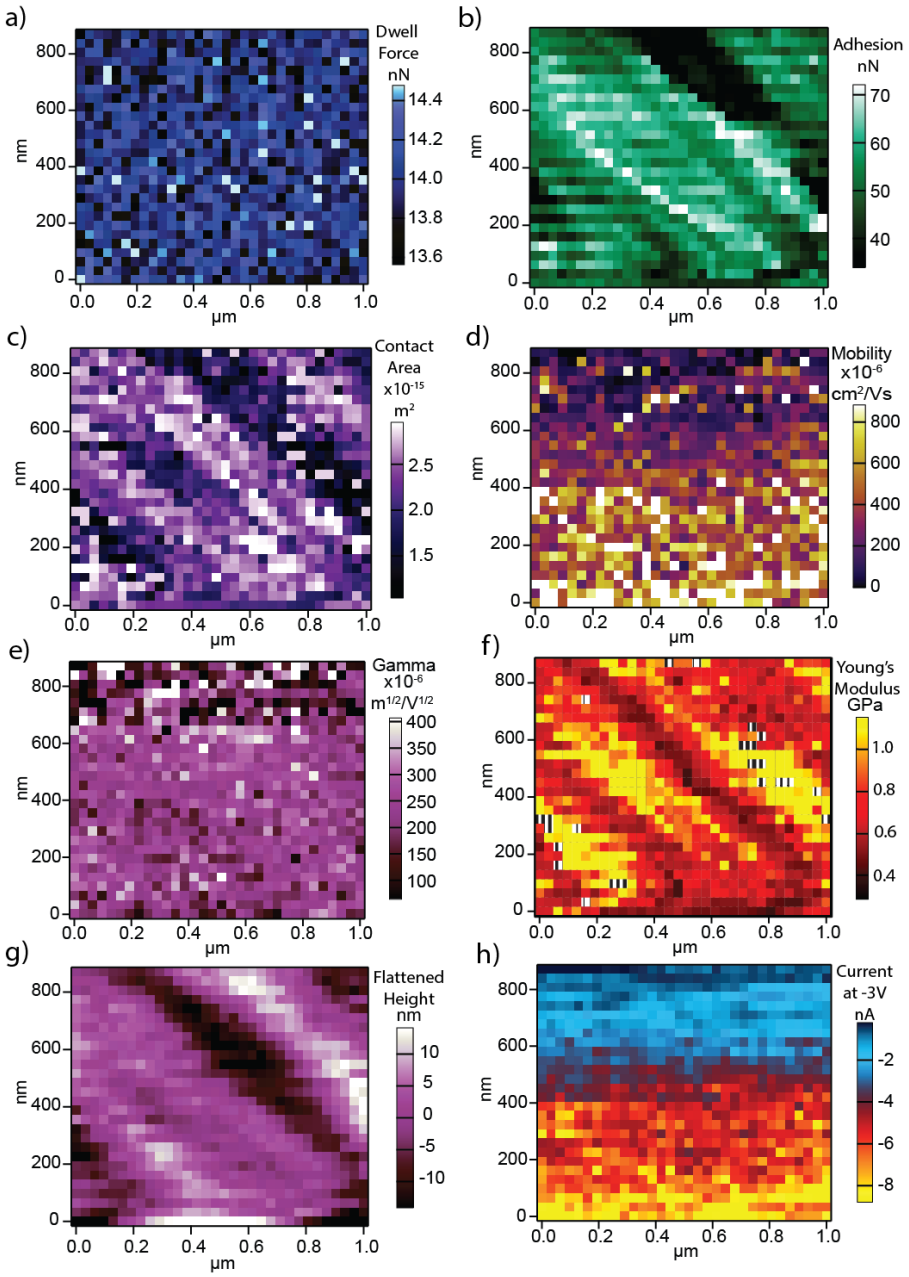

Figure 3.10: High resolution FVBS electrical and mechanical map of untreated P3HT at 30 °C, showing spatially resolved a) measured dwell force, b) adhesion, c) contact area, d) zero field mobility, e) field dependence of the mobility, f) sample's Young's Modulus, g) flattened height and h) current at -3 V. Pixels with vertical black lines show points that have no data due to poor fits. Taken with a Rocky Mountain solid platinum cantilever

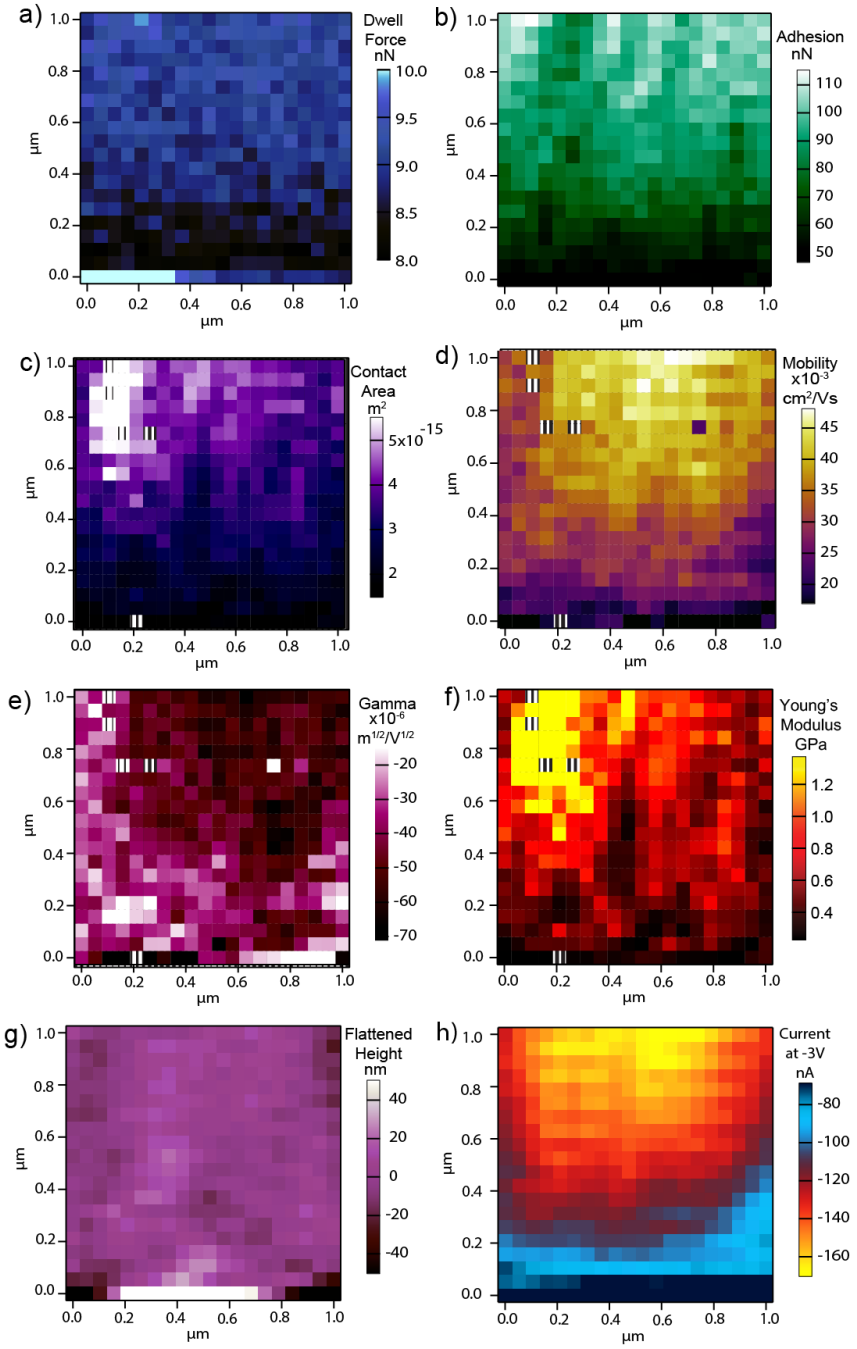

Figure 3.11: High resolution FVBS electrical and mechanical map of annealed P3HT at 130 °C, showing spatially resolved a) measured dwell force, b) adhesion, c) contact area, d) zero field mobility, e) field dependence of the mobility, f) sample's Young's Modulus, g) flattened height and h) current at -3 V. Pixels with vertical black lines show points that have no data due to poor fits.

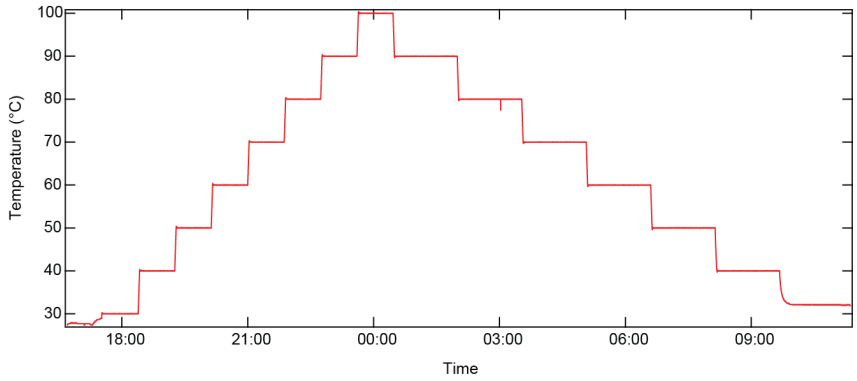

Figure 3.12: Recording of the temperature measured by the polyheater for the extent a temperature dependent FVBS measurement.

and force-distance curves for each pixel are stored and can be separately inspected.

Analysis of correlations between the multiple material properties measured by this technique can give further insight into the material's behaviour, and the experimental conditions during measurement. For example, the contact area in Figure 3.10 c) is strongly correlated to the adhesion b), however this is not correlated to the current in h). The current should be related to contact area, as in Figure 3.4, this suggests a change in conditions during the experiment that did not affect the contact area directly, most likely the contamination of the tip with polymer.

3.1.6 Temperature Dependent Mapping of P3HT

FVBS can also be used to measure the temperature dependence of the electrical and mechanical measurements. An Asylum Research Polyheater (see section 2.2.7) was used to control the temperature, with FVBS maps typically acquired at 10°C intervals form 70 to 140°C to match the standard annealing conditions of P3HT [87, 226]. To reduce the risk of tip damage or contamination and sample degradation, the size of FVBS maps was reduced.

Figure 3.12 shows the temperature changes over time during a temperature dependent experiment. When the desired temperature is reached a portion of time, 20 minutes for a temperature rise, and 40 minutes for a decrease, is spent allowing the sample to reach thermal equilibrium. This ensures that the sample doesn't drift or expand while the FVBS measurement is running. The FVBS measurement then takes place. Once finished the tip is retracted to the full range of the z-piezo, before the next temperature ramp is initiated.

The resultant changes in zero field mobility and adhesion are shown in Figure

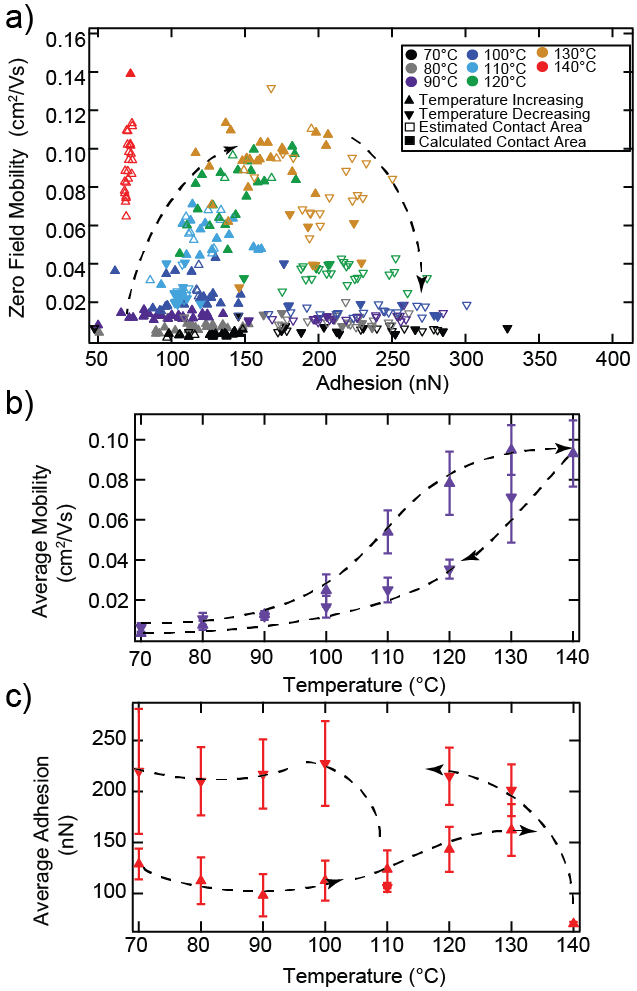

Figure 3.13: a) Temperature dependence of zero field mobility and surface adhesion when as-cast P3HT is heated from 70°C to 140°C and then cooled to the original temperature. Closed symbols use a mobility calculated from a measured contact area, open symbols have an estimated contact area. An array of 25 points was measured at each temperature. b) and c) Average values of zero field mobility and surface adhesion respectively, from a) as a function of temperature, upward triangles signify an increase in temperature. Error bars here represent the standard deviation of the data at each temperature from a). Dotted lines are guides to the eye.

3.13. The mobility shows a consistent increase with temperature, evident in both 3.13 a) and b). It is also evident that the mobility is lower when the sample is cooled, compared to the data at the same temperatures during heating for temperatures above 90°C. This can be partially attributed to sample degradation. Using the data in Figure 3.9 the degradation contributes around 40% of the difference between the mobilities measured at 100°C. However, below 90°C the mobility is higher on cooling. This is similar to work by Wu et al. who observed an increase in molecular order below 60°C in low molecular weight P3HT [98]. They attribute this to the melting of side chains upon heating. It would make sense that the increase in order from annealing allows the crystallisation of more side chains when cooled. The higher temperature of this transition, 90°C compared to the 60°C reported, could be due to the higher molecular weight P3HT used in this study or a difference between the calibration of the temperatures measured experimentally. Differential scanning calorimetry (DSC) measurements show transition temperatures increasing with molecular weight [98]. Unfortunately, a statistically robust determination of the effects of annealing on mobility is not possible from this data.

Figure 3.13 a) and c) show a gradual rise in adhesion with temperature, until 140°C where there is a rapid drop in adhesion. Upon cooling the adhesion is mostly constant at values much higher than on heating. There is however, a noticeable drop in adhesion at 110°C, which does not continue through the rest of the cooling cycle.

Figure 3.14 a) compares the average zero field mobility, μ_0, and the average value of the field dependence of the mobility, γ, as a function of temperature. The field dependence of the mobility, γ, also decreases with increased mobility with rising temperature. This is the expected behaviour as the transport should be less dependent on traps at higher temperatures [74]. Figure 3.14 b) shows the Arrhenius behaviour of the mobility, notably that, up to around 120°C the mobility exponentially decreases with inverse temperature, suggesting that over this temperature range transport occurs via a hopping mechanism [227]. Further to this the fitting of γ in b) shows a linear dependence on inverse temperature as in Blom's work, according to

$$\gamma = B\left(\frac{1}{k_B T} - \frac{1}{k_B T_0}\right) \tag{3.5}$$

with $B = 3.43\ e^{-5}$ eV $m^{1/2}/V^{1/2}$ and T_0 of 2486 K. The value of B is very similar to the $2.9\ e^{-5}$ eV $m^{1/2}/V^{1/2}$ found for PPV by Blom et al [225]. The characteristic temperature is dissimilar to the 520-660 K found by Blom et al, however this is most

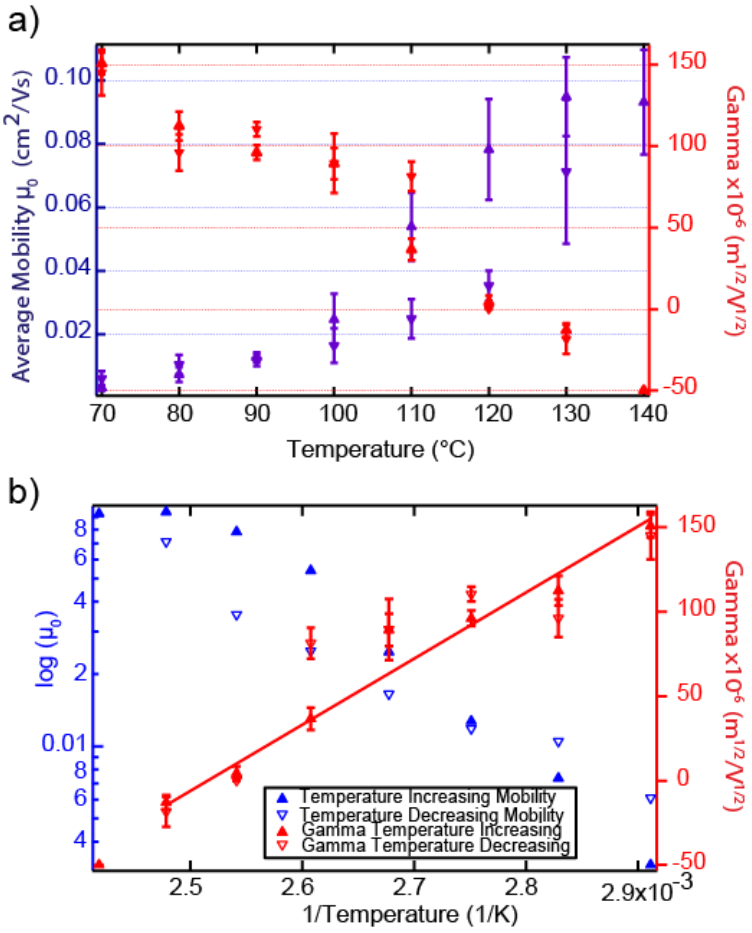

Figure 3.14: a) Temperature dependence of the average zero field mobility (blue) and γ (red). b) The mobility and γ are plotted against inverse temperature (the mobility with a logarithmic scale). For both graphs, data points as the temperature is increasing are marked with upward triangles, and at decreasing temperatures with downward triangles. The temperature dependence of γ is fitted with a linear fit.

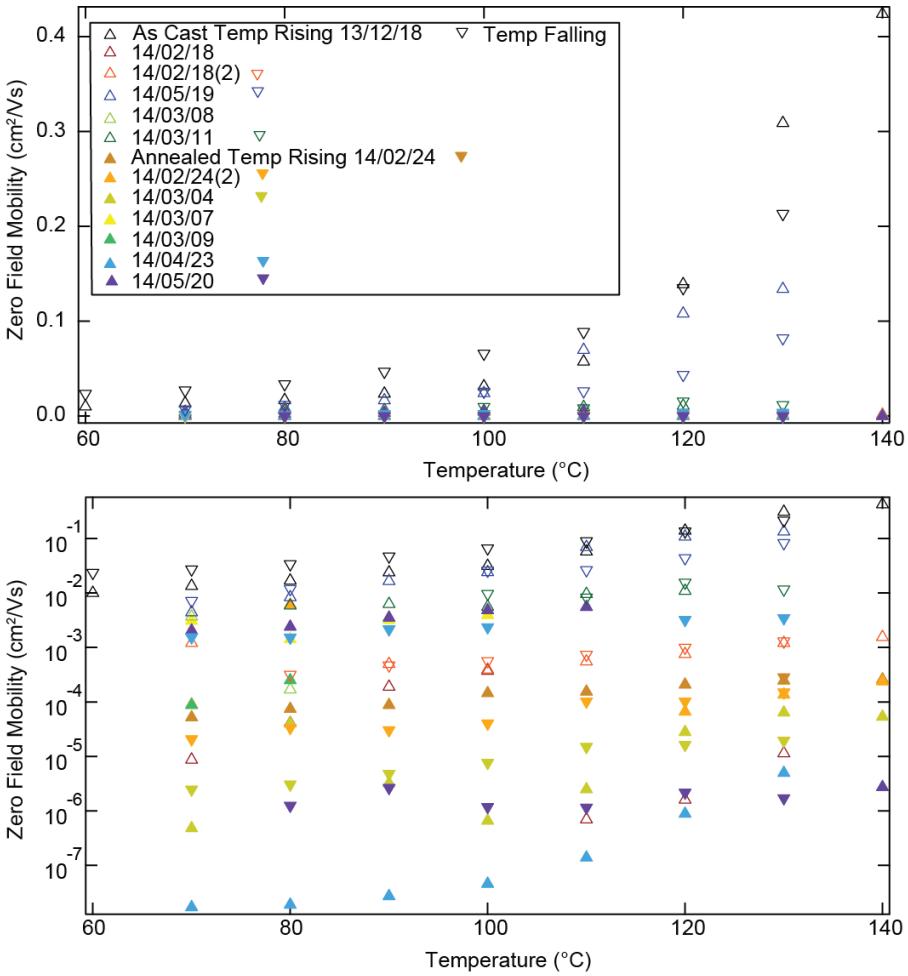

Figure 3.15: Zero field mobility of annealed (filled) and as-cast(unfilled) P3HT as a function of temperature across a range of complete and incomplete experiments.

likely due to the negative field dependence values that are a feature of the specific AFM geometry. However, the good agreement of B for a similar mobility polymer indicates that the measurement of mobility from this data is valid.

Acquiring a complete data set was challenging, and large variations between data sets were observed. The range of the data gathered during complete and incomplete data sets can be seen in Figure 3.15. However, the main observations of the mobility rising with temperature were consistent across the entire range.

In Kline et al.'s study of the temperature dependence of mobility, they found that mobility was only thermally activated below room temperature [94]. However, the results in 3.13 and 3.14 are consistent with such a thermally activated transport

process persisting above room temperature, until a transition occurs at 130°C. This is in agreement with the work of Pingel et al. whose microwave mobility data show a continual increase in mobility with temperature [228]. Studying temperatures above that of room temperature allows characterisation of annealing effects and also more realistic operating conditions to be tested.

3.1.7 Conclusions

Here, for the first time, quantitative temperature dependent CAFM measurements of OSCs have been accomplished. It has been demonstrated that by fitting a JKR model to retract curves in FVBS data and extracting the tip surface contact area, quantitative, nanoscale electrical and mechanical measurements can be acquired simultaneously. It is also possible to correlate the electrical and mechanical properties, to each other, and also spatially in point-by-point maps across an area. This itself elucidates correlations between properties that were not previously visible.

For P3HT, both electrical and mechanical properties are heterogeneous at sub-micron length scales and depend strongly on temperature. From room temperature up to around 110°C, the electrical properties of P3HT are found to be consistent with a grain boundary limited transport model, showing a roughly exponential decrease in mobility with inverse temperature. At higher temperatures, around 130°C, the IV characteristics suggest a less trap dominated behaviour, the length scale of spatial variations in mobility increases, and a correlation between sample stiffness and mobility becomes evident, suggesting an increase in molecular order in the film.

3.2 CAFM of VOPc

3.2.1 Introduction

Now we consider the application of FVBS measurements to the small molecule OSC vanadyl phthalocyanine (VOPc). In terms of data acquisition and processing VOPc presents a new challenge compared to P3HT. Reported values of Young's modulus for CuPc, similar to VOPc, are 5.20 GPa [229], significantly higher than P3HT. Hence, the JKR model previously used may not be a good fit.

VOPc and other non-planar phthalocyanines have high performances and favourable absorption profiles for use in OPV devices. Their morphology and crystallinity is heavily influenced by growth conditions and substrate choice [230, 113]. Most notably, changing the temperature of the growth substrate drastically changes

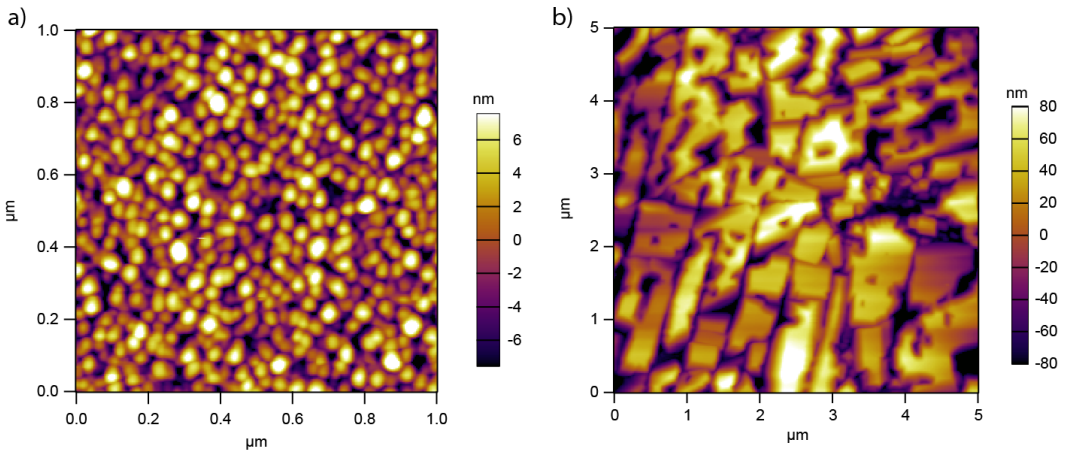

Figure 3.16: A topography comparison of a) room temperature (30°C) grown VOPc 50 nm thick and b) high temperature (130°C) VOPc on graphene on copper foil with an average film thickness of 100 nm.

the morphology of the resultant VOPc layer [231].

Due to the non-planar nature of the VOPc crystal, VOPc has anisotropic charge transport properties [232]. Like copper phthalocyanine CuPc the preferential stacking direction for VOPc is with the molecular plane perpendicular to the substrate making the π - π stacking direction along the substrate, this is preferential for transport along the plane as utilised in FET devices [233].

This work was part of a study on the growth of of VOPc without epitaxy on graphene by Marsden et al, which found that large single crystals of VOPc can be grown on homogeneous surfaces of CVD-grown graphene using elevated substrate temperatures of 155°C [2]. The relevant question covered by the section is: How does the out of plane mobility of VOPc depend on the growth temperature?

3.2.2 Topography

Figure 3.16 shows the differences in topography between VOPc grown at room temperature (30°C) a), and high temperature (130°C) b). For growths at room temperature a thin polycrystalline film is formed with a correlation length of 22 $\pm$ 3 nm. The high temperature growth in the meantime shows much larger grain sizes, exceeding a micron in length, but also a lower surface coverage. The large increase in grain size has promising implications to the mobility in the high temperature samples, as it has been shown that larger grain sizes results in an increase in mobility in FET device geometry [112]. XRD and electron diffraction showed that these

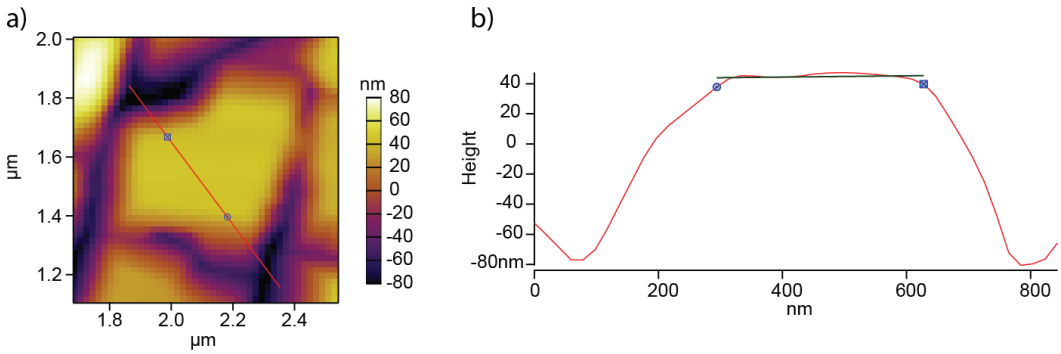

Figure 3.17: a) AFM topography of a VOPc crystal. b) The line profile from a), fitted between cursors shown with a linear fit to determine the thickness of the VOPc grain.

grains were single crystals, with edge on orientations ligand out of plane to the graphene.

The relative homogeneity of the room temperature growths is advantageous for FVBS, allowing a grid of points to be taken in the same manner as in section 3.1.4, with a high likelihood of the tip contacting with the VOPc. On the other hand, points must be chosen on grains of VOPc in the high temperature case. This can either be done in a point by point manner as shown in Figure 3.18, where there are multiple points chosen in specific places on an island, or alternatively a smaller scan can be done on a single island and a map can be taken on this island in the same manner as for the room temperature sample. The latter of these methods was used as the data can then be generated in a more or less automated fashion. Additionally, this ensures that the entire force map is on a single grain, therefore the crystal thickness is uniform across the map. This is useful as thickness is a parameter used in the fitting of mobility.

Figure 3.17 shows how the topography was used to calculate the heights of the VOPc islands by utilising the ability to take a line profile. The level of the substrate is taken as the average of the lowest 2 points on the profile. The plateaux of the profile is then fitted with a linear fit. The average value of that line is found and the difference between the two averages is taken as the height of an island.

3.2.3 How can the contact area be quantified?

As was previously stated, the expected Young's modulus values based on published results of similar molecules should be in the region of 2-5 GPa [229]. Initially FVBS was applied as described earlier for VOPc, however application of the JKR fitting

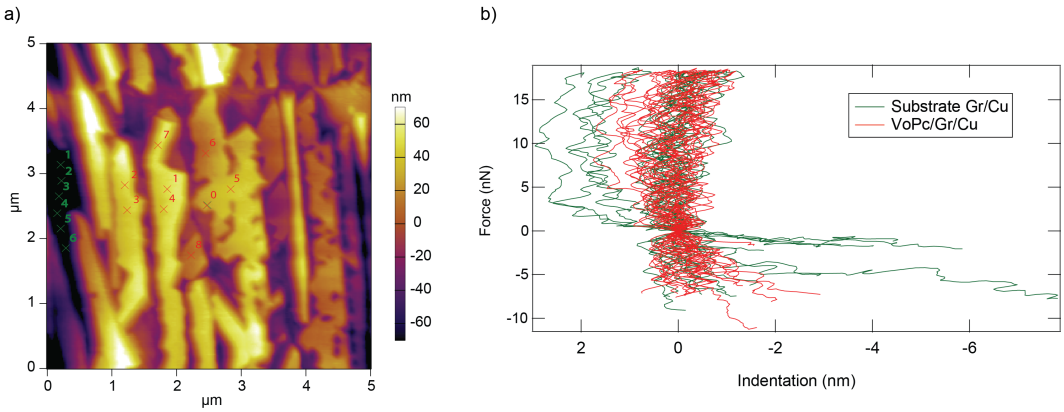

Figure 3.18: a) Tapping mode image of high temperature grown VOPc points in green are force points on the substrate, those in red are on VOPc islands. b) Force curves from substrate and VOPc shown. The curves have the same gradient indicating no difference in stiffness between islands and substrate.

proved to be unreliable, and the curves that did fit produced moduli of around 300 MPa. The question then becomes: What is being measured here?

Figure 3.18 b) shows a comparison between force curves on the VOPc grains, and force curves on the copper/graphene substrate. Their specific locations can be seen in the topography shown in a). Clearly these force curves are not a good fit for a JKR model. Although there is evidence of adhesive interactions with the surface, the indentation is minimal for both the substrate and the VOPc. The overlap of the curves would indicate that both are acting as infinitely hard surfaces with respect to the cantilever. The few more deeply indented curves are indicative of some bending in the copper. This is unlikely to be true indentation as copper's Young's modulus is around 130 GPa [234].

In order to further test the viability of measurements on VOPc, force curves were taken on two samples of known stiffness, silicon (169 GPa) and polymethylmethacrylate PMMA(2.4 - 3.4 GPa) with an Olympus AC240TM tip, measured spring constant 1.92 N/m [235, 234]. Figure 3.19 shows the results of such force curves. Regardless of the calibration of the deflection, InVOLs not being perfect in this instance, the overlap of the PMMA and silicon force curves despite the PMMA being much softer than silicon, indicates that the cantilever is too soft to be able to measure the modulus of PMMA. Consequently, the AC240TM tips would be unable to measure the modulus of VOPc either as their moduli are similar. This implies that a new approach is required because the standard cantilevers used for the CAFM measurements are too soft to indent this harder sample.

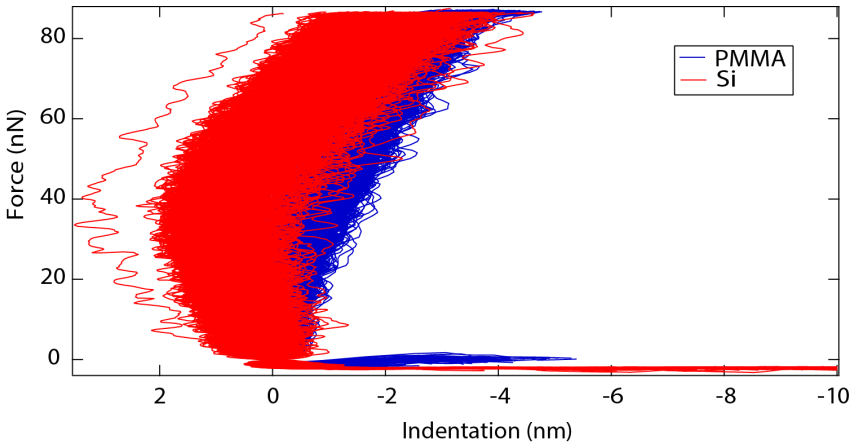

Figure 3.19: Force curves on silicon (red) and PMMA (blue) taken with an AC240TM cantilever. Curves from the PMMA and Si overlap.

Initially, the Young's modulus of VOPc needs to be determined; to do this a sample of VOPc was grown at room temperature on an ITO/glass substrate. Although the orientation of the VOPc is possibly different to that grown on graphene/-copper, it's modulus should be similar at least to within error of the AFM measurements. Following the work of Clifford and Seah [202], force curves of VOPc were taken alongside those of silicon and PMMA with a Vecco Multi130PT tip with a measured spring constant of 6.5 ± 0.9 N/m. Since both the PMMA and silicon have known modulus values, their force curves can be used to determine the modulus of the VOPc.

Figure 3.20 shows tapping mode scans of the three materials in a), b) and c) with corresponding force curves on these surfaces in d) with their averages in e). The silicon and PMMA show relatively smooth surfaces when compared to the VOPc, they also have very little spread in their respective force curves in green and blue. A slight calibration error is evident in the silicon force curve in e). Here, the curve should be a straight line through zero as with respect to the cantilever the silicon should be infinitely hard. Regardless, fitting the PMMA force curves with a JKR model yielded an average Young's modulus of 2.60 ± 0.02 GPa. This is well within range of the expected 2.4 - 3.4 GPa. Therefore, the value yielded by the fitting for VOPc should be representative of the sample, since it is similar to PMMA. Though the VOPc has a large spread the average value of the Young's modulus gathered here is 2.2 ± 0.2 GPa.

Unfortunately, since the force curves of the FVBS maps did not fit a JKR

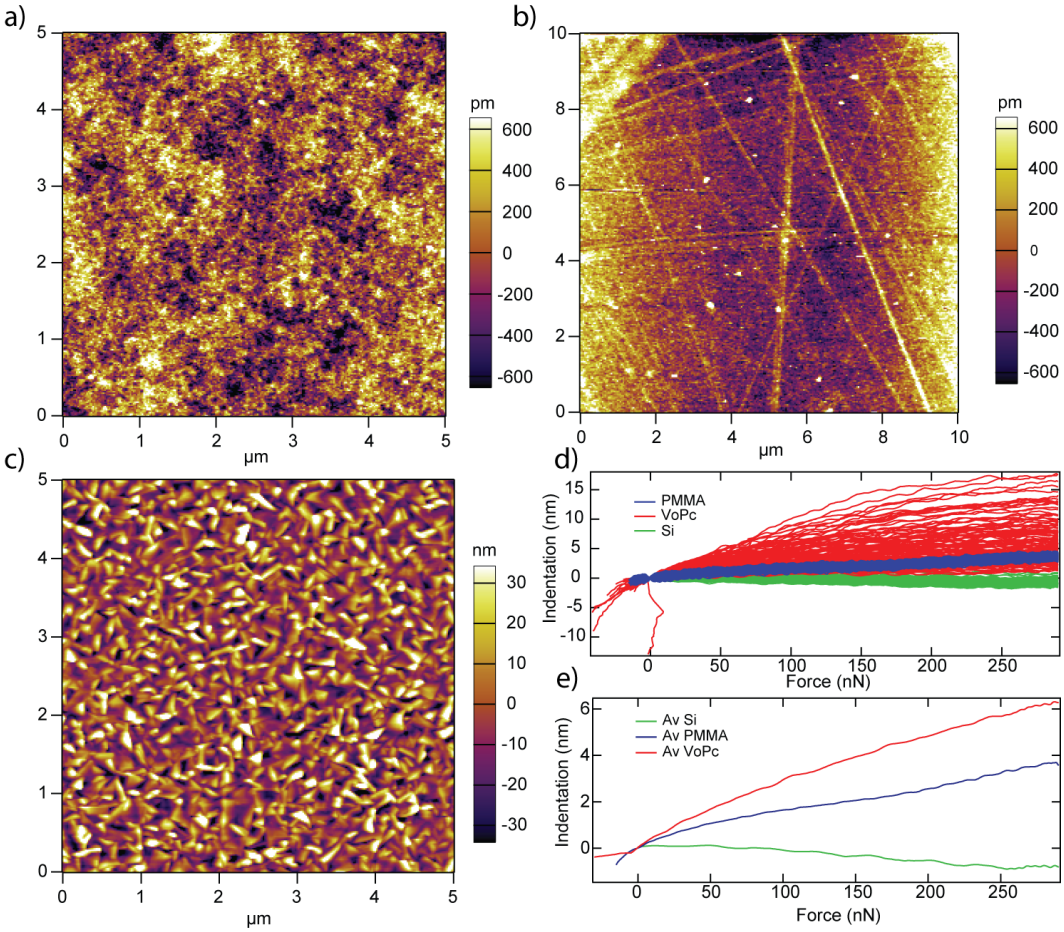

Figure 3.20: a), b) and c) show ac mode topography scans of PMMA, silicon and VOPc on ITO respectively. d) Shows force curves from each of these materials in blue, green, and red respectively. e) Shows the average curve for each material for clarity.

model an exact contact area cannot be found for each point. However, the other parameters, namely the average dwell force F_{dwell} and the adhesion force F_{ad} used to calculate the contact area are still relevant and present for every point in the FVBS. So a more accurate estimate of the contact area can be made assuming the Young's modulus is constant, by inputting these parameters into the JKR model contact area, equation 3.3.

3.2.4 Calculating Mobility

Since each point now has a contact area, the mobility can be calculated in the same manner as for the P3HT. Figure 3.21 shows a selection of the raw IV curves and a

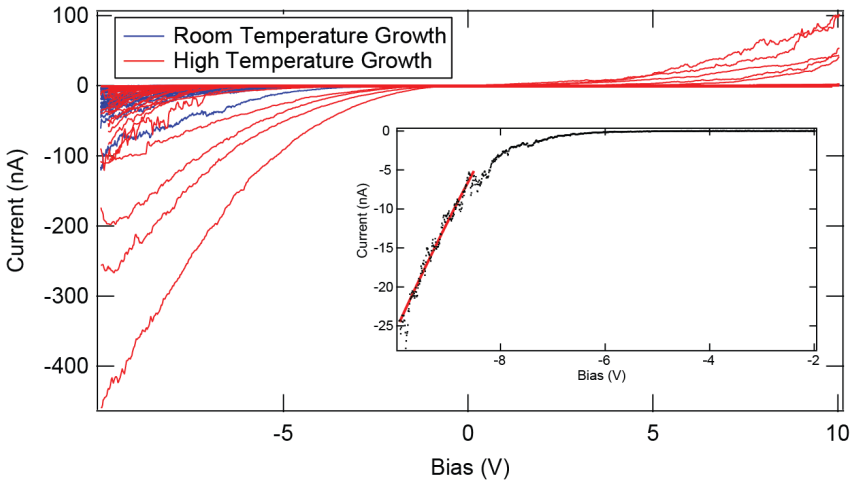

Figure 3.21: Raw IV curves on both high temperature grown, red, and room temperature grown, blue, VOPc. Inset: Shows the points in a measured curve with a modified Mott-Gurney fitting (red).

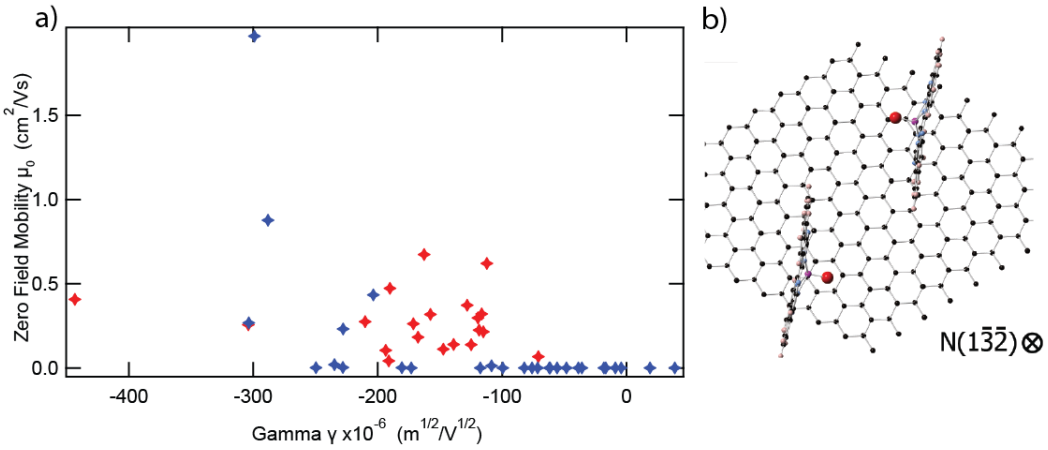

Figure 3.22: a) The zero field mobility (μ_0) and field dependence (γ) of high temperature red and room temperature blue grown VOPc. b) The crystallographic orientation of crystalline VOPc with respect to the graphene substrate, here the $1\bar{3}\bar{2}$ axis is shown into the plane reproduced from [2].

sample fitting shown in the inset. The curves show distinctly diode like behaviour with occasional leakage current in the reverse bias direction. Space charge limited current behaviour occurred at high negative biases, hence the Mott-Gurney fitting was applied across the -8 to -10 V range, when SCLC behaviour is evident.

Figure 3.22a) shows the resulting zero field mobility against the extracted field dependence of the mobility, γ, for both the high temperature and low temper-

Figure 3.23: A schematic of high temperature grown VOPc, having large single crystals ligand growing parallel to the graphene (the phthalocyanine plane displayed) compared to low temperature grains which are much smaller but still crystalline. Their orientations are however random.

ature VOPc. The high temperature points have on average a higher mobility, 0.27 $\pm$ 0.04 cm^2/Vs, than the low temperature at 0.14 $\pm$ 0.07 cm^2/Vs. The mobilities found here are on average an order of magnitude lower than those previously reported [113]. This is most likely due to the unfavourable out of plane alignment of the VOPc backbone in the high temperature grown VOPc, as shown in Figure 3.22 b). Whilst the mobilities are relatively low, their consistent and low field dependence suggests transport is unhindered by trapping, indicating high crystal order.

Figure 3.23 shows how the crystallographic orientation explains the mobility behaviour measured. The high temperature growth has the phthalocyanine perpendicular to the graphene in a crystalline structure. So when the mobility is measured, the direction of charge transport is unfavourable, however the high crystallinity results in mobilities that are consistent with a low field dependence. Whereas, in the room temperature case, the point that the AFM tip is in contact with could be any variation of the orientations shown. A small single crystal oriented favourably with the phthalocyanine in plane to the graphene is expected to return a high mobility with very low field dependence. The AFM tip could also be on a segment containing polycrystalline VOPc, this would yield much lower mobilites with a higher field dependence from the lower order. The end result of this is scattered inconsistent mobilities across the film. The low temperature results show this variety of behaviours; from very high mobilities up to 2 cm^2/Vs , with low field dependence -3 $x10^{-4}$ $m^{1/2}/V^{1/2}$, to very low mobilities of 7 $x10^{-6}$ cm^2/Vs with high field dependencies of 4 $x10^{-5}$ $m^{1/2}/V^{1/2}$. Since the structure factor of VOPc is low and the grains found here are small, it is unclear in the XRD done in Marsden's work whether the room temperature deposited VOPc is poly-crystalline or single crystal.

3.2.5 Conclusions

The technique of FVBS has been used to study how growth temperature affects the mobility of VOPc on a graphene/copper substrate. Although direct determination of contact area wasn't possible, estimations of the tip sample contact area were made by measuring the Young's modulus of VOPc using direct comparison to PMMA and silicon to ensure accurate results. The resulting analysis showed that even though high temperature deposited VOPc is oriented unfavourably for transport out of plane it has a high zero field mobility with minimal trapping. Low temperature growths however show a variety of behaviours on the nanoscale.

If attention is paid to the expected stiffness of the sample and tip FVBS has proven a valuable tool for quantifying the electrical and mechanical properties of small molecule OSCs.

3.3 Conclusions

This is the first time that FVBS has been applied to gather quantitative information of the electrical and mechanical properties of OSCs simultaneously. Nanomechanical indentation and CAFM are both popular techniques, however they are rarely used in combination. Specifically using a contact area calculated from a JKR fitting in a simultaneous IV type measurement has not been done before.

The technique has been successfully implemented on both hard and soft materials. For soft materials, care needs to be taken to ensure the tip and sample are not degrading during the course of the measurements. For hard materials, the biggest challenge is accurately determining the contact area, the stiffness of the cantilever used must be chosen to maximise indentation in order for a valid fitting of a contact mechanical model. Automation of both acquisition and analysis of data has meant that large data sets, including spatially resolved maps can be generated. This shows statistically significant correlations in electrical and mechanical properties over areas, ruling out random noise and anomalous results.

Here, it has also been shown that FVBS can be used in a temperature dependent capacity, showing the evolution of measured properties with temperature. Prospects for this technique include; optimisation of annealing techniques, predictions of macroscopic mobility prior to top electrode placement, and the ability to monitor the mobility at realistic operating temperatures. If attention is paid to how the cantilever is retracted, the additional measurement of viscoelastic creep could be added, however these come with their own challenges and the changing contact area would need to be carefully considered if applying electrical methods simultaneously.

Chapter 4

Photodependent EFM of OPVs

4.1 Introduction

In the previous chapter quantitative measurement of the mobility of organic semiconductors by conductive AFM was demonstrated. Extending this work to look at the photoactive properties of these materials would be an ideal scenario. An approach would be to replicate bulk JV measurements (as discussed in Section 1.2.3) at the nanoscale using the AFM.

Figure 4.1 shows typical JV curves of planar geometry P3HT:PCBM bulk heterojunctions. Using this, it is possible to estimate what the parameters of J_{SC} and V_{OC} would be in the AFM geometry. Typical values for J_{SC} are ~ 10 mA/cm^2. As evidenced in the previous chapter, typical AFM contact areas are ~ 3000 nm^2 =

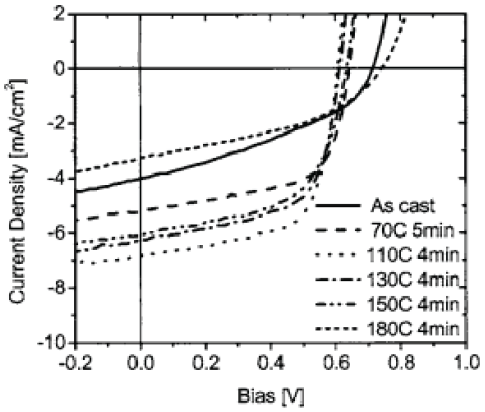

Figure 4.1: Typical JV curves measured on P3HT:PCBM after annealing at a variety of temperatures, reproduced from [88].

3×10^{-11} cm^2, hence the expected I_{SC} is around 3×10^{-13} A i.e. < 1 pA. Whilst this resolution is possible, using a 40 nA range conductive cantilever holder with a 16 bit ADC yields a resolution of 6×10^{-13} A, the noise margin in CAFM is the limiting factor. Even with high levels of averaging, achieving these numbers would be highly challenging. Additionally, these measurements would require a reliable top contact, one which a metal coated AFM tip does not provide. However, the second parameter the open circuit voltage $V_{OC} \approx 0.5$ V is measurable in the AFM by a range of techniques within the electrostatic force microscopy (EFM) family. This seems like a much more promising route to follow.

EFM and variants such as KPFM measure the surface potential, hence controlling the light incident on a sample enables the surface photovoltage (SPV) to be measured in the AFM with nanoscale resolution [80]. SPV can also be measured at the macroscopic level by techniques such as Kelvin probe, and analysis of SPV has been used to study both organic and inorganic photovoltaics [80, 81, 82, 236, 237]. Crucially, it has been found that SPV directly correlates to V_{OC} [86].

Beyond this, measurement of the time response of SPV gives insight into charge carrier recombination. Durrant and co-workers pioneered transient photovoltage (TPV) for the measurement of charge carrier dynamics [238]. TPV uses a background light bias to control the V_{OC} of the sample. Then a laser is pulsed onto the sample to perturb the V_{OC} by a small amount. Since there is no current flow the decay of the excess charge carriers is solely due to loss kinetics which can therefore be measured. Using this Shuttle et al. demonstrated that the carrier lifetime in P3HT:PCBM follows an inverse square relationship with increasing charge density, and hence with light intensity, with typical values of 10 μs at 1 sun. The carrier lifetime (τ) is directly related to J_{SC}, hence TPV gives direct insight into the performance of an OPV device.

Following this there have been many attempts to use EFM and KPFM to measure the SPV [190, 189], and a few to measure the carrier lifetime [239]. This chapter concentrates on two techniques developed by the Ginger group at the University of Washington; time resolved EFM (Tr-EFM) and intensity modulated KPFM (IM-KPFM). The archetypal bulk heterojunction (BHJ) P3HT:PCBM and the relatively new high performance BHJ PTB7:$PC_{70}BM$, courtesy of the Hatton group, were used as test materials in this study. Both techniques are developed to measure SPV (and hence V_{OC}) and τ (hence gaining insight into J_{SC}). By applying both techniques to the same systems it is possible to compare and contrast their advantages and disadvantages. For both, significant improvements in their quantification are made, as compared to previous reports, and they are combined with

temperature dependent measurements to investigate the effects of annealing and other temperature dependent phenomena.

4.2 Time Resolved EFM

4.2.1 Introduction

Tr-EFM was introduced by the Ginger group as a technique to measure photoexcited charge in polymer solar cells, with their first paper claiming 100 nm and 100 μs resolution [170]. Using this they were able to show that domain centres account for the majority of photoinduced charge collected in polyfluorene blend devices. Subsequent papers showed that Tr-EFM can be used to measure low external quantum efficiencies associated with charge transfer states [171] and also local photoxidation and trap formation [240]. They also showed that with additional equipment it is possible to enhance the time resolution to $\sim$100 ns, showing that it is possible to correlate local dynamics with device behaviour in P3HT:PCBM [172].

As implemented by the Ginger group, Tr-EFM consists of a conductive AFM tip driven near resonance with a fixed lift height from the surface. The AFM is then operated in a frequency-shift feedback mode, recording the drive frequency shift to keep the cantilever on resonance. A bias is applied to the tip, shortly followed by a light pulse applied to the sample. The bias and light pulses end in synchronous and the frequency shifts throughout are recorded. The change in frequency due to the illumination causing a charging of the tip-surface capacitor is fitted to an exponential decay. This results in a measurement of the time constant of charging, τ_c. This is not a widely used technique although at least one other group has published results from a similar technique, albeit with a much lower time resolution [241].

In this section a modified version of Tr-EFM is presented, which is used to study P3HT:PCBM and PTB7:PC_{70}BM, with the important advance of extracting not only τ_c but also the SPV. Initial results are on P3HT:PCBM, as a well studied system it seemed an appropriate choice of test system. A flow diagram for the process of Tr-EFM, as implemented here, can be seen in Figure 4.2

4.2.2 Amplitude and Phase Acquisition

Thin film samples of P3HT:PC_{60}BM were prepared by spin coating on a glass ITO substrate, as described in 2.1.3.2. The ITO electrode in this case is earthed, and the biases used for measurement were usually positive. A schematic of the sample and setup can be seen in 4.3.

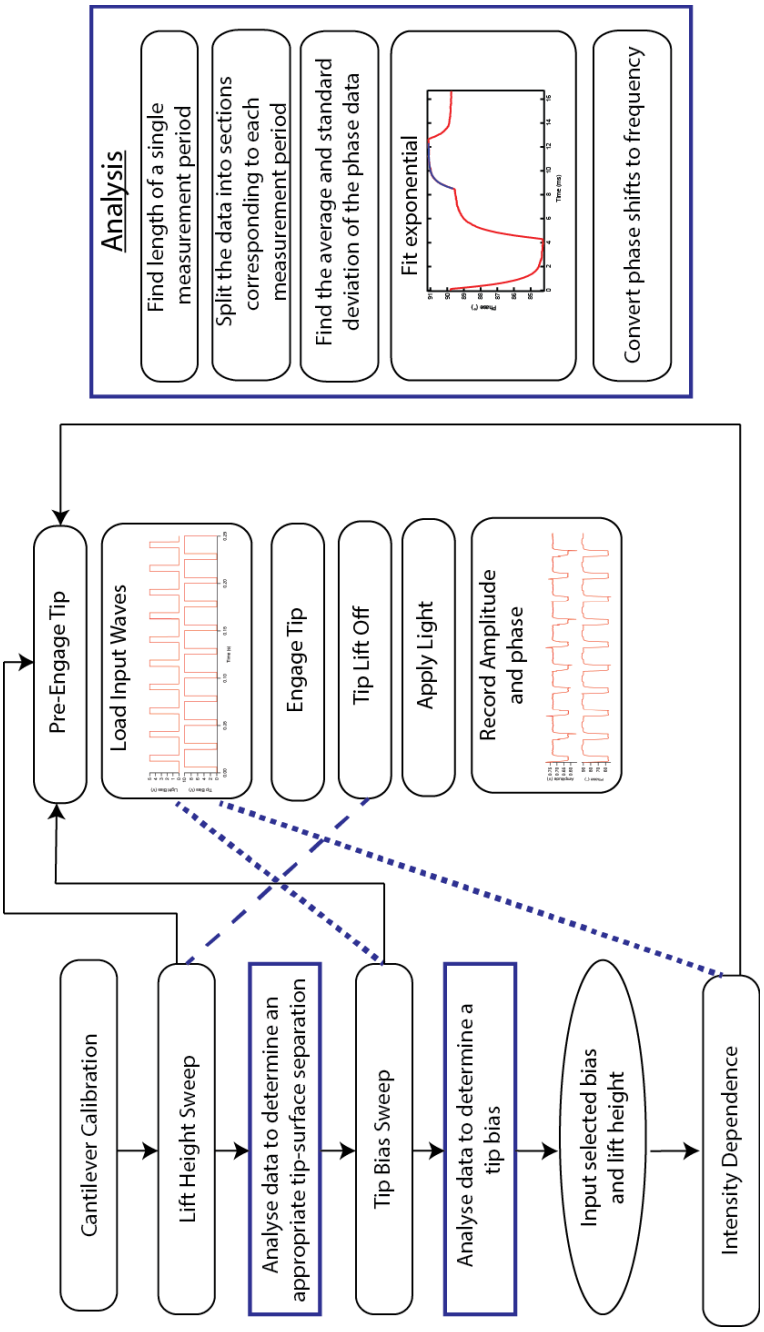

Figure 4.2: A simplified flow diagram of the process of a Tr-EFM experiment. Steps can be added in and repeated for temperature dependent results. Blue dotted lines show where parameters are changing.

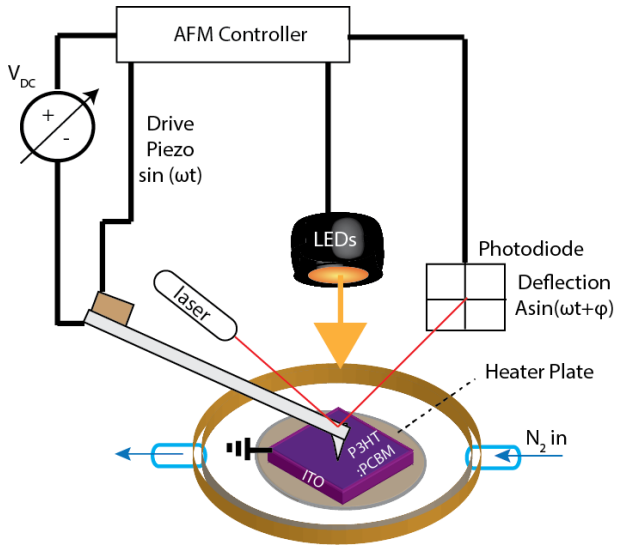

Figure 4.3: A schematic of the temperature dependent Tr-EFM experiment. This only shows the top view optic as the bottom view can't be used with the polyheater.

The process of Tr-EFM can be best visualised from the standpoint of traditional steady-state EFM, where the tip is driven near resonance with a phase of 90° at a distance of around 50 nm above the sample's surface. As the tip experiences electrostatic interactions its resonant frequency changes according to

$$\Delta f \cong \frac{f_0}{4k}\frac{\partial^2 C}{\partial z^2}V^2 \tag{4.1}$$

where f_0 is the resonant frequency and k is the spring constant of the cantilever, C is the capacitance of the tip surface capacitor and z is the tip sample distance. In Ginger group's implementation a feedback loop tracks the frequency change of the cantilever, whereas in this work there is no feedback loop applied and the phase is tracked throughout the experiment as well as the amplitude of oscillation. The phase can be converted to a frequency shift by interpolation of the cantilever tuning curve, described in more depth in 2.2.2.2. The slight disadvantage of this technique is a limited capture time, as the frequency tends to decay from its equilibrium in around 0.4 s, most likely as a result of piezoelectric creep.

In Tr-EFM there are two frequency changes to consider, the first is due to the applied voltage on the tip, thus changing V and C. The second much smaller frequency change is due to the application of illumination to the sample. Photogenerated charges respond to the electric field between tip and sample changing the capacitive gradient, and thus the cantilever frequency. A new equilibrium frequency

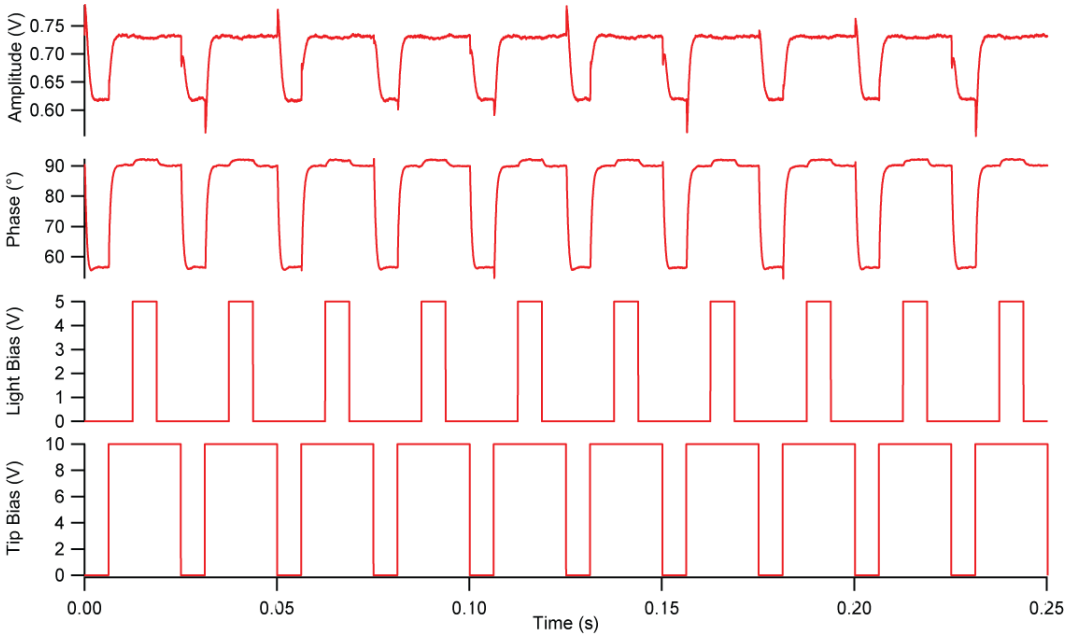

Figure 4.4: Typical Tr-EFM data, the amplitude and phase of the cantilever oscillation change in response to an applied bias and an incident light pulse.

is reached once enough charges balance the potential well created by the tip. The opposing effect occurs when the illumination and bias are discontinued.

Figure 4.4 shows a typical acquisition of the phase and amplitude in response to a bias and light pulse in Tr-EFM. Here, there is a second crucial difference to the Ginger group's implementation, the light pulse lasts half as long as the bias pulse and it happens in the middle of the time that the bias is applied. This enables both the phase change in response to the light being applied and turned off to be measured. Here, ten light and bias pulses were applied in the 0.25 s window. The capture time, and hence the number of pulses applied is limited by the data bank size of the AFM controller and the frequency drift. At the 50 kHz rate of capture it takes around 0.6 s to fill the data bank, and when this happens the software crashes, which is best avoided.

Figure 4.5 shows a single data point in a Tr-EFM experiment, that is an average of the ten light and bias pulses that were applied. There is a 0.1 ms delay between the turn on of the light and bias and the system response, this is a result of the AFM hardware, as discussed further in 2.2.8.3.

The change in phase due to the illumination starting or stopping was fitted

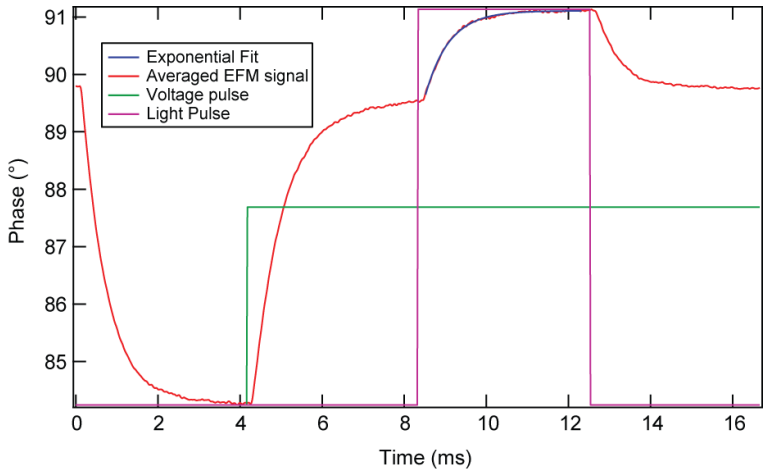

Figure 4.5: A single data point, consisting of an average of ten cycles of bias and light. Taken at 50°C, with a 5 V applied bias and with a light intensity at about 250 W/m^2. The exponential fitting here yields a characteristic time of 5.99 $\pm$ 0.06 $\times$ 10^{-4} s.

with the form

$$\phi = \phi_0 + \delta\phi \; exp\left(\frac{-(t - t_0)}{\tau}\right) \tag{4.2}$$

where ϕ, ϕ_0 and $\delta\phi$ are the phase, the initial phase and the phase change respectively. t and t_0 are the time and the initial time, with τ being the characteristic time, either of charging, τ_c, or discharging, τ_d. As a point to note, ϕ_0 and t_0 do not correspond to the values of t and ϕ before the light pulse is engaged, but correspond to where the fitting begins, for this reason $\delta\phi$ is not the complete phase shift when the light is applied. The fitting procedure is described in more detail in section 2.2.8.2.

Figure 4.6 shows the same data as Figure 4.5 but with the fitting applied to the discharge curve, rather than the charge. For this data τ_C = 5.99 $\pm$ 0.06 $\times$ 10^{-4} s and τ_d = 5.20 $\pm$ 0.05 $\times$ 10^{-4} s, where the error corresponds to the uncertainty of the parameter calculated by the fitting function. In this case, τ_c is calculated to be 13% slower than τ_d.

4.2.3 Surface Photovoltage (SPV)

There is another parameter here that can be extracted, that is the surface photovoltage (SPV), discussed in more depth in 1.2.4.3. SPV is defined as the change in surface potential induced by illumination. This occurs by the absorption of photons either creating free carriers and/or releasing captured charge carriers from trap states. The redistribution of charges within the surface or the bulk material causes

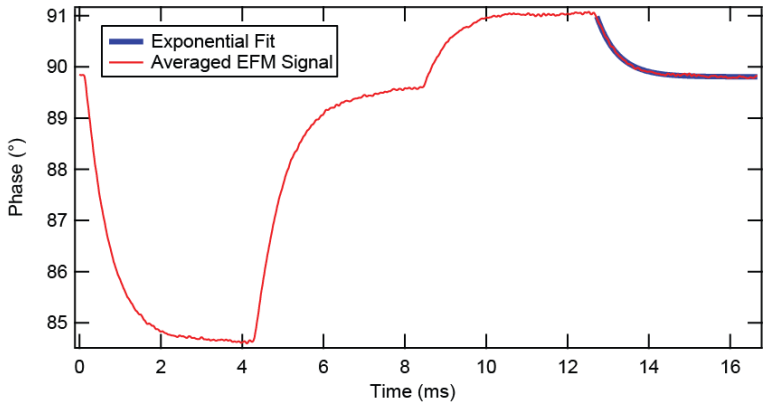

Figure 4.6: A single data point, consisting of an average of ten cycles of bias and light. Taken at 50°C, with a 5 V applied bias and with a light intensity at about 250 W/m^2. The exponential fitting is applied to the discharge section, yielding a τ_d of 5.20 $\pm$ 0.05 $\times$ 10^{-4} s.

the change in surface potential, which can be measured [80].

4.2.4 Extracting the Surface Photovoltage

From Equation 4.1, the frequency shift of the cantilever resonance is dependent on the bias applied by the tip, establishing the tip surface capacitor, however the magnitude of the bias is also dependent on the local surface potential (V_{Surf}). Thus the frequency shift due to the bias applied can be predicted to be

$$\Delta f \cong \frac{f_0}{4k}\frac{\partial^2 C}{\partial z^2}\left(V_{tip} - V_{surf}\right)^2 \tag{4.3}$$

where V_{tip} is the voltage applied to the tip.

Figure 4.7 a) shows the frequency shift as a function of applied bias for a range of lift heights. Equation 4.3 is fitted to the curves in the small bias regime assuming that $\frac{f_0}{4k}\frac{\partial^2 C}{\partial z^2}$ is a constant at a set tip-surface distance. Frequency shifts greater than around 40 Hz result in non-quadratic behaviour, this implies that the second differential of capacitance is not constant in this regime. The bias at which this deviation occurs depends greatly on tip height above the surface, this is unsurprising since the frequency shift should also depend greatly on the tip surface separation.

Figure 4.7 b) shows how the local surface potential varies with lift height. As expected there is not much deviation across the range of lift height, though it appears its effect is larger closer to the surface. Deviations in this could be due to

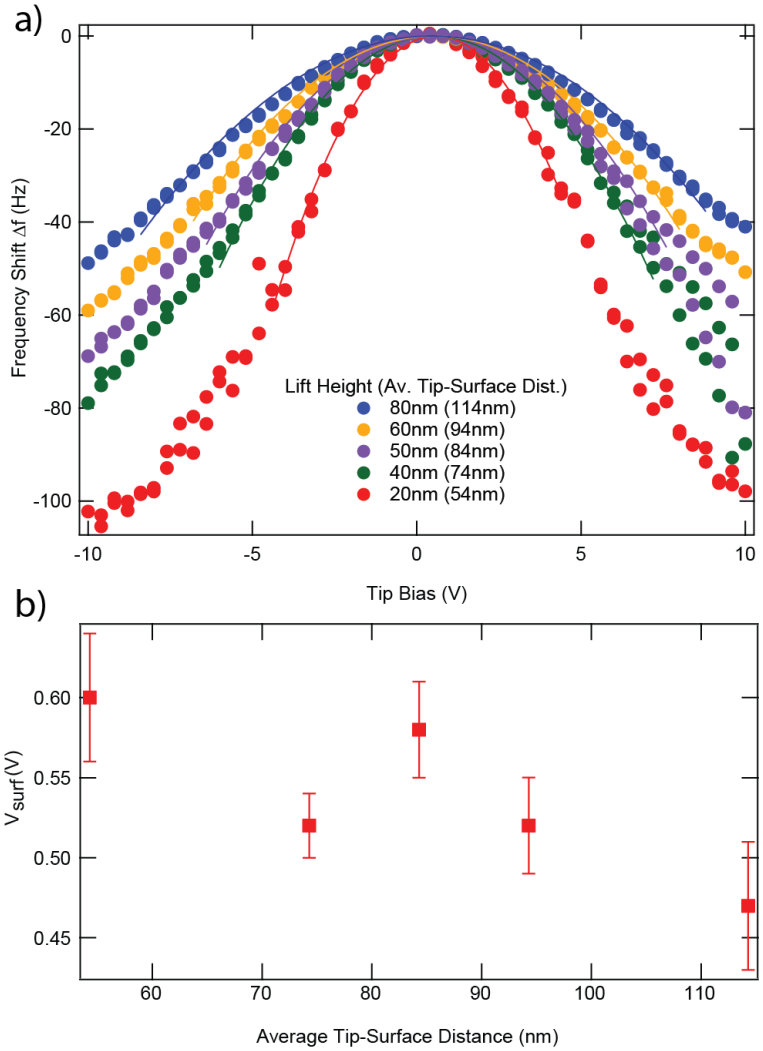

Figure 4.7: a) Frequency shift in response to applied bias, measured at varying lift heights with fitting of Equation 4.3. b) The extracted V_{surf} from the fittings in a) as a function of tip-surface distance.

Lift Height (nm)	Av. tip surface separation (nm)	prefactor (Hz/V)	V_{surf} (V)
80	114	-0.54	0.47
60	94	-0.74	0.52
50	84	-0.92	0.58
40	74	-1.17	0.52
20	54	-2.37	0.60

Table 4.1: Values of the prefactor and surface voltage for P3HT:PCBM.

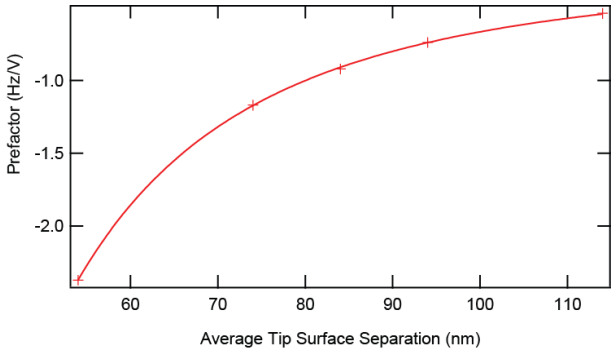

Figure 4.8: The prefactor as a function of the average tip surface separation. The solid line is a power law fit to the data of the form Az^d, giving d=-2.6 here.

differences in the sample's surface picked up on by AFM drift. Vertical and lateral drift of the AFM could add error to this measurement in addition to the fitting error displayed. Table 4.1 summarises the the results of the fitting from a), where the constant prefactor $= \frac{f_0}{4k}\frac{\partial^2 C}{\partial z^2}$. The value of V_{Surf} does change over the range of lift heights measured, the dominant change is that of the prefactor.

Figure 4.8 shows the dependence of the prefactor on the average tip surface distance. The fitting shown is that of a power law, where the prefactor scales with $z^{-2.6}$, however with only five data points a large variation is somewhat expected. Since the other parameters in the prefactor are constant, the rate of change of the gradient of capacitance changes with this dependence on lift height.

Figure 4.9 shows how the frequency shift varies as a function of the tip surface distance, measured for an applied bias of 5 V. Δf shows a $1/z^2$ relationship, this dependence should be the same as that shown in Figure 4.8 as the second differential of capacitance has the only dependence on lift height. In reality, this fitting is far more accurate. The second derivative of the tip surface capacitance is expected to follow a power law of the form z^d where d depends on the tip geometry. d=2 is

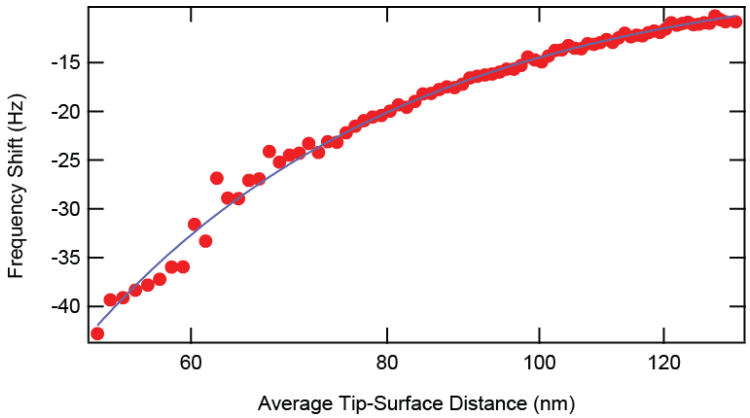

Figure 4.9: The frequency shift measured for a 5 V applied tip bias as a function of the average tip surface distance. The solid line is a power law fit of the form Az^d, here d=-2.

consistent with a model of a sphere, expected for tip surface distances less than the tip radius [242]. In this case, this is not quite true, however the oscillation amplitude is relatively large compared to the average tip surface separation, i.e the amplitude of oscillation is around 37 nm during this experiment; so the oscillation does bring the tip into this regime for smaller tip surface separations.

When the sample is illuminated, a second frequency shift (δf_0) occurs due to the SPV. The total frequency shift can be described as

$$\Delta f_0 + \delta f_0 = \frac{f_0}{4k}\frac{\partial^2 C}{\partial z^2}\left(V_{tip} - V_{surf} + \mathrm{SPV}\right)^2 . \tag{4.4}$$

To a first approximation, assuming both that the prefactor is constant and that $V_{tip} - V_{surf} >>$ SPV, the frequency shift due to the light can be separated out by subtracting by Δf_0. Leaving the frequency shift due to the light alone as

$$\delta f_0 = \frac{f_0}{4k}\frac{\partial^2 C}{\partial z^2}\left(2(V_{tip} - V_{surf})\mathrm{SPV} + \mathrm{SPV}^2\right) . \tag{4.5}$$

Solving this quadratic, yields values of SPV. This allows the comparison of SPV with τ_c and light intensity. Of course V_{Surf} and the capacitive prefactor change with tip height and between samples, so in order to get accurate measurements this calibration (as in Figure 4.7a)) described must be measured prior to, or during the course of each experiment. This calibration in essence determines the amount of photo-generated charge is produced by the illumination of the sample by measuring its electrostatic field with the AFM.

4.2.5 Light Intensity

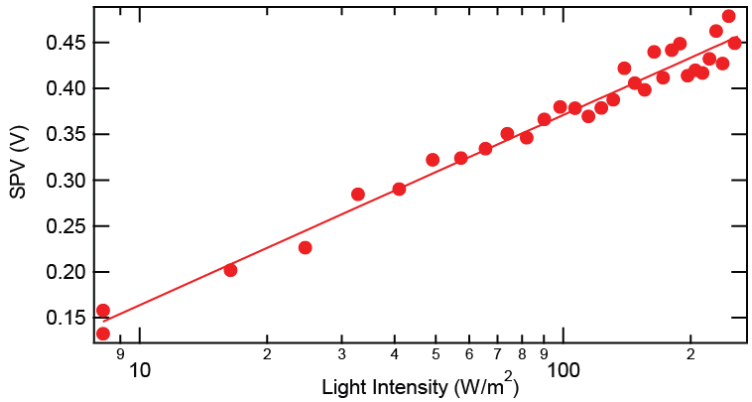

Figure 4.10: The behaviour of the SPV with light intensity extracted from Tr-EFM on P3HT:PCBM at 50°C, with a 5 V applied bias. The solid line shows a logarithmic fit of the SPV.

Figure 4.10 shows the average of two calculated SPV values as a function of light intensity at 50°C. The light intensity here was varied starting at 250 W/m^2 and decreasing to 0, before increasing back to 250 W/m^2. The SPV follows a logarithmic dependence on light intensity. This is as expected since SPV links very closely to V_{OC} [86], further discussed in 1.2.4.3. In this chapter, since the V_{OC} was not measured by an external method, the SPV will be used as an indication of the trends in V_{OC}.

The relationship for V_{OC} with light intensity can be found by solving the ideal diode equation. V_{OC} is described as

$$V_{OC} \cong \frac{nk_bT}{e} ln\left(\frac{J_{sc}}{J_0}\right) \tag{4.6}$$

where n is the ideality factor, k_b is Boltzmann's constant, T is the temperature of measurement, J_0 is the reverse bias saturation current and J_{SC} is the short circuit current density. J_{SC} can be expressed as $J_{SC} = bI$ where b is a proportionality factor and I is the illumination intensity in W/m^2, allowing V_{OC} to be written as

$$V_{OC} \cong \frac{nk_bT}{e} lnI + \frac{nKT}{e} ln\left(\frac{b}{J_0}\right). \tag{4.7}$$

Thus V_{OC} is predicted to depend on the natural log of light intensity; that this trend is seen for SPV strengthens the case that SPV is equivalent to V_{OC}.

As shown in Figure 4.11a) τ_c does not seem to have a significant dependence

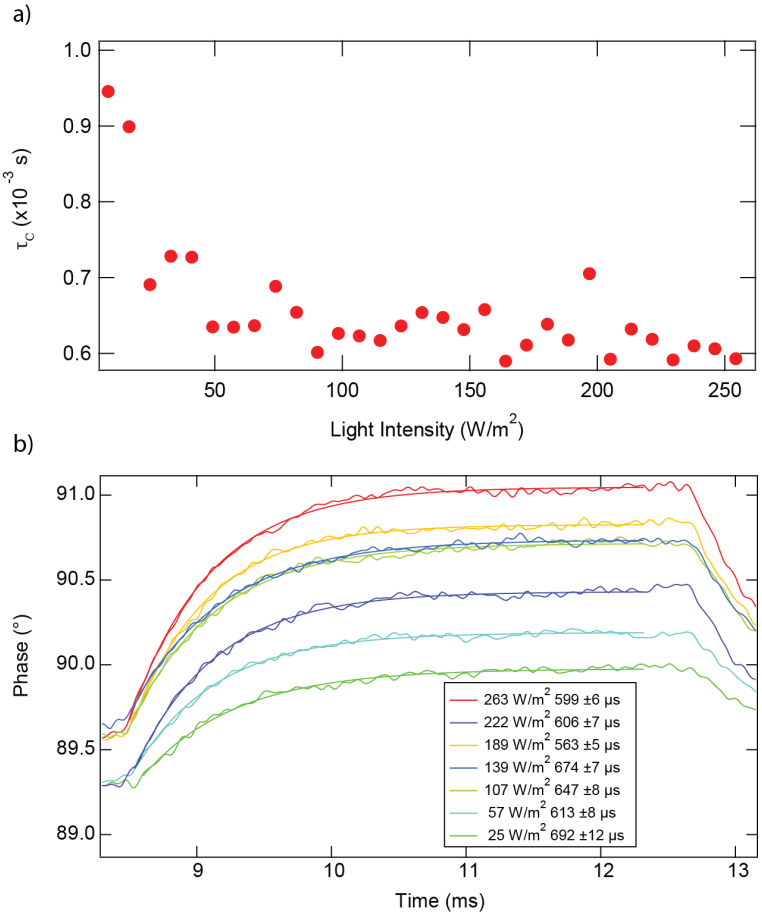

Figure 4.11: a) Tr-EFM measurement of τ_c as a function of light intensity at 50°C on P3HT:PCBM, with a 5 V applied bias. b) A selection of corresponding response curves with their exponential fittings and representative τ_c values.

on light intensity for this sample, except at low light intensities <50 W/m^2. Coffey and Ginger postulated that the rate limiting step in charging the tip-surface capacitor is the absorption of enough photons to create the negating charge [170]. This may be true for very low light levels as there is a significant increase in τ_c below 50 W/m^2, but above 50 W/m^2 τ_c is constant. This was not the case in Coffey's work, which showed a linear dependence on charging rate with light intensity, however their work focussed on a different system F8BT:PFB compared to P3HT:PCBM here.

This indicates that in P3HT:PCBM, there is a second process which dominates above 50 W/m^2. This second process is unlikely to be exciton diffusion, or charge carrier transport, as these happen on much faster timescales [243]. One pos-

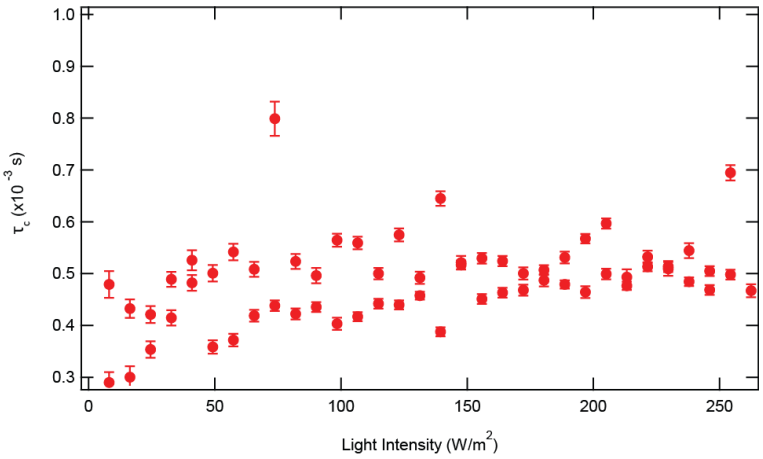

Figure 4.12: τ_c as a function of applied illumination intensity extracted from a Tr-EFM experiment on P3HT:PCBM at 50°C with an applied bias of 10 V. Lines are linear fits to the data.

sibility is, this response is caused by the de-trapping of charge carriers causing a longer timescale charging to be measured [244].

Figure 4.11b) shows a selection of representative responses in the phase domain, at different light intensities. Though there is an order of magnitude difference in the light intensity across the plot, there is no significant difference in τ_c. The curve shapes are all similar with consistent fit quality.

Figure 4.12 shows how τ_c changes with illumination intensity when measured with an applied bias of 10 V on a different sample of P3HT:PCBM. Here, there appears to be no dependence of τ_c on the applied illumination even at low light levels. Although some deviation is expected between samples, the reduction in this behaviour is significant. τ_c is also reduced when measuring at 10 V, though this is likely to be sample variation rather than a change in behaviour. This can be seen in Figure 4.13 which shows the extracted values of τ_c for the 40 nm lift height curve shown previously in Figure 4.7.

At positive biases 3 V $\leq$ V $\leq$ 10 V, τ_c is nearly constant with a slight positive gradient, higher biases yielding slower charging rate. The same is true of negative biases -10 V $\leq$ V $\leq$ -3 V, τ_c increasing as the bias becomes more positive. This has a much higher gradient $3.0 \pm 0.4 \times 10^{-5}$ s/V compared to $6 \pm 1 \times 10^{-6}$ s/V. This could indicate higher density of traps for holes than electrons. τ_c is also much longer in the negative bias regime.

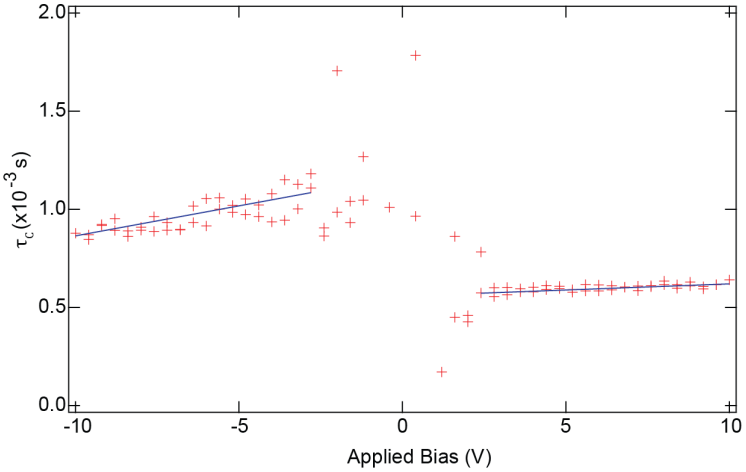

Figure 4.13: τ_c as a function of applied bias extracted from a Tr-EFM experiment on P3HT:PCBM at 50°C at an illumination intensity of ∼250 W/m^2.

4.2.6 Mapping

Like the FVBS technique discussed in the previous chapter; Tr-EFM can be performed in a point-by-point manner. Here, instead of sweeping the light intensity across a range of values it is kept fixed, and the AFM takes a Tr-EFM measurement at one point before moving on to the next. Figure 4.14 a) and b) show the results of plotting the extracted values of τ_c and SPV in a spatially resolved grid. Both τ_c and the SPV have areas of differing behaviour, however c) shows that these areas do not correlate. This is not too surprising, as although the SPV should correlate with J_{SC}, it is unclear how or if, τ_c is correlated to J_{SC}.

Mapping in this manner has the potential to highlight areas where the SPV is increased and/or the charging time shows deviations. This can highlight areas that have higher (or lower) efficiencies, coupled with topography this could increase our understanding of these devices [172]. Each map of 64 points takes around 15 minutes and scales linearly with the total number of points, thus quadratically with the resolution. This poses a significant limit on the practical achievable resolution of this technique. Time per point can be improved by sacrificing the statistical quality of the data at each point by reducing the number of repeat measurements used for averaging. If τ_d was measured, carrier lifetime could be mapped [238], which may highlight areas of increased recombination.

It can also be noted that the SPV measured as part of the map is significantly higher than its counterpart in Figure 4.10, measuring 0.737 ± 0.008 V compared to

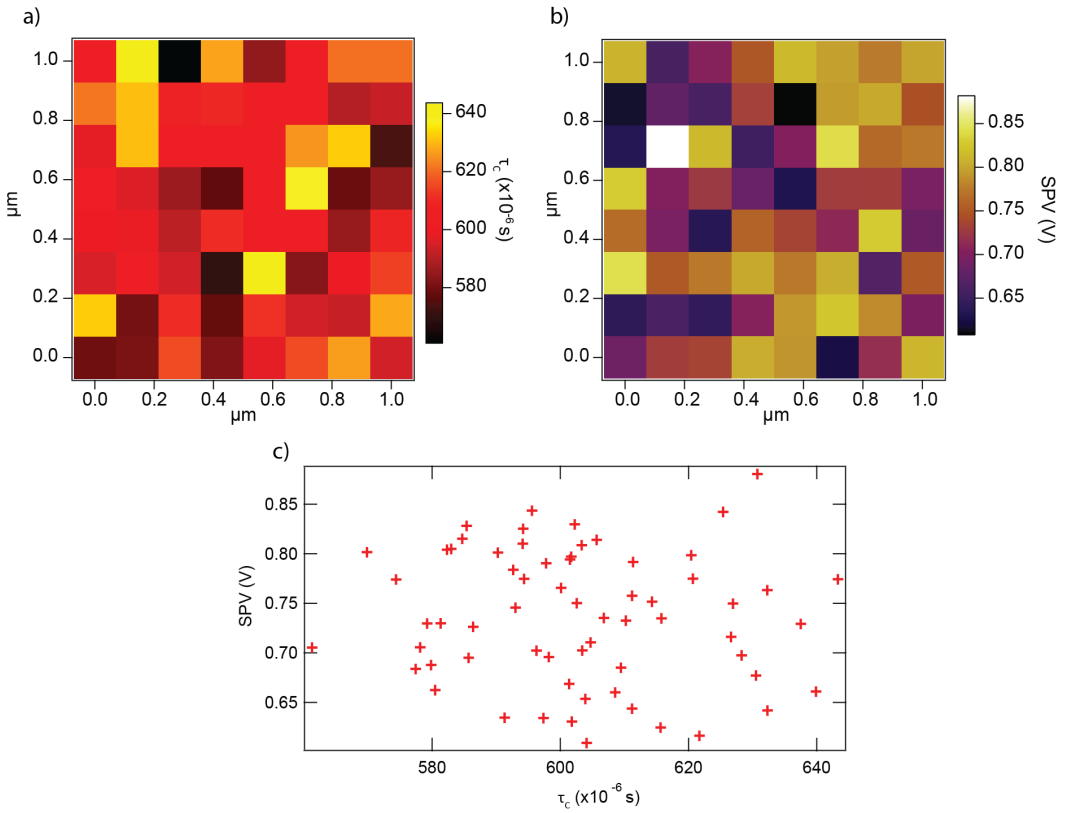

Figure 4.14: Point by point maps of a) τ_c and b) SPV, gathered across a 1 μm^2 area at 50°C, with a 5 V tip bias and light intensity of 250 W/m^2 c) Shows the spread of the data points and the absence of correlation between τ_c and SPV.

0.456 ± 0.002 V. This effect is most likely to be a symptom of the assumption that the second differential of capacitance is not dependent on light intensity. Coffey's work shows that $\frac{\partial^2 C}{\partial z^2}$ increases with light intensity in the bias dependent frequency response of the cantilever [170], whereas here this is evident in the illumination intensity dependence of the SPV.

Figure 4.15 shows the SPV dependence on light intensity for the same sample but this time measured at 90°C. This particular measurement shows a clear deviation towards higher SPV values at high illumination intensities, enough that the fitting has slightly skewed, artificially raising the gradient of the line. It appears that $\frac{\partial^2 C}{\partial z^2}$ has some dependence on the illumination intensity though it is not clear why this is the case. To first approximation the value of SPV returned is accurate up to around 100 W/m^2, above this value the SPV is overestimated. As a result of this the SPV in Figure 4.14 may be overestimated, however trends between points should be real.

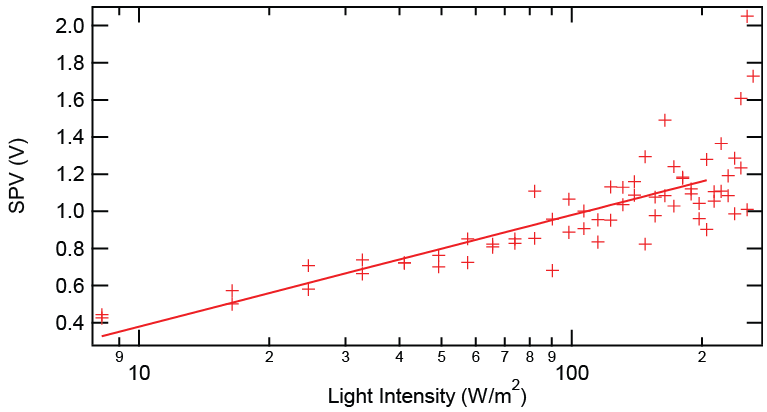

Figure 4.15: Tr-EFM data showing SPV dependence on illumination intensity at 90°C, on P3HT:PCBM with an applied tip bias of 5V.

More quantitative maps could be gathered using a lower light intensity.

4.2.7 Temperature Dependence of τ_c

Like the FVBS measurements, Tr-EFM can also be preformed at a range of temperatures using the PolyHeater and the top optical path of the MFP3D. Figure 4.16(a) and (b) show the dependence of τ_c on both light intensity and temperature while the sample is heated in increments of 10°C. A 20 minute delay at each temperature was allowed before measurement to ensure thermal equilibrium is reached before the measurement proceeds. The measurement is then carried out. In (4.16a) the colour scale corresponds to the temperature of measurement, with redder colours being higher temperatures. Here, there appear to be no general trends of τ_c and temperature, the original dependence of τ_c on illumination intensity seems to be maintained throughout the experiment. Notable deviations from this occur at 130°C and 140°C. These two points show significantly increased values of τ_c above 175 and 100 W/m^2 respectively, although the cause of this is not yet clear.

Figure 4.16 (b) shows the same data this time plotted with the temperature on the x axis and with the light intensity on the colour scale, redder colours represent higher intensities. Plotting in this manner shows a small but tangible increase in τ_c towards higher temperatures. There is also a slight increase at 100°C occurring before the majority of the increase in τ_c. The deviation from the standard behaviour with light intensity at 130°C and 140°C can also be seen in this plot, with redder points occurring at higher values of τ_c at these two points. This is most prominent for the 130°C point.

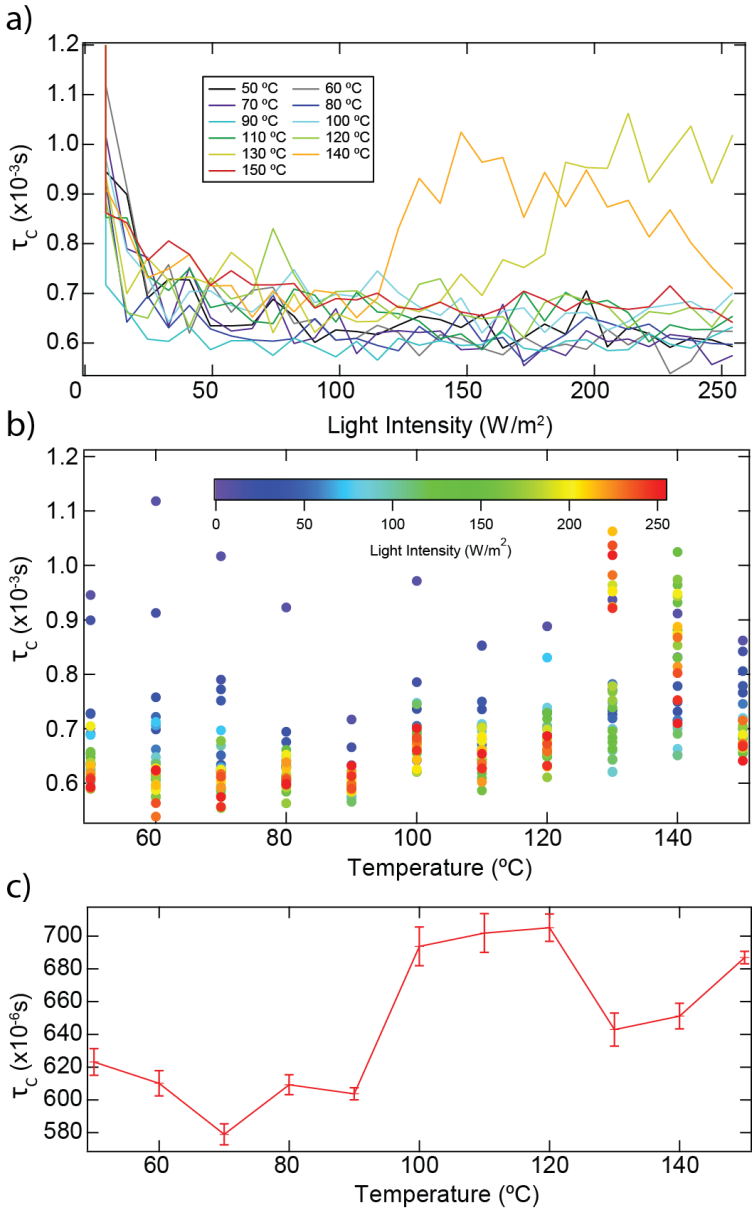

Figure 4.16: Temperature dependent Tr-EFM data of τ_c on P3HT:PCBM on heating from 50°C with a tip bias of 5 V; a) as a function of light intensity across a range of temperatures, b) as a function of temperature across a range of light intensities. c) Behaviour of τ_c at 100 W/m^2 across the range of temperatures, showing representative fitting errors on τ_c.

Figure 4.16 (c) shows the temperature dependent τ_c values measured at 100 W/m^2. The typical deviation of these values can also be seen, represented as the standard deviation from the average of the 10 fits at each point. Here the rise in τ_c above 90°C is clear, though the behaviour at 100 W/m^2 does not match the behaviour as a whole. It is worth noting that there is a significant amount of noise in the measurements of τ_c, so the trends from this one point are unlikely to be accurate.

4.2.8 Temperature Dependence of SPV

Figure 4.17a) and b) show the dependence of the SPV on light intensity and temperature, for clarity (a) shows only the fit of the SPV to the base ten logarithm of light intensity. The exception to this is the data at 90°C, which shows the representative spread. The logarithmic dependence on illumination intensity holds across the temperature range, however both the gradient and intercept change between temperatures.

The data at 90°C has an anomalously high gradient, possibly indicating a physical change in the sample. Excluding the 90°C dataset the highest values of SPV occur at the two highest temperatures 140°C and 150°C, suggesting that the SPV increases with temperature.

Comparing Figure 4.17 b) with Figure 4.16 b) shows some similarities in the behaviour of τ_c and SPV with temperature. Both τ_c and SPV increase at higher temperatures, both also show unusual behaviour at 90°C. This is less pronounced in the τ_c case, however there is a marked decrease in the spread of τ_c with illumination intensity, whilst the opposite is true for the SPV. It is difficult to speculate on what might cause this. The rise in SPV at high temperatures might be explained by a decrease in bi-molecular recombination, effectively increasing the band gap of the system [238].

In the classical p-n junction model described by equation 4.7 the gradient of the logarithmic fit of V_{OC} to light intensity should scale with the intercept, as both depend on nKT/q. Figure 4.18 shows the gradient and intercept of the fittings in Figure 4.17a), scaled to the natural logarithm. Notably, the gradient does not scale with the intercept, the two parameters seem unrelated. Also the ideality factor (shown in the inset) is calculated; the extracted values are well outside of expected bounds, although high levels of recombination have been shown to increase the ideality factor [245], .

It has however been shown that the p-n junction model does not apply to polymer fullerene systems, and a second model more accurately predicts their be-

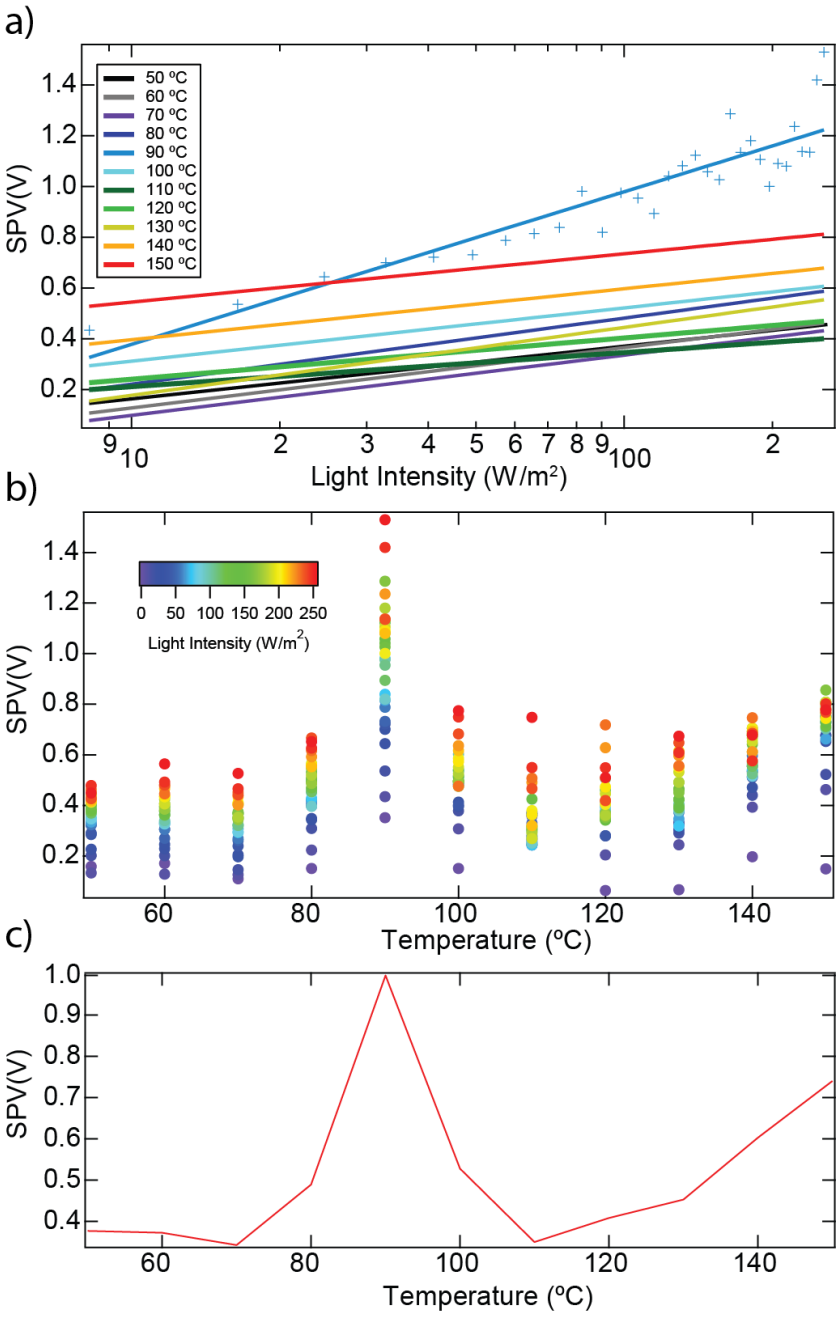

Figure 4.17: Temperature dependent Tr-EFM data from P3HT:PCBM on heating from 50°C. a) SPV as a function of light intensity across a range of temperatures. The representative spread of data is seen on the 90°C dataset. b) SPV as a function of temperature across a range of light intensities. c) SPV behaviour at 100 W/m^2 across the range of temperatures.

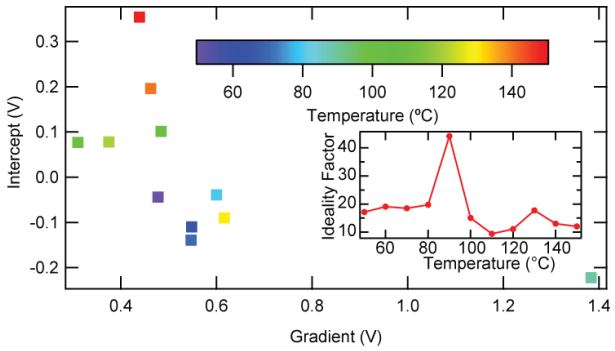

Figure 4.18: The calculated gradient and intercept of the logarithmic fits of SPV as a function of light intensity for the temperature dependent P3HT:PCBM measurements at 5 V applied tip bias. The inset shows the calculated ideality factor for the same fittings.

haviour. The V_{OC} in this model is described as

$$V_{OC} = \frac{E_{gap}}{q} - \frac{k_b T}{q} ln\left(\frac{(1-P)\,\nu N_c^2}{PG}\right) \tag{4.8}$$

where E_{gap} is the band gap of the bulk heterojunction, P is the dissociation probability of a bound electron hole pair into free charge carriers, G is the generation rate of bound electron-hole pairs, ν is the associated Langevin recombination constant and N_c is the effective density of states [246]. This model more accurately describes OPV systems by including the drift and diffusion of charge carriers, bimolecular recombination, and temperature dependent generation of free carriers. Unfortunately quantitative analysis using this equation is complicated as E_{gap} is not well defined in these heterojunctions.

4.2.9 Temperature Dependence of SPV and τ_c when Cooled

Figure 4.19 shows the behaviour of the SPV and τ_c while the sample is cooled from 150°C to 80°C. This is again performed in decrements of 10°C, with 30 minute delays between each temperature to allow for thermal equilibrium. The SPV shows similar behaviour to the heating, with a decrease evident between 140°C and 120°C. In the heating cycle there was a spike in the behaviour at 90°C, this is not evident here, however there is a similar spike at 110°C.

The behaviour of τ_c looks very similar when cooling compared to heating. The highest spread in points is at 130°C. Below 120°C τ_c remains somewhat constant. The behaviour with illumination intensity does differ below 120°C, with the dependence on illumination intensity becoming markedly stronger; brighter intensi-

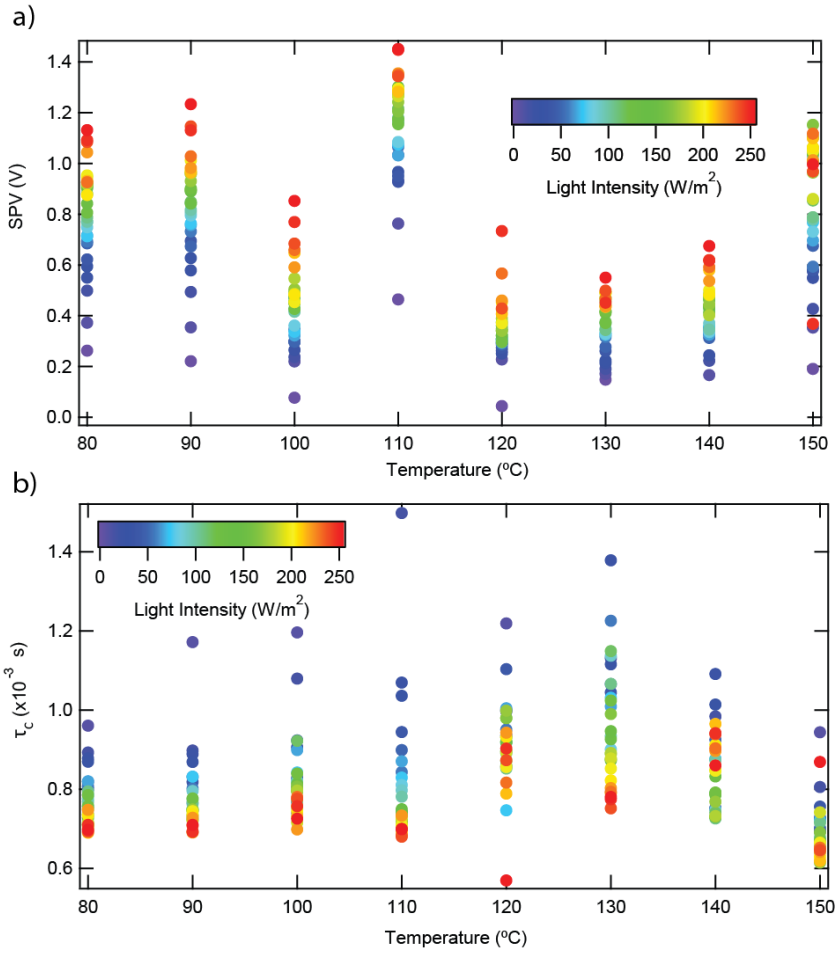

Figure 4.19: a) SPV and b) τ_c of P3HT:PCBM as a function of temperature at a range of light intensities, on cooling from 150°C to 80°C.

ties have lower τ_c values (redder points are lower). τ_c also shows an overall increase compared to the heating data. For example the data at 80°C when heated, had an average τ_c of 6.2 $\times$ 10^{-4} s compared to an average τ_c of 7.6 $\times$ 10^{-4} s. It is likely that this increase in τ_c is a result of degradation, increasing the number of traps and thus increasing the time for detrapping to occur.

Comparing the SPV before and after annealing for the 80°C points shows a significant increase in the magnitude of SPV at higher illumination intensities, with the SPV after annealing at 250 W/m^2 being double that of before. The reason for this is as yet unknown, however Bagienski et al. observed a similar trend [90].

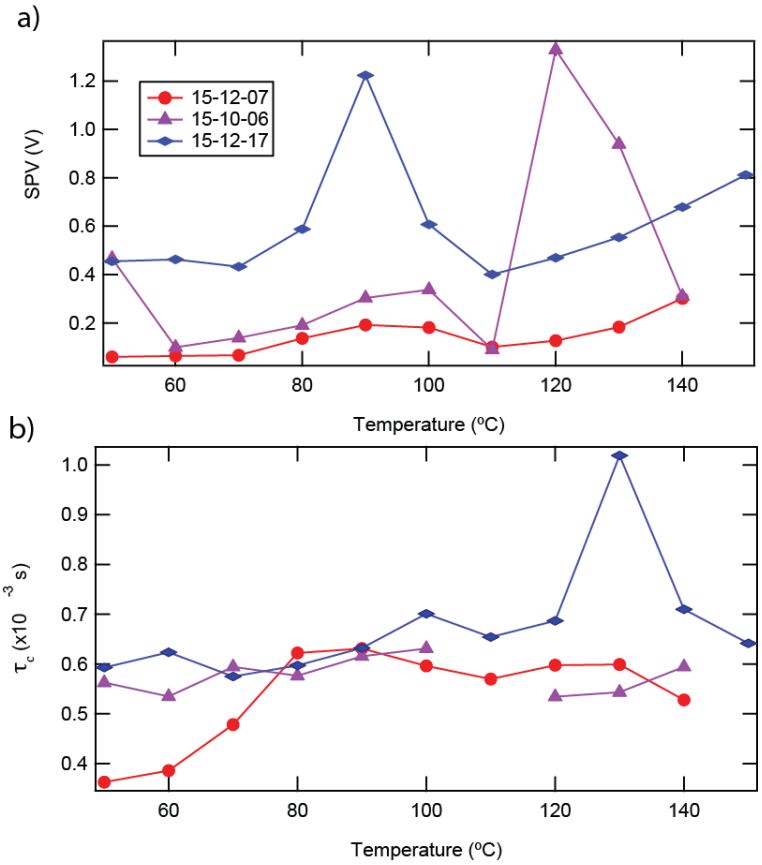

Figure 4.20: a) SPV of P3HT:PCBM at 250 W/m^2 as a function of temperature across three Tr-EFM datasets. b) The corresponding τ_c from the same datasets.

4.2.10 Reliability

Figure 4.20 (a) shows the heating data for SPV for three separate experiments on three samples. Though there are significant deviations across the range of the SPV there are also qualitative trends that can be observed. For instance, there appear to be two effects causing rises in SPV with temperature, the first occurring up to 100°C, and the second between 110°C and 150°C. This result is similar to that observed by Kim et al., who saw an increase in conformational order of nanowire P3HT at low temperature annealing followed by a subsequent decrease in local order but an overall increase in order when annealed to higher temperatures [247].

Clearly the three experiments do not agree on the magnitude of the SPV, and though there is expected to be deviations between samples tested, it is unlikely that such a large inconsistency is due to the samples themselves. Since this data was

measured at 250 W/m^2 it is likely that the SPV is overestimated, due to deviations in the capacitive prefactor at these high light intensities, though the magnitude of these deviations seems to vary between experiments and temperatures. The causes and calibrations of these deviations would be an interesting topic to consider investigating.

Figure 4.20 (b) shows the variation of τ_c across the same three experiments. It should be noted that not every dataset could be fitted adequately, hence the missing points at 150°C and 110°C, however τ_c shows little deviation across the experiments. This indicates that this method reliably measures the time scale at which charges relocate within the sample, whether this is due to charge de-trapping or some other effect is a subject for further investigation.

4.2.11 Tr-EFM of PTB7:PC$_{70}$BM

In order to test the applicability of this technique to more modern high performance BHJs, PTB7:PC$_{70}$BM devices were fabricated by the Hatton group. Like the P3HT:PCBM BHJs, these too were spin coated directly onto glass ITO substrates. Recent work on this BHJ system indicates that the photocurrents and V_{OC} values of this system should be higher than P3HT:PCBM, 0.58 V to 0.72 V and 8.03 mA/cm^2 to 14.28 mA/cm^2 respectively for P3HT:PCBM and PTB7:PC$_{70}$BM [248].

4.2.12 Calibration

Figure 4.21 shows the calibration curves on this PTB7:PC$_{70}$BM sample in order to achieve quantitative assessment of SPV. (a) shows the frequency shift as a function of the average tip-surface distance measured at the 10 V used for measurement in this case. Here, the change in frequency of the cantilever scales as 1/z, rather than the 1/z^2 displayed in Figure 4.9. This dependence on average tip-surface distance implies a shift to a line model of tip surface interaction which would be appropriate for tip-surface distances larger than the tip radius, but smaller than the tip height. Increasing the applied voltage causes a change in which model conditions are appropriate to describe the tip-surface interaction, though the reason for this is unknown.

Figure 4.21 (b) may elucidate this, as like Figure 4.7 (a) the frequency response of the cantilever deviates from the predicted V^2 relationship above 5 V. From the fitting shown of Equation 4.3, V_{surf} was calculated to be -0.5 V at 59 nm average tip-sample separation. The following measurements were taken at an average tip-surface separation of 70 nm, so using Equation 4.3 and the fitting of

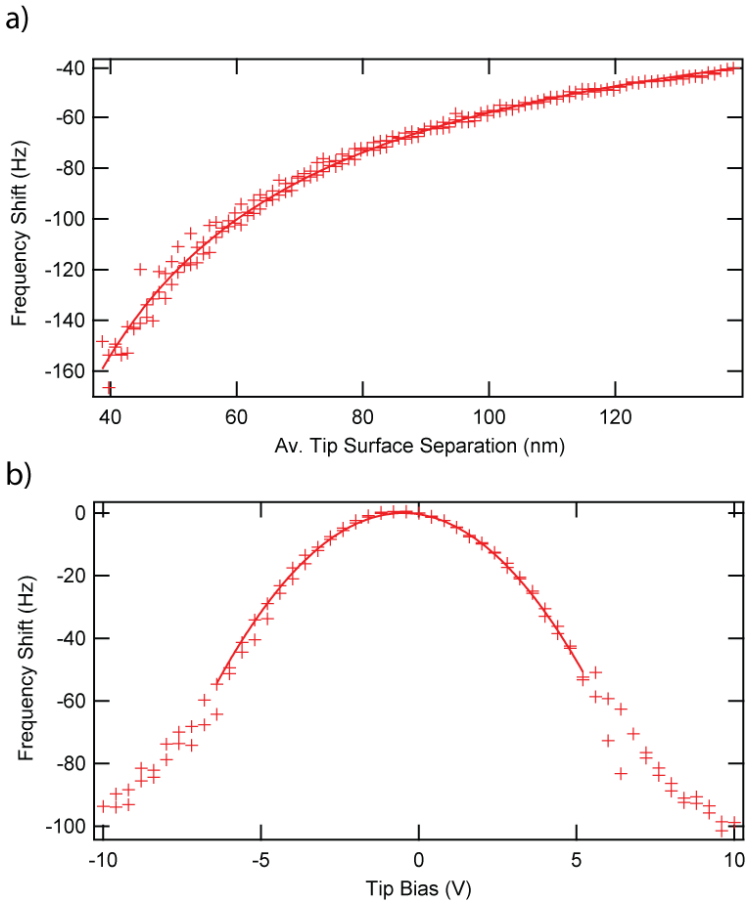

Figure 4.21: Calibration for Tr-EFM showing the frequency shift as a function of a) average tip surface separation at 10 V applied bias and b) applied bias with an average tip sample separation of 59 nm on a PTB7:$PC_{70}BM$ sample. Solid lines are fittings of z^d and Equation 4.3 respectively, where d =-1.

Figure 4.21 (a) the capacitive prefactor can be estimated to be -0.78 Hz/V, though this is unlikely to be accurate as the measurements were taken at 10 V. Using this calibration temperature dependent measurements of τ_c and SPV were performed.

4.2.13 Temperature Dependence of PTB7:$PC_{70}BM$

Figure 4.22 a) shows the measured τ_c as a function of light intensity and temperature for a sample of PTB7:$PC_{70}BM$. τ_c shows a significant increase with temperature from 50°C to 110°C, before decreasing from 110°C to 130°C. Though Tr-EFM cannot be measuring the charge separation, which has been reported to be 1.5 ps [106, 249], it is likely that τ_c is a factor related to the efficiency of the devices, as the efficiency of

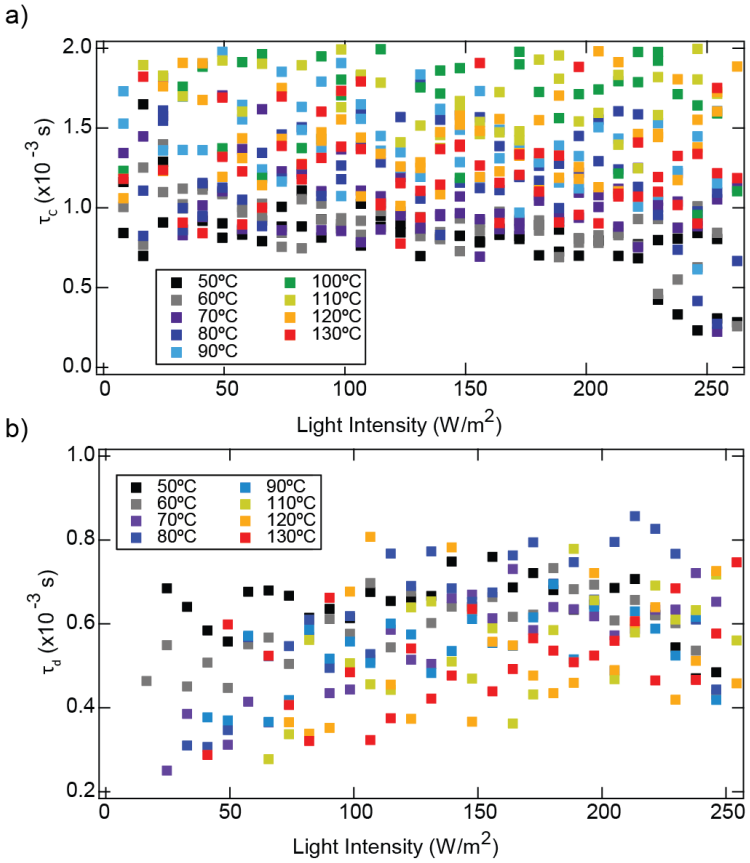

Figure 4.22: Temperature dependence of measured a) τ_c and b) τ_d for PTB7:$PC_{70}BM$, from 50°C to 130°C measured with an applied bias of 10 V and an average tip surface separation of 70 nm.

PTB1:$PC_{70}BM$ devices show a decreased efficiency when annealed due to a decrease in the interfacial area between donor and acceptor. This negatively impacts the separation and collection efficiencies of charges and decreases the free charge carrier density [250]. However, annealing also increases the pi-pi stacking order which may account for the high temperature decrease in τ_c measured.

Like in the case of P3HT:PCBM, τ_c shows little dependence on light intensity, however unlike P3HT:PCBM the exceptions to this do not occur at low illumination intensities, but instead high intensities at low temperatures show a marked decrease in τ_c. The cause of this is worth further speculation. Also the average values of τ_c are much greater in PTB7:$PC_{70}BM$ than in P3HT:PCBM which is interesting for a BHJ that is expected to be much faster than the prototypical P3HT:PCBM blend [106], this is again another aspect requiring further thought.

Figure 4.22 b) shows the measured τ_d for this same data set. τ_d shows little

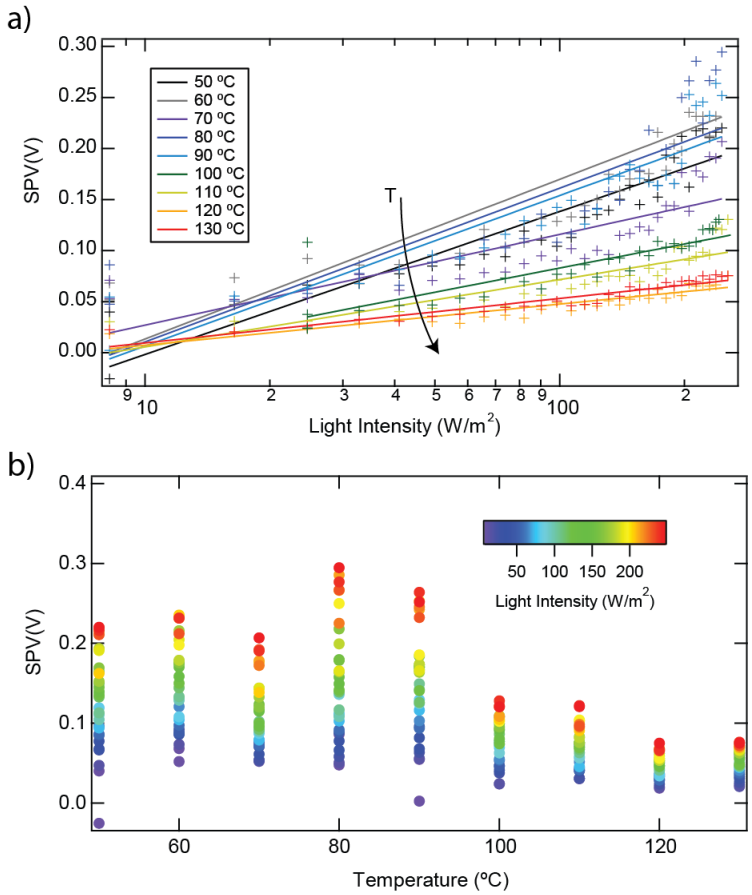

Figure 4.23: Temperature dependence of measured SPV with respect to a) illumination intensity and b) temperature for PTB7:$PC_{70}BM$, from 50°C to 130°C measured with an applied bias of 10 V and an average tip surface separation of 70 nm.

dependence on temperature though it does show a slight dependence on light intensity. At higher temperatures τ_d appears to increase slightly with higher illumination intensities. This would suggest that carrier lifetime increases with illumination intensity. This is contradictory to TPV studies of this system which show decreased carrier lifetimes for increased carrier densities [251], the application of more illumination should result in more carriers, however TPV uses small perturbations of light intensity which may explain this difference.

Figure 4.23 shows the behaviour of SPV with respect to both temperature and illumination intensity. (a) shows the illumination intensity dependence with logarithmic fits of the SPV as a function of light intensity. Here, it is clear that there is a strong dependence of SPV on light intensity, however below 100°C, this depen-

dence is not strictly logarithmic. There is a strong curvature towards higher values of SPV at high illumination intensities. This could be explained by mis-calibration of the frequency response, however if this was the case the error should be evident on all the datasets rather than just the low temperature data. It is much more likely that this is a property of the material itself. Light assisted dielectric response has shown PTB2 and PTB4 to be more capacitive under higher illuminations than P3HT:PCBM, this may lead to the increased SPV shown here [252].

The values of SPV measured here are also much lower than those measured for P3HT:PCBM. Since SPV is directly related, if not the equivalent of V_{OC}, this is somewhat surprising. As already discussed, the V_{OC} of PTB7:PC_{70}BM blends are reported to be higher than that of P3HT:PCBM. Indeed, similar studies have reported V_{OC}s of over 0.6 V at 100 W/m^2 [107]. The difference in magnitude between Ebenhoch's work and this study is likely to be the effect of imperfect calibration coupled with the high applied tip bias of measurement. Ebenhoch's study also shows the decrease of V_{OC} with temperature that is demonstrated here, albeit at lower temperatures.

Figure 4.23 (b) supports the conclusion that SPV decreases with increasing temperature. There is also a clear reduction in the gradient of the SPV with respect to light intensity, as shown by the closely grouped points at high temperatures. SPVs recorded at 80 and 90°C show increased spreads. Unfortunately no viable results for the cooling of this sample were obtained.

4.2.14 Conclusions

Here, Tr-EFM has been used to investigate the SPV and τ_c behaviour of P3HT:PCBM and PTB7:PC_{70}BM BHJ systems. It has been shown that careful calibration of the frequency shift of the cantilever response as a function of applied bias and average tip surface separation, can allow quantitative determination of SPV from Tr-EFM. Equally, the fitting of a simple exponential relationship to the charging and discharging curves resulting from the application of illumination can yield a time response that may correlate to the performance of these devices.

It is unclear what this time response measures as the time scales are too long to be charge generation or carrier transport through the heterojunction. P3HT:PCBM shows little dependence on temperature of τ_c, only marginally rising at high temperatures, however PTB7:PC_{70}BM shows a pronounced increase in τ_c with temperature. This is a good indication that Tr-EFM is measuring a system property, as opposed to solely an effect of tip-surface capacitance. The ability to measure τ_d has also been demonstrated, though it is also unclear as to what this is alluding to physi-

cally, as again the timescales are around 1000 times slower than the corresponding TPV measurements of carrier lifetime.

What is perhaps most promising of this technique is the ability to measure SPV simultaneously to τ_c and τ_d. For P3HT:PCBM the SPV showed a clear logarithmic dependence on light intensity, allowing comparison to be made to V_{OC}. Further investigation of this could yield more in depth analysis of the behaviour of the band gap and recombination in these systems. All of these parameters can also be mapped simultaneously across an area of surface, potentially highlighting areas of increased or decreased performance.

The behaviour of SPV was also measured on heating from 50°C to 150°C, showing two separate increases of SPV with temperature, the first from 70°C to 90°C and the second from 110°C to 150°C. The SPV was also measured on cooling between 150°C and 80°C. An initial decrease with temperature is seen, matching the high temperature increase. At lower temperatures the SPV maintains a higher value than its initial, likely to be the result of annealing. For the PTB7:$PC_{70}BM$ system the SPV had a more complex dependence on light intensity. However, this had a very clear decrease of SPV with temperature in agreement with published studies. A summary of these results can be seen in Table 4.2

It is clear that more involved studies of this technique are needed to fully understand the mechanisms of τ_c and τ_d, however there is potential to yield valuable insight into the nanoscale performance of these devices. The temperature dependence of these values could provide clarity in the annealing behaviour of these, and similar, systems.

	P3HT:PCBM	PTB7:$PC_{70}BM$)
Light intensity on SPV	ln I	ln I
Temp. dependence of SPV (T rising)	Increasing	Decreasing
Temp. dependence of SPV (T cool)	No change	No data
Average τ_c (50°C)	630 μs	800 μs
Light intensity of τ_c	No dependence	No dependence
Temp. dependence of τ_c (T rising)	No change	Slight Increase

Table 4.2: A summary and comparison of temperature dependent Tr-EFM on P3HT:PCBM and PTB7:$PC_{70}BM$.

4.3 Intensity Modulated Kelvin Probe Force Microscopy

4.3.1 Introduction

Intensity modulated Kelvin probe force microscopy (IM-KPFM) is an extension of the more classical KPFM techniques and has been utilised by Takihara et al. [191], to measure the minority carrier lifetime around grain boundaries in polycrystalline silicon solar cells, finding that the carrier lifetime decreases in proximity to these boundaries as they act as recombination sites and/or leakage passes [191]. More recently Shao et al. [192], from the Ginger group, have used this technique to measure the change in local recombination rates as a result of buried interfaces in OPV materials [192].

In classical KPFM the cantilever is driven by an AC bias of the form $V_{AC}\sin(\omega t)$ with a DC bias offset V_{DC}. The force acting on the cantilever can be described by

$$F = \frac{1}{2}\frac{dC}{dz}V^2 \tag{4.9}$$

where $V = V_{DC} - V_{CPD} + V_{AC}\sin(\omega t)$. When expanded out, the force as a function of the applied bias has only one component at the applied frequency,

$$F_\omega = \frac{dC}{dz}\left[V_{DC} - V_{CPD}\right]V_{AC}\sin(\omega t) \tag{4.10}$$

where V_{CPD} is the contact potential difference between the tip and the surface, describing the difference between the workfunctions of the probe and surface material. When V_{DC}=V_{CPD} the amplitude of the deflection at the applied frequency is 0, allowing the contact potential difference to be measured across a sample with the appropriate null feedback loop. Usually V_{AC} is applied at the resonant frequency of the cantilever to increase sensitivity.

The addition of a constant light source has allowed this technique to be used to measure the SPV of polymer devices, showing efficient accumulation of charge carriers on the top electrode of a device [86]. In this case the force on the cantilever at the applied frequency can be described as

$$F_\omega = \frac{dC}{dz}\left[V_{DC} - V_{CPD} - SPV\right]V_{AC}\sin(\omega t) \tag{4.11}$$

therefore the difference between the bias applied to null the amplitude when the light is on compared to off, is equal to SPV.

Figure 4.24 shows a schematic of IM-KPFM where the AFM controller controls both the light timing and the bias feedback loop, whilst the modulation of

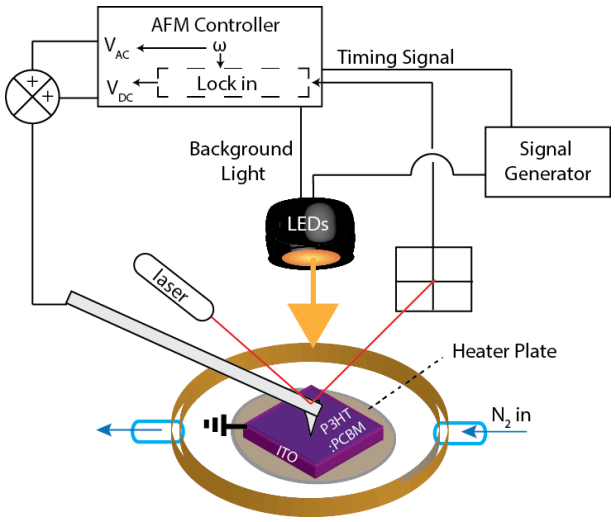

Figure 4.24: Schematic of the IM-KPFM experiment. Background light and feedback is controlled by the AFM, whilst the foreground light modulation is controlled by the signal generator, and timed by the AFM.

the light itself is done by the signal generator. The active layer of P3HT:PCBM is directly spin coated onto an ITO coated glass substrate.

Figure 4.25 shows an outline of the acquisition and analysis process in an IM-KPFM experiment. Briefly, the AFM is engaged in tapping mode, and withdrawn to a lift height of 50 nm from the surface as normally done in a force curve. Then the KPFM feedback is turned on: An AC bias is applied to the cantilever, along with the DC bias applied to minimize the amplitude signal. Before measurement can begin, the feedback gains of the potential are adjusted so that the signal to noise ratio is high and the feedback loop is stable. A single blue LED at 455 nm is set to a constant value as a background light during the experiment. This background blue light is used to control the background carrier concentration in the film, analogous to the work by Shao et al [192]. The remaining LEDs are then controlled by a square wave, alternating between the on and off states at a variable frequency. At a lower frequency there is an additional modulation, which results in the light being completely off for three periods during the measurement, as illustrated in figure 4.26. When a measurement has completed the tip withdraws to a distance of 500 nm from the sample.

Figure 4.26 shows the typical signals recorded for each single measurement in IM-KPFM. The DC bias and amplitude response of the cantilever are measured in response to the 64 kHz applied modulated illumination. The light is modulated

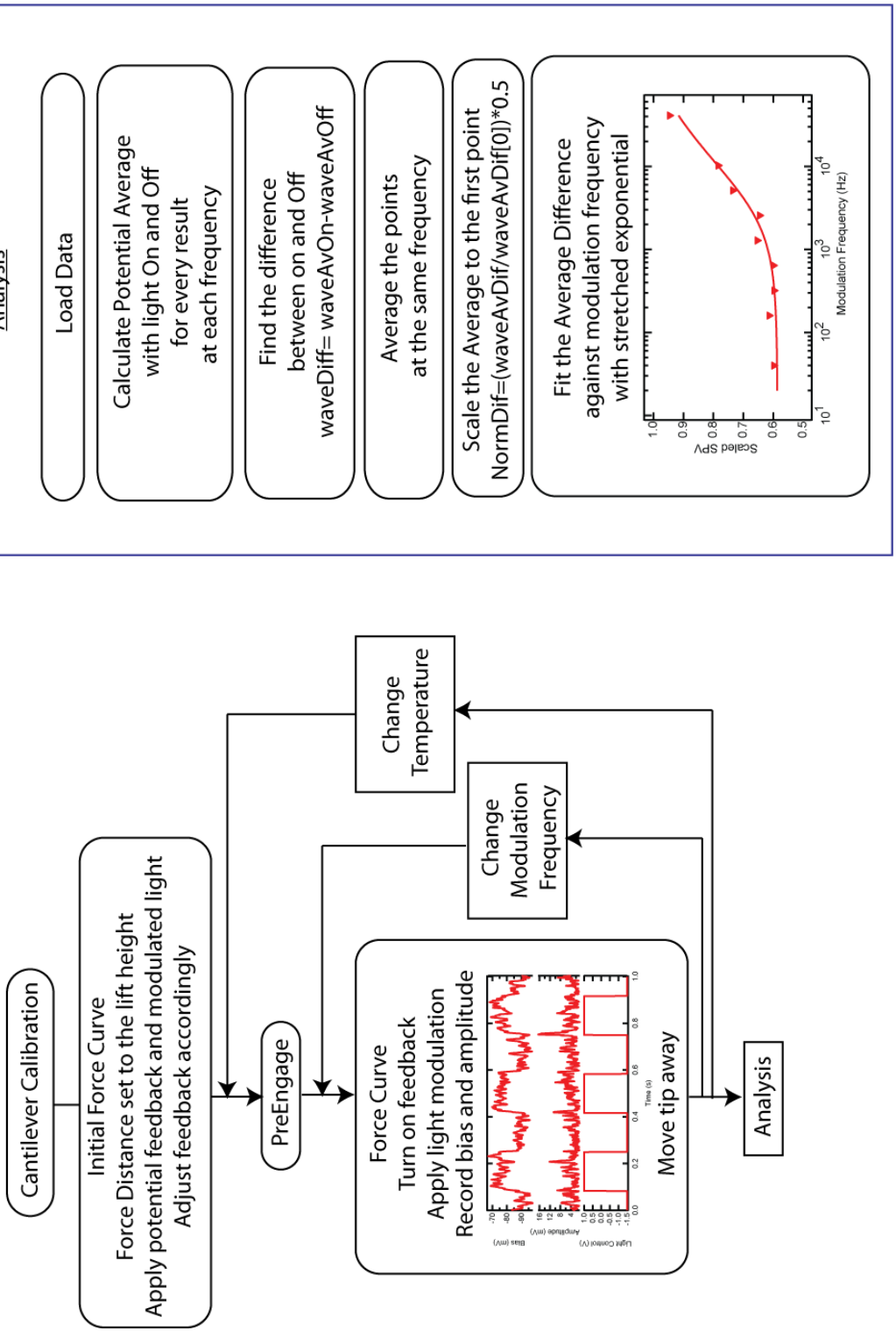

Figure 4.25: A flow diagram detailing the process of acquisition and analysis of IM-KPFM data.

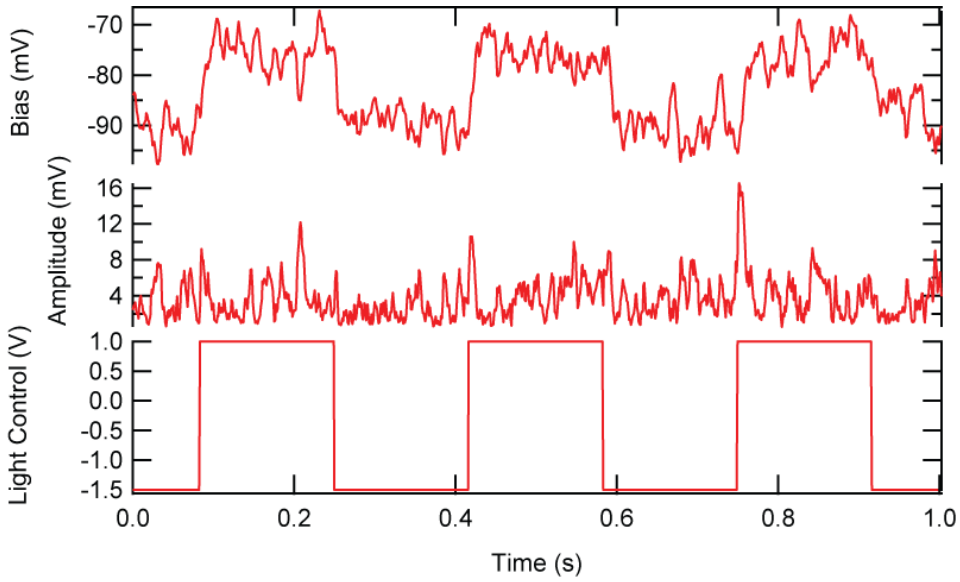

Figure 4.26: An example of the typical signals recorded in an IM-KPFM experiment, in this case on PTB7:$PC_{70}BM$ at 30°C with a modulated intensity of 182 W/m^2 and a background blue light intensity of 33 W/m^2. The illumination was modulated at 64 kHz and the cantilever had a lift height of 50 nm. The DC bias and amplitude response of the cantilever are shown. The timing of the modulated light is also shown.

at a set frequency by a signal generator; the "Light control" signal in Figure 4.26 is sent to the signal generator from the AFM controller, and turns the modulated light on (light control 1 V) and off (light control -1.5 V).

The KPFM feedback needs to be carefully controlled to reduce the error in the measurement. The error here is evident in the amplitude response of the cantilever, which should be minimised, though it is not uncommon to see spikes as the light modulation is turned on and off. Each measurement is repeated in the same location multiple times, before the modulation frequency is increased.

The analysis procedure uses the light control wave to determine when the modulation is on or off. These sections are averaged separately so that an average SPV is determined for the modulation on and off. A second average is then taken across the repeats at the same frequency. This average is then plotted against the frequency of modulation.

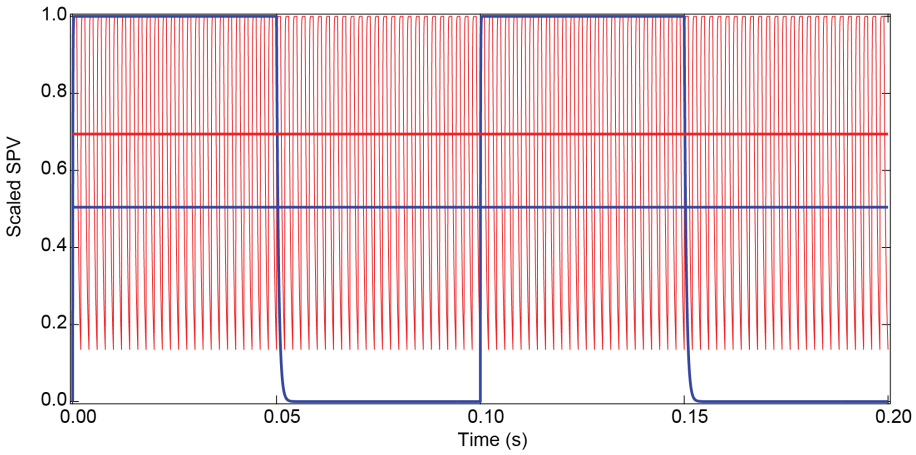

Figure 4.27: Simulated surface potential for a 10 Hz modulation (blue) and a 200 Hz modulation (red). Their averages over a second are shown by solid horizontal lines.

4.3.2 Simulating this Effect

When a photoactive material is illuminated, excitons are generated and, based on the internal field between the acceptor and donor, they split into charge carriers. In a full working device, charges would be separated by the respective electrodes providing an internal field. In this case only one electrode is present and earthed, hence there is no net current flow. Since there is no other internal field other than the LUMO/LUMO (and HOMO/HOMO) offset and any created by the ITO, the build up of charge would act to cancel these fields. The process of this can be modelled as two separate exponentials one describing the charging of the sample and the other the discharging [192, 191]. The charging of the sample can be modelled as

$$V_{sp} = 1 - (1 - V_c)e^{-t/\tau_c} \tag{4.12}$$

likewise the discharge is defined as

$$V_{sp} = V_d e^{-t/\tau_d} \tag{4.13}$$

where the V_{sp} is the normalised surface photovoltage measured, defined in the simulation to be between 0 and 1, 1 being at full charge and 0 being dark conditions; τ_c and τ_d are the characteristic lifetimes of charging and discharging respectively; and V_c and V_d are the starting values of the normalised SPV of the charging and discharging segments respectively.

Figure 4.27 shows a fast charge time of 0.5×10^{-4} s and a slow discharge

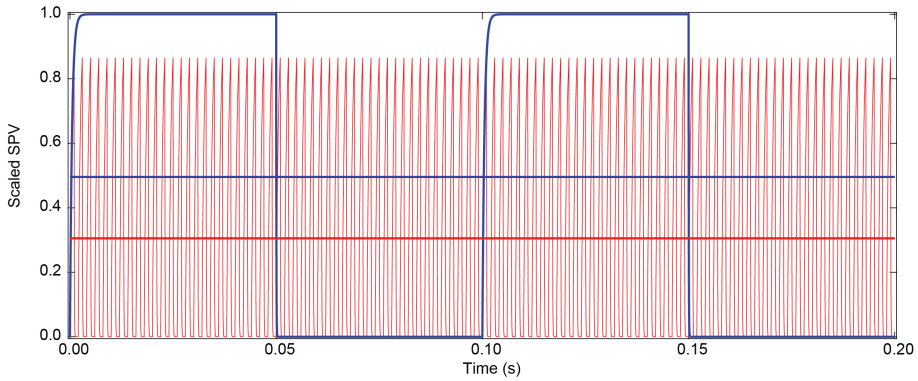

Figure 4.28: Simulated surface potential for a 10 Hz modulation (blue) and a 200 Hz modulation (red) with a slow charging rate and a fast discharge rate. Their averages over a second are shown by solid horizontal lines.

time of 0.5×10^{-3} s over a low frequency oscillation, and a second with the same values of τ_c and τ_d but at 50 times the frequency. Horizontal lines correspond to the average value across a full 1 second time window. For low frequencies the response approaches that of a square wave between 0 and the maximum generated voltage of the system, shown in blue. The average of this wave, assuming the maximum voltage produced by the system is equal to V_{max} and no back ground light, is equal to 0.5 V_{max}. In the higher frequency case the average value is increased. This is because the limited time to discharge, means the discharge is not completed whilst the charging is, hence the average increases.

Figure 4.28 shows the resulting potentials if the charging and discharging rates are swapped. Notice that when the modulation frequency increases the average value of the surface potential decreases. In this case, the sample does not fully charge as the frequency of modulation rises, resulting in the decrease of the average.

Figure 4.29 shows the behaviour of the time averaged surface potential across a range of frequencies. Following from the work of Shao et al. [192], it is possible to fit this with the equation

$$Av_{sp}(f) = \frac{1}{2} + \frac{\tau f \Gamma\left(\frac{1}{\beta}, \left(\frac{1}{2\tau f}\right)^{\beta}\right)}{\beta} \tag{4.14}$$

where f is the modulating frequency, β is a stretching exponent lying between 0 and 1, τ is the characteristic lifetime and Γ is the incomplete gamma function, defined

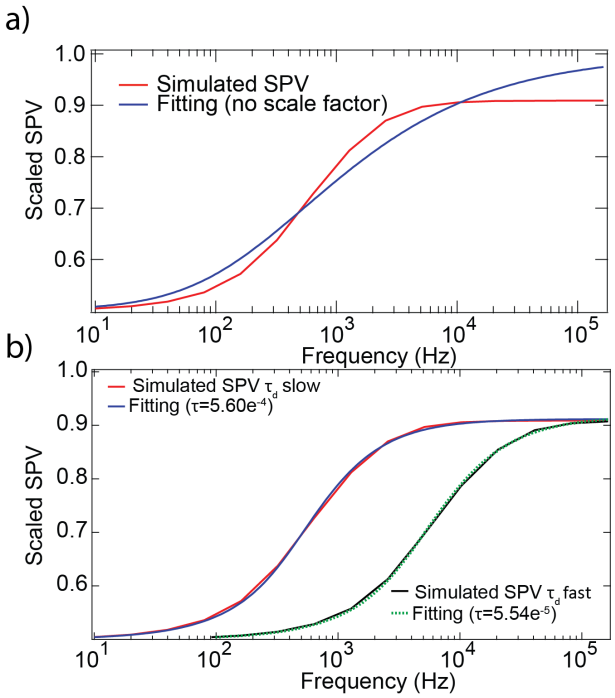

Figure 4.29: a) Shows the average surface potential as a function of frequency for a discharge 10 times slower than the charge, with the natural fitting. b) Shows the same data but allowing the fitting to have an extra scaling factor.

as

$$\Gamma(s,x) = \int_x^\infty t^{s-1}\mathrm{e}^{-t}\,\mathrm{d}t. \tag{4.15}$$

Note that a stretched exponential is used here for fitting as the processes involved are more likely to have multiple charge/discharge rates rather than the single value used in the simulation. Figure 4.29 a) shows the fit of this equation to the simulated time averaged surface potential. Clearly there is a large discrepancy here.

The fitting assumes that τ_c is infinitely small, i.e. the sample charges instantly, the simulation however has a finite τ_c thus resulting in the average surface potential not being equal to 1 at very high frequencies, and hence the equation not fitting. However it is possible to modify the equation to get a better fit by adding a scaling factor to the equation so that

$$V_{sp,avg}(f) = \frac{1}{2} + S_c\frac{\tau f\Gamma\left(\frac{1}{\beta},\left(\frac{1}{2\tau f}\right)^\beta\right)}{\beta} \tag{4.16}$$

where S_c is the scaling factor, which changes the behaviour for an infinite

frequency. The results of this fitting are shown in Figure 4.29 b). The simulation conditions have τ_c and τ_d as 0.5 x10^{-4} s and 0.5 x10^{-3} s respectively. The fitting of Equation 4.14 returns a β of 0.5 and a τ of 0.43 $\pm$ 0.08 x10^{-3} s. Whereas Equation 4.16 produces a β of 1.25, with a τ of 0.561 $\pm$ 0.008 x10^{-3} s. The τ returned by the fitting does not match either τ_c or τ_d, however it is a close approximation of τ_d, the slower response here. τ does not equal τ_d because the assumption in the fitting is that τ_c is infinitely small, when in reality it is small but still significant. This is shown by the scaling factor, S_c which in this case $S_c = 0.82$. The scaling factor is related to the relationship between τ_c and τ_d.

If the modulation frequency tends to infinity, V_c and V_d are nearly equal, and equally t tends to 0. For this reason differentiating Equation 4.12 gives

$$\begin{aligned} V_{sp} =& 1 - (1 - V_c)e^{-\frac{t}{\tau_c}} \\ \frac{d}{dt}V_{sp} =& \frac{1}{\tau_c}(1 - V_c)\, e^{-\frac{t}{\tau_c}} \qquad (4.17) \\ & \text{Since } t \ll \tau_c \\ =& \frac{1}{\tau_c}(1 - V_c) \qquad (4.18) \end{aligned}$$

And since, on charging for a time period t

$$V_d = \frac{t}{\tau_c}(1 - V_c) + A \qquad (4.19)$$

Likewise, the same approach can be taken for the discharging curve (Equation 4.13)

$$\begin{aligned} V_{sp} =& V_d e^{-t/\tau_d} \\ \frac{d}{dt}V_{sp} =& -\frac{V_d}{\tau_d} \qquad (4.20) \end{aligned}$$

So after a time t the sample has discharged back to V_c, hence

$$V_d - \frac{V_d}{\tau_d}t = V_c \qquad (4.21)$$

substituting for V_c in 4.19 yields

$$\begin{aligned} \frac{t}{\tau_c} - \frac{V_d t}{\tau_c} + \frac{V_d t^2}{\tau_c \tau_d} - \frac{V_d t}{\tau_d} &= 0 \\ & \text{Since } t \to 0 \\ \frac{\tau_d}{\tau_d + \tau_c} &= V_d \qquad (4.22) \end{aligned}$$

Since the starting value of the fitting is 0.5 the scale parameter S_c is related to V_d by

$$V_d = \frac{S_c}{2} + \frac{1}{2} \tag{4.23}$$

this means that the relationship between the two time constants can be found, providing the scaling factor is found. So that

$$\frac{\tau_d}{\tau_d + \tau_c} = \frac{S_c}{2} + \frac{1}{2} \tag{4.24}$$

The τ returned by the fitting should most closely approximate the larger of the two time constants, though with a finite τ_c it will not be an exact match. By simulating the results across a wide range of τ_c and τ_d it might be possible to determine the approximate relationship between τ_c, τ_d and τ, however this will only be useful if S_c can be determined from the experimental data.

4.3.3 Dependence on Background Light

Figure 4.30 a) shows the behaviour of the surface photovoltage as a function of the modulation frequency for a range of background light intensities on P3HT:PCBM. Naturally, without a background light applied (red curve), the difference between the surface potential with the foreground light on and off is the greatest, the more background light, the smaller the difference. It is also clear that for P3HT:PCBM the charging rate (τ_c) is quicker than the discharging rate, as the time averaged difference in photovoltage increases with frequency.

Here, the curve without the background light should most closely resemble the simulated results as the conditions are the same. When the modulated light is applied to this system the time constants correspond to the full building of charge from an intrinsic system to one dominated by photocarriers. This should always be a longer process than the partial charging that will be discussed next.

When the background light is applied an amount of photogenerated charge carriers are introduced into the donor acceptor system. Since there is no current, charges can only drift in response to the internal fields of the system. Recombination processes of excitons and charge carriers can also take place. The addition of a background light to the system increases the charge carrier density present in the active semiconductor, this increases the rate of bimolecular recombination as it is much more likely for a charge carrier to meet and recombine with the opposing species before reaching the electrode. This is reflected in the reduction of carrier lifetime seen in Figure 4.30 b) in the right shifting of the SPV difference with respect

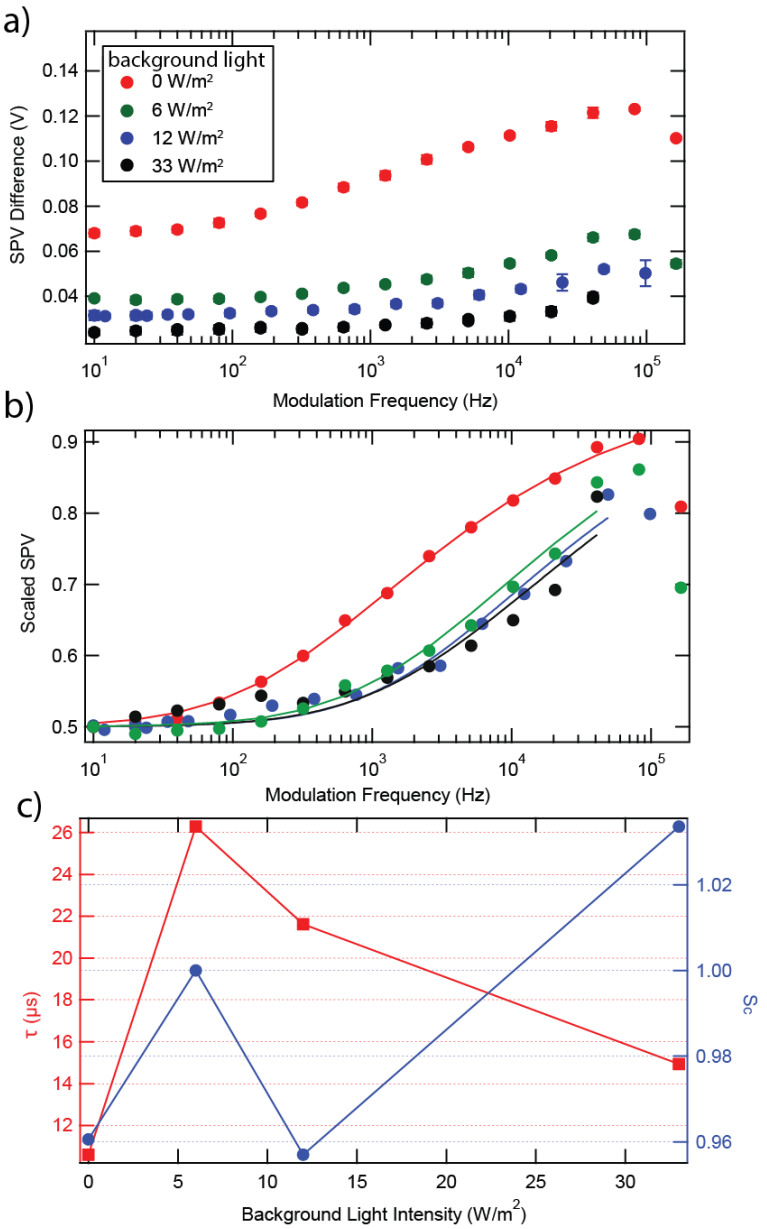

Figure 4.30: An IM-KPFM experiment on P3HT:PCBM showing a) surface photovoltage and its dependence on modulation frequency and background light intensity. b) Scaled photovoltage with respect to V_{max} with fitting. c) Values of τ and scaling for each background light from the fitting in b).

to frequency.

The net SPV depends on how many charges can be separated and stored by the system, and since the LUMO/LUMO offset between the donor and acceptor determines the splitting of the exciton, the build up of charge opposing this field should be the determining factor.

Figure 4.30 b) shows the time averaged surface photovoltage scaled to the steady state value of 0.5 V_{max}. Note here that for non-zero background light this is slightly inaccurate, because the background light also has a contribution to V_{max}. This can, however, be assumed to be small and constant throughout frequency sweeps, so has no effect on the scaling of the curves, it would only change the starting value. The fittings shown are to Equation 4.16. Like in the case of Shao et al. [192], increasing the background light intensity shifts the frequency dependent curves to higher frequencies. This should result in a decrease in the extracted τ and indicates that the lifetime of carriers is dependent on the background carrier concentration, due to the implied reduction in τ_d [192]. The extracted values of τ and S_c are shown in Figure 4.30 c). It should be noted that fitting to Equation 4.16 cannot be properly achieved when the background light is applied as the data does not saturate to V_{max}. Therefore Equation 4.14 is used instead for the following data, unfortunately this means extracting τ_c and τ_d individually is not possible.

4.3.4 SPV Dependence on Modulated Light Intensity

Figure 4.31 a) shows how the measured SPV difference depends on the intensity of modulated illumination as a function of frequency. Clearly an increase in the intensity of the modulated light results in an increased difference between the average SPV. Since an increase in illumination should produce more photocarriers; this makes sense. This behaviour is true for both low and high frequencies. The behaviour of the SPV below 145 W/m^2 is interesting, as with any additional foreground light the surface photovoltage should increase with frequency, however this is not seen to be the case. Below around 110 W/m^2 at high frequencies the SPV difference falls, suggesting that the recombination is faster than the charging at these low light levels. The reason for this behaviour is as yet unknown.

The difference between illuminating through the top and bottom optics of the AFM, can be quantified by the reproducible behaviour of the SPV. In the methodology section 2.2.8, calibration of the light through the bottom optic is presented; the full intensity of light with an open aperture was measured to be 525 W/m^2, accounting for the missing presence blue light used as background this is 363 W/m^2. And since the light is linear with current and voltage, the light intensity at 50% will

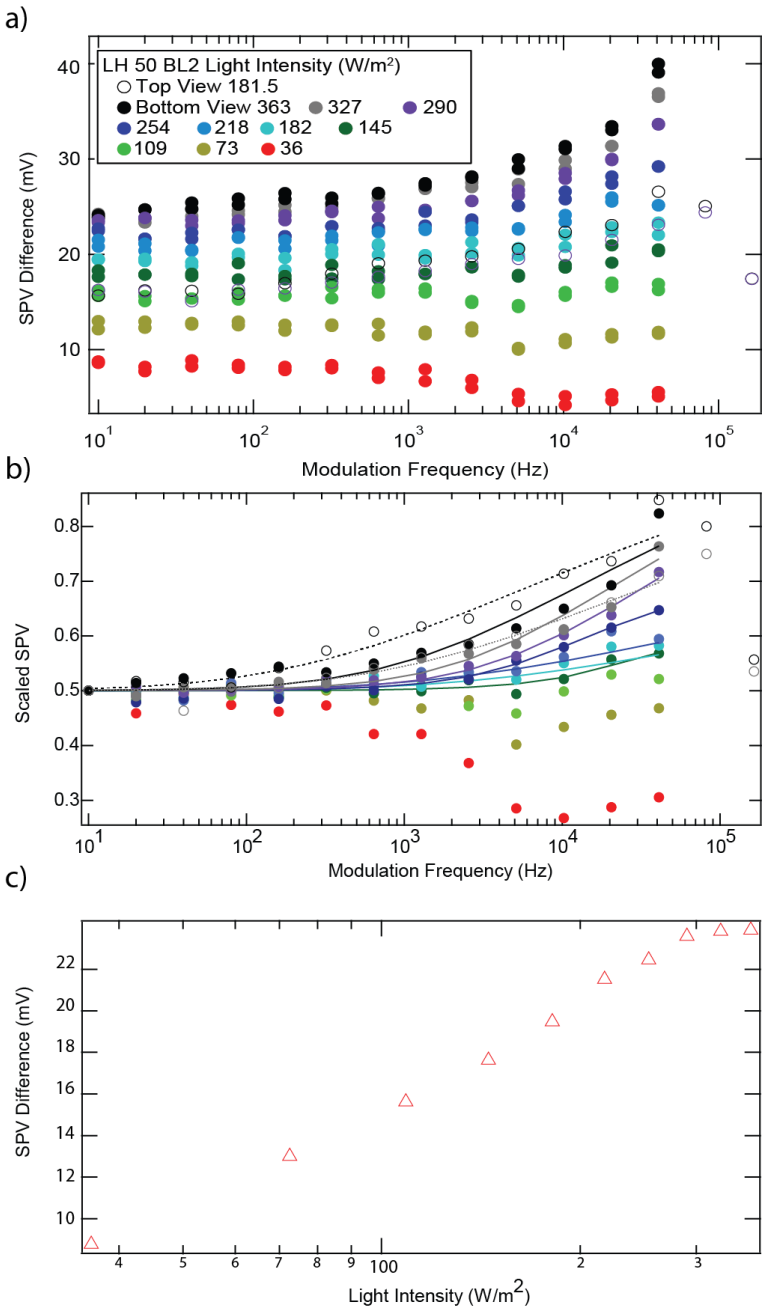

Figure 4.31: Foreground light intensity dependence of surface photovoltage measured in IM-KPFM on P3HT:PCBM, with a 33 W/m^2 background blue light and a 50 nm lift height a) is the raw surface photovoltage difference and b) is the SPV difference scaled to 0.5 V_{max} using the steady state behaviour, showing fitted lines of Equation 4.14. c) Shows the SPV difference measured at 10 Hz as a function of the applied modulated light intensity.

be 181.5 W/m^2. Since the dependence of the SPV difference on light intensity is so reproducible, the light output of the top optical path can be determined to be half of that from the lower path.

Figure 4.31 b) shows the scaled SPV difference to 0.5 V_{max} for each light intensity incident on the sample. The curves are fitted with Equation 4.14. Here, it is clear that τ increases with an increase in light intensity as the curves shift to lower frequencies. This indicates that the carrier lifetime is increased with higher light intensities, as τ is primarily a measure of τ_d. However, this is not quite true as from Equation 4.22 τ is a factor of both the charging rate and the discharging rate. Increasing the charging rate by increasing the light intensity has the effect of reducing τ. This also somewhat explains the low probing intensity behaviour, as if the probe light is less intense than the background illumination the charging time may well be longer than the recombination causing the behaviour seen.

Higher intensities of light should always decrease the lifetime of the charge carriers as in low mobility systems germinate recombination should act to reduce the carrier lifetime, close to the generation site and in higher mobility systems bimolecular recombination should dominate as the concentration of charge carriers increases. Maintaining fixed background and probe light intensities enables the study of the recombination rate in these materials with this technique.

The data also shows that even with high modulated light intensities, the frequency dependent behaviour of the SPV does not plateau at the highest frequencies measurable by this equipment, in this case 64 kHz. If the light intensity was to be increased or the modulation frequency increased it might be possible to fit the plateaux. Some higher frequency measurements were obtained, up to 164 kHz, however it was later shown that the lights could not maintain their intensity at this frequency. Figure 4.31 (c) shows the difference in SPV measured at 10 Hz as a function of the modulated light intensity. Like Tr-EFM the response is dependent on the logarithm of the light intensity on the sample. However, unlike Tr-EFM the response here saturates at light intensities around 330 W/m^2 at SPV differences of 24 mV. Since the SPV is dependent on the change of the Fermi level in the semiconductor when the semiconductor is effectively doped by the created charges the higher the charge density created the higher the measured change in SPV. since the AFM only probes the surface of the material the SPV measured may not be a complete picture of the full device like those measured in TPV. This may explain the difference in magnitude of the SPV measured here.

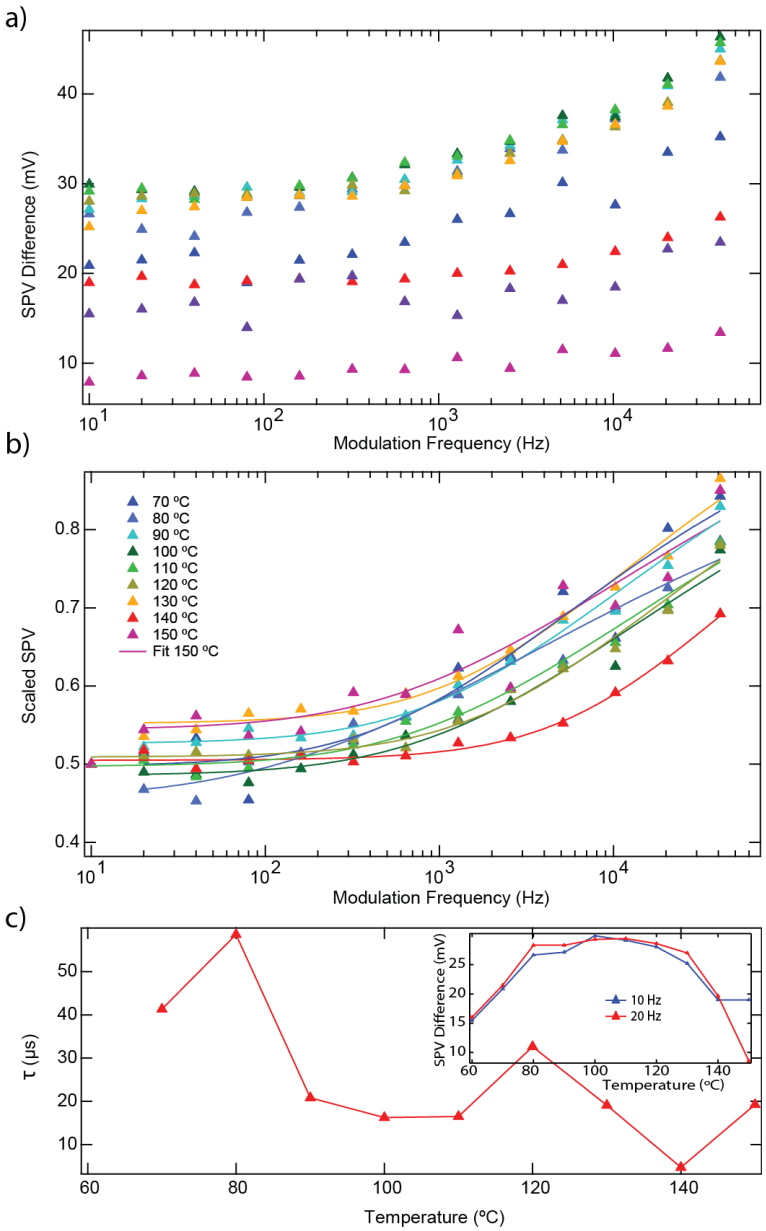

Figure 4.32: Temperature dependence of surface photovoltage, with a 33 W/m^2 background blue light and modulated intensity of 182 W/m^2 and a 50 nm lift height a) shows the SPV difference and b) is the SPV scaled to 0.5 V_{max}. c) Shows the evolution of the extracted τ across the temperature range. Inset: The average SPV difference measured at low frequencies as a function of temperature.

4.3.5 Temperature Dependence on Heating of P3HT:PCBM

The temperature dependence of τ can be tested as a function of the modulation frequency with a constant background light intensity of 33 W/m^2 and a constant modulation intensity of 182 W/m^2. Figure 4.32 a) shows the temperature dependence of the SPV difference as a function of the modulation frequency.

The measured SPV appears to have a strong dependence on temperature as the magnitude of the SPV difference increases between 70°C and 130°C. This dependence on temperature could suggest that the P3HT:PCBM has a higher charge separation efficiency at elevated temperatures. This could suggest a temperature dependent reduction in effective band gap [253]. Above 130°C the SPV difference rapidly falls possibly indicating that as the material begins to melt the disorder becomes too great to separate charges.

Figure 4.32 b) shows the SPV difference scaled to 0.5 V_{max}, which is then fitted with Equation 4.14. Though it is difficult to see the fitted curves shift to higher frequencies as the temperature increases. The extracted values of τ as a function of temperature can be seen in (c). Note that when applying the fitting here, it was not always appropriate to include the 10 Hz data as this point would skew the fitting away from the remainder of the data.

In (b) there appears to be three regimes of behaviour when comparing low modulation frequencies to high frequencies. The points at 140°C has the lowest SPV difference relative to the low frequency behaviour, and also has a low extracted τ. The reduced carrier lifetime indicates an increase in recombination. Interestingly the largest responses in the SPV difference at 70, 90, 130, and 150°C do not have the longest carrier lifetimes. This suggests the SPV difference is not correlated directly to the measured τ. Here it is again possible to see that the individual components τ_c and τ_d cannot be determined, however it is a reasonable assumption that changes in τ originate predominately from changes in τ_d.

τ and hence τ_d appear to be strongly dependent on temperature as the sample is heated. Significant increases from the general trend in τ can be seen for the data at 80°C and 120°C, which could indicate a reduction in bimolecular recombination in trap states, possibly due to a change in conformational order [238]. Above 80°C τ_d significantly decreases to an average value of around 20 μs. This correlates well to the values for τ measured by Shuttle et al. [238]. At low frequencies the SPV difference is most likely to correlate to the V_{OC}. The inset in (c) shows the evolution of the SPV difference at 10 and 20 Hz as a function of frequency. The SPV difference is highest between 80 and 130°C, and decreases by around 50% outside this range.

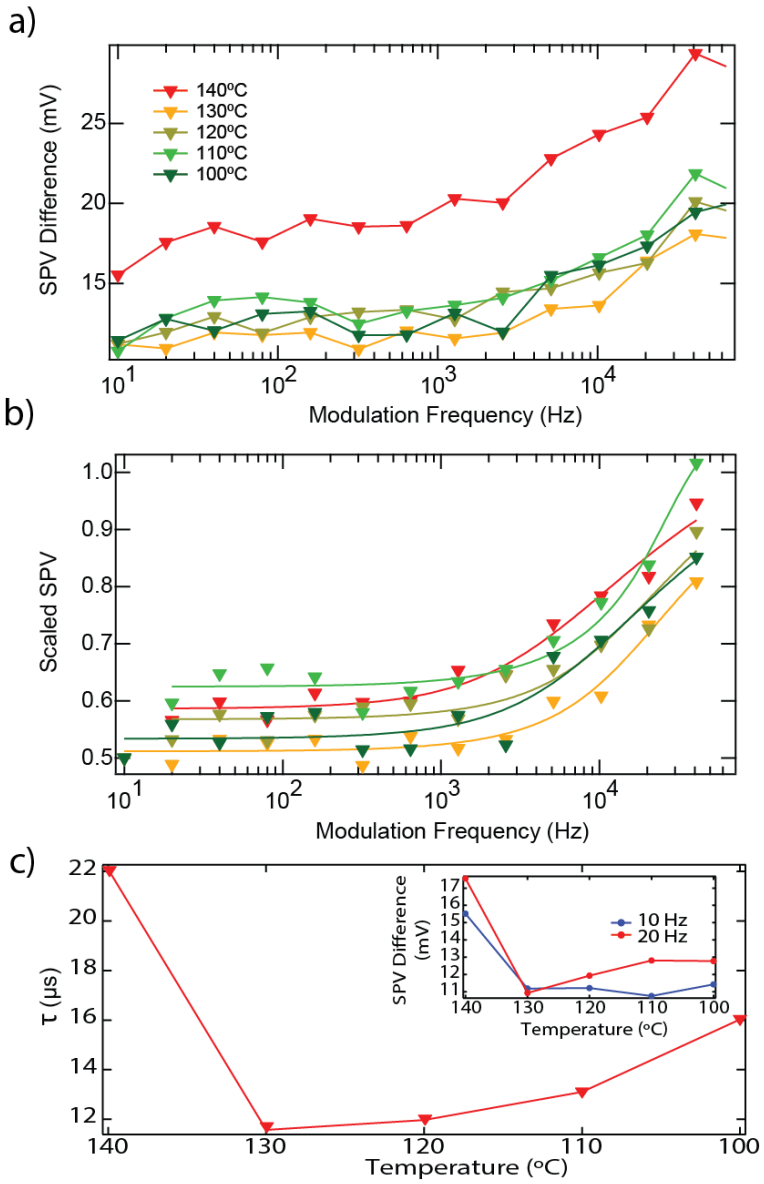

Figure 4.33: Light intensity dependence of surface photovoltage on P3HT:PCBM when cooled from 140°C, with a 33 W/m^2 background blue light and a 50 nm lift height a) is the SPV difference and b) is the scaled SPV. c) shows the evolution of the fitted τ across the temperature range. Inset: The change in net surface photovoltage at low frequency as a function of temperature.

4.3.6 Temperature Dependence on Cooling

Figure 4.33 shows the behaviour of the SPV whilst the same sample is cooled from 140°C to 100°C. Due to time constraints the full range of measurements could not

be completed. Figure 4.33 (a) shows the SPV difference as a function of modulation frequency. The net SPV difference is highest at 140°C and lowest at 130°C, having intermediate values at lower temperatures. This is noteworthy behaviour as the opposite was true when the sample was heated, making it more likely that a conformational change happens at the 140°C point.

Figure 4.33 (b) shows the scaled SPV for the data in (a) with fittings of Equation 4.14. Here, the data at 110°C in light green has distinct behaviour from the rest of the dataset, with a peak evident at around 80 kHz. This could indicate more complex behaviour than the simple double exponential used in the model. For this to occur there would need to be two charging and two discharging rates, a slow and a fast charge and discharge, with the fast effects only active for brief periods much like in the work of Takihara et al. [191]. Initially the slow timescales dominate, with the slow charge being faster than the slow discharge (causing the rise in photovoltage). Then as the frequency increases, the fast discharge and slow charge dominate, thus causing the fall in photovoltage. The rest of the behaviour, is explained by the fast charge and discharge model discussed earlier.

As to the physical causes of the different timescales measured; charge generation is most likely to be limited by trapping and recombination. It would be expected that the effects of trapping scale with temperature. Higher temperatures, should activate deeper traps, hence increasing τ_c. However, increasing the temperature also increases the hopping rate of transport, not that this is the only transport mechanism, however this would have the opposing effect. There is an interesting point to note here, in that for FVBS Chapter 3 (Figures 3.14 and 3.13), there are also anomalies occurring on the cooling cycle at 110°C for P3HT: The mobility follows the expected trend however, the gamma factor at 110°C, is much higher. Since, bimolecular recombination is strongly linked to field dependence [238], it's likely that this also strongly effects τ_d.

Figure 4.33 (c) shows the extracted τ from the fits in (b) as a function of temperature. Here, the 140°C data point shows the longest τ at 22 μs. It is worth noting that this is around the same average value of the heating behaviour. As the sample is cooled below 140°C, τ rises as the temperature decreases. This suggests that the effects of charge carrier recombination are reduced as the sample cools. The SPV difference shown in the inset shows different behaviour to the heating cycle, with the SPV difference being highest at 140°C and only displaying a small increase between 130 and 100°C. The magnitude of the SPV difference is also smaller on cooling, and is likely to be an effect of sample degradation.

The increase in carrier lifetime after annealing (the heating and cooling cycle)

matches the known behaviour of this system becoming more efficient after annealing [88]. This indicates that IM-KPFM could be used in this manner to test devices during the annealing process in an effort to increase the efficiency of new devices.

4.3.7 Mapping

IM-KPFM can give quantitative data on charge carrier lifetimes at a single point, however each measurement can take in excess of 20 minutes. It is, therefore impractical to use this technique for mapping in a point by point approach akin to FVBS. However, it is possible to use the modulated light in regular scanning KPFM mode. Provided the modulation frequency is double that of the pixel acquisition rate, the time averaged SPV can be measured at a single modulation frequency in regular scanning KPFM mode.

This is a dual pass technique where the first pass in regular tapping mode records the topographical profile of the sample. At the end of the line the tip lifts off the sample and retraces its path with an additional lift height along the surface. If the modulated and back ground illumination are applied during this process, providing the period of modulation is less than the dwell time per pixel the returned surface potential is a time average of the potential between the modulated illumination being off and on. Since the modulation frequency is fixed during scanning, if a particular point on the sample has a high level of recombination and hence a short carrier lifetime the response of the SPV to the modulated light will be smaller in magnitude to the rest of the sample. The opposite would be true for a region with a particularly high carrier lifetime. However changes in V_{OC} would have a similar contrast and the single frequency cannot differentiate between the two. By comparing KPFM with background light only to KPFM with modulated light intensity insight can be gained into spatial changes in carrier lifetime.

Figure 4.34 shows the resulting topography and surface potential when P3HT: PCBM is scanned in normal KPFM with just a background light in c) and a 32 kHz foreground light in d). The surface potential displayed in c) differs significantly to that shown in d). The average value of d) is lower than that of c), 1.118 V vs. 1.245 V. Without any background light the average surface potential is measured to be 1.208 V. So the background light produces a 37 mV abundance of negative SPV on the surface. When the modulated light is applied at 32 kHz, there is a much more positive SPV measured.

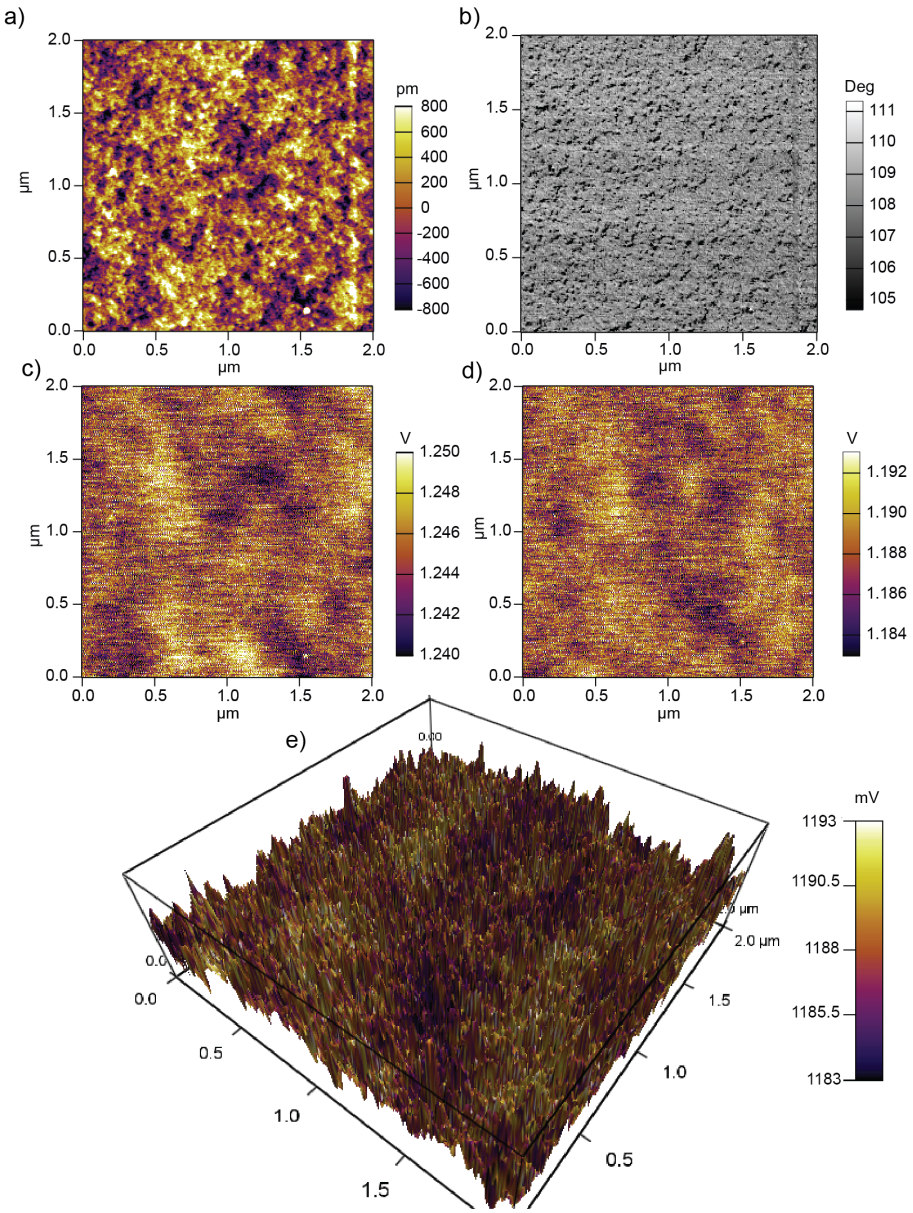

Figure 4.34: a) and b) show the topography and phase of a P3HT:PCBM sample at room temperature where c) and d) show the surface potential for just the background light and for the background light with a modulated foreground at 32 kHz. e) Shows a 3D plot where the colour scale is the measured potential and the height is the topography.

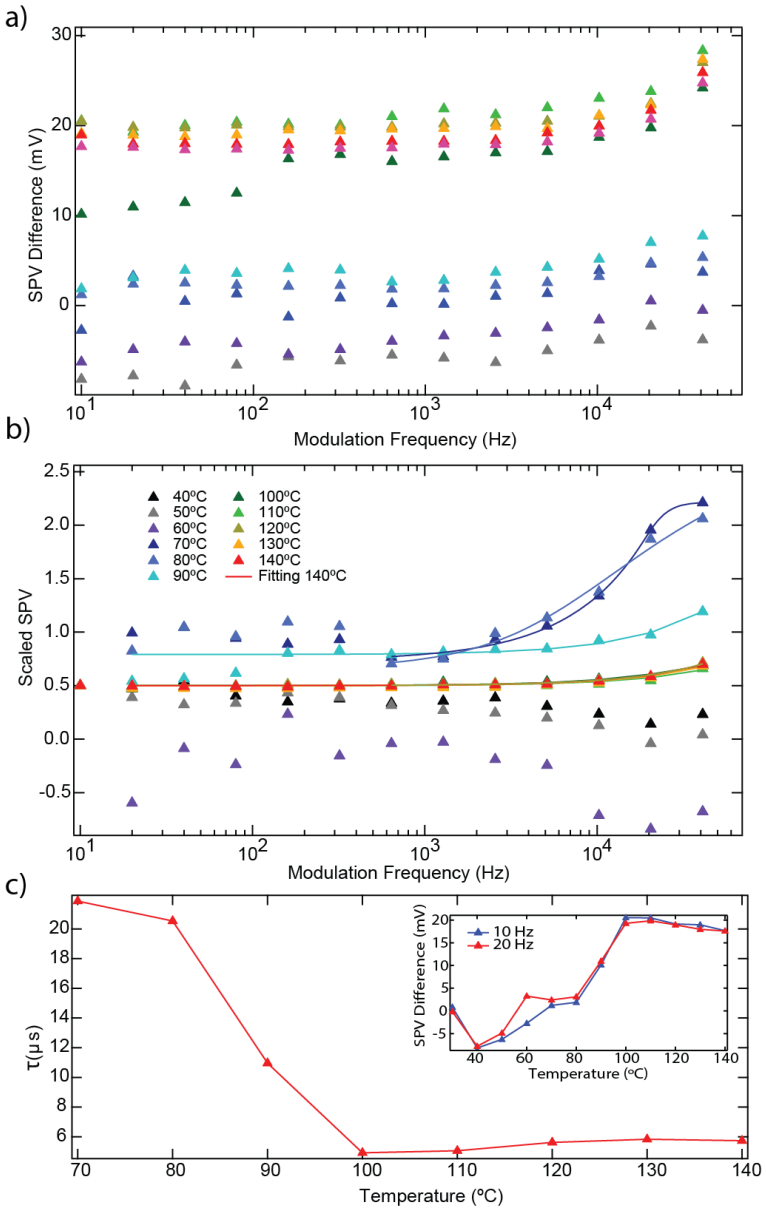

Figure 4.35: Temperature dependence on heating of the IM-KFPM response of PTB7:$PC_{70}BM$, between 10 Hz and 40 kHz, with a blue background light at 33 W/m^2 intensity. a) Shows the response of the net surface potential whilst b) shows the surface potential scaled to V_{OC} with fitting between 10 and 40 kHz. c) Shows the evolution of τ with temperature from the fitting. Inset: The evolution of the low frequency surface potential with temperature.

4.3.8 IM-KPFM of PTB7:$PC_{70}BM$

The temperature dependence of the SPV of PTB7:$PC_{70}BM$ can be measured using IM-KPFM. Figure 4.35 shows the behaviour of the SPV measured with the same parameters as the P3HT:PCBM sample, that is, with a 50 nm lift height, a 33 W/m^2 background light, and a 182 W/m^2 modulated light intensity.

Figure 4.35 (a) shows the behaviour of the SPV difference as a function of the modulation frequency as the PTB7:$PC_{70}BM$ sample is heated from 40°C to 150°C. Note here that although the sample was heated to 150°C, the data at this temperature was spurious and so is not shown.

Like in the case of P3HT:PCBM, $\tau_d > \tau_c$ for the majority of the data as the SPV difference increases with increasing modulation frequency. However, this behaviour is not ubiquitous across the dataset. The low temperature results between 40°C and 60°C show the opposite behaviour, though this is more obvious in (b).

Like P3HT:PCBM there is a strong dependence of the SPV difference on temperature. The magnitude of the SPV difference rises with temperature between 50°C and 110°C. Notably the net SPV difference is initially negative at low temperatures. This is most likely due to a band gap offset rather than an excess of holes on the surface. The SPV difference evolves with temperature to become a positive difference of around 28 mV at 64 kHz and 110°C, lower than the equivalent point for P3HT:PCBM (at $\sim$ 45 mV) despite the predicted V_{OC} and splitting potential being higher in the PTB7:$PC_{70}BM$. This could be due to a larger energy loss in the band alignment of the PTB7:$PC_{70}BM$ sample. Above 110°C the SPV difference drops but not significantly.

Figure 4.35 (b) shows the scaled SPV from (a) with the same stretched exponential fitting as previously. The temperature dependence is strongly evident here. At low temperatures curves have an inverted τ_c to τ_d relationship, i.e. $\tau_c > \tau_d$. At 70°C this behaviour changes to the more normal pattern of a rising SPV with modulation frequency. The rise in SPV with modulation frequency occurs at a relatively low modulation frequency indicating a long τ_d. As the temperature increases the frequency at which the scaled SPV increases, rises. Above 90°C, τ_d decreases significantly, with the scaled SPV data showing little to no rise even at high modulation frequencies. This suggests that charge carrier recombination increases rapidly when the temperature is raised.

This behaviour is also seen in Figure 4.35 (c) as the extracted τ falls from 22 μs at 70°C to around 5 μs at 100°C. Increasing the temperature further shows a small increase in τ, but the extracted τ does not exceed 6 μs. The inset of (c) shows the SPV difference at 10 and 20 Hz as a function of temperature. Above 80°C there

is a large increase in the magnitude of the SPV difference. This implies there are far more carriers produced above this temperature which explains the reduced carrier lifetime measured [238]. Notably, the rise in SPV difference with temperature is opposite to the behaviour of the SPV measured with Tr-EFM, suggesting that the SPV difference measured at low frequencies by KPFM is not an indication of the V_{OC} as was previously thought.

4.3.8.1 Cooling

Figure 4.36 shows how the SPV changes while the same sample is cooled from 150°C down to room temperature. The data in (a) shows how the SPV difference changes as a function of frequency as the sample cools. Cooling from 140°C to 120°C produces a drop in the net SPV difference indicating that fewer charges are produced as the temperature decreases. Below 120°C, the SPV difference increases until the sample reaches 90°C. Between 90°C and 60°C the value of the SPV difference is fairly constant. Below 60°C the SPV difference again reduces.

For the higher temperature datasets, the net SPV difference is on average smaller than it was before annealing. However, as the sample is cooled the SPV difference remains positive. For the lower temperatures the SPV difference is higher than the as-cast sample.

Figure 4.36 (b) shows the scaled SPV with fittings of Equation 4.14. Though the temperature behaviour of the scaled SPV is complicated, there is a clear left shift of the data as the temperature decreases. It also appears that the behaviour of the sample changes below 100°C as the shape of the curves changes noticeably.

Figure 4.36 (c) shows the values of τ extracted from (b) as a function of temperature. Here a consistent rise in τ is seen as the temperature decreases. This indicates that the carrier lifetime is greatly increased at lower temperatures. It is unclear whether annealing had an effect on the lifetime of the carriers at these temperatures as the low temperature data on heating could not be fitted. Nevertheless, these results on cool-down show that PTB7:$PC_{70}BM$ has a very long carrier lifetime at room temperature of over 80 μs. The SPV difference at low frequencies is of a similar magnitude as the sample is cooled, compared to when heated. However, the temperature dependent behaviour is different, with the SPV difference showing increased behaviour around 60 to 90°C, compared to the 100 to 130°C it showed on heating. A peak is also evident in the behaviour at 140°C, which was not evidenced on heating.

These results corroborate Tr-EFM results that suggest PTB7:$PC_{70}BM$ is most efficient at low temperatures prior to annealing. This system has good confor-

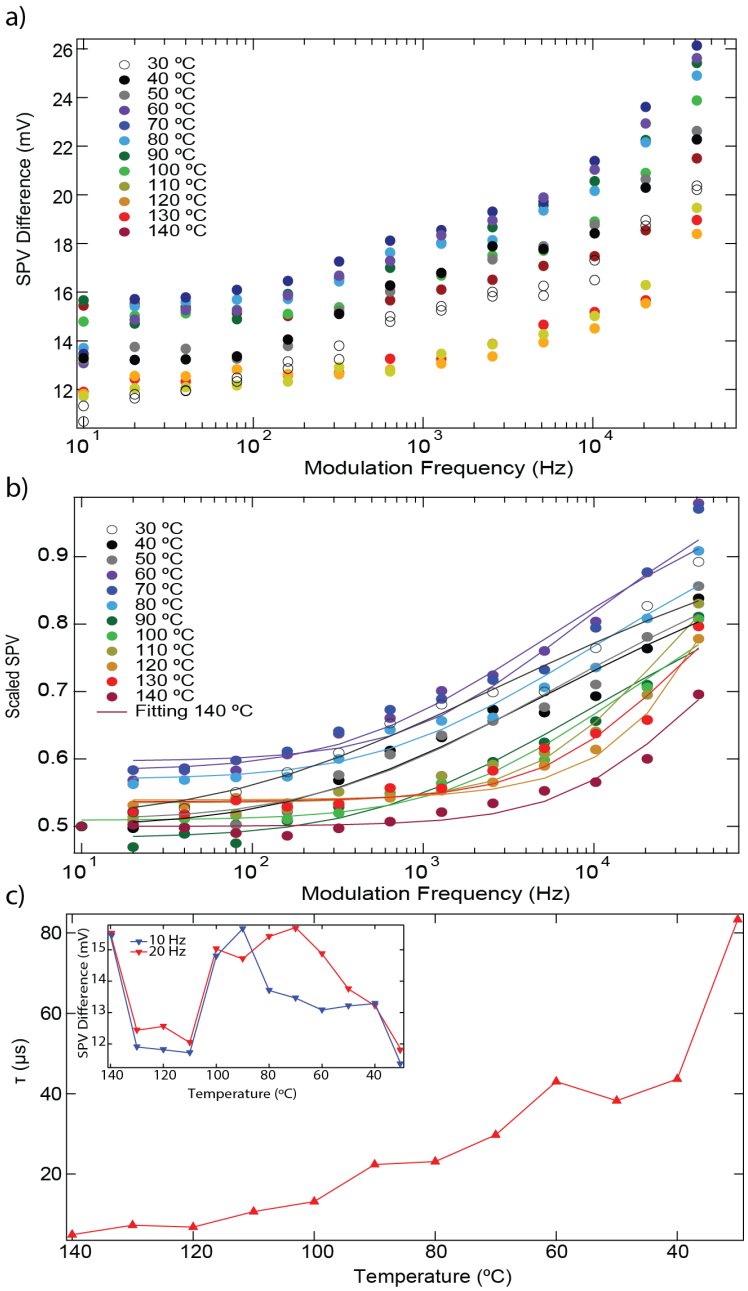

Figure 4.36: Temperature dependent IM-KFPM response on between 10 Hz and 64 kHz when cooling, with a blue background light at 33 W/m^2 intensity. a) shows the response of the net SPV difference whilst b) shows the scaled SPV with fitting between 10 and 64 kHz. c) Shows the evolution of τ with temperature from the fitting. Inset: The evolution of the low frequency surface potential difference with temperature.

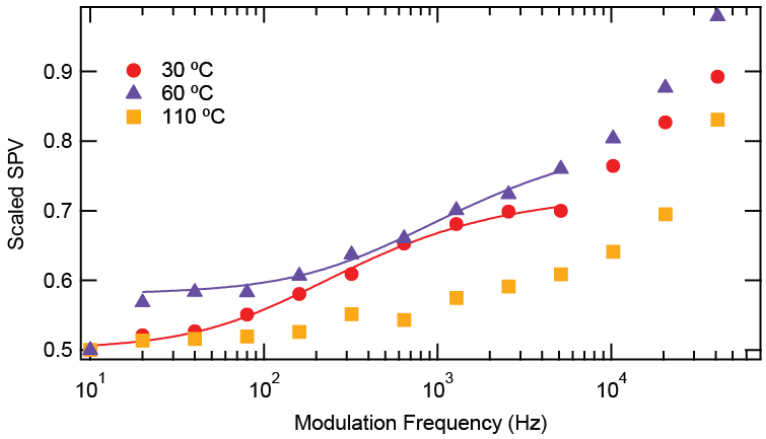

Figure 4.37: Showing the significant kink evident in normalised photovoltage, indicating a second time constant is evident in the results between 30°C and 110°C.

mational order as-cast hence its high carrier lifetime at low temperatures, annealing introduces defects in the ordering increasing the bimolecular recombination, as seen here. Although the increased SPV after annealing suggests that the carrier generation is increased by annealing, the mobility as determined by the carrier lifetime is decreased.

Figure 4.37 emphasizes the behaviour change noted in Figure 4.36 (b), showing a selection of three scaled SPV curves as a function of the modulation frequency. The curves displayed at 30°C and 60°C were fitted again with Equation 4.16 however the full data range was not used. Instead the maximum frequency fitted was 512 Hz, allowing just the visible kink to be fitted. The values of τ from this revised fitting are 118 μs and 30 μs for the 30°C and 60°C data respectively. It appears that as the temperature is decreased the longer timescale behaviour becomes increasingly dominant. It is possible that the long timescale process is active at all temperatures, but only dominates at low temperatures. This process could correspond to the trapping of charge carriers, hence its increasing significance as the temperature is decreased. It is possible that this process is the same one measured in Tr-EFM as the results for τ_d as measured by Tr-EFM are around this order of magnitude.

There is also the possibility of other effects being present in the measurements of the surface photovoltage. There is some indication that if the diffusion length of carriers is larger than the sample thickness the measured lifetime is a function of the diffusion constant and the sample thickness rather than the carrier lifetime [254], though this is unlikely in OPV materials which have short diffusion lengths. Another contribution to the frequency dependence can also be attributed

to capacitance effects of the water layer often present on the surface-air interface in ambient conditions, this may also cause surface trapping [255]. The frequency dependence of the SPV difference is also dependent on the space charge capacitance which depends on temperature and the widths of the space charge and recombination regions [85, 256], therefore it may not be possible to relate τ to the carrier lifetime without knowledge of these properties.

4.3.8.2 Topographic Measurements

Figure 4.38 (a) and (b) show topographic and phase images of a PTB7:$PC_{70}BM$ sample with no defined phase separation evident in either image. (c) shows the KPFM signal measured with just the 33 W/m^2 blue background light incident on the sample. In the potential map there is evidence of finer networks, possibly showing areas where charges are being generated. Figure 4.38 (d) shows the average potential when a 42 kHz modulated light is applied, and (e) superimposes this on the simultaneously measured topography. The potential measured with a modulated light is clearly higher than with the background light alone. Areas of higher potential on this map represent areas of decreased recombination and longer carrier lifetimes. (e) Shows that there is evidence of correlation between this and the sample's topography, specifically peaks appear to have a lower potential and troughs the inverse of this. These correlations are most likely to be geometrically induced. There are however smaller variations that could be indications of lower recombination regions, most likely to be in the middle of donor/acceptor phases.

4.3.9 Conclusions concerning IM-KPFM

Here, IM-KPFM has demonstrated its ability to quantitatively measure the discharging rates, τ_d, in both P3HT:PCBM and PTB7:$PC_{70}BM$. This has been achieved at a range of temperatures and hence shows how τ_d changes, both as a result of the elevated temperature and annealing. In both P3HT:PCBM and PTB7:$PC_{70}BM$ τ_d is larger at low temperatures. This is especially the case in PTB7:$PC_{70}BM$. Meanwhile the behaviour of P3HT:PCBM shows a much more complicated dependence with similar spikes in behaviour as seen in Tr-EFM. Unfortunately no conclusions can be drawn about the annealing behaviour of either sample. There was, however, evidence of multiple contributions to τ_d which could be the result of trapping/detrapping behaviour and with more investigation might reveal insight into the charge carrier behaviour in these and similar systems.

Whilst this aspect of IM-KPFM has been demonstrated previously by Tak-

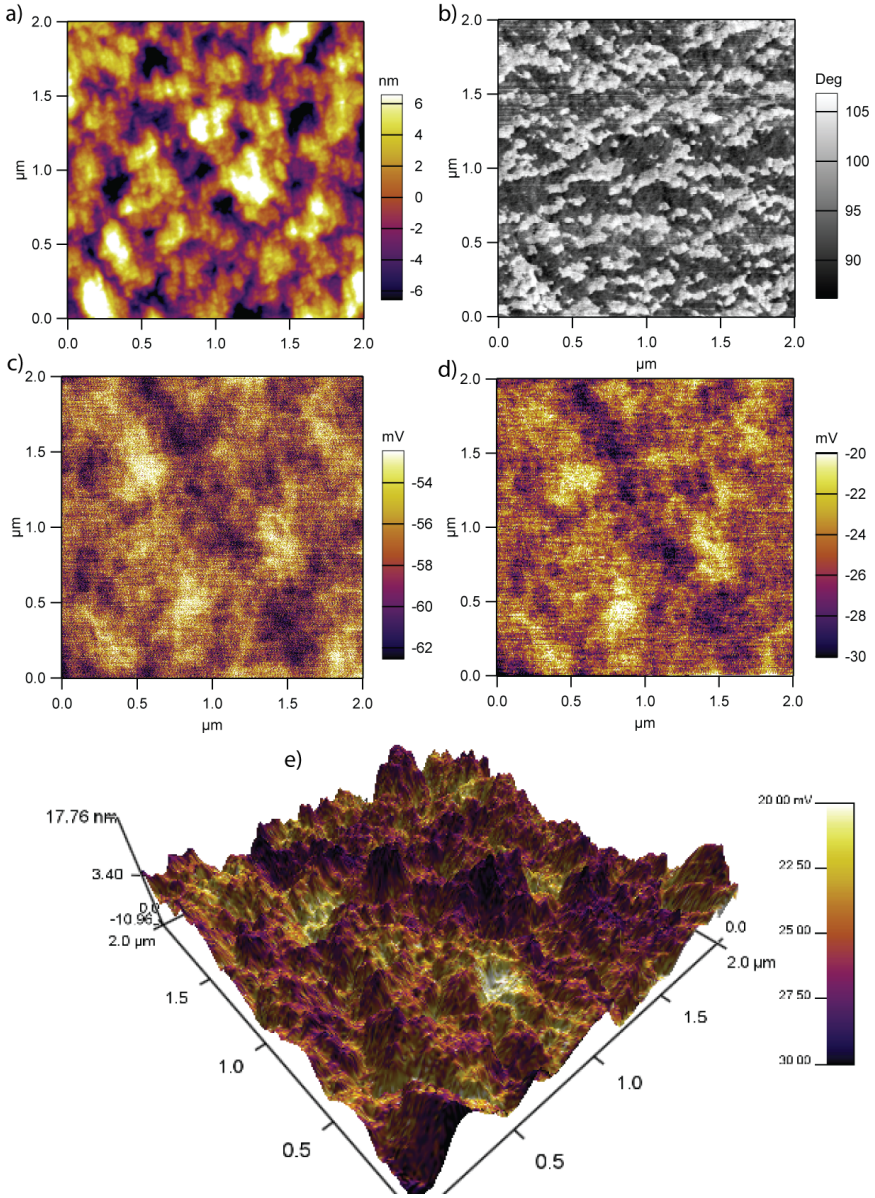

Figure 4.38: a) and b) show the topography and phase of a PTB7:$PC_{70}BM$ sample at room temperature where c) and d) show the surface potential, for c) just the background light at 33 W/m^2 and d) for the background light at 33 W/m^2 with a modulated foreground at 42 kHz at 265 W/m^2. e) shows the topography in 3D with the colour map from d) overlaid.

ihara et al. [191] and Shao et al. [192], here, the possibility of measuring τ_c has also been demonstrated, something that has not previously been achieved using this technique. In order to achieve quantitative results for both τ_c and τ_d, the intensity and modulation frequency of the light applied should be increased. Nevertheless, if this requirement was fulfilled IM-KPFM may yield insight into the charge carrier dynamics of these materials.

Once the frequency behaviour has been characterised, by using a scanning technique at a high light modulation frequency, the SPV decay behaviour can be mapped at high spatial resolution and compared to the simultaneously measured topography. A summary of these results can be seen in Table 4.3.

	P3HT:PCBM	PTB7:$PC_{70}BM$
Temp. dependence of τ (T rising)	Decreasing	Decreasing
Temp. dependence of τ (T cooling)	Increasing	Increasing
τ (70°C)	42 μs	22 μs
SPV Change (70°C)	20 mV	-3 mV
Av. SPV Change Mapping	-127 mV (32 kHz)	-32 mV (42 kHz)

Table 4.3: A summary and comparison of temperature dependent IM-KPFM on P3HT:PCBM and PTB7:$PC_{70}BM$.

4.3.10 Comparison to Tr-EFM

Both techniques, Tr-EFM and IM-KPFM, are capable of measuring a form of the charging and discharging timescales, τ_c and τ_d. They also each measure some version of the electrostatic potential generated by the sample. In the case of Tr-EFM, this is likely to be closely related to the V_{OC} of the cell, whereas in IM-KPFM this is much more likely to be dependent on the vacuum level offsets of the system coupled with the LUMO/LUMO offset of the donor and acceptor blend. The V_{OC} is likely to be the more useful parameter to measure, however, the quantification of this parameter requires careful calibration.

Figure 4.39 shows a comparison of the voltage measurements taken from Tr-EFM, IM-KPFM and similar results reproduced from Shao et al. [192], where the SPV measured using IM-KPFM and the V_{OC} measured using standard techniques are compared [192]. In the case of (a), the Tr-EFM result shows SPV scaling logarithmically with light intensity. Though the light intensity is comparatively low, no saturation of the SPV is evident.

Figure 4.39 (b) and (c) show the SPV difference as a function of light intensity from Shao's data and that presented here. Both of these datasets show a plateau

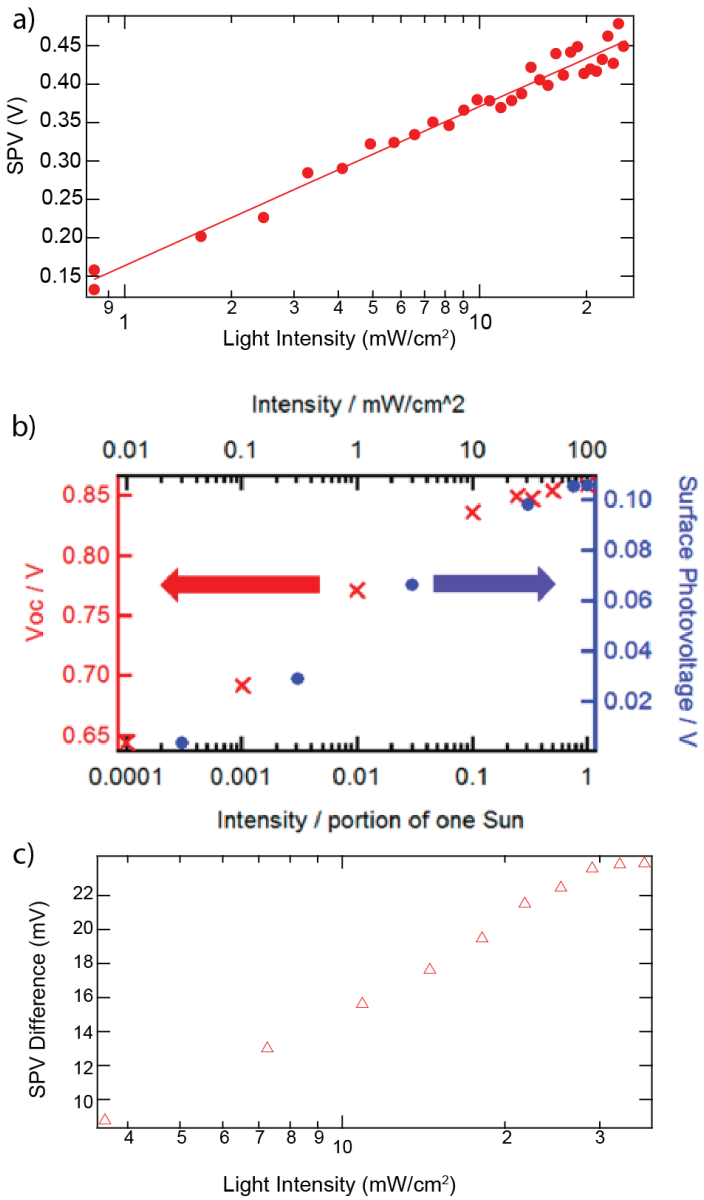

Figure 4.39: a) The behaviour of the measured SPV with light intensity of P3HT:PCBM measured by Tr-EFM. b) Reproduced from Shao et al. [192], the relation of V_{OC} and net surface photovoltage with light intensity. c) Behaviour of the measured SPV difference on P3HT:PCBM as a function of light intensity, measured by IM-KPFM.

in the SPV difference, Shao's on PCDTBT:$PC_{70}BM$ at $\sim$ 100 mW/cm^2, and this work's on P3HT:PCBM at $\sim$ 50 mW/cm^2. Published V_{OC} data for either of these systems does not show this plateaux [253, 257], suggesting that the IM-KPFM does not measure the V_{OC}, and is likely to measure the effective Fermi level change when the system generates charge coupled with the LUMO/LUMO offset of the donor and acceptor.

The other notable difference between the two techniques is the timescales measured at maximum light intensity, 256 W/m^2. Tr-EFM measured τ_c and τ_d to be 599 $\pm$ 6 μs and 520 $\pm$ 5 μs respectively for P3HT:PCBM at 50°C. At 70°C, at similar light intensities, the τ from IM-KPFM was measured to be 41 $\pm$ 18 μs. In this case the nature of the data indicates that $\tau_d > \tau_c$, a result which does not agree with the Tr-EFM data. However, published work on this subject indicates that τ_c should indeed be faster than τ_d, with $\tau_d \sim 30\mu$s [238].

There is, however, an indication in the IM-KPFM results of longer timescale behaviour under certain conditions. After the annealing of the PTB7:$PC_{70}BM$ samples a kink in the results was noted and fitted. This kink corresponded to a τ of 1.2 $\pm$ 0.1 ms, on a similar order of magnitude to the timescales measured by Tr-EFM. Since data of an equivalent light intensity and temperature was not measured across the two techniques it is uncertain as to whether these are measuring the same process, however, it seems likely. In the case of the Tr-EFM, the likely timescale measured is that of trapping and detrapping, as these have timescales in the kHz range [258]. IM-KPFM appears to measure the recombination lifetimes since they closely match those found for P3HT:PCBM measured with TPV [238], though there is evidence that the timescale measured may not be that of the carrier lifetime [256]. A comparison of the results measured here can be found in Table 4.4.

4.4 Conclusions

Here, the implementation and quantification of Tr-EFM and IM-KPFM have been demonstrated on both P3HT:PCBM and PTB7:$PC_{70}BM$. In terms of their implementation, Tr-EFM requires no external equipment other than a controllable light source, making this technique easier for stand-alone system integration. On the other hand, quantification of results requires careful calibration of the cantilever's response at the lift height used for experimentation.

IM-KPFM is in practice simpler to quantify, relying only on the fitting of the frequency dependent results, however, this technique requires a second light source, one that can ideally be modulated to frequencies exceeding 100 kHz, and a signal

generator capable of generating these driving signals. Tr-EFM is faster to acquire than IM-KPFM, and as such can be used in point by point mapping. IM-KPFM is inherently slower and hence without sacrificing statistical reliability, cannot be used in point by point mapping. This can be overcome by using a scanning technique which does not quantify the characteristic times of charging and discharging. It is clear that Tr-EFM and IM-KPFM measure different processes, as in Tr-EFM $\tau_c > \tau_d$, which is not the case for IM-KPFM or published TPV results [238]. For the archetypal P3HT:PCBM, IM-KPFM yields $\tau_d \sim 40$ μs, whereas Tr-EFM yields τ_d and $\tau_c \sim 0.5$ ms. There is evidence of both these time scales being relevant here.

Whilst Tr-EFM may not measure the timescale of recombination, the SPV measured after calibration follows the expected dependence of V_{OC} with light intensity and has the expected magnitude, suggesting it is a convenient approach for measuring V_{OC} at the nanoscale. IM-KPFM also has a logarithmic dependence on light intensity, however, this seems to saturate at relatively low values of light intensity. It is unclear what this is caused by, additionally, the magnitude does not seem to be easily related to V_{OC}. Overall, the two techniques are complimentary in their characterisation of the lifetime and SPV of OPV thin films.

	P3HT:PCBM		PTB7:$PC_{70}BM$	
	Tr-EFM	IM-KPFM	Tr-EFM	IM-KPFM
τ_c	600 μs	$<< \tau_d$	1000 μs	$<< \tau_d$
τ_d	520 μs (50°C)	40 μs (70°C)	600 μs	22 μs
SPV (70°C)	400 mV	20 mV	150 mV	-3 mV

Table 4.4: A summary and comparison of temperature dependent Tr-EFM and IM-KPFM on P3HT:PCBM and PTB7:$PC_{70}BM$. Values are approximate at comparable light intensities and temperatures, differences are stated. For IM-KPFM the SPV refers to the SPV difference.

Chapter 5

Conclusions and Further Work

5.1 Conclusions

A reliable method for testing material properties of OSCs for emerging OPV applications is crucial to understanding why some devices have superior performance to others. This work has presented three techniques; FVBS, Tr-EFM and IM-KPFM that, in combination, are capable of measuring the physical properties of device active layers, including mechanical properties and correlating them to the topography of these layers. FVBS allows measurement of zero field mobility, and the field dependence of the mobility, whilst also measuring the Young's modulus and adhesion of the sample's surface. The latter two techniques focus on measuring illumination dependent properties of the active layers including the V_{OC} and an idea of the recombination lifetime. Using all three techniques in combination could help develop materials and structures before the addition of a top contact, and probe nanoscale heterogeneities.

5.1.1 FVBS

Conductive AFM has had a long history of usage in studying OPV materials. The work presented in Chapter 3 gives a robust and comparatively easy-to-use method and analysis technique for quantitative nanoscale characterisation. By combining with nanomechanical measurements the contact area between tip and sample is also characterised, allowing more accurate quantitative results.

This work combines force volume mapping with current-voltage measurements to the effect that mechanical and electrical data can be collected simultaneously with high spatial resolution. The JKR model was used to fit the force distance data, and to determine the average contact area during the dwell period of the FVBS

mapping. A linear relation was found between the measured current at -5 V and the contact area extracted from the fitting, showing that direct measurement of the contact area is necessary for accurate charge carrier mobility determination. The contact area was then used to convert current-voltage data into JV data allowing the usage of a modified Mott-Gurney model to extract the charge carrier mobility and field dependence of the mobility. The fitting of the JKR model also allows extraction of the sample's Young's modulus, with the surface adhesion being extracted in the process of fitting.

FVBS mapping was demonstrated on two different systems: spin coated 80 - 120 nm thick P3HT on 5 nm of MoO_x deposited by OMBD on an ITO glass substrate; and OMBD grown VOPc deposited on a graphene coated copper foil.

The mechanical and electrical properties of as-cast and annealed P3HT were compared at different temperatures. Annealed P3HT tested at 130°C showed a direct correlation between the measured zero field mobility and the measured Young's modulus that was not present in the as-cast P3HT measured at 30°C, suggesting that the structure is different between the two samples. The average mobility increased from $5.1 \pm 0.1 \times 10^{-4}$ cm^2/Vs in the 30°C as-cast sample to $32.5 \pm 0.4 \times 10^{-4}$ cm^2/Vs in the 130°C annealed sample, meanwhile the average Young's modulus decreased from 0.86 ± 0.02 GPa to 0.69 ± 0.02 GPa. The spatial resolution of this data suggests that the trends observed were real, with clear areas of higher and lower mobility and Young's modulus being distinguishable. Spatial resolution and high data density also helped to determine when changes in measured parameters were due to the sample or the tip conditions changing; a feature of AFM that is notoriously hard to determine.

Using a smaller number of data points, the temperature dependence of the adhesion and zero field mobility was investigated for as-cast P3HT when heated from 70°C to 140°C and subsequently cooled over the same temperature range. The mobility was shown to rise with temperature, albeit with slightly lower values in the high temperature range when cooled. The adhesion in general rose with temperature, though it showed some interesting behaviour at specific temperatures, namely 140°C and 110°C. After cooling, the spread of adhesion across the area increased, suggesting some physical change in the sample after annealing. Unfortunately robust determination of the annealing effects could not be determined from this study, due to the effects of degradation over the timescales of the experiment.

The work on VOPc here focussed on comparing the mobility of VOPc grown at room temperature (RT) and VOPc grown at 130°C (HT). Firstly the morphology of RT grown VOPc was very different to that of the HT, with the HT presenting

large crystalline islands and the RT as polycrystalline films. FVBS was achieved on both of these topographies with only slight changes in the methodology. Quantitative analysis of the force curves gathered required that the Young's modulus of VOPc be measured with a stiffer cantilever in comparison to know moduli materials silicon and PMMA, yielding an average Young's modulus of 2.2 ± 0.2 GPa for VOPc. The contact area of the FVBS was then calculated using this value of the Young's modulus to yield average mobilities of 0.27 ± 0.04 cm^2/Vs and 0.14 ± 0.07 cm^2/Vs for the HT and RT VOPc respectively. The average mobility is higher and more uniform for HT VOPc, whilst for RT VOPc the mobility was found to vary wildly with some values higher than for the HT VOPc. This was due to the HT VOPc being oriented unfavourably for transport in a through-plane configuration, but its crystalline nature gave a more uniform response. By contrast, the random orientation of the RT VOPc meant that the mobilities measured had a very large spread.

In both cases, FVBS proved to give quantitative measures of the electrical and mechanical properties of the two systems studied.

5.1.2 Tr-EFM

Time resolved EFM is a technique recently devised and developed by the Ginger group to measure photo-excited charge with a high spatial and temporal resolution. The frequency shift of a cantilever oscillating above a surface is measured in response to an applied light pulse, and its time response analysed to determine the charging time of the tip surface capacitor.

In Chapter 4, Tr-EFM was used to study two BHJ OPV blends, P3HT:PCBM and PTB7:$PC_{70}BM$, both at room temperature and as a function of temperature. A new approach to calibrate the measurements was developed, allowing the surface photovoltage to be determines from the measured frequency shift. This required the frequency shift to be recorded as a function of applied tip bias, and as a function of the average tip-surface distance. The SPV extracted showed a logarithmic dependence as a function of light intensity, echoing the expected behaviour of V_{OC}, suggesting that this technique could be used to give a measure of V_{OC} at the nanoscale. The logarithmic dependence of the extracted SPV was evident in both the P3HT:PCBM and the PTB7:$PC_{70}BM$ samples tested, though the values of SPV measured were greater for the P3HT:PCBM than for the PTB7:$PC_{70}BM$ samples. Measurements were also made as a function of temperature, with the logarithmic behaviour persisting across the whole range measured. The P3HT:PCBM sample showed a complex dependence of the SPV on temperature, whilst the PTB7:$PC_{70}BM$

sample's SPV decreased with increasing temperature.

Tr-EFM was also used to look at the tip sample capacitance charging time of both of these samples, in measurements that were simultaneous to the determination of the SPV. For P3HT:PCBM this charging time was around 0.5 ms and had no discernible increase with light intensity or temperature, whilst the PTB7:$PC_{70}BM$ sample had a higher charging time of around 1 ms and showed some deviation with temperature showing charging times of around 2 ms at 110°C. Neither sample showed any deviation of charging time as a function of light intensity.

Maps of both the charging time and the measured SPV were made using a pixel by pixel approach on P3HT:PCBM. This showed no correlation between these two parameters however it did show the potential for spatially resolved measurements of this kind.

5.1.3 IM-KPFM

Intensity modulated Kelvin probe force microscopy (IM-KPFM) was used to study the discharging time of P3HT:PCBM and PTB7:$PC_{70}BM$. The approach is similar to that of transient photovoltage measurements in that a constant background light is used to create an equilibrium charge state. The surface potential is measured in response to a modulated incident light applied in pulses, and the potential difference between the modulated light being on or off is measured. This difference is investigated as a function of the modulation frequency and fitted to a stretched exponential to yield a timescale, τ, reminiscent of a recombination time. In this work, the surface potential was investigated as a function of the intensity of the background light applied and as a function of modulated light intensity. Increasing the background light intensity leads to shorter lifetimes measured, as expected from previous results with this method, though τ increases when the modulated light intensity was increased for P3HT:PCBM.

Using a set background and modulated light intensity, the temperature dependence of τ was investigated for P3HT:PCBM and PTB7:$PC_{70}BM$. P3HT:PCBM has a complicated response to temperature: when heated τ decreases from around 40 μs at 70°C to around 20 μs at 150°C. When cooled, τ appeared to increase as the temperature decreased though results below 100°C on cooling were not gathered. PTB7:$PC_{70}BM$ showed a rapid decrease in τ with increasing temperature, dropping from around 22 μs at 70°C to around 6 μs at 140°C. On cooling, this behaviour was reversed, rising to around 30 μs at 70°C and further to around 80 μs at 30°C.

Spatially resolved information can be gathered using a constant modulation frequency and scanning the sample in lift off SKPM mode. This was also demon-

strated for both sets of samples, though no definite conclusions could be drawn.

5.2 Further Work

5.2.1 FVBS

The work presented in Chapter 3 focussed mainly on P3HT. For direct comparison with the results from Tr-EFM and IM-KPFM studies, it would be interesting to apply FVBS to the blended structure P3HT:PCBM. It may also be beneficial to apply more sophisticated models of contact mechanics to this system to achieve more accurate contact areas and hence more accurate mobilities, though the applicability of these models will always be dependent on the specific tip and sample used. In terms of the P3HT work and its conclusions, it would be interesting to explore the nature of the mechanical and electrical properties as a function of the annealing temperature. However, the data gathered by this technique is often unreliable due to changing tip properties during measurement, hence this kind of study may be infeasible as it would require long time scale scans over many samples.

The addition of photodependence to FVBS would be a worthwhile aim, although initial calculations predict currents below the noise limit of the AFM used here. However, it may be possible to investigate this if an AFM was built with the explicit purpose of having high intensity incident illumination on the sample and a high sensitivity, low noise current pre-amplifier.

Although FVBS was applied here only to OSCs, the technique is generically applicable to conducting samples. Appropriate nanomechanical (JKR, DMT, Hertz..) and electrical (ohmic, diode, tunnelling...) models can be applied through similar methodology.

5.2.2 Tr-EFM

Firstly, it would be useful to obtain a full set of data on both systems tested for the full range of temperatures from 30°C to 150°C. Due to time constraints this was not possible. In order to properly compare τ from Tr-EFM measurements to the IM-KPFM values, τ_d should be extracted from the Tr-EFM data. For the results presented in Chapter 4 there was little difference between the results of τ_c and τ_d for Tr-EFM most likely due to the limited ($\sim 10\mu$s) time resolution of the AFM controller. However, if this was improved, the data from these two techniques may be more comparable.

With an increase in the time resolution and consistent calibration, the map-

ping of SPV and τ_c, and τ_d at high resolution on surfaces could prove to be a useful technique for elucidating how different regions of a sample respond to incident light. Equally, measuring the response to different wavelengths of applied light may be useful to investigate the behaviour of the donor or acceptor.

5.2.3 IM-KPFM

Like the Tr-EFM getting a full data set for IM-KPFM also took a lot of time, hence on the heating cycle the starting temperature tended to be high at 70°C. With more time to study starting at 30°C and covering up to 150°C on heating and cooling would be preferable. This may reveal the annealing behaviour of these samples more clearly. Equally, conducting comparisons between as-cast and annealed samples without the full temperature dependence may yield differences in the nanoscale behaviour of τ. Temperature dependent measurements above 150°C may yield interesting results. Higher temperatures may also only be possible in the non contact regimes offered by Tr-EFM and IM-KPFM.

The surface potential difference in IM-KPFM depended greatly on the background light intensity, with more background illumination creating shorter measured lifetimes and incomplete fitting. The background light allows IM-KPFM to be compared with transient photovoltage measurements, however, using a background light meant that the frequency dependent curves were incomplete due to the low lifetimes measured. If brighter light, or lights that were able to modulate more swiftly were used, it may be possible to determine the relationship between the charging time and discharging time. The exact relationship may be determined by simulating the behaviour with a range of charging and discharging timescales and examining the fitting behaviour of the scaling factor. Investigating this further may give unique information.

Both Tr-EFM and IM-KPFM measure timescales τ_c and τ_d, and a form of SPV. It would be beneficial to determine how these relate to V_{OC}, J_{SC} or the recombination lifetime of the systems studied. Since the values for τ measured in IM-KPFM agree very well with values achieved by Shuttle et al. [238] it is likely that the IM-KPFM measure of τ_d measures the charge carrier lifetime, though the possible contributions from the capacitance of the space charge region should also be further investigated [256]. However, it is likely that τ_c and τ_d measured by Tr-EFM correspond to capacitive properties of the material and their possible links to J_{SC} are worth exploring. Equally, the SPV measured by Tr-EFM is likely to be closely related, if not identical to V_{OC}, the validity of this, is also worth testing. Ideally, this could be performed en situ to the AFM so that the same light source

is used for both measurements. Shadow mask deposited top contacts would allow device measurements and AFM measurements to be taken on the same devices as the gaps between contacts are large enough for AFM measurements to occur. The relation of SPV measured in IM-KPFM to material properties is another question that warrants further study and could be achieved in a similar manner.

5.3 Appendix

5.3.1 JKR Model Fitting

The code for achieving a JKR model fitting is displayed below, along with an explanation of its usage.

```
function fitJKR(Ind, Force, W_coef, adh, Vsigma)
  wave Ind, Force, W_coef, Vsigma //Indentation wave, force wave,
    fitting coefficients and fitting errors
  variable adh //calculated adhesion


  W_coef[0] = {30e-9, 0.5e9, (adh), 1} //initial conditions
    corresponding to tip radius, combined Young's Modulus, adhesion
    force and a tolerance parameter.

  Variable V=DimSize(Ind,0)
  Variable W=DimSize(Force,0)

  Make/N=(V)/O fitwaveJKR
  fitwaveJKR=0
  Make/N=(V)/O ResidualJKR
  ResidualJKR=0
  Make/O/T/N=3 T_Constraints
  T_Constraints[0] = {"K0 < 100e-9", "K0 > 5e-9", "K1 > 0","K3 > 0.9","
    K3 < 1.1"} //constraints to the fitting variables

  Variable V_fitOptions = 4 //allows error reporting
  Variable V_FitError = 0
  Variable V_fitQuitReason=0
  FuncFit/NTHR=0/Q/W=2/ODR=0/H="0010" JKRDawnOffset W_coef  Ind /X=
    Force /D=fitwaveJKR /C=T_constraints /R=ResidualJKR /A=0 //fitting
    command
  wave W_sigma

  Vsigma=W_sigma
  Killwaves W_sigma
  variable x

  ResidualJKR=abs(ResidualJKR)  //error checking
  Duplicate/O Ind, IndAbs
  IndAbs=abs(Indabs)
  V=DimSize(Force,0)
  Redimension/N=(V-1) ResidualJKR, IndAbs
```

```
33    Integrate ResidualJKR /X=Force /D=Res_Int
      Integrate IndAbs /X=Force /D=Ind_Int
35    V=DimSize(Res_Int,0)
      W=DimSize(Ind_Int,0)
37    if(ResidualJKR > (0.1*IndAbs))
        x=1
39
      else
41      x=0
      endif
43
      return x
45  End
```

Here, "JKRDawnOffset" fits Equation (2.4) − (2.5), with a Levenberg-Marquardt least squares fitting method, finding the minimum of a function expressed as the sum of the squares of non-linear functions [259]. In this case there are only three fitting variables: the tip radius, combined Young's modulus and a tolerance parameter. The tolerance parameter allows for a 10% mis-calibration of the cantilever force by applying a scaling parameter to the force data, constrained between 0.9 and 1.1. This way, if there is an imperfect calibration, the fitting doesn't fail by default.

The residual wave is used as an indication of the quality of fit. The residual wave and the indentation data wave are integrated and if the integral value of the residual is over 10% of the indentation integral, the fitting is determined to have failed and a value of 1 is returned by the function. This is used to filter whether data points are accurate or not.

5.3.2 Modified Mott-Gurney Model Fitting

The procedure for fitting the modified Mott-Gurney model is displayed.

```
1   threadsafe function fitModMG(curr, bias, W_coef, Vsigma, dev)
      Wave curr, bias, W_coef, Vsigma, dev //Current and bias wave, then
        the coefficient and error waves, followed by the standard deviation
        of the current
3     variable x


5
      W_coef[0] = {1e-6,1e-4,0} //Initial conditions of the fitting
        corresponding to the zero field mobility, gamma and y offset.
7
      Variable V=DimSize(curr,0)
```

```
    Make/N=(V)/O fitwave  //fitting wave creation
    fitwave=0
    Make/N=(V)/O posRes //Residual wave creation
    posRes=0
    Variable V_fitOptions = 4 //values allow for error reporting
    Variable V_FitError = 0
    Variable V_FitQuitReason=0

    FuncFit/NTHR=0/Q/W=2/ODR=0 ModMG W_coef  curr /R=posRes /X=bias /D=
      fitwave /I=1 /W=dev //fitting command
    Wave W_sigma

    Vsigma=W_sigma
    x=V_chisq

    return  V_FitQuitReason
End
```

The residual wave, posRes, describes the difference between the fitting and the data and can be used to check the quality of the fit. The variable V_ FitQuitReason, depends on the exit parameters of the fitting algorithm. If the fitting performs correctly, V_ FitQuitReason is equal to zero, if this is not the case the fitting is deemed inaccurate and the result not shown. On completion of a successful fit, the fit parameters are extracted and the mobility is scaled using the contact area calculated from the JKR fitting.

5.3.3 Tr-EFM Macro

Before the measurement takes place, the tip is engaged to within range of the sample, and delayed here for 20 s. The delay after this engage allows drift from a large movement in the z-piezo to settle, any further movements should not cause significant drift. This is not shown in Figure 5.1 as, providing the temperature is kept constant, this only needs to occur once. After this occurs, the steps in Figure 5.1 can be iterated over, each iteration can occur at a distinct temperature, lift height, tip bias or light intensity.

1 The tip is engaged onto the sample's surface and the program delays for 0.2 s to ensure any movement is finished.

2-6 The output signals are then set up. The AFM will need to read in the amplitude and the phase, so blank waves are created here for them. The light signal and the bias applied to the tip are controlled by a procedure that writes

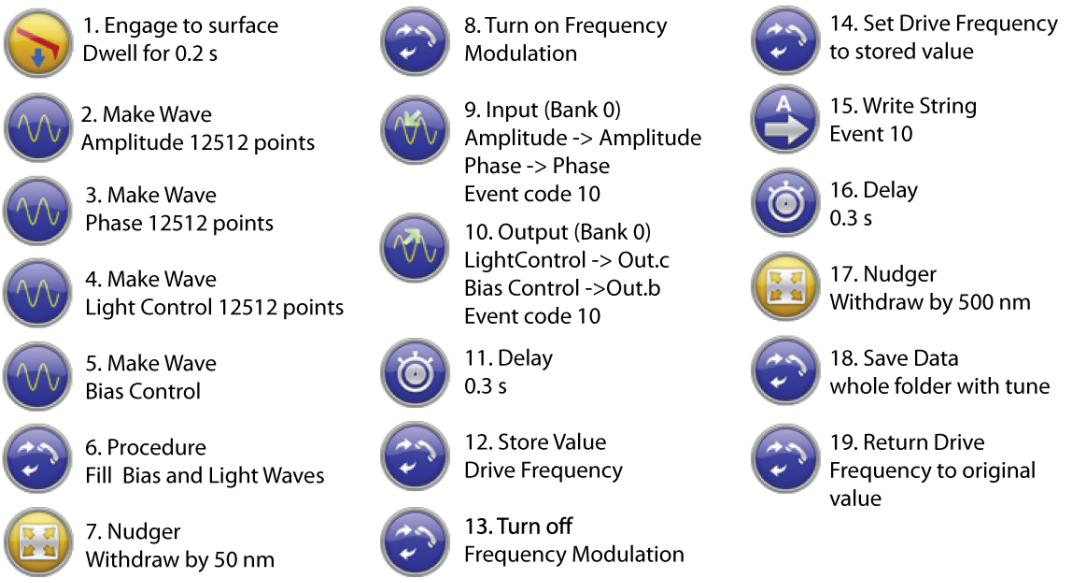

Figure 5.1: Tr-EFM macro: showing elements contained within a loop structure common to each Tr-EFM measurement.

these waves before each separate experiment. Setting up these waves takes approximately 0.2 s so the tip does not dwell on the surface. A pre-set tip bias is also applied at this point.

7 The tip is withdrawn to a pre-set lift height above the surface.

8 Frequency modulation is turned on allowing the effective cantilever resonance frequency to be found at the measurement bias and tip height.

9-10 These steps tell the program what will be transmitted, measured and when to do so. The Input and Output steps point to the waves that were created earlier, which are then sent to the appropriate inputs and outputs in the AFM controller. The event code displayed here is the command to start the reading and writing of the data for the measurement.

11 This short delay allows the frequency modulation to settle to an equilibrium value before the experiment starts.

12 The drive frequency reached by the feedback loop is stored.

13 The feedback loop is turned off as the phase during the measurement needs to be recorded.

14 The stored drive frequency is applied to the piezo, this is the frequency used during measurement.

15 The event code is written to the AFM, starting the measurement.

16 This 0.3 s delay allows the measurement to complete.

17 The nudge command withdraws the tip to a safe distance from the surface so that any drift does not result in the tip crashing.

18 All data gathered is stored, including the cantilever tuning information (not shown in Figure 5.1).

19 The cantilever drive frequency is restored to the original value from the tuning.

Changes to the process must be made for temperature dependent measurements as 500 nm is no longer a safe distance to retract when the temperature rises. Hence, the pre-engage of the tip and a withdraw command need to be added in an external loop whenever the temperature rises.

5.3.4 IM-KPFM Macro

Figure 5.2 displays a simplified procedure for performing IM-KPFM. The initial engage allows the tip to be close to the sample minimising z piezo drift during the experiment. Once this is completed the waves are allocated in which to store the data and the experimental parameters are initialised. Typically 3 modulation pulses are used per point in the experiment, the light intensity of the modulated light is set at its maximum value (1 corresponding to 10 V on the LEDs) and the force distance i.e. distance above the surface used for measurement was 50 nm. A loop structure is then shown, this allows the modulation frequency to be iterated over. In reality there is a second loop repeating the experiment 10 times at each frequency. The other parameters, light intensity and force distance can also be iterated over in the same manner as the modulation frequency.

The measurement commences when a force curve is taken, positioning the tip 50 nm above the samples surface, a short delay allows this to be fully completed. The background light is then turned on followed by the surface potential feedback. While the feedback loop is operating the output and input waves are setup and the experiment is performed. The slight delay here allows the feedback to be stable before the measurement occurs. The feedback and background light are then turned off and the data is saved. A nudger operation is then used to withdraw the tip a short

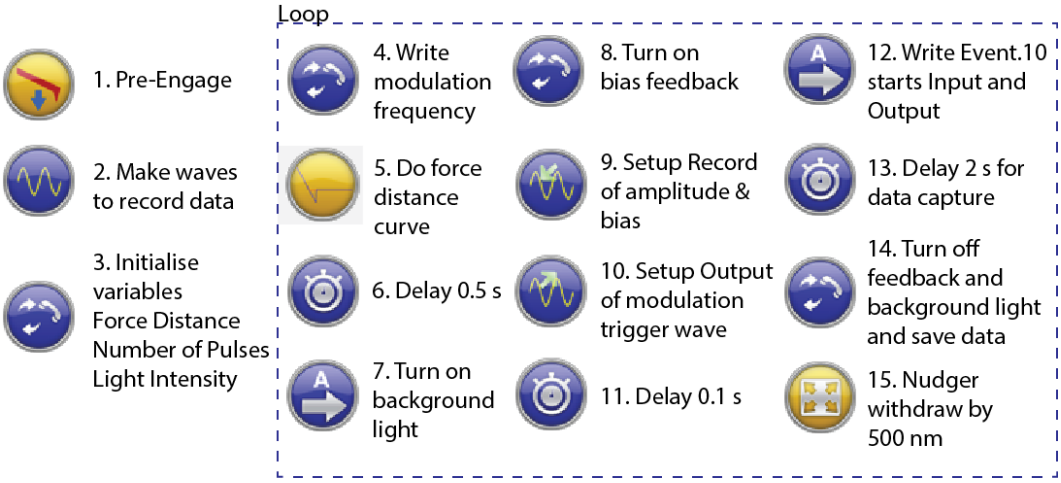

Figure 5.2: Simplified Macro for IM-KPFM experiment, a loop structure is defined by the blue box.

distance before the next iteration commences. Once complete the tip withdraws. Each single measurement takes around 5 s.

5.3.5 IM-KPFM Analysis

The timing wave from the AFM is used to define when the modulation is on or off and the program averages the on and off sections independently. The difference between the modulated light being on and off is calculated and normalised to the response at 10 Hz, which is defined as 0.5, i.e. the response should be halfway between on and off for low modulation frequencies. The responses at each frequency are averaged, this is normally an average of 10, though the exact number can be changed in the experiment. A stretched exponential is fitted to the normalised difference as a function of modulation frequency. The fitting follows the following procedure

```
Make/N=4/O W_coef
W_coef[0]={10^-4,0.5,1,0.5} //Initial conditions
Make/O/T/N=3 T_Constraints //Constraints
T_Constraints[0] = {"K0 > 0","K1 > 0","K2 > 0","K2 < 0.99","K3 > 0","
  K3 < 1.5"} //, "K2 > 0","K2 < 0.95" //Constraints
FuncFit/NTHR=0/Q/W=2/H="0000" FitKPM W_coef NormDif[1,12] /X=
  waveAvMF /D=Fit /C=T_Constraints /I=1/W=waveSdDif
```

where the equation fitted called FitKPM corresponds to

$$V_{sp,avg}(f) = C + S_c \frac{\tau f \Gamma\left(\frac{1}{\beta}, \left(\frac{1}{2\tau f}\right)^{\beta}\right)}{\beta} \tag{5.1}$$

where C is the normalised value at 10 Hz, S_c is the scaling factor, Γ describes the incomplete mathematical gamma function, β is the stretching factor, f is the frequency of modulation and τ is the time scale. The initial conditions given by W_coef describe τ, β, S_c and C respectively. This fitting also requires these variables to be constrained with all four variables being defined to be positive, and S_c being less than 1. C can and should be fixed at 0.5 providing the normalisation is correct and the data matches expected patterns. The fitting also takes account of the standard deviation from the mean in order to increase the accuracy of the fitting.

Bibliography

[1] D. Wood, I. Hancox, T. S. Jones, and N. R. Wilson. Quantitative Nanoscale Mapping with Temperature Dependence of the Mechanical and Electrical Properties of Poly(3-Hexythiophene) by Conductive Atomic Force Microscopy. *J. Phys. Chem. C*, page 150427142253007, 2015.

[2] A. J. Marsden, L. A. Rochford, D. Wood, A. J. Ramadan, Z. P. L. Laker, T. S. Jones, and N. R. Wilson. Growth of Large Crystalline Grains of Vanadyl-Phthalocyanine without Epitaxy on Graphene. *Advanced Functional Materials*, pages 1–9, 2016.

[3] L. L. Kazmerski. Photovoltaics: A review of cell and module technologies. *Renew. Sustain. Energy Rev.*, 1(1-2):71–170, 1997.

[4] M. A. Green. Photovoltaics: Technology overview. *Energy Policy*, 28(14):989–998, 2000.

[5] B. Parida, S. Iniyan, and R. Goic. A review of solar photovoltaic technologies. *Renew. Sustain. Energy Rev.*, 15(3):1625–1636, 2011.

[6] R. Williams. Bequerel photovoltaic effect in binary compounds. *J. Chem. Phys.*, 32(5):1505–1514, 1960.

[7] M. A. Green, A. Ho-Baillie, and H. J. Snaith. The emergence of perovskite solar cells. *Nat. Photonics*, 8(7):506–514, 2014.

[8] J. Perlin. *From space to earth: the story of solar electricity*. Earthscan, 1999.

[9] M. A. Green. High efficiency silicon solar cells. In *Seventh EC Photovoltaic Solar Energy Conference*, pages 681–687. Springer, 1987.

[10] National Renewable Energy Laboratory. Best Research-Cell Efficiencies. `http://www.nrel.gov/ncpv/images/efficiency_chart.jpg`, Accessed on 27/07/2016.

[11] The Economist Newspaper Limited. Sunny Uplands. http://www.economist.com/news/21566414-alternative-energy-will-no-longer-be-alternative-sunny-uplands, Accessed on 06/01/2017.

[12] J. Markoff. Start-Up Sells Solar Panels at Lower-Than-Usual Cost, dec 2007.

[13] D. E. Carlson and C. R. Wronski. Amorphous silicon solar cell. *Appl. Phys. Lett.*, 28(11):671–673, 1976.

[14] J. Britt and C. Ferekides. Thin-film CdS/CdTe solar cell with 15.8% efficiency. *Appl. Phys. Lett.*, 62(22):2851–2852, 1993.

[15] K. Ramanathan, M. A. Contreras, C. L. Perkins, S. Asher, F. S. Hasoon, J. Keane, D. Young, M. Romero, W. Metzger, R. Noufi, J. Ward, and A. Duda. Properties of 19.2% efficiency ZnO/CdS/CuInGaSe2 thin-film solar cells. *Prog. Photovoltaics Res. Appl.*, 11(4):225–230, 2003.

[16] EnergyTrend of TrendForce Corp. PV Spot Price. http://pv.energytrend.com/pricequotes.html, Accessed on 06/01/2017.

[17] F. Kessler and D. Rudmann. Technological aspects of flexible CIGS solar cells and modules. *Sol. Energy*, 77(6):685–695, 2004.

[18] V. M. Fthenakis. Life cycle impact analysis of cadmium in CdTe PV production. *Renew. Sustain. Energy Rev.*, 8(4):303–334, aug 2004.

[19] D. M. K. Cyrus Wadia, A. Paul Alivisatos. Materials Availability Expands the Opportunity for Large-Scale Photovoltaics Deployment. *Environ. Sci. Technol*, 43(6):2072–2077, 2009.

[20] P. Sinsermsuksakul, K. Hartman, S. Bok Kim, J. Heo, L. Sun, H. Hejin Park, R. Chakraborty, T. Buonassisi, and R. G. Gordon. Enhancing the efficiency of SnS solar cells via band-offset engineering with a zinc oxysulfide buffer layer. *Appl. Phys. Lett.*, 102(5):053901, 2013.

[21] G. Conibeer. Third-generation photovoltaics. *Mater. Today*, 10(11):42–50, 2007.

[22] W. Shockley and H. J. Queisser. Detailed balance limit of efficiency of p-n junction solar cells. *J. Appl. Phys.*, 32(3):510–519, 1961.

[23] M. A. Green. Third generation photovoltaics: Solar cells for 2020 and beyond. *Physica E: Low-Dimensional Systems and Nanostructures*, 14(1-2):65–70, 2002.

[24] F. C. Krebs. Polymer solar cell modules prepared using roll-to-roll methods: Knife-over-edge coating, slot-die coating and screen printing. *Solar Energy Materials and Solar Cells*, 93(4):465–475, 2009.

[25] M. Pope and C. E. Swenberg. *Electronic processes in organic crystals and polymers*. Oxford University Press on Demand, 1999.

[26] J. Park. Full color OLED and method of fabricating the same, February 9 2010. US Patent 7,659,661.

[27] F. Garnier, R. Hajlaoui, A. Yassar, and P. Srivastava. All-polymer field-effect transistor realized by printing techniques. *Science*, 265(5179):1684–1686, 1994.

[28] SolarTE. Technology. `http://solarte.de/en/#welcome`, Accessed on 25/08/2016.

[29] Heliatek. Heliatek. `http://www.heliatek.com/en/`, Accessed on 25/08/2016.

[30] C. W. Tang. Two-layer organic photovoltaic cell. *Applied Physics Letters*, 48(2):183–185, 1986.

[31] B. Kippelen and J.-L. Brédas. Organic photovoltaics. *Energy & Environmental Science*, 2(3):251, 2009.

[32] J. J. M. Halls, C. A. Walsh, N. Greenham, C., E. A. Marseglia, R. Friend, H., S. C. Moratti, A. Holmes, and B. Efficient photodiodes from interpenetrating polymer networks. *Nature*, 376(6540):498–500, 1995.

[33] K. Kawano, R. Pacios, D. Poplavskyy, J. Nelson, D. D. C. Bradley, and J. R. Durrant. Degradation of organic solar cells due to air exposure. *Solar Energy Materials and Solar Cells*, 90(20):3520–3530, 2006.

[34] M. Jørgensen, K. Norrman, and F. C. Krebs. Stability/degradation of polymer solar cells. *Solar Energy Materials and Solar Cells*, 92(7):686–714, 2008.

[35] G. Dennler, C. Lungenschmied, H. Neugebauer, N. Sariciftci, M. Latrèche, G. Czeremuszkin, and M. Wertheimer. A new encapsulation solution for flexible organic solar cells. *Thin Solid Films*, 511-512:349–353, jul 2006.

[36] J. Ahmad, K. Bazaka, L. J. Anderson, R. D. White, and M. V. Jacob. Materials and methods for encapsulation of OPV: A review. *Renewable and Sustainable Energy Reviews*, 27:104–117, 2013.

[37] R. Søndergaard, M. Hösel, D. Angmo, T. T. Larsen-Olsen, and F. C. Krebs. Roll-to-roll fabrication of polymer solar cells. *Materials Today*, 15(1-2):36–49, 2012.

[38] H. Kim, C. M. Gilmore, A. Piqué, J. S. Horwitz, H. Mattoussi, H. Murata, Z. H. Kafafi, and D. B. Chrisey. Electrical, optical, and structural properties of indiumtinoxide thin films for organic light-emitting devices. *Journal of Applied Physics*, 86(11):6451–6461, 1999.

[39] M. Pitts. Endangered elements? *New Scientist*, 209(2799):26–27, 2011.

[40] A. J. Medford, M. R. Lilliedal, M. Jørgensen, D. Aarø, H. Pakalski, J. Fyenbo, and F. C. Krebs. Grid-connected polymer solar panels: initial considerations of cost, lifetime, and practicality. *Optics Express*, 18(103):A272–A285, 2010.

[41] J.-S. Yu, I. Kim, J.-S. Kim, J. Jo, T. T. Larsen-Olsen, R. R. Søndergaard, M. Hösel, D. Angmo, M. Jørgensen, and F. C. Krebs. Silver front electrode grids for ITO-free all printed polymer solar cells with embedded and raised topographies, prepared by thermal imprint, flexographic and inkjet roll-to-roll processes. *Nanoscale*, 4(19):6032, 2012.

[42] T. Tokuno, M. Nogi, M. Karakawa, J. Jiu, T. T. Nge, Y. Aso, and K. Suganuma. Fabrication of silver nanowire transparent electrodes at room temperature. *Nano Research*, 4(12):1215–1222, 2011.

[43] Y. Galagan, J.-E. J.M. Rubingh, R. Andriessen, C.-C. Fan, P. W.M. Blom, S. C. Veenstra, and J. M. Kroon. ITO-free flexible organic solar cells with printed current collecting grids. *Solar Energy Materials and Solar Cells*, 95(5):1339–1343, 2011.

[44] M. Manceau, D. Angmo, M. Jørgensen, and F. C. Krebs. ITO-free flexible polymer solar cells: From small model devices to roll-to-roll processed large modules. *Org. Electron.*, 12(4):566–574, 2011.

[45] Y. Galagan, E. W. C. Coenen, S. Sabik, H. H. Gorter, M. Barink, S. C. Veenstra, J. M. Kroon, R. Andriessen, and P. W. M. Blom. Evaluation of ink-jet printed current collecting grids and busbars for ITO-free organic solar cells. *Solar Energy Materials and Solar Cells*, 104:32–38, 2012.

[46] T. Aernouts, P. Vanlaeke, W. Geens, J. Poortmans, P. Heremans, S. Borghs, R. Mertens, R. Andriessen, and L. Leenders. Printable anodes for flexible organic solar cell modules. *Thin Solid Films*, 451-452:22–25, 2004.

[47] Y.-Y. Choi, S. J. Kang, H.-K. Kim, W. M. Choi, and S.-I. Na. Multilayer graphene films as transparent electrodes for organic photovoltaic devices. *Solar Energy Materials and Solar Cells*, 96:281–285, 2012.

[48] J. E. Carlé and F. C. Krebs. Technological status of organic photovoltaics (OPV). *Solar Energy Materials and Solar Cells*, 119:309–310, dec 2013.

[49] M. Jørgensen, J. E. Carlé, R. R. Søndergaard, M. Lauritzen, N. A. Dagnæs-Hansen, S. L. Byskov, T. R. Andersen, T. T. Larsen-Olsen, A. P. Böttiger, B. Andreasen, L. Fu, L. Zuo, Y. Liu, E. Bundgaard, X. Zhan, H. Chen, and F. C. Krebs. The state of organic solar cellsA meta analysis. *Solar Energy Materials and Solar Cells*, 119:84–93, dec 2013.

[50] K. Antoine. Fermi level, work function and vacuum level. *Mater. Horizons*, 1(1):96, 2015.

[51] J. L. Brédas, D. Beljonne, V. Coropceanu, and J. Cornil. Charge-transfer and energy-transfer processes in π-conjugated oligomers and polymers: A molecular picture. *Chemical Reviews*, 104(11):4971–5003, 2004.

[52] Y. Kim, S. Cook, S. M. Tuladhar, S. A. Choulis, J. Nelson, J. R. Durrant, D. D. C. Bradley, M. Giles, I. McCulloch, C.-S. Ha, and M. Ree. A strong regioregularity effect in self-organizing conjugated polymer films and high-efficiency polythiophene:fullerene solar cells. *Nature Materials*, 5(3):197–203, 2006.

[53] T. M. Clarke and J. R. Durrant. Charge carrier photogeneration in organic solar cells. *Chem. Rev.*, 110:6736–6767, 2010.

[54] R. R. Lunt, N. C. Giebink, A. A. Belak, J. B. Benziger, and S. R. Forrest. Exciton diffusion lengths of organic semiconductor thin films measured by spectrally resolved photoluminescence quenching. *Journal of Applied Physics*, 105(5), 2009.

[55] R. Steim, F. R. Kogler, and C. J. Brabec. Interface materials for organic solar cells. *Journal of Materials Chemistry*, 20(13):2499, 2010.

[56] N. Beaumont, I. Hancox, P. Sullivan, R. A. Hatton, and T. S. Jones. Increased efficiency in small molecule organic photovoltaic cells through electrode modification with self-assembled monolayers. *Energy Environ. Sci.*, 4:1708–1711, 2011.

[57] A. Cravino, P. Schilinsky, and C. J. Brabec. Characterization of organic solar cells: The importance of device layout. *Advanced Functional Materials*, 17(18):3906–3910, 2007.

[58] V. Shrotriya, G. Li, Y. Yao, T. Moriarty, K. Emery, and Y. Yang. Accurate measurement and characterization of organic solar cells. *Advanced Functional Materials*, 16(15):2016–2023, 2006.

[59] Newport. Technical Notes: Simulation of Solar Irradiation. `https://www.newport.com/n/simulation-of-solar-irradiation`, Accessed on 26/09/2016.

[60] B. P. Rand, J. Genoe, P. Heremans, and J. Poortmans. Solar cells utilizing small molecular weight organic semiconductors. *Prog. Photovoltaics Res. Appl.*, 15(8):659–676, 2007.

[61] F. Ortmann, F. Bechstedt, and K. Hannewald. Charge transport in organic crystals: Theory and modelling. *Phys. Status Solidi B-Basic Solid State Phys.*, 248(3):511–525, 2011.

[62] A. Miller and E. Abrahams. Impurity conduction at low concentrations. *Physical Review*, 120(3):745–755, 1960.

[63] M. Pollak and B. Shklovskii. *Hopping transport in solids*, volume 28. Elsevier, 1991.

[64] F. Laquai, D. Andrienko, R. Mauer, and P. W. M. Blom. Charge carrier transport and photogeneration in P3HT:PCBM photovoltaic blends. *Macromolecular Rapid Communications*, 36(11):1001–1025, 2015.

[65] H. Sirringhaus, T. Sakanoue, and J.-F. Chang. Charge-transport physics of high-mobility molecular semiconductors. *Phys. Status Solidi*, 249(9):1655–1676, 2012.

[66] A. Troisi, D. L. Cheung, and D. Andrienko. Charge transport in semiconductors with multiscale conformational dynamics. *Phys. Rev. Lett.*, 102(11), 2009.

[67] C. Poelking, K. Daoulas, A. Troisi, and D. Andrienko. Morphology and charge transport in P3HT: A theorist's perspective. In *Adv. Polym. Sci.*, number May 2012, pages 139–180. 2014.

[68] S. M. Sze and K. K. Ng. Metal-Insulator-Semiconductor Capacitors. In *Phys. Semicond. Devices*, pages 7–74. John Wiley & Sons, Inc., Hoboken, NJ, USA, apr 2006.

[69] N. F. Mott and R. W. Gurney. *Electronic processes in ionic crystals*. Oxford University Press, 2nd edition edition, 1948.

[70] P. N. Murgatroyd. Theory of space-charge-limited current enhanced by Frenkel effect. *J. Phys. D. Appl. Phys.*, 3(2):308, 1970.

[71] C. Tanase, P. Blom, and D. de Leeuw. Origin of the enhanced space-charge-limited current in poly(p-phenylene vinylene). *Physical Review B*, 70(19):193202, 2004.

[72] R. Coehoorn, W. F. Pasveer, P. A. Bobbert, and M. A. J. Michels. Charge-carrier concentration dependence of the hopping mobility in organic materials with Gaussian disorder. *Physical Review B - Condensed Matter and Materials Physics*, 72(15):1–20, 2005.

[73] C. Groves, J. C. Blakesley, and N. C. Greenham. Effect of charge trapping on geminate recombination and polymer solar cell performance. *Nano Lett.*, 10(3):1063–1069, 2010.

[74] Z. Chiguvare and V. Dyakonov. Trap-limited hole mobility in semiconducting poly(3-hexylthiophene). *Phys. Rev. B*, 70(23):235207, 2004.

[75] J. Szmytkowski. On the tendency of temperature and electric field dependences of interface recombination in a P3HT:PCBM organic bulk heterojunction solar cell. *Semicond. Sci. Technol.*, 26(10):105012, 2011.

[76] O. Oklobia and T. Shafai. Correlation between charge carriers mobility and nanomorphology in a blend of P3HT/PCBM bulk heterojunction solar cell: Impact on recombination mechanisms. *Sol. Energy Mater. Sol. Cells*, 122:158–163, 2014.

[77] A. Pivrikas, G. Juska, A. K., M. Scharber, A. Mozer, N. Sariciftci, H. Stubb, and R. Österbacka. "Charge carrier transport and recombination in bulk-heterojunction solar-cells", in Organic Photovoltaics VI, Zakya H. Kafafi; Paul A. Lane, Editors,. In *Proc. SPIE Vol. 5938 , 59380N.*, 2005.

[78] A. K. Thakur, G. Wantz, G. Garcia-Belmonte, J. Bisquert, and L. Hirsch. Temperature dependence of open-circuit voltage and recombination processes in polymer-fullerene based solar cells. *Sol. Energy Mater. Sol. Cells*, 95(8):2131–2135, 2011.

[79] A. B. Matheson, S. J. Pearson, A. Ruseckas, and I. D. W. Samuel. Charge Pair Dissociation and Recombination Dynamics in a P3HT PCBM Bulk Heterojunction. *J. Phys. Chem. Lett.*, 4(23):4166–4171, 2013.

[80] L. Kronik and Y. Shapira. Surface photovoltage phenomena: Theory, experiment, and applications. *Surf. Sci. Rep.*, 37(1):1–206, 1999.

[81] B. Goldstein, D. Redfield, D. J. Szostak, and L. A. Carr. Electrical characterization of solar cells by surface photovoltage. *Appl. Phys. Lett.*, 39(3):258–260, 1981.

[82] D. J. Szostak and B. Goldstein. Photovoltage profiling of hydrogenated amorphous Si solar cells. *J. Appl. Phys.*, 56(2):522, 1984.

[83] E. Johnson. Measurement of minority carrier lifetimes with the surface photovoltage. *Journal of Applied Physics*, 28(11):1349–1353, 1957.

[84] C. Munakata, N. Honma, and H. Itoh. A non-destructive method for measuring lifetimes for minority carriers in semiconductor wafers using frequency-dependent ac photovoltages. *Japanese Journal of Applied Physics*, 22(2A):L103, 1983.

[85] R. J. Hamers and D. G. Cahill. Ultrafast time resolution in scanned probe microscopies. *Applied Physics Letters*, 57(19):2031, 1990.

[86] Y. J. Lee, J. Wang, and J. W. P. Hsu. Surface photovoltage characterization of organic photovoltaic devices. *Appl. Phys. Lett.*, 103(May 2016):5, 2013.

[87] M. T. Dang, L. Hirsch, and G. Wantz. P3HT:PCBM, Best Seller in Polymer Photovoltaic Research. *Adv. Mater.*, 23(31):3597–3602, 2011.

[88] G. Li, V. Shrotriya, Y. Yao, and Y. Yang. Investigation of Annealing Effects and Film Thickness Dependence of Polymer Solar Cells based on Poly(3-hexylthiophene). *J. Appl. Phys.*, 98(4):043704, 2005.

[89] Y. Kim, S. A. Choulis, J. Nelson, D. D. C. Bradley, S. Cook, and J. R. Durrant. Device annealing effect in organic solar cells with blends of regioregular poly(3-hexylthiophene) and soluble fullerene. *Applied Physics Letters*, 86(6), 2005.

[90] W. Bagienski and M. Gupta. Temperature dependence of polymer/fullerene organic solar cells. *Sol. Energy Mater. Sol. Cells*, 95(3):933–941, 2011.

[91] M. T. Dang, G. Wantz, H. Bejbouji, M. Urien, O. J. Dautel, L. Vignau, and L. Hirsch. Polymeric solar cells based on P3HT:PCBM: Role of the casting solvent. *Solar Energy Materials and Solar Cells*, 95(12):3408–3418, 2011.

[92] C. Nicolet, D. H. Deribew, C. Renaud, C. Brochon, E. Cloutet, L. Vignau, H. Cramail, M. Geoghegan, and G. Hadziioannou. Molecular weight P3HT dependence of the binary phase diagram with PCBM and its relationship to the photovoltaic performance. 52(2):966–967, 2011.

[93] C. Goh, R. J. Kline, M. D. McGehee, E. N. Kadnikova, and J. M. J. Frechet. Molecular-weight-dependent mobilities in regioregular poly(3-hexylthiophene) diodes. *Applied Physics Letters*, 86(12):122110, 2005.

[94] R. Kline, M. McGehee, and E. Kadnikova. Dependence of regioregular poly (3-hexylthiophene) film morphology and field-effect mobility on molecular weight. *Macromolecules*, 38:3312–3319, 2005.

[95] M. L. Jones, D. M. Huang, B. Chakrabarti, and C. Groves. Relating molecular morphology to charge mobility in semicrystalline conjugated polymers. *J. Phys. Chem. C*, 120(8):4240–4250, 2016.

[96] S. Berson, R. DeBettignies, S. Bailly, and S. Guillerez. Poly(3-hexylthiophene) fibers for photovoltaic applications. *Advanced Functional Materials*, 17(8):1377–1384, 2007.

[97] Y. Zhao, S. Shao, Z. Xie, Y. Geng, and L. Wang. Effect of poly (3-hexylthiophene) nanofibrils on charge separation and transport in polymer bulk heterojunction photovoltaic cells. *The Journal of Physical Chemistry C*, 113(39):17235–17239, 2009.

[98] Z. Wu, A. Petzold, T. Henze, T. Thurn-Albrecht, R. H. Lohwasser, M. Sommer, and M. Thelakkat. Temperature and molecular weight dependent hierarchical equilibrium structures in semiconducting poly(3-hexylthiophene). *Macromolecules*, 43(10):4646–4653, 2010.

[99] R. Noriega, J. Rivnay, K. Vandewal, F. P. V. Koch, N. Stingelin, P. Smith, M. F. Toney, and A. Salleo. A general relationship between disorder, aggregation and charge transport in conjugated polymers. *Nature materials*, 12(11):1038–44, 2013.

[100] P. E. Hopkinson, P. A. Staniec, A. J. Pearson, A. D. F. Dunbar, T. Wang, A. J. Ryan, R. A. L. Jones, D. G. Lidzey, and A. M. Donald. A Phase Diagram of the P3HT:PCBM organic photovoltaic system: Implications for device processing and performance. *Macromolecules*, 44(8):2908–2917, 2011.

[101] T. T. Ngo, D. N. Nguyen, and V. T. Nguyen. Glass transition of PCBM, P3HT and their blends in quenched state. *Advances in Natural Sciences: Nanoscience and Nanotechnology*, 3(4):045001, 2012.

[102] B. A. Collins, J. R. Tumbleston, and H. Ade. Miscibility, crystallinity, and phase development in P3HT/PCBM solar cells: Toward an enlightened understanding of device morphology and stability. *J. Phys. Chem. Lett.*, 2(24):3135–3145, 2011.

[103] D. Chen, A. Nakahara, D. Wei, D. Nordlund, and T. P. Russell. P3HT/PCBM bulk heterojunction organic photovoltaics: Correlating efficiency and morphology. *Nano Letters*, 11(2):561–567, 2011.

[104] A. H. Rice, R. Giridharagopal, S. X. Zheng, F. S. Ohuchi, D. S. Ginger, and C. K. Luscombe. Controlling vertical morphology within the active layer of organic photovoltaics using poly(3-hexylthiophene) nanowires and phenyl-C61-butyric acid methyl ester. *ACS nano*, 5(4):3132–40, 2011.

[105] F. Machui, S. Rathgeber, N. Li, T. Ameri, and C. J. Brabec. Influence of a ternary donor material on the morphology of a P3HT:PCBM blend for organic photovoltaic devices. *Journal of Materials Chemistry*, 22(31):15570, 2012.

[106] L. Lu and L. Yu. Understanding low bandgap polymer PTB7 and optimizing polymer solar cells based on IT. *Adv. Mater.*, 26(26):4413–4430, 2014.

[107] B. Ebenhoch, S. a.J. Thomson, K. Genevičius, G. Juška, and I. D. Samuel. Charge carrier mobility of the organic photovoltaic materials PTB7 and PC71BM and its influence on device performance. *Org. Electron.*, 22:62–68, 2015.

[108] Y. Huang, E. J. Kramer, A. J. Heeger, and G. C. Bazan. Bulk Heterojunction Solar Cells: Morphology and Performance Relationships. *Chem. Rev.*, 114(14):7006–7043, 2014.

[109] F. Liu, W. Zhao, J. R. Tumbleston, C. Wang, Y. Gu, D. Wang, A. L. Briseno, H. Ade, and T. P. Russell. Understanding the morphology of PTB7:PCBM blends in organic photovoltaics. *Advanced Energy Materials*, 4(5):1–9, 2014.

[110] J. Kniepert, I. Lange, J. Heidbrink, J. Kurpiers, T. J. Brenner, L. J. A. Koster, and D. Neher. Effect of solvent additive on generation, recombination, and extraction in ptb7: Pcbm solar cells: A conclusive experimental and numerical simulation study. *The Journal of Physical Chemistry C*, 119(15):8310–8320, 2015.

[111] Sigma-Aldrich. Vanadyl Phthalocyanine. `http://www.sigmaaldrich.com/catalog/product/aldrich/791997?lang=en&region=GB`, Accessed on 16/01/2017.

[112] X. J. Yu, J. B. Xu, W. Y. Cheung, and N. Ke. Optimizing the growth of vanadyl-phthalocyanine thin films for high-mobility organic thin-film transistors. *J. Appl. Phys.*, 102(10), 2007.

[113] H. Wang, D. Song, J. Yang, B. Yu, Y. Geng, and D. Yan. High mobility vanadyl-phthalocyanine polycrystalline films for organic field-effect transistors. *Appl. Phys. Lett.*, 90(25):2005–2008, 2007.

[114] L. Wang, G. Liu, H. Wang, D. Song, B. Yu, and D. Yan. Switch-on transient behavior of vanadium phthalocyanine based organic transistors. *Appl. Phys. Lett.*, 91(6):2005–2008, 2007.

[115] K. S. Karimov, B. F. Irgaziev, I. Qazi, I. Murtaza, Z. M. Karieva, and H. B. Senin. Electric Properties of Organic-on-Inorganic n-Si / VOPc Heterojunction. 11:115–119, 2009.

[116] H. Ying Mao, R. Wang, Y. Wang, T. Chao Niu, J. Qiang Zhong, M. Yang Huang, D. Chen Qi, K. Ping Loh, A. Thye Shen Wee, and W. Chen. Chemical vapor deposition graphene as structural template to control interfacial molecular orientation of chloroaluminium phthalocyanine. *Appl. Phys. Lett.*, 99(9), 2011.

[117] N. Balke, D. Bonnell, D. S. Ginger, and M. Kemerink. Scanning probes for new energy materials: Probing local structure and function. *Mrs Bulletin*, 37(7):633–637, 2012.

[118] G. Binnig and C. F. Quate. Atomic Force Microscope. *Physical Review Letters*, 56(9):930–933, 1986.

[119] J. E. Lennard-Jones. Cohesion. *Proceedings of the Physical Society*, 43(5):461, 1931.

[120] A. J. Marsden, M. Phillips, and N. R. Wilson. Friction force microscopy: a simple technique for identifying graphene on rough substrates and mapping the orientation of graphene grains on copper. *Nanotechnology*, 24(25):255704, 2013.

[121] X. N. Xie, H. J. Chung, C. H. Sow, and A. T. S. Wee. Nanoscale materials patterning and engineering by atomic force microscopy nanolithography. 54:1–48, 2006.

[122] A. M. Goossens, V. E. Calado, A. Barreiro, K. Watanabe, T. Taniguchi, and L. M. K. Vandersypen. Mechanical cleaning of graphene. *Applied Physics Letters*, 100(7):98–101, 2012.

[123] N. Lindvall, A. Kalabukhov, and A. Yurgens. Cleaning graphene using atomic force microscope. *Journal of Applied Physics*, 111(6), 2012.

[124] H. Hamaker. The Londonvan der Waals attraction between spherical particles. *Physica*, 4(10):1058–1072, 1937.

[125] V. L. Popov. *Contact Mechanics and Friction.* Springer Berlin Heidelberg, Berlin, Heidelberg, 2010.

[126] B. Cappella and G. Dietler. Force-distance curves by atomic force microscopy. *Surface Science Reports*, 34(1-3):1–104, 1999.

[127] D. Moerman, N. Sebaihi, S. E. Kaviyil, P. Leclère, R. Lazzaroni, and O. Douhéret. Towards a unified description of the charge transport mechanisms in conductive atomic force microscopy studies of semiconducting polymers. *Nanoscale*, 6:10596, 2014.

[128] Á. Rodríguez-Rodríguez, M. Soccio, D. E. Martínez-Tong, T. A. Ezquerra, B. Watts, and M.-C. García-Gutiérrez. Competition between phase separation and structure confinement in P3HT/PCDTBT heterojunctions: Influence on nanoscale charge transport. *Polymer*, 77:70–78, 2015.

[129] M. Dante, J. Peet, and T. Q. Nguyen. Nanoscale charge transport and internal structure of bulk heterojunction conjugated polymer/fullerene solar cells by scanning probe microscopy. *Journal of Physical Chemistry C*, 112(18):7241–7249, 2008.

[130] Q. S. Li, G. Y. H. Lee, C. N. Ong, and C. T. Lim. AFM indentation study of breast cancer cells. *Biochemical and Biophysical Research Communications*, 374(4):609–613, 2008.

[131] H. Ladjal, J. L. Hanus, A. Pillarisetti, C. Keefer, A. Ferreira, and J. P. Desai. Atomic force microscopy-based single-cell indentation: Experimentation and finite element simulation. *2009 IEEE/RSJ International Conference on Intelligent Robots and Systems, IROS 2009*, pages 1326–1332, 2009.

[132] H.-J. Butt, B. Cappella, and M. Kappl. Force measurements with the atomic force microscope: Technique, interpretation and applications. *Surf. Sci. Rep.*, 59(1-6):1–152, 2005.

[133] D. Maugis. Adhesion of spheres: The JKR-DMT transition using a dugdale model. *J. Colloid Interface Sci.*, 150(1):243–269, 1992.

[134] D. Tabor. Surface forces and surface interactions. *J. Colloid Interface Sci.*, 58(1):2–13, 1977.

[135] P. Schön, K. Bagdi, K. Molnár, P. Markus, B. Pukánszky, and G. Julius Vancso. Quantitative mapping of elastic moduli at the nanoscale in phase separated polyurethanes by AFM. *European Polymer Journal*, 47(4):692–698, 2011.

[136] J. Erath, S. Schmidt, and A. Fery. Characterization of adhesion phenomena and contact of surfaces by soft colloidal probe AFM. *Soft Matter*, 6(7):1432, 2010.

[137] J. Song, D. Tranchida, and G. J. Vancso. Contact mechanics of UV/Ozone-treated PDMS by AFM and JKR testing: Mechanical performance from nano- to micrometer length scales. *Macromolecules*, 41(18):6757–6762, 2008.

[138] M. E. Dokukin and I. Sokolov. Quantitative mapping of the elastic modulus of soft materials with HarmoniX and PeakForce QNM AFM modes. *Langmuir*, 28(46):16060–71, 2012.

[139] Y. Sun, B. Akhremitchev, and G. C. Walker. Using the adhesive interaction between atomic force microscopy tips and polymer surfaces to measure the elastic modulus of compliant samples. *Langmuir*, 20(14):5837–5845, 2004.

[140] M. P. Nikiforov and S. B. Darling. Improved conductive atomic force microscopy measurements on organic photovoltaic materials via mitigation of contact area uncertainty. *Prog. Photovoltaics*, 21(7):1433–1443, 2013.

[141] A. W. Knoll. Nanoscale contact-radius determination by spectral analysis of polymer roughness images. *Langmuir*, 29(45):13958–66, 2013.

[142] A. Bietsch, M. A. Schneider, M. E. Welland, and B. Michel. Electrical testing of gold nanostructures by conducting atomic force microscopy. *J. Vac. Sci. Technol. B Microelectron. Nanom. Struct.*, 18(3):1160, 2000.

[143] K. Daeinabi and M. H. Korayem. Indentation analysis of nano-particle using nano-contact mechanics models during nano-manipulation based on atomic force microscopy. *J. Nanoparticle Res.*, 13(3):1075–1091, 2010.

[144] W. Oliver and G. Pharr. An improved technique for determining hardness and elastic modulus using load and displacement sensing indentation experiments. *J. Mater. Res.*, 7(06):1564–1583, 1992.

[145] X. Li, H. Gao, C. J. Murphy, and K. K. Caswell. Nanoindentation of silver nanowires. *Nano Lett.*, 3(11):1495–1498, 2003.

[146] V. M. Masterson and X. Cao. Evaluating particle hardness of pharmaceutical solids using AFM nanoindentation. *International Journal of Pharmaceutics*, 362(12):163 – 171, 2008.

[147] E. Barthel. Adhesive elastic contacts: JKR and more. *J. Phys. D. Appl. Phys.*, 41(16):163001, 2008.

[148] M. Chyasnavichyus, S. L. Young, and V. V. Tsukruk. Probing of polymer surfaces in the viscoelastic regime. *Langmuir*, 2014.

[149] D. A. Kamkar, M. Wang, F. Wudl, and T. Q. Nguyen. Single nanowire OPV properties of a fullerene-capped P3HT dyad investigated using conductive and photoconductive AFM. *ACS Nano*, 6(2):1149–1157, 2012.

[150] O. G. Reid, K. Munechika, and D. S. Ginger. Space charge limited current measurements on conjugated polymer films using conductive atomic force microscopy. *Nano Lett.*, 8(6):1602–1609, 2008.

[151] L. Yang, C. Kuegeler, K. Szot, A. Ruediger, and R. Waser. The influence of copper top electrodes on the resistive switching effect in TiO_2 thin films studied by conductive atomic force microscopy. *Applied Physics Letters*, 95(1):013109, 2009.

[152] N. K. Unsworth, I. Hancox, C. A. Dearden, T. Howells, P. Sullivan, R. Lilley, J. Sharp, and T. S. Jones. Highly conductive spray deposited poly (3, 4-ethylenedioxythiophene): poly (styrenesulfonate) electrodes for indium tin oxide-free small molecule organic photovoltaic devices. *Applied Physics Letters*, 103(17):173304, 2013.

[153] H. Cohen, C. Nogues, D. Uilien, S. Daube, R. Naaman, and D. Porath. Electrical characterization of self-assembled single- and double-stranded DNA monolayers using conductive AFM. *Faraday Discuss*, 131:367–402, 2006.

[154] S. Hunter and T. D. Anthopoulos. Observation of unusual, highly conductive grain boundaries in high-mobility phase separated organic semiconducting blend films probed by lateral-transport conductive-AFM. *Advanced Materials*, 25(31):4320–4326, 2013.

[155] C. Musumeci, A. Liscio, V. Palermo, and P. Samorì. Electronic characterization of supramolecular materials at the nanoscale by conductive atomic force and Kelvin probe force microscopies. *Mater. Today*, 17(10):504–517, 2014.

[156] G. A. MacDonald, P. A. Veneman, D. Placencia, and N. R. Armstrong. Electrical property heterogeneity at transparent conductive oxide/organic semiconductor interfaces: Mapping contact ohmicity using conducting-tip atomic force microscopy. *ACS nano*, 6(11):9623–9636, 2012.

[157] W. C. Tsoi, P. G. Nicholson, J. S. Kim, D. Roy, T. L. Burnett, C. E. Murphy, J. Nelson, D. D. C. Bradley, J.-S. Kim, and F. A. Castro. Surface and subsurface morphology of operating nanowire:fullerene solar cells revealed by photoconductive-AFM. *Energy & Environmental Science*, 4(9):3646, 2011.

[158] M. Guide, X. D. Dang, and T. Q. Nguyen. Nanoscale characterization of tetrabenzoporphyrin and fullerene-based solar cells by photoconductive atomic force microscopy. *Advanced Materials*, 23(20):2313–2319, 2011.

[159] D. C. Coffey, O. G. Reid, D. B. Rodovsky, G. P. Bartholomew, and D. S. Ginger. Mapping local photocurrents in polymer/fullerene solar cells with photoconductive atomic force microscopy. *Nano Lett.*, 7(3):738–44, mar 2007.

[160] X.-D. Dang, A. Mikhailovsky, and T.-Q. Nguyen. Measurement of nanoscale external quantum efficiency of conjugated polymer:fullerene solar cells by photoconductive atomic force microscopy. *Applied Physics Letters*, 97(11):113303, 2010.

[161] C. J. Takacs, S. D. Collins, J. A. Love, A. A. Mikhailovsky, D. Wynands, G. C. Bazan, T.-Q. Nguyen, and A. J. Heeger. Mapping orientational order in a bulk heterojunction solar cell with polarization-dependent photoconductive atomic force microscopy. *ACS Nano*, 8(8):8141–8151, 2014.

[162] R. García. Dynamic atomic force microscopy methods. *Surface Science Reports*, 47(6-8):197–301, 2002.

[163] J. P. Cleveland, B. Anczykowski, A. E. Schmid, and V. B. Elings. Energy dissipation in tapping-mode atomic force microscopy. *Appl. Phys. Lett.*, 72(20):2613–2615, 1998.

[164] Y. Martin, D. W. Abraham, and H. K. Wickramasinghe. High-resolution capacitance measurement and potentiometry by force microscopy. *Appl. Phys. Lett.*, 52(13):1103–1105, 1988.

[165] C. Bohm, F. Saurenbach, P. Taschner, C. Roths, and E. Kubalek. Voltage contrast in integrated circuits with 100 nm spatial resolution by scanning force microscopy. *J. Phys. D*, 26:1801–1805, 1993.

[166] Y. Liang, D. a. Bonnell, W. D. Goodhue, D. D. Rathman, and C. O. Bozler. Observation of electric field gradients near field-emission cathode arrays. *Appl. Phys. Lett.*, 66(9):1147, 1995.

[167] J. E. Stern, B. D. Terris, H. J. Mamin, and D. Rugar. Deposition and imaging of localized charge on insulator surfaces using a force microscope. *Appl. Phys. Lett.*, 53(26):2717–2719, 1988.

[168] B. D. Terris. Localized charge force microscopy. *J. Vac. Sci. Technol. A Vacuum, Surfaces, Film.*, 8(1):374, 1990.

[169] M. Jaquith, E. M. Muller, and J. A. Marohn. Time-resolved electric force microscopy of charge trapping in polycrystalline pentacene. *J. Phys. Chem. B*, 111(27):7711–7714, 2007.

[170] D. C. Coffey and D. S. Ginger. Time-resolved electrostatic force microscopy of polymer solar cells. *Nat. Mater.*, 5(9):735–740, 2006.

[171] P. A. Cox, M. S. Glaz, J. S. Harrison, S. R. Peurifoy, D. C. Coffey, and D. S. Ginger. Imaging charge transfer state excitations in polymer/fullerene solar cells with time-resolved electrostatic force microscopy. *J. Phys. Chem. Lett.*, pages 2852–2858, 2015.

[172] R. Giridharagopal, G. E. Rayermann, G. Shao, D. T. Moore, O. G. Reid, A. F. Tillack, D. J. Masiello, and D. S. Ginger. Submicrosecond time resolution atomic force microscopy for probing nanoscale dynamics. *Nano Lett.*, 12(2):893–8, 2012.

[173] G. Li, B. Mao, F. Lan, and L. Liu. Practical aspects of single-pass scan Kelvin probe force microscopy. *Rev. Sci. Instrum.*, 83(11):113701, 2012.

[174] C. S. S. R. Kumar. *Surface Science Tools for Nanomaterials Characterization.* Springer Berlin Heidelberg, Berlin, Heidelberg, 2015.

[175] S. Liu, X. Ma, B. Wang, X. Shang, W. Wang, and X. Yu. Nanostructure-dependent interfacial interactions between poly(3-hexylthiophene) and graphene oxide. *Macromolecules*, 48(16):5791–5798, 2015.

[176] A. Liscio, V. Palermo, and P. Samorì. Probing local surface potential of quasi-one-dimensional systems: A KPFM study of P3HT nanofibers. *Advanced Functional Materials*, 18(6):907–914, 2008.

[177] K. Okamoto, K. Yoshimoto, Y. Sugawara, and S. Morita. KPFM imaging of Si(1 1 1) $5\sqrt{3} \times 5\sqrt{3}$ -Sb surface for atom distinction using NC-AFM. *Appl. Surf. Sci.*, 210(1-2 SPEC.):128–133, 2003.

[178] Y. Leng, C. C. Williams, L. C. Su, and G. B. Stringfellow. Atomic ordering of GaInP studied by Kelvin probe force microscopy. *Applied Physics Letters*, 66(10):1264, 1995.

[179] G. H. Enevoldsen, T. Glatzel, M. C. Christensen, J. V. Lauritsen, and F. Besenbacher. Atomic scale Kelvin probe force microscopy studies of the surface potential variations on the TiO_2(110) surface. *Physical Review Letters*, 100(23):2–5, 2008.

[180] Y. Rosenwaks, R. Shikler, T. Glatzel, and S. Sadewasser. Kelvin probe force microscopy of semiconductor surface defects. *Physical Review B*, 70(8):085320, 2004.

[181] H. Shin, B. Lee, C. Kim, H. Park, D.-K. Min, J. Jung, S. Hong, and S. Kim. Measurement and visualization of doping profile in silicon using Kelvin probe force microscopy (KPFM). *Electronic Materials Letters*, 2(2):127–133, 2005.

[182] E. Koren, Y. Rosenwaks, J. E. Allen, E. R. Hemesath, and L. J. Lauhon. Nonuniform doping distribution along silicon nanowires measured by Kelvin probe force microscopy and scanning photocurrent microscopy. *Applied Physics Letters*, 95(9):092105, 2009.

[183] A. Kikukawa, S. Hosaka, and R. Imura. Silicon pn junction imaging and characterizations using sensitivity enhanced Kelvin probe force microscopy. *Applied Physics Letters*, 66(25):3510, 1995.

[184] A. Doukkali, S. Ledain, C. Guasch, and J. Bonnet. Surface potential mapping of biased pn junction with kelvin probe force microscopy: application to cross-section devices. *Applied Surface Science*, 235(4):507–512, 2004.

[185] W. Melitz, J. Shen, A. C. Kummel, and S. Lee. Kelvin probe force microscopy and its application. *Surface Science Reports*, 66(1):1–27, 2011.

[186] S. Watanabe, Y. Fukuchi, M. Fukasawa, T. Sassa, A. Kimoto, Y. Tajima, M. Uchiyama, T. Yamashita, M. Matsumoto, and T. Aoyama. In situ KPFM imaging of local photovoltaic characteristics of structured organic photovoltaic devices. *ACS Applied Materials & Interfaces*, 6(3):1481–1487, 2014.

[187] E. J. Spadafora, R. Demadrille, B. Ratier, and B. Grevin. Imaging the carrier photogeneration in nanoscale phase segregated organic heterojunctions by Kelvin probe force microscopy. *Nano Letters*, 10(9):3337–3342, 2010.

[188] R. Shikler, M. Chiesa, and R. H. Friend. Photovoltaic performance and morphology of polyfluorene blends: The influence of phase separation evolution. *Macromolecules*, 39(16):5393–5399, 2006.

[189] E. M. Tennyson, J. L. Garrett, J. A. Frantz, J. D. Myers, R. Y. Bekele, J. S. Sanghera, J. N. Munday, and M. S. Leite. Nanoimaging of open-circuit voltage in photovoltaic devices. *Adv. Energy Mater.*, pages 1–8, 2015.

[190] M. Chiesa, L. Bürgi, J.-s. Kim, R. Shikler, R. H. Friend, and H. Sirringhaus. Correlation between surface photovoltage and blend morphology in polyfluorene-based photodiodes. *Nano Lett.*, 5(4):559–563, 2005.

[191] M. Takihara, T. Takahashi, and T. Ujihara. Minority carrier lifetime in polycrystalline silicon solar cells studied by photoassisted Kelvin probe force microscopy. *Appl. Phys. Lett.*, 93(2):021902, 2008.

[192] G. Shao, M. S. Glaz, F. Ma, H. Ju, and D. S. Ginger. Intensity-Modulated Scanning Kelvin Probe Microscopy for Probing Recombination in Organic Photovoltaics. *ACS Nano*, 8(10):10799–10807, oct 2014.

[193] I. Hancox. *Utilising High Work Function Metal Oxides as Hole Extracting Layers for Organic Photovoltaic Cells*. PhD thesis, 2013.

[194] I. Hancox, P. Sullivan, K. Chauhan, N. Beaumont, L. Rochford, R. Hatton, and T. Jones. The effect of a MoO_x hole-extracting layer on the performance of organic photovoltaic cells based on small molecule planar heterojunctions. *Org. Electron.*, 11(12):2019–2025, 2010.

[195] G. Sauerbrey. Verwendung von Schwingquarzen zur Wagungdiinner Schichten und zur Mikrowagung. *Zeitschrift fur Phys.*, 155:206–222, 1959.

[196] M. S. Tyler, I. M. Nadeem, and R. A. Hatton. An electrode design rule for high performance top-illuminated organic photovoltaics. *Materials Horizons*, 2016.

[197] X. Li, W. Cai, J. An, S. Kim, J. Nah, D. Yang, R. Piner, A. Velamakanni, I. Jung, E. Tutuc, S. K. Banerjee, L. Colombo, and R. S. Ruoff. Large-area synthesis of high-quality and uniform graphene films on copper foils. *Science (80-.).*, 324(5932):1312–1314, 2009.

[198] N. R. Wilson, A. J. Marsden, M. Saghir, C. J. Bromley, R. Schaub, G. Costantini, T. W. White, C. Partridge, A. Barinov, P. Dudin, A. M. Sanchez, J. J. Mudd, M. Walker, and G. R. Bell. Weak mismatch epitaxy and structural feedback in graphene growth on copper foil. *Nano Res.*, 6(2):99–112, 2013.

[199] N. Sahu, B. Parija, and S. Panigrahi. Fundamental understanding and modeling of spin coating process: A review. *Indian J. Phys.*, 83(4):493–502, 2009.

[200] Thin Film Devices. Catalogue Prices. `http://tfdinc.com/Wordpress2/catalog-prices/`, Accessed on 05/05/2016.

[201] D. Neerinck and T. Vink. Depth profiling of thin ITO films by grazing incidence X-ray diffraction. *Thin Solid Films*, 278(1-2):12–17, 1996.

[202] C. A. Clifford and M. P. Seah. Quantification issues in the identification of nanoscale regions of homopolymers using modulus measurement via AFM nanoindentation. *Applied Surface Science*, 252(5):1915–1933, 2005.

[203] J. E. Sader, J. W. M. Chon, and P. Mulvaney. Calibration of Rectangular Atomic Force Microscope Cantilevers. *Rev. Sci. Instrum.*, 70(10):3967–3969, 1999.

[204] J. Brujic, R. I. Hermans Z, S. Garcia-Manyes, K. a. Walther, J. M. Fernandez, and R. I. Z. Hermans. Dwell-time distribution analysis of polyprotein unfolding using force-clamp spectroscopy. *Biophys. J.*, 92(8):2896–2903, 2007.

[205] L. Wildling, C. Rankl, T. Haselgrübler, H. J. Gruber, M. Holy, A. H. Newman, M. F. Zou, R. Zhu, M. Freissmuth, H. H. Sitte, and P. Hinterdorfer. Probing binding pocket of serotonin transporter by single molecular force spectroscopy on living cells. *Journal of Biological Chemistry*, 287(1):105–113, 2012.

[206] D. Tranchida, S. Piccarolo, and M. Soliman. Nanoscale mechanical characterization of polymers by AFM nanoindentations: Critical approach to the elastic characterization. *Macromolecules*, 39(13):4547–4556, 2006.

[207] Asylum Research. PolyHeater. `http://www.asylumresearch.com/Products/PolyHeater/PolyHeater.shtml`, Accessed on 20/07/2016.

[208] R. De Bettignies, J. Leroy, M. Firon, and C. Sentein. Accelerated lifetime measurements of P3HT:PCBM solar cells. *Synthetic Metals*, 156(7-8):510–513, 2006.

[209] V. Shrotriya, G. Li, Y. Yao, C.-W. Chu, and Y. Yang. Transition metal oxides as the buffer layer for polymer photovoltaic cells. *Appl. Phys. Lett.*, 88(7):073508, 2006.

[210] ThorLabs. 4-Wavelength High-Power LED Source. `https://www.thorlabs.de/newgrouppage9.cfm?objectgroup_id=3836`, Accessed on 26/08/2016.

[211] DolanJenner. B and BX Type (Glass) Fiber Optic Assemblies. `http://www.dolan-jenner.com/Pro/B&BX_Type.htm`, Accessed on 27/08/2016.

[212] I. Zorić, M. Zäch, B. Kasemo, and C. Langhammer. Gold, platinum, and aluminum nanodisk plasmons: Material independence, subradiance, and damping mechanisms. *ACS Nano*, 5(4):2535–2546, 2011.

[213] J. Sun, K. Pimcharoen, S. R. Wagner, P. M. Duxbury, and P. Zhang. Nanoscale imaging of dense fiber morphology and local electrical response in conductive regioregular poly(3-hexylthiophene). *Org. Electron.*, 15(2):441–448, 2014.

[214] M. S. Skilbeck, a. J. Marsden, G. Cao, I. a. Kinloch, R. J. Young, R. S. Edwards, and N. R. Wilson. Multimodal microscopy using 'half and half' contact mode and ultrasonic force microscopy. *Nanotechnology*, 25(33):335708, 2014.

[215] K. Kanai, K. Koizumi, S. Ouchi, Y. Tsukamoto, K. Sakanoue, Y. Ouchi, and K. Seki. Electronic structure of anode interface with molybdenum oxide buffer layer. *Org. Electron. physics, Mater. Appl.*, 11(2):188–194, 2010.

[216] R. Schlaf, H. Murata, and Z. Kafafi. Work function measurements on indium tin oxide films. *J. Electron Spectros. Relat. Phenomena*, 120(1-3):149–154, 2001.

[217] C. A. Grant, A. Alfouzan, T. Gough, P. C. Twigg, and P. D. Coates. Nanoscale temperature sependent visco-elastic properties of polyethylene terephthalate (PET) using atomic force microscope (AFM). *Micron*, 44:174–178, 2013.

[218] D. W. Pohl. Some design criteria in scanning tunneling microscopy. *IBM Journal of Research and Development*, 30(4):417–427, 1986.

[219] A. Alexeev, J. Loos, and M. M. Koetse. Nanoscale electrical characterization of semiconducting polymer blends by conductive atomic force microscopy. *Ultramicroscopy*, 106(3):191–199, 2006.

[220] D. Tahk, H. H. Lee, and D. Y. Khang. Elastic moduli of organic electronic materials by the buckling method. *Macromolecules*, 42:7079–7083, 2009.

[221] W. Pasveer, J. Cottaar, C. Tanase, R. Coehoorn, P. Bobbert, P. Blom, D. de Leeuw, and M. Michels. Unified description of charge-carrier mobilities in disordered semiconducting polymers. *Phys. Rev. Lett.*, 94(20):206601, 2005.

[222] D. Chirvase, Z. Chiguvare, M. Knipper, J. Parisi, V. Dyakonov, and J. C. Hummelen. Temperature dependent characteristics of poly(3 hexylthiophene)-fullerene based heterojunction organic solar cells. *J. Appl. Phys.*, 93(6):3376–3383, 2003.

[223] P. Pingel and D. Neher. Comprehensive picture of p-type doping of P3HT with the molecular acceptor F4TCNQ. *Phys. Rev. B - Condens. Matter Mater. Phys.*, 87(11):1–9, 2013.

[224] C. Wang, D. T. Duong, K. Vandewal, J. Rivnay, and A. Salleo. Optical measurement of doping efficiency in poly(3-hexylthiophene) solutions and thin films. *Phys. Rev. B - Condens. Matter Mater. Phys.*, 91(8):1–7, 2015.

[225] P. W. M. Blom, M. J. M. de Jong, and M. G. van Munster. Electric-field and temperature dependence of the hole mobility in poly(p-phenylene vinylene). *Physical Review B*, 55(2):R656–R659, 1997.

[226] W. Ma, C. Yang, X. Gong, K. Lee, and A. J. Heeger. Thermally stable, efficient polymer solar cells with nanoscale control of the interpenetrating network morphology. *Adv. Funct. Mater.*, 15:1617–1622, 2005.

[227] V. Coropceanu, J. Cornil, D. A. da Silva Filho, Y. Olivier, R. Silbey, and J.-L. Brédas. Charge transport in organic semiconductors. *Chem. Rev.*, 107:926–952, 2007.

[228] P. Pingel, A. Zen, R. D. Abellón, F. C. Grozema, L. D. Siebbeles, and D. Neher. Temperature-resolved local and macroscopic charge carrier transport in thin P3HT layers. *Adv. Funct. Mater.*, 20(14):2286–2295, 2010.

[229] M. Kanari, H. Kawamata, T. Wakamatsu, and I. Ihara. Intermolecular elastic and plastic characteristics of organic phthalocyanine thin films evaluated by nanoindentation. *Applied Physics Letters*, 90(6):061921, 2007.

[230] P. Sullivan, T. S. Jones, A. J. Ferguson, and S. Heutz. Structural templating as a route to improved photovoltaic performance in copper phthalocyanine/-fullerene (C60) heterojunctions. *Appl. Phys. Lett.*, 91(23):2005–2008, 2007.

[231] L. Huang, C. Liu, X. Qiao, H. Tian, Y. Geng, and D. Yan. Tunable field-effect mobility utilizing mixed crystals of organic molecules. *Adv. Mater.*, 23(30):3455–3459, 2011.

[232] R. W. I. de Boer, M. E. Gershenson, A. F. Morpurgo, and V. Podzorov. Organic single-crystal field-effect transistors. *Phys. status solidi*, 201(6):1302–1331, 2004.

[233] K. Xiao, Y. Liu, G. Yu, and D. Zhu. Influence of the substrate temperature during deposition on film characteristics of copper phthalocyanine and field-effect transistor properties. *Appl. Phys. A Mater. Sci. Process.*, 77(3-4):367–370, 2003.

[234] G. Laby and T. H. Kaye. *Tables of Physical and Chemical Constants*. Longman, London, UK, 15th edition, 1993.

[235] M. a. Hopcroft, W. D. Nix, and T. W. Kenny. What is the Young's Modulus of Silicon? *J. Microelectromech. S.*, 19(2):229–238, 2010.

[236] D. J. Ellison, J. Y. Kim, D. M. Stevens, and C. D. Frisbie. Determination of quasi-fermi levels across illuminated organic donor/acceptor heterojunctions by kelvin probe force microscopy. *J. Am. Chem. Soc.*, 133(35):13802–13805, 2011.

[237] J. N. Barisci, R. Stella, G. M. Spinks, and G. G. Wallace. Study of the surface potential and photovoltage of conducting polymers using electric force microscopy. *Synth. Met.*, 124(2-3):407–414, 2001.

[238] C. G. Shuttle, B. O'Regan, A. M. Ballantyne, J. Nelson, D. D. C. Bradley, J. De Mello, and J. R. Durrant. Experimental determination of the rate law for charge carrier decay in a polythiophene: Fullerene solar cell. *Appl. Phys. Lett.*, 92(9):90–93, 2008.

[239] L. Bürgi, T. Richards, M. Chiesa, R. H. Friend, and H. Sirringhaus. A microscopic view of charge transport in polymer transistors. *Synth. Met.*, 146(3):297–309, 2004.

[240] O. Reid, G. Rayermann, D. Coffey, and D. S. Ginger. Imaging local trap formation in conjugated polymer solar cells: A comparison of time-resolved electrostatic force microscopy and scanning Kelvin probe. *J. Phys. Chem. C*, pages 1–6, 2010.

[241] M. J. Jaquith, J. E. Anthony, and J. a. Marohn. Long-lived charge traps in functionalized pentacene and anthradithiophene studied by time-resolved electric force microscopy. *J. Mater. Chem.*, 19(34):6116, 2009.

[242] S. Belaidi, P. Girard, and G. Leveque. Electrostatic forces acting on the tip in atomic force microscopy: Modelization and comparison with analytic expressions. *J. Appl. Phys.*, 81(3):1023–1030, 1997.

[243] D. Amarasinghe Vithanage, a. Devižis, V. Abramavičius, Y. Infahsaeng, D. Abramavičius, R. C. I. MacKenzie, P. E. Keivanidis, a. Yartsev, D. Hertel, J. Nelson, V. Sundström, and V. Gulbinas. Visualizing charge separation in bulk heterojunction organic solar cells. *Nat. Commun.*, 4:2334, 2013.

[244] D. Natali and M. Sampietro. Field-dependent mobility from space-charge-limited currentvoltage curves. *J. Appl. Phys.*, 92(9):5310, 2002.

[245] M. A. Naby, A. Zekry, F. El Akkad, and H. Ragaie. Dependence of dark current on zinc concentration in znxcd1- xs/znte heterojunctions. *Solar energy materials and solar cells*, 29(2):97–108, 1993.

[246] L. J. A. Koster, V. D. Mihailetchi, R. Ramaker, and P. W. M. Blom. Light intensity dependence of open-circuit voltage of polymer:fullerene solar cells. *Appl. Phys. Lett.*, 86(12):1–3, 2005.

[247] J. S. Kim, S. Wood, S. Shoaee, S. J. Spencer, F. a. Castro, W. C. Tsoi, C. E. Murphy, M. Sim, K. Cho, J. R. Durrant, and J.-S. Kim. Morphology-performance relationships in polymer/fullerene blends probed by complemen-

tary characterisation techniques effects of nanowire formation and subsequent thermal annealing. *J. Mater. Chem. C*, 3:9224–9232, 2015.

[248] A. Guerrero, N. F. Montcada, J. Ajuria, I. Etxebarria, R. Pacios, G. Garcia-Belmonte, and E. Palomares. Charge carrier transport and contact selectivity limit the operation of PTB7-based organic solar cells of varying active layer thickness. *J. Mater. Chem. A*, 1(39):12345, 2013.

[249] J. M. Szarko, B. S. Rolczynski, S. J. Lou, T. Xu, J. Strzalka, T. J. Marks, L. Yu, and L. X. Chen. Photovoltaic function and exciton/charge transfer dynamics in a highly efficient semiconducting copolymer. *Adv. Funct. Mater.*, 24(1):10–26, 2014.

[250] J. Guo, Y. Liang, J. Szarko, B. Lee, H. J. Son, B. S. Rolczynski, L. Yu, and L. X. Chen. Structure, dynamics, and power conversion efficiency correlations in a new low bandgap polymer: PCBM solar cell. *J. Phys. Chem. B*, 114(13):4746–4746, 2010.

[251] I. Etxebarria, A. Guerrero, J. Albero, G. Garcia-Belmonte, E. Palomares, and R. Pacios. Inverted vs standard PTB7:PC70BM organic photovoltaic devices. the benefit of highly selective and extracting contacts in device performance. *Org. Electron. physics, Mater. Appl.*, 15(11):2756–2762, 2014.

[252] H. Zang, Y. Liang, L. Yu, and B. Hu. Intra-molecular donor-acceptor interaction effects on charge dissociation, charge transport, and charge collection in bulk-heterojunction organic solar cells. *Adv. Energy Mater.*, 1(5):923–929, 2011.

[253] N. K. Elumalai and A. Uddin. Open circuit voltage of organic solar cells: an in-depth review. *Energy Environ. Sci.*, 5692:1–5, 2016.

[254] N. Honma, C. Munakata, H. Itoh, and T. Warabisako. Nondestructive measurement of minority carrier lifetimes in si wafers using frequency dependence of ac photovoltages. *Japanese journal of applied physics*, 25(5R):743, 1986.

[255] C. Munakata, H. Tamura, N. Honma, M. Ozawa, and K. Yagi. Ac surface photovoltages in p-type silicon wafers oxidized in water-free and wet ambients. *Japanese journal of applied physics*, 27(9R):1770, 1988.

[256] W. M. M. Lin, D. Bozyigit, O. Yarema, and V. Wood. Transient photovoltage measurements in nanocrystal-based solar cells. *The Journal of Physical Chemistry C*, 120(23):12900–12908, 2016.

[257] D. Rauh, A. Wagenpfahl, C. Deibel, and V. Dyakonov. Relation of open circuit voltage to charge carrier density in organic bulk heterojunction solar cells. *Appl. Phys. Lett.*, 98(13):1–4, 2011.

[258] Y. T. Set, M. D. Heinemann, E. Birgersson, and J. Luther. On the origin of the quadrant I semicircle in intensity-modulated photocurrent spectra of P3HT:PCBM bulk heterojunction solar cells: Evidence of degradation-related trap-assisted recombination. *J. Phys. Chem. C*, 117(16):7993–8000, 2013.

[259] M. I. A. Lourakis. A brief description of the Levenberg-Marquardt algorithm implemened by levmar. *Matrix*, 3:2, 2005.